ICTRS 2014

Third International Conference on
Telecommunications and Remote Sensing

Proceedings

Luxembourg, Grand Duchy of Luxembourg • 26-27 June 2014

Organized by: CREST

In Collaboration with: tudor PUBLIC RESEARCH CENTRE HENRI TUDOR

Under the auspices of: U.R.S.I.

Cooperating Organizations: ARISTOTLE UNIVERSITY OF THESSALONIKI, AMAKOTA

ICTRS 2014

Proceedings of the
Third International Conference on
Telecommunications and Remote Sensing

Luxembourg, Grand Duchy of Luxembourg
26-27 June 2014

Organized by
IICREST - Interdisciplinary Institute for Collaboration and Research on Enterprise Systems and Technology

In Collaboration with
TUDOR – Public Research Centre Henri Tudor

Cooperating Organizations
AUTH - Aristotle University of Thessaloniki
AMAKOTA Ltd.

Under the Auspices of
URSI - International Union of Radio Science

Edited by Blagovest Shishkov

Graphics Production by Canka Petrova

Printed in Bulgaria

ISBN: 978-989-758-033-8

Depósito Legal: 374970/14

http://www.ictrs.org

secretariat@iicrest.org

BRIEF CONTENTS

KEYNOTE SPEAKER

Francois Lefeuvre

CNRS

France

CHAIR AND PROGRAM COMMITTEE

CHAIR

Blagovest Shishkov, Bulgarian Academy of Sciences, Bulgaria

PROGRAM COMMITTEE

Oleksiy Agapitov, Taras Shevchenko Kyiv National University, Ukraine

Catherine Algani, CNAM, France

Mauro Assis, Brazilian Committee of URSI, Brazil

Krassimir Atanassov, Bulgarian Academy of Sciences, Bulgaria

Boncho Balabanov, NBU, Bulgaria

Vera Behar, Bulgarian Academy of Sciences, Bulgaria

Maurice Bellanger, CNAM, France

Lyubka Doukovska, Bulgarian Academy of Sciences, Bulgaria

Yoshiharu Fuse, USEF, Japan

Ivan Garvanov, Bulgarian Academy of Sciences, Bulgaria

Mihail Iliev, University of Ruse "Angel Kanchev", Bulgaria

Hristo Kabakchiev, Sofia University St. Kliment Ohridski, Bulgaria

Dorina Kabakchieva, UNWE, Bulgaria

Kazuya Kobayashi, Chuo University, Japan

Mesut Kartal, Istanbul Technical University, Turkey

Mohamed Latrach, ESEO, France

Andon Lazarov, Burgas Free University, Bulgaria

Frank Little, Texas A & M University, USA

Marco Luise, University of Pisa, Italy

Olga Maltseva, Institute of Physics, Southern Federal University, Russia

Andrea Massa, University of Trento, Italy

Galia Marinova, Technical University of Sofia, Bulgaria

PROGRAM COMMITTEE (CONT.)

Wolfgang Mathis, Leibniz Universitaet Hannover , Germany

Lyudmila Mihaylova, Lancaster University, UK

T**omohiko Mitani**, Kyoto University, Japan

Tadao Nagatsuma, Osaka University, Japan

Shoichi Narahashi, NTT DOCOMO Inc., Japan

Marin Nenchev, Technical University of Sofia, Bulgaria

Martin O'Droma, University of Limerick, Ireland

Takashi Ohira, Toyohashi University of Technology, Japan

Jacques Palicot, SUPELEC, France

Hermann Rohling, Hamburg University of Technology, Germany

Sana Salous, Durham University, UK

Hamit Serbest, Cukurova University, Turkey

Naoki Shinohara, Kyoto University, Japan

Boris Shishkov, IICREST, Bulgaria

Alexander Shmelev, Russian Academy of Sciences, Russia

Angela Slavova, Bulgarian Academy of Sciences, Bulgaria

Jun-Ichi Takada, Tokyo Institute of Technology, Japan

Hiroyuki Tsuji, NIICT, Japan

Marten Van Sinderen, University of Twente, The Netherlands

Satoshi Yagitani, Kanazawa University, Japan

Tsuneki Yamasaki, Nihon University, Japan

BEST PAPERS SELECTION

The authors of around three selected papers presented at ICTRS'14
will be invited to submit revised and extended versions of their papers
to a special issue of the international journal
ANNALS OF TELECOMMUNICATIONS

FOREWORD

This book contains the proceedings of ICTRS 2014 - the Third International Conference on Telecommunications and Remote Sensing, held in Luxembourg, Grand Duchy of Luxembourg, on 26-27 June 2014. The proceedings consist of 17 high-quality research and experience papers that have not been published previously.

The conference has been organized and sponsored by the Interdisciplinary Institute for Collaboration and Research on Enterprise Systems and Technology (IICREST) in collaboration with the Public Research Centre Henri Tudor (TUDOR). Cooperating organizations have been Aristotle University of Thessaloniki (AUTH) and AMAKOTA Ltd.

ICTRS 2014 is performed under the auspices of the International Union of Radio Science (URSI). The conference covers topics relevant to the work in a number of URSI Commissions, namely Commission A, Commission B, Commission C, Commission D, Commission E, Commission F, Commission G, Commission H and Commission K. All this has inspired and influenced the scientific program of the conference that is concerned with the international developments and applications in the following areas:

(i) Radio-Communications and Signal Processing
(ii) Electronics and Photonics
(iii) Electromagnetic Environment and Interference
(iv) Solar Power Satellite Systems
(v) Remote Sensing
(vi) Electromagnetic Fields and Waves
(vii) Context Awareness

As seen from the above areas, the first four ones are mainly concerned with Telecommunications, while the others are mainly concerned with Remote Sensing and Context Awareness. This research orientation as well as the ICTRS' 'heritage' clearly show that even though ICTRS has adopted the URSI research agenda, it is also spreading its influence to a broader audience including all those researchers and practitioners who are interested in the topics of the conference. It is seen as well that since the start in 2011 well until now, we have been successful in establishing a small but focused Community of experienced academicians and practitioners who are inspiring the ICTRS developments. These developments are considered useful not only for URSI but also in general for the Telecommunications Community.

Considering two types of submissions, namely invited paper submissions and regular paper submissions, we have selected, based on a review process driven by rigorous quality standards, 17 papers with authors from 10 countries in 4 continents. 11 of these papers were selected for a 30-minutes oral presentation (Full Papers) and 6 papers were selected for a 20-minutes oral presentation (Short Papers). In addition, two expert presentations will be delivered by experienced specialists, with abstracts published in the current proceedings.

FOREWORD (CONT.)

In terms of participants and quality of papers, the ICTRS 2014 event is comparable to the previous ones and this indicates for a stable development which we aim at sustaining and reinforcing in the future. The published papers are a good selection representing work concerning different relevant topics, touching upon: Intelligent Methods of Radio Signals and Systems, Wave Propagation and Remote Sensing, Solar Power Satellite Systems, Context Awareness, and so on.

Further, the authors of around three selected papers presented at ICTRS'14 will be invited to submit revised and extended versions of their papers to a special issue of the international journal ANNALS OF TELECOMMUNICATIONS, published by Springer-Verlag.

Finally, the high quality of the ICTRS 2014 program is enhanced by a Keynote Lecture, delivered by a distinguished guest: Prof. Dr. Francois Lefeuvre who is a renowned experts in Geophysics and outstanding representative of the URSI Community (former URSI President). Prof. Lefeuvre who is also a good friend of mine and former colleague, is famous for developing analysis techniques for waves and turbulence in space plasmas. He was involved in several wave experiments embarked on satellites.

Building an interesting and successful program for the conference required the dedicated efforts of many people. We firstly thank the Authors whose research results are recorded here. We turn with special gratitude to the Program Committee for their reviews and support. We are certainly grateful to the Organizer, IICREST and its logistics partner, AMAKOTA Ltd., for the excellent organization. We thank SCITEPRESS for their willingness to publish the current proceedings. And with regard to the proceedings preparation, we have to mention also the excellent collaboration with Canka Petrova (who worked on behalf of IICREST in close collaboration with the Publisher, SCITEPRESS) on compiling the book. Last but not least, we thank the Keynote Speaker for his invaluable contribution and for taking the time to synthesize and deliver his talk. We would be happy if IICREST continues with organizing further editions of ICTRS, under the auspices of URSI!

We wish you all an inspiring conference and enjoyable stay in the beautiful city of Luxembourg. We look forward to seeing you next year, for the Fourth International Conference on Telecommunications and Remote Sensing (ICTRS 2015), details of which will be made available at http://www.ictrs.org.

Blagovest Shishkov
Bulgarian Academy of Sciences
President of Bulgarian URSI Committee
Chair of ICTRS 2014

CONTENTS

KEYNOTE SPEAKER

Application of the Radio-Window Concept to the Propagation of VLF and MF Waves through Night Time Ionosphere Above Powerful VLF Transmitters

Francois Lefeuvre
LPC2E / CNRS, 3A, Avenue de la Recherche Scientifique, 45071 Orléans cedex 2, France
lefeuvre@cnrs-orleans.fr

Keywords: VLF transmitter, MF waves

Abstract: Surprisingly, the propagation of radio waves through the ionosphere is still not completely understood. This has been recently pointed out from night time observations made by the DEMETER satellite (~700 km altitude) over powerful VLF ground-based transmitters used for communications with submarines. If it seems quite reasonable to observe high-power densities of VLF waves over geographical areas located at latitudes slightly below the ones of the VLF transmitters and their conjugated regions, it is difficult to explain: (i) the geographical extension of the VLF observations, and (ii) high-power densities of MF waves (lightning-generated whistlers) observed in the ~2. – 2.5 MHz band, over the same geographical areas than for VLF waves. The mechanism proposed to explain those observations is based on the radio-windows concept. The propagation characteristics of radio waves are derived from the Appleton-Hartree formula. The refractive index n2 is a function of the X = fpe2/f2 and Y= fce/f parameters (with f the wave frequency, fpe the electron plasma frequency and fce the electron gyrofrequency). Under given conditions for propagation, upgoing rays which reach the altitude of the X = 1 plasma cut-off are not reflected but converted to another propagation mode. As an example, for a propagation from below the ionosphere up to the 700 km altitude, assuming a given night time electron density profile, numerical simulations show that a 25 kHz VLF waves crosses a X = 1 plasma cut-off at ~ 90 km altitude (the entry into the ionosphere) whereas a 2.2 MHz MF wave crosses a first X = 1 plasma cut-off at ~ 250 km altitude (entry into the ionosphere) and a second one at ~ 400 km altitude (output from the ionosphere). The half angles of the transmission cones at the X=1 plasma cut-offs depend on the level of wave heating at those altitudes and so on the increases in collision frequencies generated by powerful VLF ground-based transmitters. Numerical simulations show that: (1) in the VLF frequency range, the wave heating being maximum at the altitude of the Ordinary mode resonance region, i.e. just above the X = 1 plasma cut-off, the half angle of the transmission cone may reach several dozens degrees, (2) in the MF frequency range, the wave heating being maximum at the altitude where the product of the electronic density and the collision frequency is maximum, the opening of the transmission cones strongly depend on the relative altitudes of the maximum heating and of the X=1 plasma cut-offs.

Brief Bio François Lefeuvre is a CNRS Research Director Emeritus at the LPC2E laboratory (Laboratoire de Physique et Chimie de l'Environnement et de l'Espace) of the French National Centre for Scientific Research (CNRS) and the University of Orleans. He is presently Past President of URSI (International Union of Radio Science). He obtained his first thesis in 1970 at the "Groupe de Recherche Ionospherique", Saint-Maur des Fossés, received a fellowship from ESRO (now ESA) for studying natural ELF and VLF emissions in the magnetosphere at the Physics Department of

the Sheffield University in UK (1970), got a permanent position at CNRS in 1972 and obtained is second thesis (thèse d'état) in 1977 at the University of Orleans. In 1979/1980 he was a visiting scientist in the Radio Science Group at the Stanford University. He has published scientific papers in several domains including radio wave propagation within the ionosphere and the magnetosphere, inverse problems, signal analysis, risk management. He was Co-Investigator for several space missions (GEOS, AUREOL 3, INTERBALL, DEMETER), Principal Investigator for a wave experiment on the INTERBALL mission, and PI mission for the TARANIS project. He was Director of LPCE (Laboratoire de Physique et Chimie de l'Environnement) from 1994 to 2003, chaired the ESA Space Weather Working Team (2002-2005) and was President of URSI (International Union of Radio Science) from 2005 to 2008 then from 2009 to 2011

PAPERS

Full Papers

Radar Cross Section Analysis of a Terminated, Semi-Infinite Parallel-Plate Waveguide with Four-Layer Material Loading

Kazuya Kobayashi
Department of Electrical, Electronic, and Communication Engineering, Chuo University
1-13-27 Kasuga, Bunkyo-ku, Tokyo 112-8551, Japan
kazuya@tamacc.chuo-u.ac.jp

Keywords: Wiener-Hopf technique, scattering and diffraction, radar cross section, cavity

Abstract: A rigorous radar cross section (RCS) analysis of a terminated, semi-infinite parallel-plate waveguide with four-layer material loading is carried out for both E and H polarizations using the Wiener-Hopf technique. Introducing the Fourier transform for the unknown scattered field and applying boundary conditions in the transform domain, the problem is formulated in terms of the simultaneous Wiener-Hopf equations. The Wiener-Hopf equations are solved via the factorization and decomposition procedure leading to the exact solution. The scattered field in the real space is evaluated by taking the Fourier inverse of the solution in the transform domain. Numerical examples on the RCS are presented for various physical parameters and far field scattering characteristic of the waveguide are discussed in detail.

1 INTRODUCTION

Analysis of the scattering from open-ended metallic waveguide cavities has received much attention recently in connection with the prediction and reduction of the radar cross section (RCS) of a target (Lee and Marhefka, 1989; Stone, 1990; Bernard, Pelosi, and Ufimtsev, 1995). This problem serves as a simple model of duct structures such as jet engine intakes of aircrafts and cracks occurring on surfaces of general complicated bodies. Hence, investigation of the scattering mechanism in case of the presence of open cavities is an important subject in the area of the RCS prediction and reduction.

A number of scientists have thus far analyzed the diffraction problems involving various two- and three-dimensional (2-D and 3-D) cavities by means of high-frequency ray techniques and numerical methods (Lee and Ling, 1989). It appears, however, that the solutions obtained by these approaches are not uniformly valid for arbitrary cavity dimensions. The Wiener-Hopf technique (Noble, 1958; Mittra and Lee, 1971; Kobayashi, 1990) is one of the powerful approaches for analyzing wave scattering and diffraction problems associated with canonical geometries, and it is mathematically rigorous in the sense that the edge condition, required for the uniqueness of the solution, is explicitly incorporated into the analysis. It is known that the Wiener-Hopf technique can be effectively applied to cavity scattering problems with high accuracy, and there are some important contributions to studies on the cavity RCS based on the Wiener-Hopf technique (Büyükaksoy, Birbir, and Erdoğan, 1995; Çetiner, Büyükaksoy, and Güneş, 2000).

In our previous papers, we have considered a terminated, semi-infinite parallel-plate waveguide with three-layer material loading as an example of canonical 2-D cavities, and carried out a rigorous RCS analysis with the aid of the Wiener-Hopf technique (Koshikawa and Kobayashi, 1997, 2000). It has been verified that our final solutions are valid over a broad frequency range and can be used for validating numerical methods and high-frequency ray techniques. As an important generalization to the analysis in our previous papers (Koshikawa and Kobayashi, 1997, 2000), we shall consider in this paper a 2-D cavity formed by a terminated, semi-infinite parallel-plate waveguide with four-layer material loading, and analyze the plane wave diffraction for both E and H polarizations by means of the Wiener-Hopf technique. Our final solution is

shown to be uniformly valid for arbitrary waveguide dimensions. Since the analytical details are already published elsewhere (Shang and Kobayashi, 2009a, 2009b), we shall summarize main results in this paper.

The time factor is assumed to be $e^{-i\omega t}$ and suppressed throughout this paper.

2 WIENER-HOPF ANALYSIS OF THE E POLARIZATION

2.1 Formulation of the Problem

We consider the diffraction of an E-polarized plane wave by a terminated, semi-infinite parallel-plate waveguide with four-layer material loading, as shown in Figure 1, where the waveguide plates are infinitely thin, perfectly conducting, and uniform in the y-direction. The material layers $\mathrm{I}(-d_1 < z < -d_2)$, $\mathrm{II}(-d_2 < z < -d_3)$, $\mathrm{III}(-d_3 < z < -d_4)$, and $\mathrm{IV}(-d_4 < z < -d_5)$ are characterized by the relative permittivity/permeability $(\varepsilon_{rm}, \mu_{rm})$ for $m = 1$, 2, 3, and 4, respectively.

Let the total electric field $\phi^t(x,z)$ $[\equiv E_y^t(x,z)]$ be

$$\phi^t(x,z) = \phi^i(x,z) + \phi(x,z), \tag{1}$$

where $\phi^i(x,z)$ is the incident field defined by

$$\phi^i(x,z) = e^{-ik(x\sin\theta_0 + z\cos\theta_0)} \tag{2}$$

for $0 < \theta_0 < \pi / 2$ with k $[\equiv \omega(\varepsilon_0\mu_0)^{1/2}]$ being the free-space wavenumber. We shall assume that the vacuum is slightly lossy as in $k = k_1 + ik_2$ with $0 < k_2 \ll k_1$, and take the limit $k_2 \to +0$ at the end of analysis. Let us define the Fourier transform of the scattered field with respect to z as

$$\Phi(x,\alpha) = (2\pi)^{-1/2}\int_{-\infty}^{\infty}\phi(x,z)e^{i\alpha z}dz,$$
$$\alpha = \mathrm{Re}\,\alpha + i\,\mathrm{Im}\,\alpha\ (\equiv \sigma + i\tau). \tag{3}$$

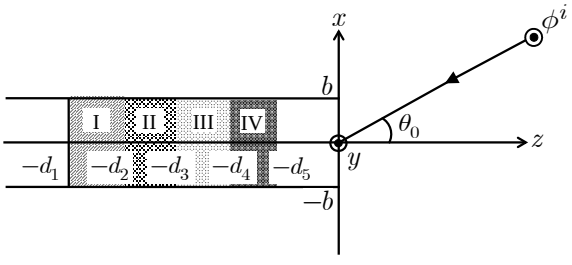

Figure 1: Geometry of the problem.

Taking the Fourier transform of the 2-D Helmholtz equation and solving the resultant transformed wave equations, we derive, after application of the boundary conditions, that

$$\begin{aligned}\Phi(x,\alpha) &= \Psi_{(+)}(\pm b,\alpha)e^{\mp\gamma(x\mp b)} \text{ for } x \gtrless \pm b,\\ &= \Psi_{(+)}(b,\alpha)\frac{\sinh\gamma(x+b)}{\sinh 2\gamma b}\\ &\quad - \Psi_{(+)}(-b,\alpha)\frac{\sinh\gamma(x-b)}{\sinh 2\gamma b}\\ &\quad - \frac{1}{b}\sum_{n=1}^{\infty}\frac{c_{5n}^e(\alpha)}{\alpha^2+\gamma_n^2}\sin\frac{n\pi}{2b}(x+b)\\ &\quad - \frac{1}{b}\sum_{m=1}^{4}\sum_{n=1}^{\infty}\frac{c_{mn}^e(\alpha)}{\alpha^2+\Gamma_{mn}^2}\\ &\qquad \cdot\sin\frac{n\pi}{2b}(x+b) \text{ for } |x| < b,\end{aligned} \tag{4}$$

where $\gamma = (\alpha^2 - k^2)^{1/2}$ with $\mathrm{Re}\,\gamma > 0$, and

$$\Psi_{(+)}(\pm b,\alpha) = (1/2)[U_{(+)}^e(\alpha) \pm V_{(+)}^e(\alpha)], \tag{5}$$

$$\gamma_n = [(n\pi/2b)^2 - k^2]^{1/2}, \tag{6}$$

$$\Gamma_{mn} = [(n\pi/2b)^2 - \mu_{rm}\varepsilon_{rm}k^2]^{1/2},\quad m = 1,2,3,4. \tag{7}$$

In (4), $c_{mn}^e(\alpha)$ for $m = 1$, 2, 3, 4, 5 are unknown coefficients introduced due to the existence of material layers, and their definition is omitted.

Applying boundary conditions in the Fourier transform domain appropriately, it is found the functions $U_{(+)}^e(\alpha)$ and $V_{(+)}^e(\alpha)$ in (5) satisfy the simultaneous Wiener-Hopf equations

$$\begin{aligned}J_-^{de}(\alpha) &= -\frac{U_{(+)}^e(\alpha)}{M^e(\alpha)} - \sum_{n=1,\mathrm{odd}}^{\infty}\frac{n\pi}{b^2}\\ &\quad\cdot\left[\frac{c_{5n}^e(\alpha)}{\alpha^2+\gamma_n^2} + \sum_{m=1}^{4}\frac{c_{mn}^e(\alpha)}{\alpha^2+\Gamma_{mn}^2}\right],\end{aligned} \tag{8}$$

$$\begin{aligned}J_-^{se}(\alpha) &= -\frac{V_{(+)}^e(\alpha)}{N^e(\alpha)} + \sum_{n=2,\mathrm{even}}^{\infty}\frac{n\pi}{b^2}\\ &\quad\cdot\left[\frac{c_{5n}^e(\alpha)}{\alpha^2+\gamma_n^2} + \sum_{m=1}^{4}\frac{c_{mn}^e(\alpha)}{\alpha^2+\Gamma_{mn}^2}\right].\end{aligned} \tag{9}$$

In (8) and (9), $J_-^{de,se}(\alpha)$ are unknown functions corresponding to the surface currents induced on the waveguide plates, and $M^e(\alpha)$ and $N^e(\alpha)$ are the kernel functions defined by

$$M^e(\alpha) = \gamma^{-1}e^{-\gamma b}\cosh\gamma b, \tag{10}$$

$$N^e(\alpha) = \gamma^{-1}e^{-\gamma b}\sinh\gamma b. \tag{11}$$

2.2 Solution of the Wiener-Hopf Equations

The kernel functions defined by (10) and (11) are factorized as (Koshikawa and Kobayashi, 1997)

$$M^e(\alpha) = M^e_+(\alpha)M^e_-(\alpha), \tag{12}$$

$$N^e(\alpha) = N^e_+(\alpha)N^e_-(\alpha), \tag{13}$$

where

$$\begin{aligned} M^e_+(\alpha)\,[= M^e_-(-\alpha)] &= (\cos kb)^{1/2} e^{i\pi/4}(k+\alpha)^{-1/2} \\ &\cdot \exp\left\{(i\gamma b\,/\,\pi)\ln\left[\left(\alpha-\gamma\right)/\,k\right]\right\} \\ &\cdot \exp\left\{(i\alpha b\,/\,\pi)\left[1-C\right.\right. \\ &\left.\left.+\ln(\pi\,/\,2kb)+i\pi\,/\,2\right]\right\} \\ &\cdot \prod_{n=1,\text{odd}}^{\infty}\left(1+\alpha\,/\,i\gamma_n\right)e^{2i\alpha b/n\pi}, \end{aligned} \tag{14}$$

$$\begin{aligned} N^e_+(\alpha)\,[= N^e_-(-\alpha)] &= (\sin kb\,/\,k)^{1/2} \\ &\cdot \exp\left\{(i\gamma b\,/\,k)\ln[(\alpha-\gamma)\,/\,k]\right\} \\ &\cdot \exp\left\{(i\alpha b\,/\,\pi)\left[1-C\right.\right. \\ &\left.\left.+\ln(2\pi\,/\,kb)+i\pi\,/\,2\right]\right\} \\ &\cdot \prod_{n=2,\text{even}}^{\infty}\left(1+\alpha\,/\,i\gamma_n\right)e^{2i\alpha b/n\pi} \end{aligned} \tag{15}$$

with $C\ (=0.57721566\cdots)$ being Euler's constant.

We multiply both sides of (8) and (9) by $M^e_-(\alpha)$ and $N^e_-(\alpha)$, respectively and decompose the resultant equations. This yields, after some manipulations,

$$\frac{U^e_{(+)}(\alpha)}{b} = \frac{M^e_+(\alpha)}{b^{1/2}}\left[-\frac{A_e}{b\left(\alpha-k\cos\theta_0\right)} + \sum_{n=1}^{\infty}\frac{\delta^e_{2n-1}a^e_n p^e_n u^+_{en}}{b\left(\alpha+i\gamma_{2n-1}\right)}\right], \tag{16}$$

$$\frac{V^e_{(+)}(\alpha)}{b} = \frac{N^e_+(\alpha)}{b^{1/2}}\left[\frac{B_e}{b\left(\alpha-k\cos\theta_0\right)} + \sum_{n=1}^{\infty}\frac{\delta^e_{2n}b^e_n q^e_n v^+_{en}}{b\left(\alpha+i\gamma_{2n}\right)}\right], \tag{17}$$

where

$$a^e_n = \frac{[(n-1\,/\,2)\pi]^2}{bi\gamma_{2n-1}}, b^e_n = \frac{(n\pi)^2}{bi\gamma_{2n}}, \tag{18}$$

$$p^e_n = \frac{M^e_+(i\gamma_{2n-1})}{b^{1/2}}, q^e_n = \frac{N^e_+(i\gamma_{2n})}{b^{1/2}}, \tag{19}$$

$$\delta^e_n = \frac{\left[\rho_{3n}e^{-2\Gamma_{4n}(d_4-d_5)}-\rho_{4n}\right]e^{-2\gamma_n d_5}}{1-\rho_{3n}\rho_{4n}e^{-2\Gamma_{4n}(d_4-d_5)}}, \tag{20}$$

$$u^+_{en} = \frac{U^e_{(+)}(i\gamma_{2n-1})}{b}, v^+_{en} = \frac{U^e_{(+)}(i\gamma_{2n})}{b}, \tag{21}$$

$$A_e = -\left(\frac{2b}{\pi}\right)^{1/2}\frac{i\cos(kb\sin\theta_0)}{M^e_+(k\cos\theta_0)}, \tag{22}$$

$$B_e = \left(\frac{2b}{\pi}\right)^{1/2}\frac{\sin(kb\sin\theta_0)}{N^e_+(k\cos\theta_0)} \tag{23}$$

with

$$\rho_{3n} = \frac{(\mu_4\,/\,\mu_3)\Gamma_{3n}-\delta_{2n}\Gamma_{4n}}{(\mu_4\,/\,\mu_3)\Gamma_{3n}+\delta_{2n}\Gamma_{4n}}, \tag{24}$$

$$\rho_{4n} = \frac{\mu_4\gamma_n-\Gamma_{4n}}{\mu_4\gamma_n+\Gamma_{4n}}, \tag{25}$$

$$\delta_{2n} = \frac{1-\rho_{2n}e^{-2\Gamma_{3n}(d_3-d_4)}}{1+\rho_{2n}e^{-2\Gamma_{3n}(d_3-d_4)}}, \tag{26}$$

$$\rho_{2n} = \frac{(\mu_3\,/\,\mu_2)\Gamma_{2n}-\delta_{1n}\Gamma_{3n}}{(\mu_3\,/\,\mu_2)\Gamma_{2n}+\delta_{1n}\Gamma_{3n}}, \tag{27}$$

$$\delta_{1n} = \frac{1-\rho_{1n}e^{-2\Gamma_{2n}(d_2-d_3)}}{1+\rho_{1n}e^{-2\Gamma_{2n}(d_2-d_3)}}, \tag{28}$$

$$\rho_{1n} = \frac{(\mu_2\,/\,\mu_1)K_n-\Gamma_{2n}}{(\mu_2\,/\,\mu_1)K_n+\Gamma_{2n}}, \tag{29}$$

$$K_n = \frac{\Gamma_{1n}+e^{-2\Gamma_{1n}(d_1-d_2)}}{1-e^{-2\Gamma_{1n}(d_1-d_2)}}. \tag{30}$$

Equations (16) and (17) are the exact solutions to the Wiener-Hopf equations (8) and (9), respectively, but they are formal since the infinite series with the unknown coefficients u^+_{en} and v^+_{en} for $n=1,2,3,\cdots$ are involved. These unknowns can be determined with high accuracy by solving appropriate matrix equations numerically.

2.3 Scattered Field

The scattered field in the real space can be derived by taking the inverse Fourier transform of (4) in accordance with

$$\phi(x,z) = (2\pi)^{-1/2}\int_{-\infty+ic}^{\infty+ic}\Phi(x,\alpha)e^{-i\alpha z}d\alpha, \quad -k_2 < c < k_2\cos\theta_0. \tag{31}$$

Substituting (4) into (31) and evaluating the resultant integral for $|x| < b$ with the aid of (5), (16), and (17),

we find that the total field inside the waveguide is expressed in terms of the TE modes as in

$$\begin{aligned}\phi^t(x,z) &= \sum_{n=1}^{\infty} T_{1n}\sinh\Gamma_{1n}(z+d_1)\\ &\quad\cdot\sin\frac{n\pi}{2b}(x+b)\\ &\quad \text{for } -d_1 < z < -d_2,\\ &= \sum_{n=1}^{\infty}\Big[T_{mn}^{-}e^{\Gamma_{mn}(z+d_{m+1})}\\ &\quad -T_{mn}^{+}e^{-\Gamma_{mn}(z+d_m)}\Big]\sin\frac{n\pi}{2b}(x+b)\\ &\quad \text{for } -d_m < z < -d_{m+1}, m=2,3,4,\\ &= \sum_{n=1}^{\infty}\Big[T_{n}^{-}e^{\gamma_n(z+d_5)}\\ &\quad -T_{n}^{+}e^{-\gamma_n(z+d_5)}\Big]\sin\frac{n\pi}{2b}(x+b)\\ &\quad \text{for } -d_5 < z < 0, \end{aligned} \tag{32}$$

where the definition of the coefficients $T_{1n}, T_{mn}^{\pm}$, and $T_n^{\pm}$ is omitted.

Let us introduce the cylindrical coordinates $(\rho_{1,2},\theta_{1,2})$ centered at the waveguide edges $(x,z) = (\pm b, 0)$ as follows:

$$\begin{aligned} x-b &= \rho_1\sin\theta_1, z = \rho_1\cos\theta_1\\ &\quad \text{for } 0<\theta_1<\pi, \end{aligned} \tag{33}$$

$$\begin{aligned} x+b &= \rho_2\sin\theta_2, z = \rho_2\cos\theta_2\\ &\quad \text{for } -\pi<\theta_2<0. \end{aligned} \tag{34}$$

Evaluating (31) for $|x| > b$ with the aid of the saddle point method, the scattered far field is derived as

$$\begin{aligned}\phi(\rho_{1,2},\theta_{1,2}) &\sim \pm\Big[\Psi_{(+)}(\pm b, -k\cos\theta_{1,2})\\ &\quad -\tilde{\Phi}(\pm b, -k\cos\theta_{1,2})\Big]\\ &\quad\cdot k\sin\theta_{1,2}\frac{e^{i(k\rho_{1,2}-\pi/4)}}{(k\rho_{1,2})^{1/2}}\\ &\quad -e^{\mp ikb\sin\theta_0}\Bigg\{e^{-ik\rho_{1,2}\cos(\theta_{1,2}-\theta_0)}\\ &\quad\cdot F\left[(2k\rho_{1,2})^{1/2}\cos\frac{\theta_{1,2}+\theta_0}{2}\right]\\ &\quad +e^{-ik\rho_{1,2}\cos(\theta_{1,2}+\theta_0)}\\ &\quad\cdot F\left[(2k\rho_{1,2})^{1/2}\cos\frac{\theta_{1,2}+\theta_0}{2}\right]\Bigg\} \end{aligned} \tag{35}$$

for $x \gtrless \pm b$ as $k\rho_{1,2}\to\infty$, where

$$\tilde{\Phi}(\pm b,\alpha) = \frac{e^{\mp ikb\sin\theta_0} i(k+k\cos\theta_0)^{1/2}}{(2\pi)^{1/2}(\alpha+k)^{1/2}(\alpha-k\cos\theta_0)}, \tag{36}$$

and $F(\cdot)$ is the Fresnel integral defined by

$$F(x) = \frac{e^{-i\pi/4}}{\pi^{1/2}}\int_x^{\infty} e^{it^2}dt. \tag{37}$$

Equation (35) gives the scattered far field expression, which is uniformly valid in incidence angle θ_0 and observation angles $\theta_{1,2}$.

Taking into account the asymptotic expansion of the Fresnel integral, we can also derive a non-uniform asymptotic expression of the scattered far field with the result that

$$\begin{aligned}\phi(\rho,\theta) &\sim \phi^g(\rho,\theta)+\phi^d(\rho,\theta),\\ &\quad \theta_{1,2} \not\approx \pm\pi \mp \theta_0 \end{aligned} \tag{38}$$

for $k\rho\to\infty$, where (ρ,θ) are the cylindrical coordinate defined by

$$\begin{aligned} x &= \rho\sin\theta, z = \rho\cos\theta\\ &\quad \text{for } -\pi<\theta<\pi. \end{aligned} \tag{39}$$

In (38), $\phi^g(\rho,\theta)$ and $\phi^d(\rho,\theta)$ are the geometrical optics field and the diffracted field, respectively, given by

$$\begin{aligned}\phi^g(\rho,\theta) &= -e^{-ik\rho\cos(\theta-\theta_0)}\\ &\quad \text{for } -\pi<\theta_2<-\pi+\theta_0,\\ &= 0 \text{ for } -\pi+\theta_0<\theta_2<0,\\ &\quad 0<\theta_1<\pi-\theta_0,\\ &= -e^{-2ikb\sin\theta_0}e^{-ik\rho\cos(\theta+\theta_0)}\\ &\quad \text{for } \pi-\theta_0<\theta_1<\pi, \end{aligned} \tag{40}$$

$$\begin{aligned}\phi^d(\rho,\theta) &= \pm\Big[U_{(+)}^{e}(-k\cos\theta)\\ &\quad \pm V_{(+)}^{e}(-k\cos\theta)\Big]\\ &\quad\cdot k\sin\theta e^{\mp ikb\sin\theta}\frac{e^{i(k\rho-\pi/4)}}{2(k\rho)^{1/2}},\ \theta\gtrless 0. \end{aligned} \tag{41}$$

3 WIENER-HOPF ANALYSIS OF THE H POLARIZATION

We now consider the diffraction problem involving the same waveguide geometry for the H-polarized plane wave incidence. Following a procedure similar

to that presented in Section 2, we derive a scattered field representation in the Fourier transform domain as in

$$\begin{aligned}\Phi(x,\alpha) &= -\Psi'_{(+)}(\pm b,\alpha)\gamma^{-1}e^{\mp\gamma(x\mp b)} \\ &\qquad \text{for } x \gtrless \pm b, \\ &= \Psi'_{(+)}(b,\alpha)\frac{\cosh\gamma(x+b)}{\gamma\sinh 2\gamma b} \\ &\quad - \Psi'_{(+)}(-b,\alpha)\frac{\cosh\gamma(x-b)}{\gamma\sinh 2\gamma b} \\ &\quad - \frac{1}{b}\sum_{n=0}^{\infty}\nu_n\frac{c^h_{5n}(\alpha)}{\alpha^2+\gamma_n^2} \\ &\qquad \cdot\cos\frac{n\pi}{2b}(x+b) \\ &\quad - \frac{1}{b}\sum_{m=1}^{4}\sum_{n=0}^{\infty}\nu_n\frac{c^h_{mn}(\alpha)}{\alpha^2+\Gamma_{mn}^2} \\ &\qquad \cdot\cos\frac{n\pi}{2b}(x+b) \\ &\qquad\qquad \text{for } \left|x\right| < b, \end{aligned} \tag{42}$$

where $c^h_{mn}(\alpha)$ for $m = 1,2,3,4,5$ are unknown coefficients, and

$$\Psi'_{(+)}(\pm b,\alpha) = (1/2)[U^h_{(+)}(\alpha) \pm V^h_{(+)}(\alpha)], \tag{43}$$

$$\gamma_0 = -ik, \Gamma_{m0} = -i(\mu_m\varepsilon_m)^{1/2}k, \tag{44}$$

$$\begin{aligned}\nu_n &= 1/2,\ n = 0, \\ &= 1,\ n \geq 1. \end{aligned} \tag{45}$$

In (42), γ and γ_n, Γ_{mn} for $n \geq 1$ are known constants already defined in Section 2.1, whereas $U^h_{(+)}(\alpha)$ and $V^h_{(+)}(\alpha)$ in (43) are unknown functions. Applying boundary conditions and carrying out some manipulations, we can show that $U^h_{(+)}(\alpha)$ and $V^h_{(+)}(\alpha)$ satisfy the Wiener-Hopf equations

$$\begin{aligned}J^{dh}_-(\alpha) &= -\frac{U^h_{(+)}(\alpha)}{M^h(\alpha)} - \sum_{n=1,\text{odd}}^{\infty}\frac{2}{b} \\ &\quad \cdot\left[\frac{c^h_{5n}(\alpha)}{\alpha^2+\gamma_n^2} + \sum_{m=1}^{4}\frac{c^h_{mn}(\alpha)}{\alpha^2+\Gamma_{mn}^2}\right], \end{aligned} \tag{46}$$

$$\begin{aligned}J^{sh}_-(\alpha) &= -\frac{V^h_{(+)}(\alpha)}{N^h(\alpha)} + \sum_{n=0,\text{even}}^{\infty}\frac{2\nu_n}{b} \\ &\quad \cdot\left[\frac{c^h_{5n}(\alpha)}{\alpha^2+\gamma_n^2} + \sum_{m=1}^{4}\frac{c^h_{mn}(\alpha)}{\alpha^2+\Gamma_{mn}^2}\right], \end{aligned} \tag{47}$$

where

$$M^h(\alpha) = \gamma e^{-\gamma b}\cosh\gamma b, \tag{48}$$

$$N^h(\alpha) = \gamma e^{-\gamma b}\sinh\gamma b. \tag{49}$$

Equations (46) and (47) are solved by the factorization and decomposition procedure leading to the exact solution as in

$$\begin{aligned}U^h_{(+)}(\alpha) &= b^{1/2}M^h_+(\alpha)\left[-\frac{A_h}{b\left(\alpha - k\cos\theta_0\right)}\right. \\ &\quad \left. -\sum_{n=1}^{\infty}\frac{\delta^h_{2n-1}a^h_n p^h_n u^+_{hn}}{b\left(\alpha + i\gamma_{2n-1}\right)}\right], \end{aligned} \tag{50}$$

$$\begin{aligned}V^h_{(+)}(\alpha) &= b^{1/2}N^h_+(\alpha)\left[\frac{B_h}{b\left(\alpha - k\cos\theta_0\right)}\right. \\ &\quad \left. -\sum_{n=1}^{\infty}\frac{\nu_{2n-2}\delta^h_{2n-2}b^h_n q^h_n v^h_n}{b\left(\alpha + i\gamma_{2n-2}\right)}\right], \end{aligned} \tag{51}$$

where the definition of $\delta^{\boldsymbol{h}}_{\boldsymbol{n}}$ is omitted, and

$$a^h_n = (bi\gamma_{2n-1})^{-1}, b^h_n = (bi\gamma_{2n-2})^{-1}, \tag{52}$$

$$p^h_n = b^{1/2}M^h_+(i\gamma_{2n-1}), q^h_n = b^{1/2}N^h_+(i\gamma_{2n-2}), \tag{53}$$

$$u^+_{hn} = U^h_{(+)}(i\gamma_{2n-1}), v^+_{hn} = V^h_{(+)}(i\gamma_{2n-2}), \tag{54}$$

$$A_h = -\left(\frac{2b}{\pi}\right)^{1/2}\frac{k\sin\theta_0\cos(kb\sin\theta_0)}{M^h_+(k\cos\theta_0)}, \tag{55}$$

$$B_h = -\left(\frac{2b}{\pi}\right)^{1/2}\frac{ik\sin\theta_0\sin(kb\sin\theta_0)}{N^h_+(k\cos\theta_0)}, \tag{56}$$

$$\begin{aligned}M^h_+(\alpha)\ [&= M^h_-(-\alpha)] \\ &= (\cos kb)^{1/2}e^{i3\pi/4}(k+\alpha)^{1/2} \\ &\quad \cdot\exp\{(i\gamma b/\pi)\ln[(\alpha-\gamma)/k]\} \\ &\quad \cdot\exp\{(i\alpha b/\pi)[1-C \\ &\quad + \ln(\pi/2kb) + i\pi/2]\} \\ &\quad \cdot\prod_{n=1,\text{odd}}^{\infty}\left(1+\alpha/i\gamma_n\right)e^{2i\alpha b/n\pi}, \end{aligned} \tag{57}$$

$$\begin{aligned}N^h_+(\alpha)\ [&= N^h_-(-\alpha)] \\ &= (k\sin kb)^{1/2}\exp(i\pi/2) \\ &\quad \cdot\exp\{(i\gamma b/k)\ln[(\alpha-\gamma)/k]\} \\ &\quad \cdot\exp\{(i\alpha b/\pi)[1-C \\ &\quad + \ln(2\pi/kb) + i\pi/2]\} \\ &\quad \cdot(1+\alpha/i\gamma_0) \\ &\quad \cdot\prod_{n=2,\text{even}}^{\infty}\left(1+\alpha/i\gamma_n\right)e^{2i\alpha b/n\pi} \end{aligned} \tag{58}$$

with C being Euler's constant (see Section 2.2)..

The scattered field in the real space is evaluated by substituting (50) and (51) into (42) and taking the inverse Fourier transform according to the formula (31). In particular, the field inside the waveguide is

expressed in term of the TM modes, whereas the field outside waveguide is evaluated using the saddle point method leading to a far field expression. The details are omitted here.

4 NUMERICAL RESULTS AND DISCUSSION

In this section, we shall show illustrative numerical examples of the RCS to investigate the far field backscattering characteristics of the waveguide in detail. Since the problem considered here is of the 2-D scattering, the RCS per unit length is defined by

$$\frac{\sigma}{\lambda} = \lim_{\rho\to\infty}\left(k\rho\left|\phi^d \,/\, \phi^i\right|^2\right), \tag{59}$$

where λ is the free-space wavelength, ϕ^d is the diffracted field given by (41) for E polarization.

Figures 2 shows the normalized monostatic RCS $\sigma \,/\, \lambda$ as a function of incident angle θ_0, where the values of $\sigma \,/\, \lambda$ are plotted in decibels [dB] by computing $10\log_{10}\sigma \,/\, \lambda$. In order to investigate the scattering mechanism over a broad frequency range, we have carried out numerical computation for two typical values of the normalized waveguide aperture width $kb = 3.14$ and 31.4. For a fixed kb, the ratio

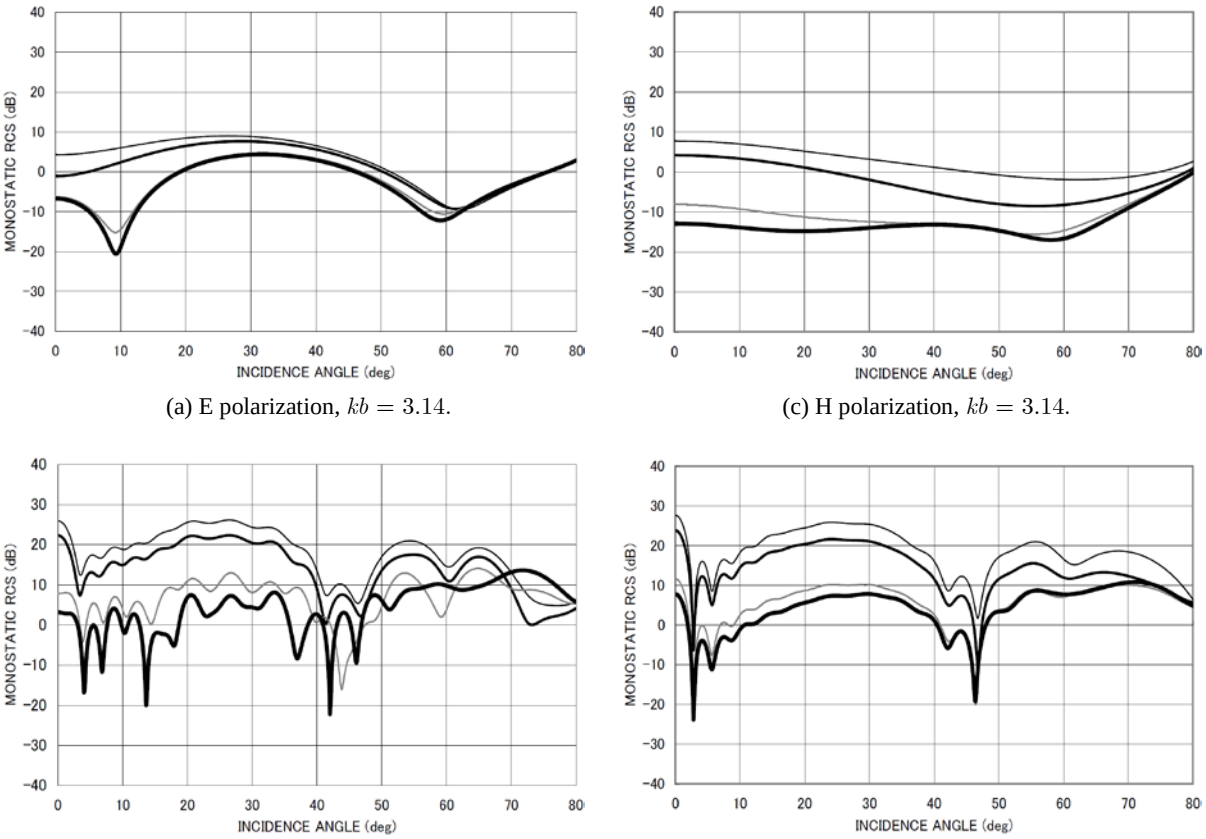

(a) E polarization, $kb = 3.14$.

(c) H polarization, $kb = 3.14$.

(b) E polarization, $kb = 31.4$.

(d) H polarization, $kb = 31.4$.

Figure 2: Monostatic RCS $\sigma \,/\, \lambda$ [dB] for $d_1 \,/\, 2b = 1.0,\ k\Delta = 0.628$.

——————: cavity with no loading (regions I-IV: vacuum).

——————: cavity with single-layer loading (region I: ferrite, regions II-IV: vacuum).

——————: cavity with three-layer loading (regions I-III: Emerson & Cuming AN-73, region IV: vacuum).

——————: cavity with four-layer loading (regions I-III: Emerson & Cuming AN-73, region IV: ferrite).

of the cavity depth d_1 to the waveguide aperture width $2b$ has been chosen as $d_1 / 2b = 1.0$. In numerical computation, we have chosen ferrite (single-layer material) (Lee and Ling, 1989) for region IV and Emerson & Cuming AN-73 (three-layer material) (Lee and Ling, 1989) for regions I-III to form the existing four-layer material loaded on the planar termination inside the waveguide. The material constants for ferrite (region IV) and Emerson & Cuming AN-73 (regions I-III) are $\varepsilon_4 = 2.4 + i1.25$, $\mu_4 = 1.6 + i0.9$ and $\varepsilon_1 = 3.14 + i10.0$, $\mu_1 = 1.0$, $\varepsilon_2 = 1.6 + i0.9$, $\mu_2 = 1.0$, $\varepsilon_3 = 1.4 + i0.35$, $\mu_3 = 1.0$, respectively. The thickness of the three-layer material (Emerson & Cuming AN-73) is chosen such that $d_1 - d_2 = d_2 - d_3 = d_3 - d_4$. The thickness of the ferrite is taken to be the same as the thickness of each layer of Emerson & Cuming AN-73 so that $d_1 - d_2 = d_2 - d_3 = d_3 - d_4 = d_4 - d_5$ $(= \Delta)$. The normalized layer thickness is chosen as $k\Delta = 0.628$. In order to investigate the effect of the four-layer loading in detail, we have also computed the RCS for the single-layer case (region I: ferrite, regions II-IV: vacuum) and the three-layer case (regions I-III: Emerson & Cuming AN-73, region IV: vacuum). The results for no material loading (regions I-IV: vacuum) have also been added to enable comparison.

We shall first investigate the RCS reduction characteristics by comparing the results for empty and loaded cavities. It is seen from Figure 2 that the monostatic RCS exhibits fairly large values for cavities with no material loading due to the interior irradiation, whereas the RCS is reduced for the case of material loading inside the cavities. We also observe that this RCS reduction is noticeable for larger cavities. By comparing the RCS results for material-loaded cavities between the single- and four-layer cases, it is found that the RCS reduction is more significant in the four-layer case. Comparing the results for the four-layer case with those for the three-layer case, more RCS reduction is seen in the four-layer case. From these characteristics, it is inferred that the multi-layer loading gives rise to better RCS reduction over a broad frequency range.

Let us now make some comparison of the RCS characteristics between two different polarizations. Comparing the RCS curves in Figures 2(a,b) for the E polarization with those in Figures 2(c,d) for the H polarization, we see differences in all numerical examples. In particular, the monostatic RCS for the H polarization oscillates rapidly in comparison to the E-polarized case. This difference is due to the fact that the edge diffraction depends on the incident polarization. We also see that, if the waveguide aperture opening is small as in $kb = 3.14$, there are great differences in the RCS characteristics between E and H polarizations. This is because the diffraction phenomena at low frequencies strongly depend on the incident polarization. It is also found that, with an increase of the waveguide aperture opening, the RCS for E and H polarizations exhibits close features to each other.

5 CONCLUSIONS

In this paper, we have carried out a rigorous RCS analysis of a terminated, semi-infinite parallel-plate waveguide with four-layer material loading with the aid of the Wiener-Hopf technique. Both E and H polarizations have been analyzed. The scattered field inside and outside the waveguide has been explicitly evaluated. It is to be noted that our final results presented in this paper are uniformly valid for arbitrary cavity dimensions.

We have shown numerical examples of the monostatic RCS for various physical parameters to discuss the far field backscattering characteristics of the waveguide in detail. In particular, it has been clarified that the multi-layer material loading inside the cavity plays an important role in the RCS reduction over a broad frequency range. We have also verified that the four-layer material loading gives rise to a better RCS reduction compared with the three-layer case. The results obtained in this paper serve as a reference solution and can be used for validating other commonly-used approximate methods such as high-frequency techniques and numerical methods.

REFERENCES

Lee, S.-W. and Marhefka, R. J. (1989). Data book of high-frequency RCS: Version 2. *Tech. Rep., Univ. Illinois, Urbana.*

Stone, W. R. (Ed.) (1990). *Radar Cross Sections of Complex Objects*. New York: IEEE Press.

Bernard, J. M. L., Pelosi, G., and Ufimtsev, P. Ya. (Eds.) (1995). Special Issue on Radar Cross Section of Complex Objects. *Ann. Telecommun.*, 50 (5-6).

Lee, S.-W. and Ling, H. (1989). Data book for cavity RCS: Version 1. *Tech. Rep., Univ. Illinois, Urbana, No. SWL 89-1.*

Noble, B. (1958). *Methods Based on the Wiener-Hopf Technique for the Solution of Partial Differential Equations*. London: Pergamon.

Mittra, R. and Lee, S.-W. (1971). *Analytical Techniques in the Theory of Guided Waves*. New York: Macmillan.

Kobayashi, K. (1990). Wiener-Hopf and modified residue calculus techniques. In Yamashita, E. (Ed.), *Analysis Methods for Electromagnetic Wave Problems* (Chap. 8). Boston: Artech House.

Büyükaksoy, A, Birbir, F., and Erdoğan, E. (1995). Scattering characteristics of a rectangular groove in a reactive surface. *IEEE Trans. Antennas and Propagat.*, 43, 1450-1458.

Çetiner, B. A., Büyükaksoy, A., and Güneş, F. (2000). Diffraction of electromagnetic waves by an open ended parallel plate waveguide cavity with impedance walls. *Progress In Electromagnetics Research*, 26, 165-197.

Koshikawa, S. and Kobayashi, K. (1997). Diffraction by a terminated, semi-infinite parallel-plate waveguide with three-layer material loading. *IEEE Trans. Antennas and Propagat.*, 45, 949-959.

Koshikawa, S. and Kobayashi, K. (2000). Diffraction by a terminated, semi-infinite parallel-plate waveguide with three-layer material loading; the case of H polarization. *Electromagnetic Waves & Electronic Systems*, 5, 13-23.

Shang, E. H. and Kobayashi, K. (2009a). Diffraction by a terminated, semi-infinite parallel-plate waveguide with four-layer material loading. *Progress In Electromagnetics Research B*, 12, 1-33.

Shang, E. H., and Kobayashi, K. (2009b). Diffraction by a terminated, semi-infinite parallel-plate waveguide with four-layer material loading: the case of H Polarization. *Progress In Electromagnetics Research B*, 12, 139-162.

Remote Sensing for Scientific Research in Earth Sciences in the Russian Far East

Evgeny Gordeev [1], Vera Naumova [2], and Sergey Diakov [3]
[1]*Institute of Volcanology and Seismology FEB RAS, Petropavlovsk-Kamchatsky, Russia*
[2]*Far East Geological Institute FEB RAS, Vladivostok, Russia*
[3]*Institute of Automation and Control Processes FEB RAS, Vladivostok, Russia*
gordeev@kscnet.ru,naumova@fegi.ru

Keywords: Earth science, satellite data, remote sensing.

Abstract: Long-term researches conducted by scientists from the institutes of the Russian Academy of Sciences have resulted in a large volume of data in Earth Sciences. The research data are systematized at the institutes. Archives, databases, Geo Information Systems, Data Retrieval Systems, and Digital Libraries have been establishing. Due to new methods for data collection, the amount of data increases constantly, the data acquisition becomes more efficient, and the change-over to whole new digital technologies of data collection, processing, distribution and using is almost complete. The Earth remote sensing space systems, systems of surface and aerial laser scanning, other digital and electrical geodetic equipment, digital areal cameras are used to get the initial data. The new digital and electronic environment for data in Earth Sciences makes it possible to use modern informational technologies.

Satellite data are widely used in geological and geophysical investigations. In order to encourage scientists in the Russian Far East to use satellite images, a system that provides data derived from satellite imagery for geological and geophysical investigations is being developed. This system is supposed to provide data from satellite imagery to users, IR-channels from AVHRR and MODIS radiometers, and measurements of visible channels from AQUA and TERRA, as well as LANDSAT.

1 INTRODUCTION

From time immemorial the Russian Far East has been attracting geologists and geophysicists due to its location in the global system of fold structures of the Pacific ore-tectonic belt and at the same time as the area of transition from the largest continent to the greatest ocean. It seemed that here exactly a scientist could find the solution for a lot of contentious issues in endogenic geology and reveal general regularities in order to increase the amount of tasks to be solved by developing of large theoretical problems. Indeed, travelling eastwards from the inner regions of the Asian continent to the Pacific Ocean, one can observe consistent change of Precambrian shield areas into Palaeozoic, Mesozoic and Cenozoic fold (orogenic) belts, then into depressions of modern margin-continental seas and into seismo-tectonic active volcanic island arcs and associated deep-sea trenches. And further is a wide deep-ocean floor, which is outwardly calm but shows active submarine tholeiite -basaltic volcanism. This is the most complete set of structures characterizing the transition from the ancient parts of a thick and extremely complex continental crust through its intermediate types to a thin ocean crust with a rather simple structure (Khanchuk et al.,2009).

2 SATELLITES AND SATELLITE DATA RECEIVING AND PROCESSING CENTERS

In the Far East, existing Earth Observation Satellite Systems and data processing technologies provide hundreds of millions of measurements of various ocean, atmosphere and land geophysical and space parameters every day.

There are two centers for the Natural Environment Satellite Monitoring in this region: the

center of the Russian Academy of Sciences (RAS) in Vladivostok and the Branch of Scientific and Research Centre on Space Hydrometeorology "Planeta" (SRC "Planeta") in Khabarovsk.

SRC "Planeta" is the leading organization in Russia on exploitation and development of national space systems for the hydro-meteorological, oceanographic, helio-geophysical and natural environment monitoring and also on receiving and processing of data from foreign satellites. It cooperates with national hydro-meteorological services and space agencies in more than 30 countries: USA, EU, Japan, India, China, Korea and etc. The Branch of SRC "Planeta" receives and processes the real-time data from meteorological satellites Meteor M-1, MTSAT-1R, MTSAT-2, POES NOAA, Terra, Aqua, Suomi NPP and RadarSat-1 satellite. The satellite imagery processing is aimed to make a weather forecast from the information on the atmosphere state and the Earth's surface physical parameters reconstruction.

The multiple-access regional center for the natural environment satellite monitoring of FEB RAS receives, holds and distributes satellite and relevant data for scientific investigations in the Russian Far East, makes the data processing automatic and integrates the data into global information systems, as well as conducts primary processing-correction, calibration and geographic reference of the imagery (Remote Sensing of Environment, 2013). Several receiving stations work simultaneously in the center. Using the ordering system, the customer is given temperature fields, reflection coefficients and other physical parameters in the form of instantaneous and composite measurements. Historically, the laboratory for satellite monitoring of the Institute of Automation and Control Processes of FEB RAS, on the base on which the center was established, was aimed to provide the data on the ocean surface temperatures fields to the Pacific Scientific-Research Fisheries Center and the Pacific Oceanological Institute of FEB RAS. This aim predetermined the choice of the polar-orbiting satellites: POES NOAA, AQUA, TERRA, FY-1C, FY-1D, MetOp, Meteor M-1, MTSAT-1R, MTSAT-2, FY-2B, FY-2C. Using these and other satellite Centers data, the researches solve geological and volcanological problems in the Russian Far East.

2.1 Volcanogenic Processes Analysis

Daily satellite monitoring of Kamchatka volcanoes, using MTSAT, NOAA (AVHRR), TERRA и AQUA (MODIS) imagery, is carried out to reveal the increase of volcanic activity, predict volcanic eruptions, and track on-going eruptions (Girina, 2013; Gordeev and Girina, 2014).

Volcanogenic process is analyzed in detail. The data from TERRA ASTER, LANDSAT and other satellites allow studying thermal anomalies, ash plumes, extrusive cones, distribution and morphology of eruptive products (lava and pyroclastic flows, tephras etc).

Detail analysis of volcanic processes (the development of thermal anomalies and the state of volcanoes) allows revealing, for example, a gradual decrease of activity at Kizimen Volcano in 2013, and vice versa a resumption of explosive activity at Karymsky Volcano. Different satellite imagery showed aerosol clouds and plumes, ash clouds and plumes, lava flows and their height and length.

2.2 The Development of a Satellite Monitoring System the Kurile Island

The territory of the Russian Far East hosts 66 active volcanoes, 36 of them on the Kurile Islands, 30 active volcanoes on the Kamchatka Peninsula. Though the Kuriles are almost uninhabited at the present time, the probable ash emissions from volcanic eruptions into the upper atmosphere are extremely dangerous to aviation. In 2003 SVERT (Sakhalin Volcanic Eruption Response Team) was established on the base of the Institute of Marine Geology and Geophysics of FEB RAS in cooperation with the Sakhalin Geophysical Survey of RAS and the Russian Federal Geological Fund "RosGeolFund" of the Federal Subsoil Agency RosNedra with the support from the Alaska Volcano Observatory (AVO, the University of Alaska Fairbanks). The SVERT members process the data from the MODIS/AQUA into one satellite imagery per day to have the information on the current state of the Kurile Islands volcanoes (Diakov and Rybin, 2013). Satellites do not provide nighttime images and prevent from observations of "hot spots", which are the eruption precursors.

The members of the Center for Regional Satellite Monitoring of Environment FEB RAS organized full automatic delivery of satellite data for the SVERT specialists.

The pseudocolor images for detection of gas and steam emissions, ash emissions and hot spots (in case of the nighttime satellite images), the monochrome images of 11micron and 12micron, 8 micron and 12 microns channels differential for ash clouds detection and the monochrome images of

3,75 micron and 11micron channels differential for hot spots detection are delivered.

In addition to the products developed on the basis of the TERRA MODIS and AQUA MODIS data, the analogous products developed on the basis of the AVHRR/POES NOAA data are delivered.

2.3 The Development of Technologies for Satellite Data Analysis in Order to Find the Solution of Problems of Structural Geology and Tectonics

The detection of linear structures, faults, tectonic blocks of various recycling rate, the definition of boundaries of different types geological structures and zones.

Usually to solve the problems of structural geology and tectonics based on the data from remote sensing we apply hyper-spectral method, using the data on the visible and near-IR spectrum and the ground temperature inversion. This technology does not fit the conditions of the Far East, therefore the main method to solve this problem is to detect the linear structure on the basis of the data from the channels of the visible band of electromagnetic spectrum and the data from the radar sounding.

One of the examples of such works, being carried out in the Far East, is the work of the researches of the Institute of Tectonics and Geophysics FEB RAS (Melnichenko et al., 2013). They estimated the absolute value of the relief gradient, analyzed the linear structure, investigated the morphometric characteristics of the bottom and the character of its deformations in Philippine Sea. They revealed that structurally the Philippine Sea is a very special, isolated part of the Pacific Ocean. Its west part comprises of fault structures of the ocean, which were renovated in the new Cenozoic Period of the Philippine Sea development. Its east part developed in sharply changed geodynamic conditions and is the newest overlaid structure.

2.4 The Remote Sensing Survey in the Russian Far East Ore-Bearing Areas for Minerogenic Reconstruction

The characteristic feature of the south-east of Russia is the abundance of the alluvial and the hard-rock gold occurrences and the platinum-group elements. More than 15 Late Mesozoic minerogenic belts and their fragments were revealed in the east of the continental part. The existence of not evident signs of Late Mesozoic intraplate magmatics zonal distribution allows assuming that location of the platinum-metal and the gold-bearing massifs within the raise areas is caused by the influence of homogeneous processes and their probable belonging to the single structure of the stagnate 410-670 km-deep mantle slab associated with the subduction zone. If we consider tectonic zones and belts to be dissipative structures, then we can apply the same methods of investigation. This approach opens the possibility of integration of the results from the remote space, geophysical and geochemical observations with the possibility of a formal test of hypotheses of a logic deposits location (Shevyrev, 2013).

2.5 The Development of the System Providing Satellite Measurements Data to the Far East Scientific Investigations in Geology

The usual source of satellite data to solve such problems are the U.S. Geological Survey's EarthExplorer and GloVis. The EarthExplorer and GloVis services provide an open access to a large amount of satellite data available upon the request. The request execution time for the full-resolution images can take up to three days, the formats for the results presentation could be of interest for the experts in satellite data processing and interpretation. At present time the data from satellite sounding are hardly used in the Far Eastern geological investigations. One of the ways to activate the use of satellite data is the decision to establish the System providing satellite measurements data to the Far Eastern investigations in the field of geology. We assume that this system will provide the access to the main satellite data useful for geological investigations such as: the satellite topography data, the infrared channels of the Advanced Very High Resolution Radiometer (AVHRR) and The Moderate Resolution Imaging Spectroradiometer (MODIS) data, the data from the visible channels of the TERRA MODIS and AQUA MODIS measurements, the data from the Landsat series satellites.

The specific features of this system should be the limited amount of satellite images because the geological objects are rather constant and the observation conditions for selected images are rather similar and this should make the search and comparison of satellite images easier. On the other hand, in order to make the immediate use of the data easier, we offer to use the GeoTIFF data formats for

the Geographic Information System (GIS) projects and the ESRI Grid format for the measurements results and digital products. This system is being developed in the Far East Geological Institute FEB RAS. In 2013 the functional prototype of the System, providing the access to the satellite topography data STRM and the data from Landsat 8, Landsat 7 satellites was realized. The functional prototype helps to investigate the data domain and work out the interaction of the Far East Geological Institute GIS portal with the other systems providing the access to satellite data (Diakov and Naumova, 2013).

We can distinguish the main application fields for the data and the data processing technologies of this System:

types of underlying surfaces classification (basalts, granites and so on) on data from the visible channels of MODIS, OLI (LANDSAT-8), ETM+ (LANDSAT-7);

heat capacity mapping of the earth's surface (the data from IR radiometers);

use of the satellite topography (STRM, Aster) data for geo-morphological analysis of the earth's surface, topographic bases generation and etc.;

search and analysis of geometric structures at the Earth's surface: faults, ring structures on the basis of satellite topography data and measurements in the visible spectrum;

"hot spots" and "hot" faults investigation on data from MODIS and AVHRR IR spectrum radiometers;

monitoring of gas composition penetrating into atmosphere through the earth's crust;

REFERENCES

Diakov S.E., Naumova V.V., 2013. Satellite data providing system for a investigations on the Far East of Russia // *Remote Sensing of Environment: Scientific and Applied Research in Asia-Pacific (RSAP2013): Abstracts of the International Conference, 24-27 September 2013, Vladivostok, Russia. Vladivostok: Dalnauka.*

Diakov S.E., Rybin A.V., 2013. Satellite monitoring of volcanic activity in the Kuril Islands // *Remote Sensing of Environment: Scientific and Applied Research in Asia-Pacific (RSAP2013): Abstracts of the International Conference, 24-27 September 2013, Vladivostok, Russia. – Vladivostok: Dalnauka.*

Khanchuk A.I. , Kemkin I.V, Golosubov V.V., 2009. Tectonics and regional geology// *The Far East Geological Institute. 50 years of Life. — Vladivostok: Dalnauka.*

Melnichenko Yu.F., Gilmanova G.Z., Rybas O.V., Sedin V.T.. 2013. Relief and geodynamics of the Philippine Sea floor. *The 8th All-Russian symposium "Geospheres physics", The reports' materials, September 2-6, Vladivostok.*

Multiple Access Centre for Regional Satellite Monitoring of Environment, FEB RAS, 2013 //*Remote Sensing of Environment: Scientific and Applied Research in Asia-Pacific (RSAP2013): Abstracts of the International Conference, 24-27 September 2013, Vladivostok, Russia. – Vladivostok: Dalnauka.*

Girina O.A. , 2013. Satellite monitoring of Bezymianny volcano, Kamchatka // *Remote Sensing of Environment: Scientific and Applied Research in Asia-Pacific (RSAP2013): Abstracts of the International Conference, 24-27 September 2013, Vladivostok, Russia. – Vladivostok: Dalnauka.*

Shevyrev S., Khomich V., Boriskina N., Shevyreva M., 2013. Remote sensing of ore-bearing areas of Russian Far East for mineragenic reconstruction // *Remote Sensing of Environment: Scientific and Applied Research in Asia-Pacific (RSAP2013): Abstracts of the International Conference, 24-27 September 2013, Vladivostok, Russia. Vladivostok: Dalnauka.*

Gordeev E. I., Girina O. A., 2014 Volcanoes are Hazardous for Aviation, *Herald of the Russian Academy of Sciences, Vol.84, No. 2, pp. 134-142.*

Wireless Power Transfer at Higher Frequency for SPS and for Commercial WPT

Naoki Shinohara[1]
[1]*Research Institute for Sustainable Humanosphere, Kyoto University, GOkasho, Uji, Kyoto, Japan*
shino@rish.kyoto-u.ac.jp

Keywords: Wireless Power Transfer, Microwave Power Transmission, Solar Power Satellite, Millimeter Wave

Abstract: One of the promising future power stations is a solar power satellite (SPS) station in geostationary orbit (36,000 km above the surface of Earth) that uses wireless microwave power-transfer technology. In this system, the power generated would be transmitted to the ground by a microwave beam. The SPS would be a very large satellite with a large transmitting phased-array antenna that would work at 2.45 or 5.8 GHz. The size of the transmitting antennas is theoretically determined by Maxwell's equations. However, we must reduce the size of the antennas to reduce the cost and to produce a small prototype satellite as a first step to the SPS. The only way to reduce the size of the antennas is to use a higher frequency. We developed rectennas that are optimized for 24 and 60 GHz transmission. In addition, we developed a monolithic microwave integrated circuit (MMIC) rectenna for 24 GHz transmission and with dimensions of 1 mm × 3 mm. The maximum radio-frequency to direct-current (RF-DC) conversion efficiency is 47.9% for a 210 mW microwave input power with a 120 Ω load. We also designed a rectenna for 60 GHz transmission whose maximum RF-DC conversion efficiency is 46.2% for a 80 mW input power at 60 GHz with a 100 Ω load. Finally, based on rectenna technology, we propose other satellite experiments.

1 INTRODUCTION

A solar power satellite (SPS) station is a very suitable application for a wireless power transfer (WPT) via radio waves, especially via microwaves (microwave power transfer or MPT). SPSs are one of the promising future power stations for a sustainable power source that uses solar cells (Mankins, 2014). Current SPS design envisions a 2 km diameter antenna that would transmit at 5.8 GHz in space. The beam efficiency between such a transmitting antenna and a 2 km receiving rectenna 36,000 km away is approximately 90% (Shinohara, 2014). The size of antennas is determined by Maxwell's equations and cannot be reduced (Shinohara, 2014). In working toward the SPS, we must carry out small-scale satellite experiments. The low Earth orbit (LEO) of 400 km would be used for such an experiment. If the small satellite system is the same as the SPS at 5.8 GHz, the antenna and the rectenna must each be approximately 200 m long. However, a 200 m antenna is too large for a small satellite; the size limit is more on the order of 10 m. Therefore, instead of simulating a SPS, we use a small satellite to study the other objectives of MPT.

The same problem arises with commercial applications of MPT. Theoretically, the size of antenna required is over 10 m in diameter for MPT over 1 km at 5.8 GHz with 90% beam efficiency. This size is too large for a commercial MPT system to compete with wired power transmission. This is the reason that no commercial MPT system exists in the world. Therefore, we propose WPT at a higher frequency, for example, 24 or 60 GHz. However, there are two problems with WPT at a higher frequency: (1) an increase in absorption by air and (2) a decrease in circuit efficiency and power. The latter problem can be solved by technical means.

2 DEVELOPMENT OF 24 AND 60 GHZ RECTENNA

At Kyoto University, we propose a wireless system that simultaneously transmits information and power in the millimeter wave range. Higher frequency

results in higher communication speed and lower antenna sizes. The first application considered is a fixed wireless access system proposed by NTT Corp., Japan (Seki, 2011).

First, we choose 24 GHz, which is in the industrial, science, and medical (ISM) band, and develop a rectifying circuit in the MPT receiver. We normally use a Schottky diode with $\lambda_g/4$ distributed line and a capacitance that is called a "single-shunt rectifier" and with theoretical radio-frequency to direct-current (RF-DC) conversion efficiency is 100%. For example, the maximum efficiency of the proposed single-shunt rectifier is over 90% at 2.45 GHz and is 80% at 5.8 GHz. For the millimeter wave system, we consider that the capacitance is a weak point that prevents optimizing the efficiency. Therefore, we propose a new single-shunt rectifier with a class-F load, which is composed of open stub resonators for even and odd harmonics, instead of the capacitance. The rectifying principle exploited by a conventional single-shunt rectifier and the class-F load rectifier is the same and both have a theoretical RF-DC conversion efficiency (with only one diode) of 100%.

The rectifying circuit is composed of a microstrip line and two diodes in parallel. Dimensions of the developed 24 GHz MMIC rectenna are 1 mm × 3 mm on GaAs [Fig. 1(a)], with a maximum RF-DC conversion efficiency of 47.9% for a 210 mW microwave input signal at 24 GHz with a 120 Ω load [Fig. 1(b)] (Hatano, 2013).

(a)

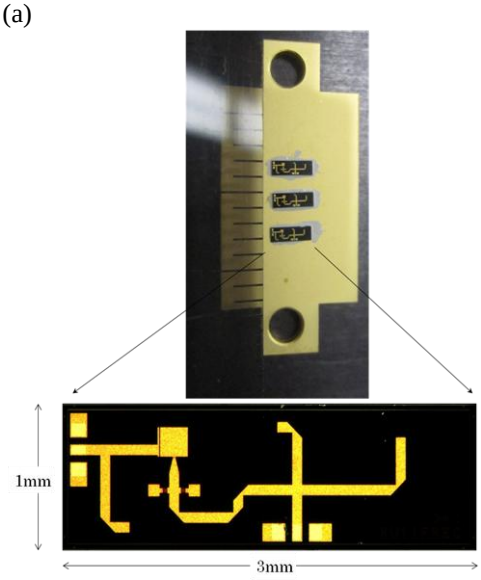

(b)

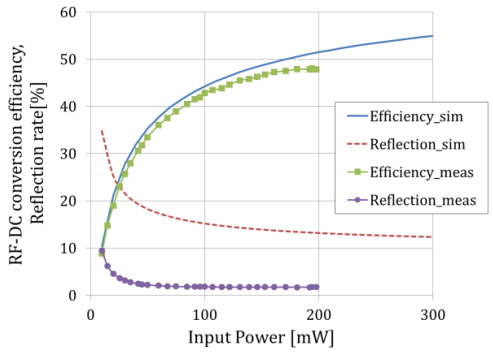

Figure 1 : (a) Developed 24 GHz MMIC rectenna and (b) RF-DC conversion efficiency (Hatano, 2013).

Next, we designed a rectifying circuit that operates at 60 GHz. The rectifying circuit is composed of a microstrip line on a Teflon substrate and two diodes connected in parallel. For the 60 GHz rectifying circuit, we focused on three points to increase the RF-DC conversion efficiency: (1) First is the length of the microstrip line between each diode with a through hall, which in turn is connected to ground plane. Upon changing the length of this microstrip line, the efficiency goes through a maximum and a minimum. (2) Second is the number of corresponding harmonics of the class-F load. We estimated a relationship between the number of corresponding harmonics of the class-F load and the efficiency, and concluded that to increase the efficiency, it is sufficient to use only one stub resonator for a fundamental wave. (3) Finally, the impedance of the class-F load. We increased the impedance of the class-F load. The rectifying circuit designed is shown in Fig. 2. An ADS simulation of the maximum RF-DC conversion gives an efficiency of 46.2% for 80 mW input power at 60 GHz with a 100 Ω load.

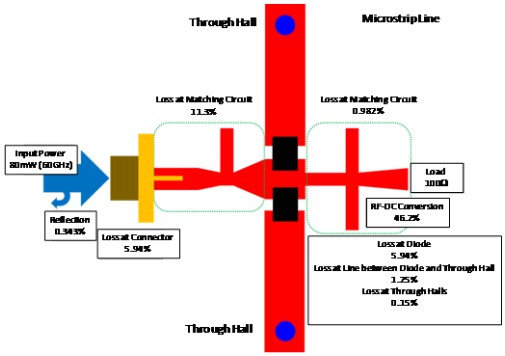

Fig.ure 2 : Designed and simulated 60 GHz rectifying circuit.

Figure 3 shows the frequency dependence of the RF-DC conversion efficiency of rectifying circuits for rectennas developed since the 1960s. The star marks are our contributions, which are at 24 and 60 GHz. The RF-DC conversion efficiency in the millimeter-wave frequency range is sufficient to use millimeter waves for WPT.

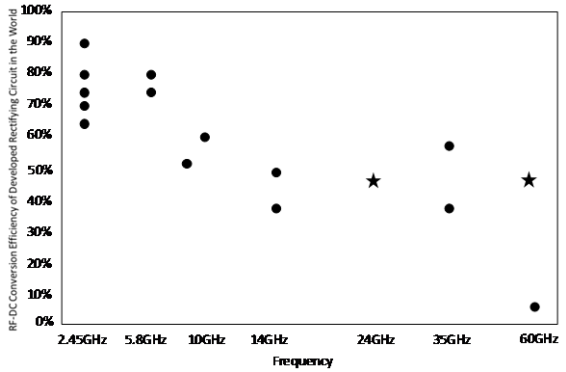

Figure 3 : Frequency dependence of RF-DC conversion efficiency of rectifying circuits for rectennas developed since the 1960s.

3 PROPOSED SATELLITE MPT EXPERIMENT FOR SPS

In 2009 in Japan, the Basic Plan for Space Policy was published, which states "As a program that corresponds to following major social needs and goals for the next 10 years, a Space Solar Power Program will be targeted for the promotion of the 5-year development and utilization plan." We thus need both a technical advance and a "surprise" in the next space experiment based on the Basic Plan for Space Policy. In 2013, the Basic Plan for Space Policy was revised, but it still promoted the SPS for Japan. In addition, the SPS figures in the Japanese "Basic Plan for Energy Policy" from April, 2014.

As a first step to the SPS, a WPT experiment in space or from space to ground is very important. Only three MPT rocket experiments have been done in the world, and they were done in Japan. In 1983, Professor Matsumoto of Kyoto University conducted the first MPT rocket experiment, which was called the Microwave Ionosphere Nonlinear Interaction Experiment (MINIX). This experiment was in collaboration with Kobe University and the Institute of Space and Astronautical Science (ISAS) (Matsumoto, 1986). In the MINIX experiment, they used a 2.45 GHz cooker-type magnetron and waveguide antenna as microwave transmitter. In 1993, Professor Matsumoto's group carried out their second rocket experiment, which was called the International Space Year Microwave Energy Transmission in Space (ISY-METS) experiment (Kaya, 1993). This experiment used a phased array at 2.411 GHz. The MINIX and ISY-METS were space-to-space MPT experiments. The third and last WPT rocket experiment was carried out in 2006, by Professor Kaya of Kobe University, ISAS, and the European Space Agency (Kaya, 2006). This is the only a rocket MPT experiment whose microwave was transmitted from the rocket back to the ground. However, the microwave was diffused and did not qualify as a power beam.

The difficulty of the MPT experiment from space to ground is caused by the low frequency of microwave radiation. A small satellite must orbit at 300 to 400 km. A distance of several hundred kilometers is too far to create a microwave beam at 2.45 or 5.8 GHz (these frequencies are too low). Therefore, we propose an MPT space experiment at 24 GHz that is based on the technologies described in Section 2. In the early 1990s, a 24 GHz MPT satellite experiment was proposed and studied in Japan (Matsumoto, 1993). However, this was a space-to-space MPT experiment. Herein, we propose a space-to-ground MPT experiment.

Using the microwave frequency of 24 GHz has the following advantages and disadvantages:

Advantages

(1) The antenna size of the MPT can be decreased to a tenth of the size of Tx × Rx antenna.

(2) 24 GHz is in the ISM band so there are very few users.

Disadvantages

(1) Efficiency and power are lower than at 2.45 GHz.

(2) Absorption in air is greater.

(3) Technical obstacles are greater.

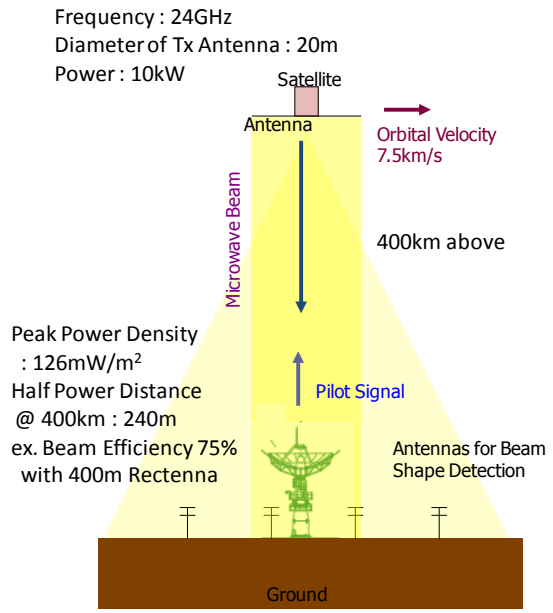

Fig. 4 Parameters of proposed 24 GHz satellite MPT experiment.

However, we can transmit microwave power from a 400 km orbit to the ground with higher beam collection efficiency if appropriately calibrate the values for experimental parameters. Estimated values for the parameters are shown in Fig. 4. With these parameters, we can receive sufficient microwave power from the space. Therefore, provided the requisite technical advance and "surprise," the 24 GHz space experiment can be conducted.

4 CONCLUSIONS

In working toward the SPS, an MPT satellite experiment is desired as soon as possible. However, Maxwell's equations and the required satellite orbit render an effective MPT experiment difficult. Therefore, to perform the MPT satellite experiment, we consider using frequencies of 24 GHz or higher. We have already developed 24 and 60 GHz rectifying circuits for a rectenna with sufficient RF-DC conversion efficiency.

There are still technical problems preventing an MPT experiment with higher frequency. For example, the experiment would require a high-power transmitter and amplifier with high DC-RF conversion efficiency. We hope the advance of radio-wave technologies will support the MPT satellite experiment and realize the SPS.

REFERENCES

Hatano, K., Shinohara, N., Seki, T., and Kawashima, M., 2013, Development of MMIC Rectenna at 24GHz, *Proc. of 2013 IEEE Radio & Wireless Symposium (RWS)*, pp.199-201

Kaya, N., Matsumoto, H., and Akiba, R., 1993, Rocket Experiment METS Microwave Energy Transmission in Space", *Space Power*, Vol.11, No.1&2, pp.267 – 274

Kaya, N., Iwashita, M., Tanaka1, K., Nakatsuka, S., and Summerer, L., 2006, Rocket Experiment on Microwave Power Transmission with Furoshiki Deployment, *Proc. of IAC2006*, IAC-06-C3.3.03.pdf

Mankins, J. C., 2014, *The case for space solar power*, The Virginia Edition, Inc., USA

Matsumoto, H, and Kimura, I., 1986, Nonlinear Excitation of Electron Cyclotron Waves by a Monochromatic Strong Microwave : Computer Simulation Analysis of the MINIX Results, *Space Power*, vol.6, pp.187-191

Matsumoto, H., Kaya, N., Kinai, S., Fujiwara, T., and Kochiyama, J., 1993, A Feasibility study of power supplying satellite (PSS), *Space Power*, Vol.12, No.1&2, pp.1-6

Seki, T., Hiraga, K., Nishimori, K., Nishikawa, K., and Uehara, K., 2011, High Speed Parallel Data Transmission and Power Transmission Technology for Wireless Repeater System, *Proc.* of *European Conference on Antennas and Propagation (Eu-CAP)*, pp. 3913-3916

Shinohara, N., 2014, *Wireless Power Transfer via Radiowaves*, ISTE Ltd. and John Wiley & Sons, Inc., UK and USA

Adaptive Clipping for a Deterministic Peak-To-Average Power Ratio

Diallo Mamadou Lamarana and Palicot Jacques
SUPELEC/IETR:, Avenue de la Boulaie-CS 47601-35576 CESSON-SEVIGNE CEDEX, France
{Mamadou-Lamarana.Diallo,Jacques.Palicot}@supelec.fr

Keywords: OFDM, PAPR Mitigation, Clipping and CCDF.

Abstract: Orthogonal Frequency Division Multiplexing (OFDM) is the most commonly used multicarriers modulation in telecommunication systems due to the efficient use of frequency resources and its robustness to multipath fading channel. However, as multicarriers modulation in general, OFDM suffers from high Peak-to-Average Power Ratio (PAPR). Many works exist in literature for PAPR mitigation among which Clipping is one of the most efficient adding signal techniques in terms of numerical complexity. However, clipping techniques is a probabilistic technique for PAPR mitigation. In other words, the instantaneous PAPR of each clipped OFDM symbol depends on its content and then the PAPR at any value of the Complementary Cumulative Distribution Function (CCDF) increases when its corresponding CCDF values decreases. In this paper, we propose an adaptive clipping which offers a constant PAPR, so deterministic, at any value of the CCDF and so this approach outperforms the classical clipping in terms of signal degradation with the same performance in terms of PAPR reduction. Simulation results validate the interest of this approach.

.

1 INTRODUCTION

Clipping is an efficient technique for PAPR mitigation which was firstly proposed by X. Li and J. Cimini (Li and Cimini, 1997). The clipping technique consists to clip the amplitudes of the signal which exceed a predefined threshold A. In practice, a normalized predefined threshold $\rho = \frac{A}{P_{x_n}}$ is used, where P_{x_n} represents the mean power of the discrete signal x_n which we want reduce the PAPR. It can be remarked that, ρ defines the PAPR below which the signal is not clipped. Due the strong amplitude variations of the OFDM symbol in the time domain, the instantaneous PAPR of each OFDM symbols highly depends on its content. Therefore, the instantaneous PAPR after Classical Clipping method (Li and Cimini, 1997) (CC) with a predefined ρ also depends on its content. Then, for each positive scalar value Φ if we denote by PAPR(Φ) the upper bounded PAPR at the value CCDF(Φ), it can be remarked that PAPR(Φ) increases when CCDF(Φ) decreases. In this paper, this upper bounded PAPR(Φ) will be called simply PAPR at the CCDF value CCDF(Φ).

Many clipping functions are proposed in the literature in order to avoid some drawbacks inherent in the classical clipping (CC) such as Out-of-Band emission, mean power Degradation and bit error rate (BER) degradation. Generally, clipping is associated with filtering in order to filter out-of-band emission (Li and Cimini, 1997). But this filter generates the peak-regrowth phenomena. In(Kimura et al., 2008) the authors propose Deep-Clipping to reduce the peak-regrowth phenomena and Out-of-Band emission. Mean-Power degradation can be reduced by using a clipping based on Gaussian function (Guel, 2009). However, all these approaches degrade the BER and the instantaneous output PAPR of this techniques also depends on the content of each OFDM symbol. Note that, BER degradation drawbacks is solved by means of tone reservation (TR) clipping (Guel and Palicot, 2009; Wang and Tellambura, 2008). Nevertheless, this approach degrades the performances in terms of PAPR reduction.

In practice, the desired PAPR(Φ) for the Input Back Off (IBO) definition on the High Power Amplifier (HPA) is defines at CCDF(Φ) close to zeros

(10^{-4}). In this paper, this value will be denoted by $\text{PAPR}_{\text{CC}}^{(0)}$. So, due to the fact that $\text{PAPR}(\Phi)$ increases when $\text{CCDF}(\Phi)$ decreases, it can be remarked that, many OFDM symbol are more severely clipped than necessary or unnecessary clipped with respect to the desired output PAPR ($\text{PAPR}_{\text{CC}}^{(0)}$). That is the reason why we propose in this paper, an adaptive clipping (AC) in order to obtain a deterministic output PAPR i.e a same upper bounded PAPR at any value of the CCDF. The main goal of this approach is to make $\text{PAPR}(\Phi)$ constant at any value of the CCDF and so minimized the signal degradation with respect to classical clipping. For this purpose, the normalized threshold is adapted to the content of each OFDM symbol in order to get the desired PAPR after clipping. Therefore, in contrast the CC where the instantaneous PAPR depends on the content of the OFDM symbol, in the AC the instantaneous PAPR does not depends on the content of the OFDM symbol. Therefore, we qualify this approach as Adaptive Clipping with a constant output PAPR ($\text{PAPR}(\Phi)$).

The paper is organized as follows: In Section 2, we briefly present the clipping technique and the problem formulation. In Section 3, we will present the Adaptive Clipping. A comparative study by simulation with the classical clipping will then be conducted in Section 4. The conclusion will be presented in Section 5.

2 CLASSICAL CLIPPING PRINCIPLE AND PROBLEM FORMULATION

In this paper, the scalars in the time domain and in the frequency domain will be denoted by lower case letters and capital letter respectively. The vectors containing the times domain samples and frequency domain samples will be represented by lower case letter in bold and upper case letter in bold respectively.

If $z(t)$ represents a signal in continuous time domain its PAPR in continuous time domain and discrete time domain will be denoted by PAPR_z and $\text{PAPR}_{[z]}$ respectively.

2.1 Peak-To-Average Power Ratio Definition

One OFDM symbol at instant t in time interval $nT \leq t \leq (n+1)T$ can be expressed as follows:

$$x_n(t) = \sum_{k=0}^{N-1} X_{n,k} e^{2\pi jkFt} \tag{1}$$

Where F represents the inter-carrier frequency spacing, $T = 1/F$ is the OFDM symbol duration, $X_{n,k}$ is the *n-th* QAM symbols conveyed by the sub-carrier of index k.

The PAPR of this OFDM symbol in continuous time domain can be expressed as in (Louet and Palicot, 2005) by:

$$\text{PAPR}_{x_n(t)} = \frac{\underset{t\in[0,T]}{max}\,|x_n(t)|^2}{\mathbb{E}[|x_n(t)|^2]} \tag{2}$$

In practical, discrete OFDM symbol is used to evaluate the PAPR. In order to get a good approximation of the true analog PAPR it is necessary to oversampled the OFDM signal. Thus, as in (Ochiai and Imai, 2001) and (Louet and Hussain, 2008), many authors have shown that an oversampling factor of $L \geq 4$ is sufficient to obtain a good approximation of the analog signal PAPR. In OFDM system, an oversampled signal can be efficiently computed by an IFFT transformation and can be expressed as follows:

$$x_{n,m} = \sum_{m=0}^{NL-1} X_{n,m} e^{2j\pi n \frac{m}{NL}}, \tag{3}$$

where $\mathbf{X}_n = [X_{n,0}, \ldots, X_{n,NL-1}]$ is the L times oversampling equivalent QAM vector, generated by zeros padding $\mathbf{X}_n$ with $N(L-1)$ zeros. Therefore, from this NL OFDM samples, the discrete time PAPR can be expressed as in (Louet and Palicot, 2005) by following expression:

$$\text{PAPR}_{[x_n]} = \frac{\|\mathbf{x}_n\|_\infty^2}{\mathbf{E}(\|\mathbf{x}_n\|_2^2)}, \tag{4}$$

where $\mathbf{x}_n = [x_{n,0}, \ldots, x_{n,NL-1}]^T$ is the vector containing the NL samples of the OFDM signal $x_n(t)$.

2.2 Classical Clipping (CC) Principle

Classical clipping (CC) is a simple adding signal techniques for PAPR mitigation in that the output signal $\mathbf{y}_n = [y_{n,0}, \ldots, y_{n,NL-1}]$ after PAPR reduction is given as follows:

$$y_{n,m} = \begin{cases} x_{n,m} & \text{if } |x_{n,m}| > A \\ Ae^{j\arg(x_{n,m})} & \text{else} \end{cases} \tag{5}$$

In general, to evaluate the performances of the PAPR mitigation techniques the CCDF of the PAPR of signal $\mathbf{y}_n$ is computed or simulated. The CCDF function is defined as follows:

$$\text{CCDF}_{\mathbf{y}_n}(\Phi) = \mathbb{P}\left[\text{PAPR}_{[\mathbf{y}_n]} \geq \Phi\right] \tag{6}$$

This CCDF function for classical OFDM signal is presented in Figure1.

2.3 Problem Formulation

Let be the Figure 1 in which the CCDF of the CC technique and Ideal Clipping for PAPR reduction are shown. Ideal Clipping is a clipping with a **constant** upper bounded output PAPR. In other words, the Ideal Clipping output PAPR could not be greater than the desired output PAPR ($= \text{PAPR}_0$), which is represented in the figure by the vertical solid line curve and would like to achieve by AC method.

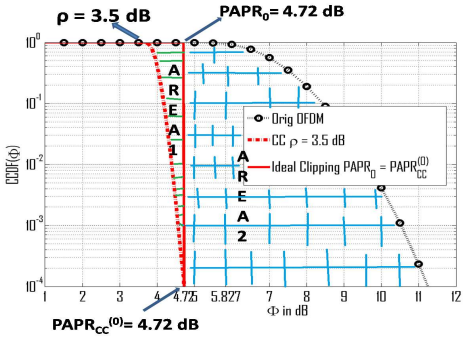

Figure 1: Scenario of CCDF curves of a classical clipping and Ideal Clipping

In this figure, $\text{PAPR}_{\text{CC}}^{(0)}$ represents the PAPR (upper bounded PAPR) of the clipped signal by CC $\mathbf{y}_n$ at the value of CCDF equal to 10^{-4} and PAPR_0 is the desired output PAPR of the ideal clipping at any value of the CCDF. In the AC method, the adapted threshold is computed for each symbol in function of PAPR_0.

Figure 1 shows that if the CCDF of the AC approaches the ideal clipping CCDF then AC will less degrade the signal than the CC with the same performance in terms of PAPR reduction.

In fact, let be AREA1 and AREA2 the domains represented in Figure 1. These domains illustrate the percentage of the number of OFDM symbols which PAPR is included in $\left[\rho, \text{PAPR}_{\text{CC}}^{(0)}\right]$ and exceed $\text{PAPR}_{\text{CC}}^{(0)}$ respectively. From Figure 1, it can be remarked that when $\text{PAPR}_0 = \text{PAPR}_{\text{CC}}^{(0)}$:

- AREA2 represents the OFDM symbols which are both clipped by CC and ideal clipping. Therefore, with respect to $\text{PAPR}_{\text{CC}}^{(0)}$, these OFDM symbols are clipped more severely than necessary in CC.
- AREA1 represents the OFDM symbols which are not clipped by ideal clipped but clipped in CC. These OFDM symbols are clipped unnecessary in CC with respect to $\text{PAPR}_{\text{CC}}^{(0)}$.

Now, let be Ω_ρ the following probability:

$$\Omega_\rho = \mathbb{P}\text{rob}\left[\text{PAPR}_{[x_n]} \in \text{AREA1}\right]. \quad (7)$$

When ρ decreases, $\text{PAPR}_{\text{CC}}^{(0)}$ decreases and then $\Omega_\rho \simeq 0$. Thus, to well characterize the probability that an OFDM symbol is unnecessary clipped, the following probability will be considered:

$$\Theta_\rho = \frac{\mathbb{P}\text{rob}\left[\text{PAPR}_{[x_n]} \in \text{AREA1}\right]}{1 - \mathbb{P}\text{rob}\left[\text{PAPR}_{[x_n]} \in \text{AREA2}\right]}. \quad (8)$$

We remark that Θ_ρ represents the probability that an OFDM symbol is unnecessarily clipped knowing that their PAPR $\notin$ AREA2.
Ω_ρ^1 can be computed as follows:

$$\begin{aligned}\Omega_\rho &= \mathbb{P}\text{rob}\left[\text{PAPR}_{[x_n]} \in \text{AREA1}\right] \\ &= \text{CCDF}_{x_n}(\rho) - \text{CCDF}_{x_n}(\text{PAPR}_{\text{CC}}^{(0)})\end{aligned} \quad (9)$$

Many works exist in the literature on computing the CCDF of OFDM signal. In (Van Nee and de Wild, 1998), the authors give an approximation of the CCDF from a direct computation. However, other authors propose an approximation of the CCDF based on statistical studies (Louet and Hussain, 2008; Ochiai and Imai, 2001) when the oversampling factor $L \geq 4$. This approach gives a better approximation of the CCDF. In this paper we use this Y. Louet formula to compute Ω_ρ which is given by the following equation

$$\text{CCDF}_{\mathbf{x}_n}(\Phi) = 1 - (1 - e^{-\Phi})^{\tau_2 N^\mu}, \quad (10)$$

where $\tau_2 = \left(\frac{5.12}{\sqrt{e}}\right)^\mu e^{-0.5704}$ and $\mu = 1.07$. So, using (10), Θ_ρ can be expressed as follows:

$$\Theta_\rho = \frac{\left(1 - e^{-\text{PAPR}_{\text{CC}}^{(0)}}\right)^{\tau_2 N^\mu} - (1 - e^{-\rho})^{\tau_2 N^\mu}}{\left(1 - e^{-\text{PAPR}_{\text{CC}}^{(0)}}\right)^{\tau_2 N^\mu}} \quad (11)$$

Figures 2 and 3 represent the curves of Ω_ρ and Θ_ρ.

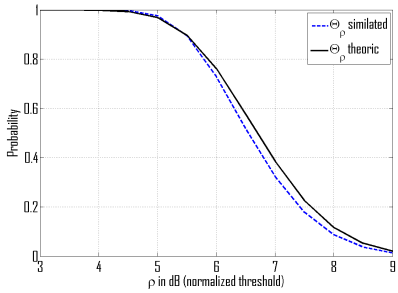

Figure 2: Probability that an OFDM symbol is unnecessarily clipped knowing that their PAPR $\notin$ AREA2.

From these figures, we remark that:

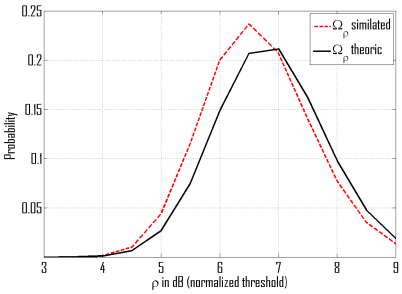

Figure 3: Probability that an OFDM symbol is unnecessarily clipped.

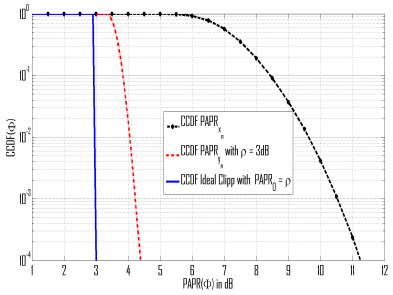

Figure 4: Illustration of Scenario 1 in terms of PAPR reduction

- If $0 \leq \rho \leq 5$dB.

Each OFDM symbol is clipped more severely than necessary with high probability and the probability to clip the symbol unnecessary is very low. Indeed, when $0 \leq \rho \leq 5$dB, $\Theta_\rho \simeq 1$ and $\Omega_\rho \simeq 0$ and then $\mathbb{P}\text{rob}\left[\text{PAPR}_{[x_n]} \in \text{AREA2}\right] \simeq 1$.

- If $5 \leq \rho \leq 6.5$dB.

Some signals are more severely clipped than necessary while others are clipped unnecessarily.
Indeed, we remark that when ρ increases, the percentage of the signals clipped more severely than necessary i.e $\mathbb{P}\text{rob}\left[\text{PAPR}_{[x_n]} \in \text{AREA2}\right] = \text{CCDF}_{[x_n]}\left(\text{PAPR}_{\text{CC}}^{(0)}\right)$ decreases and at the same time Ω_ρ increases (see Figure 3) and then the advantages in terms of signal degradation (BER degradation, Out-of-Band emission and Mean Power degradation) of the AC with respect to the CC will not unchanged. Thus, we would expect that the AC gives better performances in terms of signal degradation than the CC when $\text{PAPR}_0 = \text{PAPR}_{\text{CC}}^{(0)}$ and $\rho \in [0, 6.5\text{db}]$.

- If $\rho \geq 6.5$dB.

Θ_ρ and Ω_ρ decrease both and then AC will have the same behavior than the CC.

The main goal of the AC is to minimize the domain designed by AREA1 (see Figure 1) by adapting the normalized threshold clipping to the content of each OFDM symbol in order to get a constant PAPR equal to PAPR_0 at any value of the CCDF.

In the following section, the AC is presented and compared to the CC in terms of PAPR reduction, adjacent channels pollution and data degradation. To achieve this comparison, two scenarios will be considered.

- Scenario 1:

This scenario compares the classical clipping at ρ and AC at $\text{PAPR}_0 = \rho$. Figure 4 illustrates this scenario in terms of PAPR reduction.

- Scenario 2:

In this scenario, CC at ρ is compared to AC at $\text{PAPR}_0 = \text{PAPR}_{\text{CC}}^{(0)}$. Figure 5 illustrates this scenario in terms of PAPR reduction.

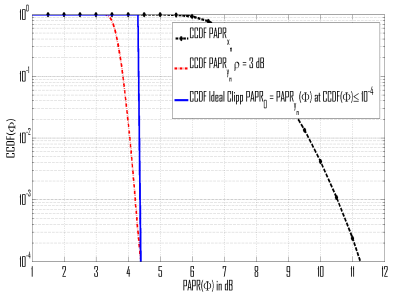

Figure 5: Illustration of Scenario 2 in terms of PAPR reduction

As we discussed on Figure 1, we expect that in scenario 1, AC will give worse performances in terms of BER degradation, adjacent channels pollution and mean power degradation than CC, at the opposite in scenario 2, AC should give better performances. Note that, in Figure 4 and 5, the solid line curve are drawn and represent the ideal clipping CCDF which we would like to obtain by AC.

3 ADAPTIVE CLIPPING

Let be $\mathbf{x}_n$ an OFDM signal which we would like to reduce its PAPR by classical clipping at threshold $\rho = 20\text{Log}_{10}\left(\frac{A}{\sqrt{P_{x_n}}}\right)$. Note that in CC ρ represents the ideal PAPR which we would like to obtain after clipping. But, due to the Mean Power degradation $\text{PAPR}_{[y_n]} \geq \rho$ for any $\mathbf{y}_n$ and then $\text{PAPR}_{\text{CC}}^{(0)} \geq \rho$.

Indeed, for each OFDM symbol $\mathbf{x}_n$ the instanta-

neous PAPR of $\mathbf{y}_n$ is given as follows:

$$\begin{aligned} \text{PAPR}_{[y_n]} &= \frac{\max\limits_{m=0,\ldots,NL-1}\left\{|x_{n,m}|^2\right\}}{P_{y_n}} \\ &= \frac{A^2}{P_{y_n}} \end{aligned}$$

Since, $A = \left(10^{\frac{\rho}{20}}\right)\sqrt{P_{x_n}}$ the instantaneous PAPR of $\mathbf{y}_n$ can be rewritten as follows:

$$\begin{aligned} \text{PAPR}_{[y_n]} &= \frac{\left(10^{\frac{\rho}{20}}\right)^2 P_{x_n}}{P_{y_n}} \\ &= \left(10^{\frac{\rho}{10}}\right)\left(\frac{P_{x_n}}{P_{y_n}}\right) \end{aligned} \quad (12)$$

Thus, since CC degrades the mean power of the clipped signal then $\frac{P_{x_n}}{P_{y_n}} \geq 1$. So the instantaneous PAPR of $\mathbf{y}_n$ satisfies the following inequality for each OFDM symbol:

$$\text{PAPR}_{[y_n]} \geq 10^{\frac{\rho}{10}} (= \rho \text{ in dB}), \quad (13)$$

therefore $\text{PAPR}_{[y_n]} \geq \rho$ for any $\mathbf{y}_n$ i.e $\text{PAPR}_{\text{CC}}^{(0)} \geq \rho$. Furthermore, if we denote by $\text{PAPR}_{[y_n]}(\Phi)$ the output PAPR at any value of the CCDF, then when $\text{CCDF}_{y_n}(\Phi)$ increases $\text{PAPR}_{[y_n]}(\Phi)$ decreases, so, some OFDM symbols are more severely clipped than necessary or unnecessary clipped with respect to $\text{PAPR}_{\text{CC}}^{(0)}$ (see Figure 1).

The main goal of the AC method, is to minimize the percentage of the OFDM symbols which are more severely clipped than necessary or unnecessary clipped with respect to the suitable output PAPR. Other adaptive clipping methods exist in the literature (Kim et al., 2003; Byuong Moo Lee, 2013). In (Kim et al., 2003), the authors proposed to adapt the normalized threshold ρ in function of the mapping constellation of the OFDM signal for a better compromise between PAPR reduction and BER degradation. In (Byuong Moo Lee, 2013), the authors proposed an iterative clipping and filtering scheme (Armstrong, 2002) in which the computation of the amplitude threshold A from the predefined normalized threshold, is processed at each iteration. This approach improves the performances on PAPR reduction but degrades more the signal. However, to the best of our knowledge this is the first work dealing with the threshold adaptation at each OFDM symbol in order to minimize the percentage of the OFDM symbols which are more severely clipped than necessary or unnecessary clipped with respect to the suitable output PAPR.

Let be PAPR_0 the constant desired output PAPR given by an ideal clipping at any value of the CCDF, so in AC approach, ρ is unknown and it is determined by the following equation for each OFDM symbol:

$$\text{PAPR}_0 = \left(10^{\frac{\rho}{10}}\right)\left(\frac{P_{x_n}}{P_{y_n}}\right). \quad (14)$$

From equation 14, we remark that in AC ρ depends on the content of each OFDM symbol.

3.1 Theoretical Analysis

From equation (14), we can easily deduce the following equation.

$$10^{\frac{\rho}{10}} = \text{PAPR}_0\left(\frac{P_{y_n}}{P_{x_n}}\right)$$

So, if we replace this expression in equation (12) the instantaneous PAPR of the clipped signal by AC is expressed as follows:

$$\begin{aligned} \text{PAPR}_{[y_n]} &= \left(\text{PAPR}_0\frac{P_{y_n}}{P_{x_n}}\right)\left(\frac{P_{x_n}}{P_{y_n}}\right) \\ &= \text{PAPR}_0, \end{aligned} \quad (15)$$

therefore we can conclude that AC gives a constant output PAPR (upper bounded PAPR) i.e $\text{PAPR}_{[y_n]}(\Phi) = \text{PAPR}_0$ at any value of the CCDF.

3.2 Adapted ρ Computation

The computation of the adapted normalized threshold from equation 14 is a complex problem since P_{y_n} depends on the unknown ρ. Thus, we propose in this paper an exhaustive search to approximate the solution of the equation (14).

The following algorithm describes this approach.

Algorithm 1 Normalized threshold computation in AC

Require: $x_n, \varepsilon, \text{PAPR}_0$
Ensure: y_n
  $\rho_0 \leftarrow \text{PAPR}_0$
  Compute A such as $\rho_0 = \frac{A}{\sqrt{P_{x_n}}}$
  $y_n \leftarrow f(x_n, A)$
  while $|\text{PAPR}_{[y_n]} - \text{PAPR}_0| > \varepsilon$ **do**
    $\rho_0 \leftarrow \rho_0 - \varepsilon$
    Compute A such as $\rho_0 = \frac{A}{\sqrt{P_{x_n}}}$
    $y_n \leftarrow f(y_n, A)$
  end while

4 SIMULATION RESULTS

The simulations are performed for a 64 sub-carriers OFDM system with 16-QAM modulation on each carrier. For a good approximation of the true analog PAPR the signal is oversampled at a factor $L = 4$.

Figure 6 shows the performance in terms of PAPR reduction for two different case thresholds $\rho = 3.5$dB and $\rho = 5$dB.

4.1 Scenario 1: Comparison Between AC and CC with $\text{PAPR}_0 = \rho$

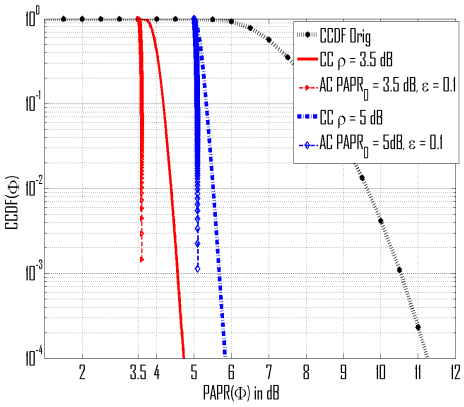

Figure 6: Comparison between CC and AC in terms of PAPR reduction for different thresholds $\rho = 3.5$dB and $\rho = 5$dB

The simulation results show that AC outperforms CC when $\text{PAPR}_0 = \rho$. We can remark also that AC converges to the ideal clipping and gives a deterministic PAPR equal to $\text{PAPR}_0 + \varepsilon$ at any value of the CCDF. This results confirm our theoretical analysis equation (15)

4.1.1 Comparison in Terms of BER Degradation

In this subsection, BER degradation are evaluated in the context of scenario 1.

The Figures 7 and 8 show the performances of AC compared to classical clipping.

The simulation results (Figure 7,8) confirm that the CC less degrades the In-Band data than the AC. Indeed, in order to get a PAPR equal to ρ (normalized threshold of the CC) the OFDM symbol with high PAPR are clipped by an adapted threshold smaller than ρ.

4.1.2 Comparison in Terms of Mean Power Degradation and Out-of-Band Emission

In this section, the performances in terms of mean power degradation and adjacent channels pollution

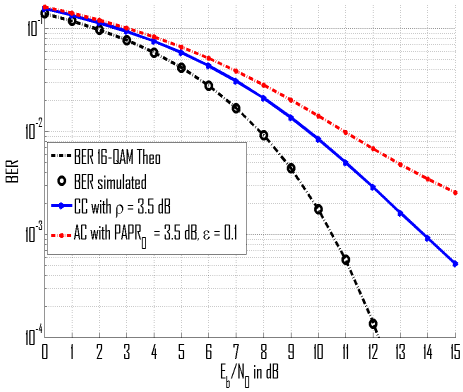

Figure 7: Comparison of CC and AC in terms of BER degradation for $\rho = 3.5$ dB

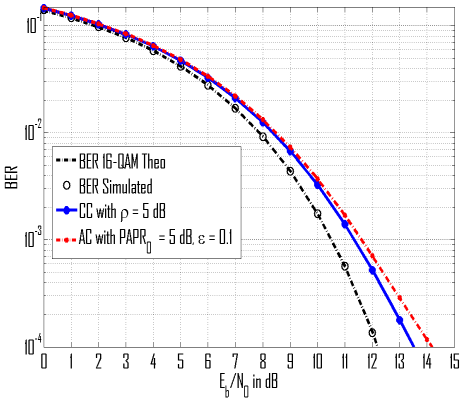

Figure 8: Comparison of CC and AC in terms of BER degradation for $\rho = 5$ dB.

which are achieved.

The Figure 9 compares AC and CC in terms of mean power variations.

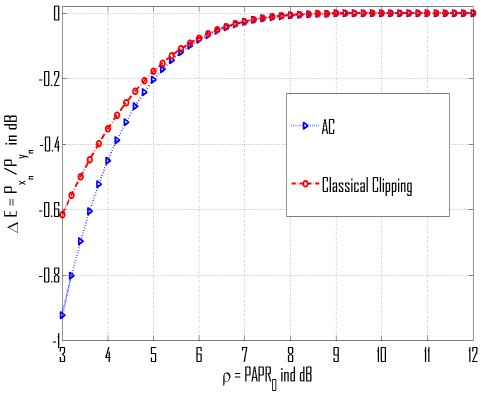

Figure 9: Comparison of CC and AC in terms of mean power degradation

Figure 9 shows that the Mean Power degradation created by AC is more severe than the CC one. These simulation results are consistent with our expectations.

The Figures 10 and 11 represent the DSP of OFDM signal before and after PAPR reduction by AC and CC.

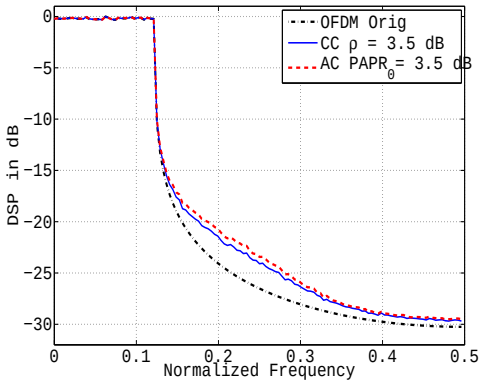

Figure 10: Comparison of DSP of the AC and CC methods for $\rho = 3.5$dB.

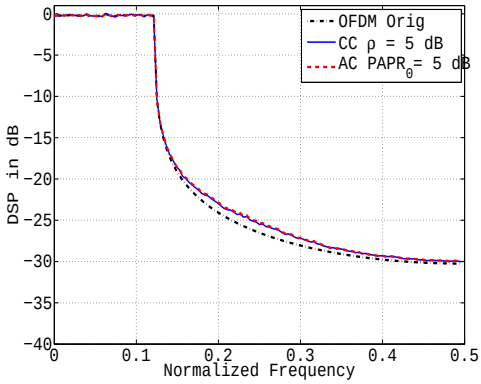

Figure 11: Comparison of DSP of the AC and CC methods for $\rho = 5$dB.

As in terms of mean power variations, the Out-Of-Band Emission (Figure 10,11) created by the AC will be more polluting than those due to the classical clipping. In addition, we remark that, when ρ increases the Out-of-Band emission due to the AC is the same as in classical clipping (Figure 11). Nevertheless, when ρ increases $\text{PAPR}_{\text{CC}}^{(0)} - \rho$ decreases and therefore AC and classical clipping give same performances in terms of PAPR reduction.

In conclusion, these simulation results (Figure 7,8, 9, 10,11) are consistent with our theoretical analysis. Indeed, from equation (14), we can show that for each OFDM symbol, the corresponding adapted threshold is smaller than ρ. This remark can be directly deduced from the algorithm used for the adapted threshold computation.

4.2 Scenario 2: Comparison Between AC and CC with $\text{PAPR}_0 = \text{PAPR}_{\text{CC}}^{(0)}$

In this section, comparison between AC and CC at same performance in terms of PAPR reduction i.e: $\text{PAPR}_0 = \text{PAPR}_{\text{CC}}^{(0)}$ is achieved.

Figure 12 shows the performances in terms of PAPR reduction for two different case thresholds $\rho = 3.5$dB and $\rho = 5$dB.

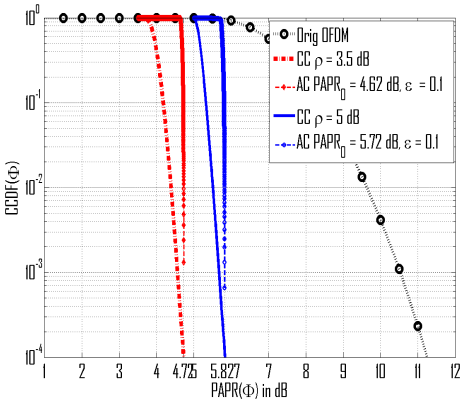

Figure 12: Comparison of CC and AC in terms of PAPR reduction for different thresholds $\rho = 3.5$dB and $\rho = 5$dB.

The simulation results confirm that when $\text{PAPR}_0 = \text{PAPR}_{\text{CC}}^{(0)}$ AC gives a same performances in terms of PAPR reduction than classical clipping. As in the previous scenario (Section 4), We remark that the AC converges to the ideal clipping and gives a deterministic PAPR equal to $\text{PAPR}_0 + \varepsilon$ at any $\text{CCDF}(\Phi)$. This results confirm our theoretical analysis equation (15).

In the following subsection, AC and CC will be compared in terms of signal degradation.

4.2.1 Performance in Terms of BER Degradation

In this subsection, the AC are compared to clipping in terms of BER degradation.

The Figures 13 and 14 compare the BER degradation due to AC and CC after PAPR reduction.

As in the theoretical analysis section, the simulation results (Figure 14 and 13) show that AC outperforms CC in terms of BER degradation. This results confirm the theoretical analysis (see Figure 2,3) in that we have shown that many OFDM symbols are clipped more severely than necessary ($\rho = 3, \ldots, 5$dB) or unnecessarily (5 dB $\leq \rho \leq$ 6.5 dB) with respect to $\text{PAPR}_{\text{CC}}^{(0)}$.

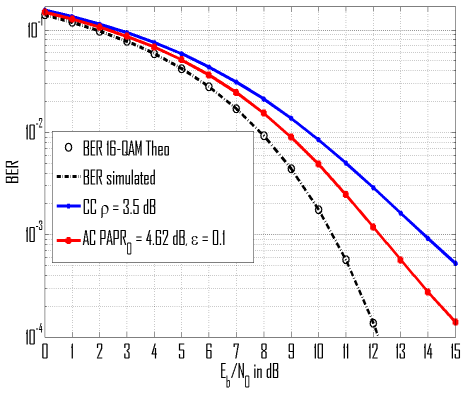

Figure 13: Comparison of CC and AC in terms of BER degradation for $\rho = 3.5$ dB.

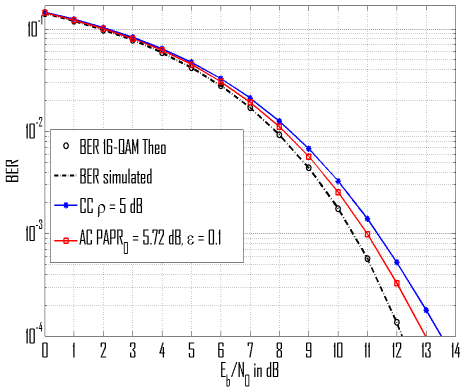

Figure 14: Comparison of CC and AC in terms of BER degradation for $\rho = 5$ dB.

4.2.2 Performance in Terms of Mean Power Degradation and Out-of-Band Emission

As in subsection 4.1.2, the performances in terms of mean power degradation and adjacent channels pollution which is caused by the OOB components, are studied.

The Figure 15 shows the mean power variation of the signal due to the CC and AC method.

The simulation results (see Figure 15) show that AC less degrades the Mean Power of the clipped signal than the CC for the same output PAPR at the CCDF value less or equal to 10^{-4}. For example, for an output PAPR equal to 4.5dB, $\Delta E = -0.4$dB in CC method and $\Delta E = -0.2$dB in AC approach.

The Figures 16 and 17 represent the DSP of OFDM signal before and after PAPR reduction by AC and CC.

The simulation results (Figure 16,17) show that the AC less pollutes the adjacent channels than the CC with the same performances in terms of PAPR reduction.

These simulation results in terms of BER degradation, mean power variations and adjacent channels pollution are consistent with our theoretical analysis of the ideal clipping. Indeed, we have shown that (Figures 1A, B) when $0 \leq \rho \leq 6.5$dB and $\text{PAPR}_0 = \text{PAPR}_{\text{CC}}^{(0)}$ many OFDM symbol are clipped more severely than necessary or unnecessarily in CC with respect to $\text{PAPR}_{\text{CC}}^{(0)}$.

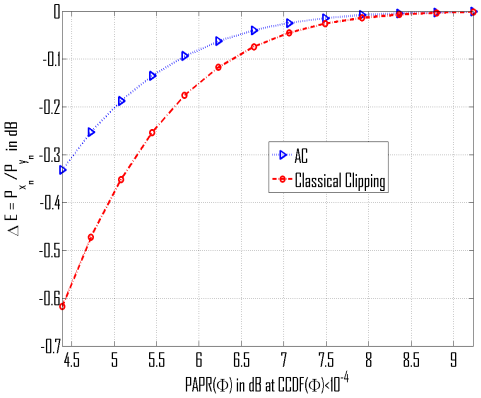

Figure 15: Comparison of CC and AC in terms of mean power degradation

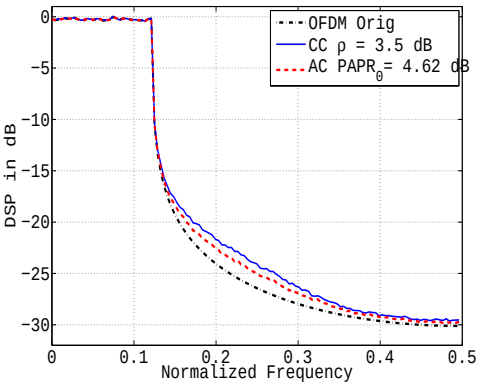

Figure 16: Comparison of DSP of the AC and CC methods for $\rho = 3.5$dB.

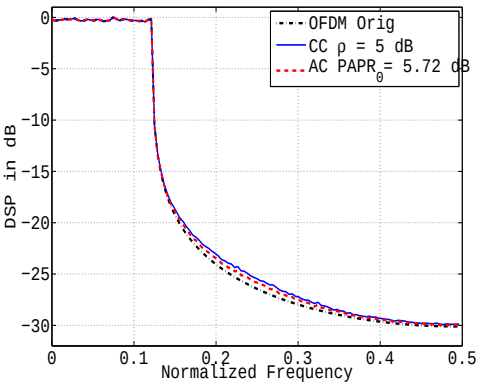

Figure 17: Comparison of DSP of the AC and CC methods for $\rho = 5$dB.

In conclusion, these simulation results (Figure 13, 14,15,16 and 17) are consistent with our theoretical analysis.

Indeed, as in section 4.1, we can show from equation (14) that for each OFDM symbol, the corresponding adapted threshold is greater than ρ when $\text{PAPR}_0 = \text{PAPR}_{\text{CC}}^{(0)}$. This remark can be directly deduced from the algorithm used for the adapted threshold computation.

5 CONCLUSION AND FUTURE WORK

In this paper an adaptive clipping is presented and compared to classical clipping in terms of PAPR reduction and signal degradation. This comparison has been achieved by a theoretical study and validated by simulation. We have shown that AC approaches the ideal clipping and then have same performance in terms of PAPR reduction but outperforms classical clipping in terms of signal degradation. Furthermore, AC gives a deterministic PAPR which is very important for IBO definition on high power amplification (HPA). However, the computation of the adapted threshold in AC is complex. A more simple iterative approach is being studied.

REFERENCES

Armstrong, J. (2002). Peak-to-average power reduction for OFDM by repeated clipping and frequency domain filtering. *Electronics Letters*, 38(5):246–247.

Byuong Moo Lee, Y. K. (2013). An adaptive clipping and filtering technique for PAPR reduction of OFDM signals. *Circuit, Systems and Signal Processing*, 32:1335–1349.

Guel, D. (2009). *Etude de nouvelles techniques de réduction de "facteur de crête" compatibilité descendante pour les systemes multiporteuses.* PhD thesis, Université de Rennes 1.

Guel, D. and Palicot, J. (2009). FFT/IFFT Pair Based Digital Filtering for the transformation of adding signal PAPR reduction techniques in Tone Reservation Techniques. In *Wireless and Mobile Communications, 2009. ICWMC '09. Fifth International Conference on*, pages 200–204.

Kim, H. J., Cho, S. C., Oh, H. S., and Ahn, J. M. (2003). Adaptive clipping technique for reducing PAPR on OFDM systems. In *Vehicular Technology Conference, 2003. VTC 2003-Fall. 2003 IEEE 58th*, volume 3, pages 1478–1481 Vol.3.

Kimura, S., Nakamura, T., Saito, M., and Okada, M. (2008). PAR reduction for OFDM signals based on deep clipping. In *Communications, Control and Signal Processing, 2008. ISCCSP 2008. 3rd International Symposium on*, pages 911–916.

Li, X. and Cimini, L. (1997). Effects of clipping and filtering on the performance of OFDM. In *Vehicular Technology Conference, 1997, IEEE 47th*, volume 3, pages 1634–1638 vol.3.

Louet, Y. and Hussain, S. (2008). Peak-to-mean envelope power ratio statistical analysis of continuous OFDM signal. In *Vehicular Technology Conference, 2008. VTC Spring 2008. IEEE*, pages 1681–1685.

Louet, Y. and Palicot, J. (2005). Power ratio definitions and analysis in signals carrier modulation. In *in 13th European Signal Processing Conference, EUSIPCO*, volume 63, pages 351–368.

Ochiai, H. and Imai, H. (2001). On the distribution of the peak-to-average power ratio in OFDM signals. *Communications, IEEE Transactions on*, 49(2):282–289.

Van Nee, R. and de Wild, A. (1998). Reducing the peak-to-average power ratio of OFDM. In *Vehicular Technology Conference, 1998. VTC 98. 48th IEEE*, volume 3, pages 2072–2076 vol.3.

Wang, L. and Tellambura, C. (2008). Analysis of clipping noise and tone-reservation algorithms for peak reduction in OFDM systems. *Vehicular Technology, IEEE Transactions on*, 57(3):1675–1694.

Moving Target FSR Shadow Detection Using GPS Signals

Hristo Kabakchiev[1], Ivan Garvanov[2], Vera Behar[3], Panayot Daskalov[4] , and Hermann Rohling[5]
[1] *Sofia University, 15 Tsar Osvoboditel Blvd,1504 Sofia Sofia, Bulgaria*
[2]*ULSIT, bul. Carigadsko Shouse № 119, 1784 Sofia, Bulgaria*
[3] *IICT- Bulgarian Academy of Sciences, Serdika St 4, 1000 Sofia, Bulgaria*
[4]*UNWE, ulitsa 8-mi dekemvri, 1700 Sofia, Bulgaria*
[5]*TU Hamburg-Harburg Institut für Nachrichtentechnik Eißendorfer Straße 40 D-21073 Hamburg, Germany*
ckabakchievr@fmi.uni-sofia.bg, i.garvanov@unubit.bg, dkabakchieva@fmi.uni-sofia.bg, rohlingr@tu-harburg.de

Keywords: FS effect, FSR, GPS, detection and estimation.

Abstract: Forward Scatter GPS (FS-GPS) radio shadows obtained from different objects are investigated in this article. FS radio shadow is essential physical phenomenon, which can be used to extract some useful information about the objects that generate it. Registration of FS-GPS radio shadows from moving and stationary objects is performed using a small commercial GPS antenna and mobile and stationary receiver. Topology of the experiment meets the requirements for the appearance of the FS effect. The results presented in this article show that from FS-GPS radio shadows of different objects can be extracted information about the parameters of the object (size, speed and direction of movement, distance to the receiver). The information obtained can be used in various applications like those in classic radar, including radio barriers, security, classification and identification of moving and stationary objects.

1 INTRODUCTION

Forward Scattering Radar operates in the narrow area of the forward scattering effect where the bistatic angle is close to 1800, and the target moves near the transmitter-receiver baseline (Fig.1) [1].

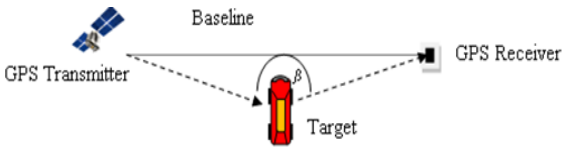

Figure 1: FSR topology.

In FSR, the Babinet principle is exploited to form the forward scatter signature of a target (see figure 2). The Babinet principle says "A plane absorbing screen of limited dimensions may be replaced by a complementary infinite plane screen with an aperture shaped exactly like the original screen (the complementary screen has openings where the original screen is closed and vice versa). The incident field diffracted at the aperture gives rise to the field coinciding with the shadow field of the original absorbing screen, (except for the sign)' (Fig.2).

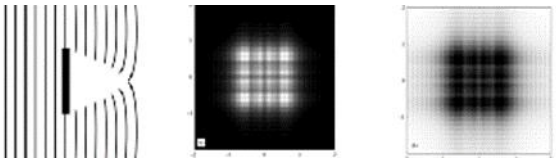

Figure 2: Babinet's principle applied to the FS case with the receiver positioned on the other side of the targets at β = 180°.

Due to the forward scattering effect, the Radar Cross Section (RCS) of targets extremely increases (by 2-3 orders) and mainly depends on the target's physical cross section and is independent of the target's surface shape and the absorbing coating on the surface. The use of GPS signals as a passive radar system is becoming increasingly popular as an alternative to radar systems. The idea to apply a GPS L1 receiver to FSR for air target detection is discussed in [2]. Some experimental results of a GPS L1 receiver concerning the detection of air targets are shown and discussed in [3]. A possible algorithm for

air target detection in a GPS L5-based FSR system is described in [4], and the detection probability characteristics are calculated in [5] in case of low-flying and poorly maneuverable air targets in the urban interference environment. GPS L1 FSR system is researched in [6, 7] for detection of FSR shadows from stationary ground objects. Target detection is indicated if the signal integrated from some satellites exceeds a predetermined threshold. In this paper a passive FSR system, similar to the GPS L1 FSR system, in which GPS satellites are exploited as non-cooperative transmitters, is studied. The aim of this study is to verify the possibility to detect FSR shadow of moving ground targets when GPS satellites are located at small elevation angles. The experimental scenarios include stationary or moving targets, stationary or moving GPS-FSR receivers that register different FS shadows. The paper investigates the possibility of extracting useful information from the radio shadow The obtained experimental results can be used to develop software applications to a GPS receiver that could measure traffic movement, target velocity and target classification.

2 FSR EXPERIMENT DESCRIPTION

The purpose of the experiments is to verify that with a small and omnidirectional commercial GPS antenna is possible to record differences in GPS FS shadows of moving and stationary targets depending on the size of the target and the target velocity, and also to verify whether the difference in the shadows allows classifying the objects (Fig.3).

Figure 3: Experimental equipment

The paper discusses three experimental scenarios. In the first two scenarios the objects are stationary (bridge and building) and GPS receiver moves while in the third scenario - the object moves and GPS receiver is stationary. In all scenarios the condition for the occurrence of FS-GPS effect are guaranteed. In the registration of shadows from buildings and vehicles are selected satellites located low on the horizon. In a study of radio shadow from the trestle are selected satellites located high above the horizon, so that the baseline "receiver-satellite" is always perpendicular to the plane of the object (building, station, and car). The purpose of these experiments is to check whether the type of the registrated FS shadows depends not only on the dimensions of the object, but also the speed of the GPS receiver or the object. The dependence of the type of FS shadow on the size and speed of the marine targets using coastal FSR radars is established in [1]. During the first scenario the GPS recording system is mounted at a car. In this study we verify the possibility of detection of ground targets by using a GPS L1-based FSR system when GPS satellites are located at small elevation angles (Fig.4).

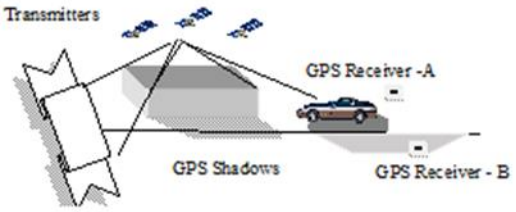

Figure 4: GPS-FSR topology (GPS receiver – A is moving, GPS receiver – B is stationary)

During the experiment, the car with the GPS receiver moves parallel to the building and records the GPS signal in order to registrate the FS shadow from the beginning to the end of the building. The idea of this experiment is to verify whether the energy of the signal from the satellite and the proposed from us the signal processing trough accumulation of the navigation message from GPS within several hundred milliseconds is sufficient to form the FS shadow of a stationary object with large dimensions, which can be registered with the experimental equipment. During the second experiment the car with mounted GPS receiver moves with velocity of 60-70 km. under the large bridge (Fig.4). The third scenario includes a moving targets and stationary-based GPS-FSR system that records FS shadow of cars moving on the road (Fig.4). The car with the GPS receiver is positioned from the one side of the road and records the signal from GPS. For recording are selected such visible satellites, which are located at low elevation angles and form a baseline (between satellite and receiver) perpendicular to the road, in order to form the FS effect. During the experiment are recorded the satellite signals when cars move on the road. Cars passing on the road have different dimensions (cars, buses, trucks, etc.).

3 SIGNAL PROCESSING

The general block-scheme of a possible algorithm for FSR shadow detection using several (M) visible satellites is shown in Fig 4 [1, 8]. According to this block-scheme, several visible GPS satellites are acquired and tracked over the complete duration of recorded signals. We consider the case when the acquisition and tracking algorithms of a GPS receiver are implemented in MATLAB. The absolute values of the Ip component at the output of the Code&Carrier tracking block are then integrated during N milliseconds. These integrated output signals from M satellites are additionally summed in order to improve SNR before detection. Target detection is indicated if the signal integrated from M satellites exceeds a predetermined threshold H. In such a system, the signal integrated at the output of the Code&Carrier tracking block (message bits) of a GPS receiver can be used for detection of the FSR shadow created by moving targets.

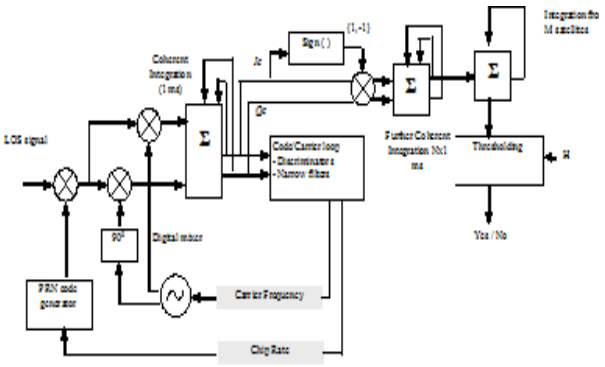

Figure 5: Signal processing used for target detection in a passive FSR using GPS signals from *M* satellites

In this paper we propose to additionally integrate the output signals from M visible satellites in order to improve the SNR before detection. Target detection is indicated if the signal integrated from M satellites exceeds a predetermined threshold.

4 EXPERIMENTAL RESULTS

Experiment 1. The receiver GNSS_SRR records the signals received from the satellite when moving along straight path behind a large building. The scenario topology is shown in Fig.6. Straight line shows the path of the GPS receiver mounted on the car. Dashed line indicates the direction of the necessary baseline "receiver-satellite" in which there is a condition for the occurrence of FS effect. That line is shown in Fig. 6 and Fig.7. With this line we choose the most suitable experimental satellite. Satellites that are visible during this experiment are shown in Fig.7.

Figure 6: Experiment 1

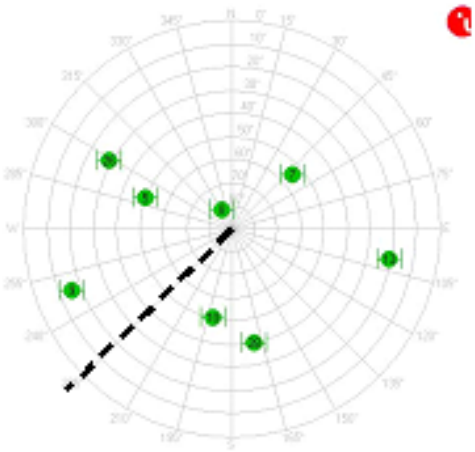

Figure 7: Satellite constellation

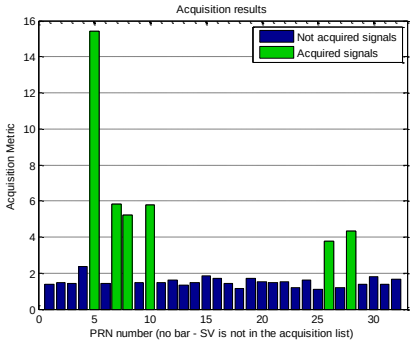

Figure 8: Acquisition results (Experiment 1)

The intensity of the signals from all visible satellites is shown in Fig.8. From Fig. 7 and Fig.8 follows that the most suitable for this experiment is satellite 9

because it is very close to the direction of the baseline where can be occur the FS effect, and is located the lowest elevation angles. The coherent integration of the I_P component power is made during 200ms, and results of integration are shown in Fig.9.

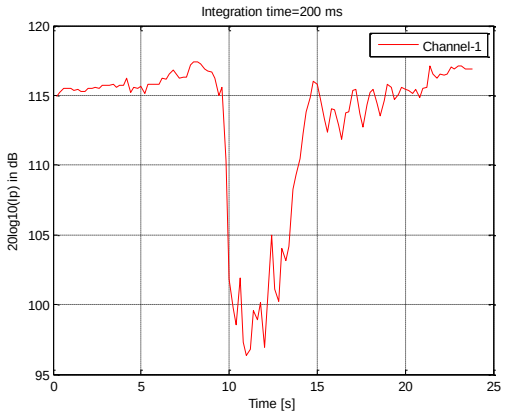

Figure 9: Integrated power of the message (200ms)

In the paper [6] it has been found that the interval of integration of the message is better to be 200ms because this interval of integration allows you to keep the shape of the shadow and to remove random fluctuations. It can be seen that the shadow due to the target (large building) can be exploited for detection of the target (large building).

Experiment 2. The car with GPS receiver moves with a constant velocity of 60 km/h under the small bridge (Fig. 10). The output of C/A code acquisition performance is shown in Fig. 11. It can be seen that during this experiment seven satellites are visible, three of which with numbers 12, 29 and 25 have the strongest signals. The signals from these satellites will be used for detection of the FS shadow created be a bridge.

Figure 10: Experiment 2

These satellites are located at the high elevation angles and should be meet the requirements for the occurrence of the FS effect. Navigation messages at the output of the Code&Carrier loop received from the satellites 12, 25 and 28 are shown in Figs. 12-14.

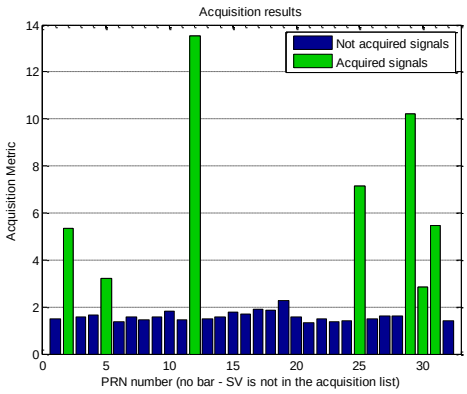

Figure 11: Acquisition results (Experiment 2)

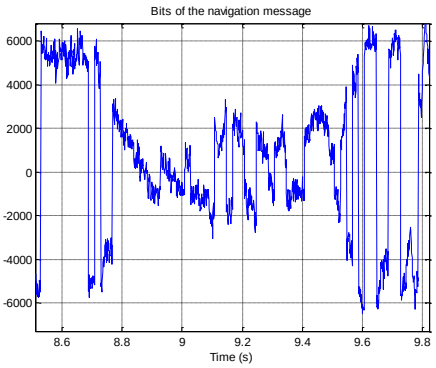

Figure 12: Navigation message of satellite 12

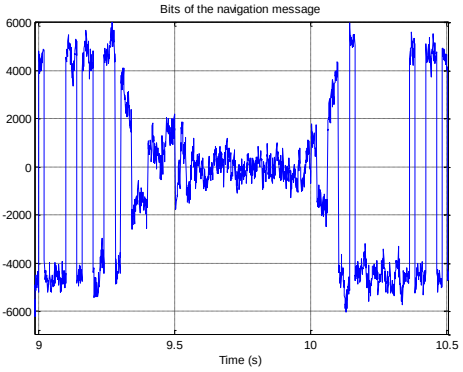

Figure 13: Navigation message of satellite 29

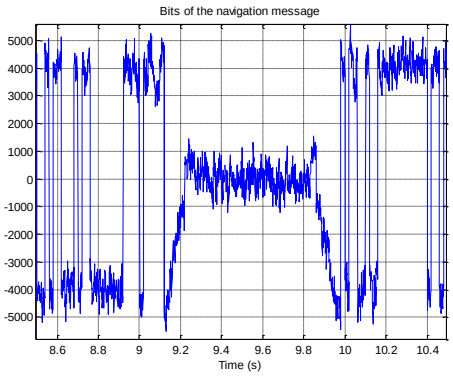

Figure 14: Navigation message of satellite 25

From figures 12-14, it is seen that during the passage of the vehicle under the bridge, the intensity of the information signal drastically reduces and forms a FS shadow with the certain geometry and form. The integrated messages from the three satellites obtained with a sliding window of 200 ms are shown in Fig. 15.

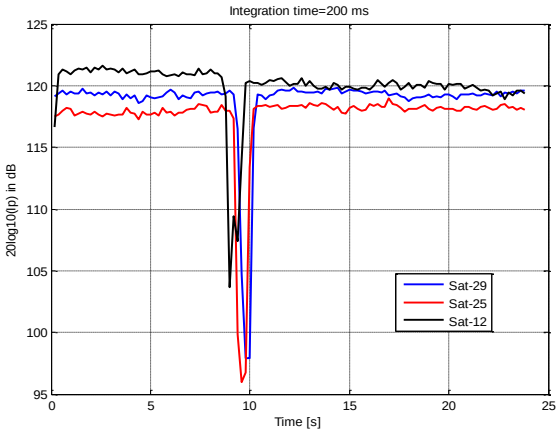

Figure 15: Integrated messages of satellites 12, 25 and 29

As seen from Fig. 15, the shape and size of the shadow depends on the direction (the position of the satellite) of the incoming signal from the satellites. The deepest shadow is obtained by satellite 25, which shows that this satellite creates the best conditions for the occurrence of the FS effect.

Experiment 3. The GPS receiver is positioned at the one side of the road (Fig. 16).The street has four lanes width of 4m, two in one direction. On the west of the receiver has a high building, so the GPS receiver only sees the GPS satellites from the east. During the experiment, several cars moves with a velocity about 10 - 20 km/h relative to the GPS receiver.

Figure 16: Experiment 3

The position of the visible satellites and the intensity of the incoming signals from them are shown in Fig. 17 and Fig.18. It can be seen that during this experiment six satellites are visible, two of which with numbers 16 and 32 create the best conditions for the occurrence of the FS effect. They are the most low on the horizon and the car crosses the baseline "satellite - receiver" at the angle of about 90 degrees. Satellites 1 and 30 are too low on the horizon, but in their case the vehicle crosses the baseline “”satellite-receiver”” at an angle other than 90 degrees.

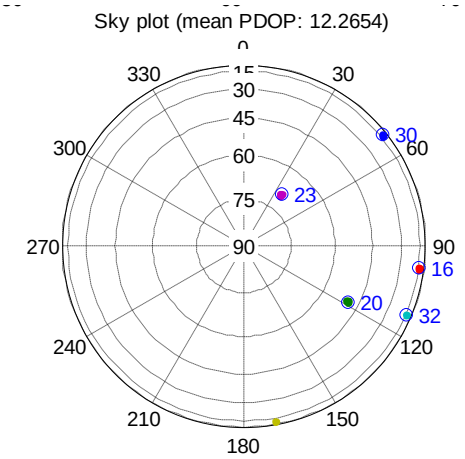

Figure 17: Satellite constellation

In the case of satellites 1 and 30, the conditions of the occurrence of FS effect are violated. Satellite 20 is located at the elevation angle close to 90 degrees, i.e. high above the horizon, which worsens the conditions of the occurrence of the FS effect. It is so because the direction of propagation of the waves from the satellite is not orthogonal with respect to the cross section of the vehicle. The same was observed for the satellite 23. The integrated signals from these satellites 16 and 32 are shown on Fig. 19 and 20.

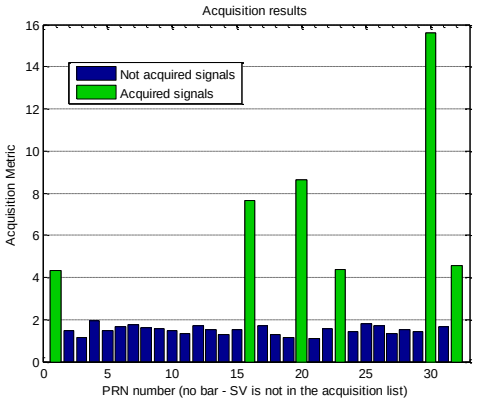

Figure 18: Acquisition results (Experiment 3)

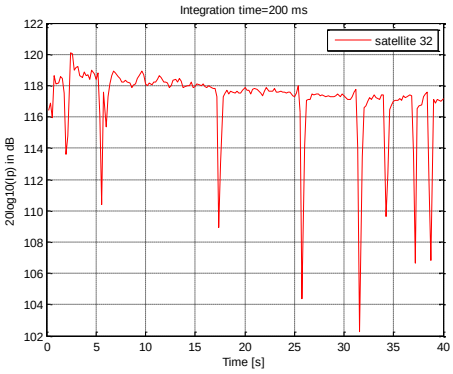

Figure 19: Integrated message from satellite 32

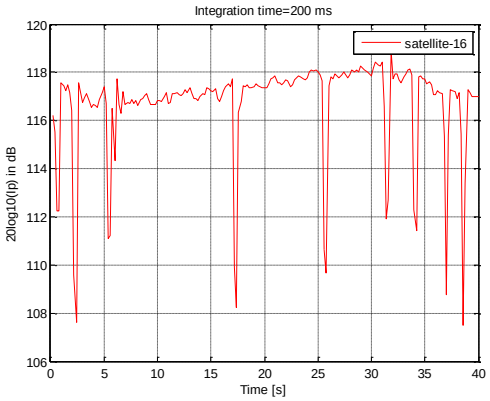

Figure 20: Integrated message from satellite 16

These figures show a series of FS shadows from different cars passing by the GPS receiver. As shown, the depth and shape of the shadow provides information about the size of the car, the speed and the direction of movementof the car, and the distance from the vehicle to the GPS receiver

.As can be seen that cars passing very close to the receiver have the deepest FS shadow (about 8-10 dB). A car passing at a distance of 4 meters from the GPS receiver creates the deepest FS shadow (about 8-10 dB). With increasing distance to 16 meters the depth of the FS shadow decreases by several dB (3-4 dB). The experimental results show that the size, the depth and the shape of the FS shadow could provide information about the car velocity and the intensity of the traffic. Using a predetermined multi-level threshold can be defined the distance to the vehicle from GPS receiver. It can be seen that the shape of the FS shadow (the first peak) can be used to determine the direction of the movement of the vehicle. In such a way it can be realized a selection and classification of vehicles.

The FS shadows obtained from 1 and 30 satellites are shown in Fig. 21 and Fig. 22.

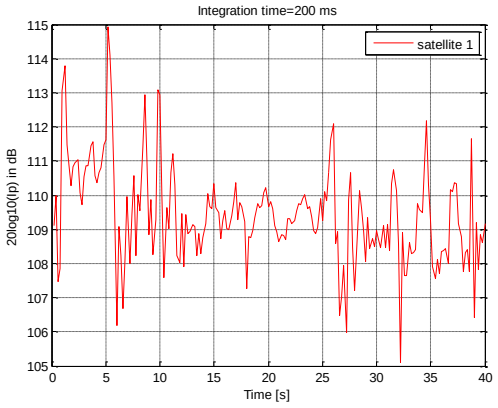

Figure 21: Integrated message from satellite 1

It can be seen that unlike the satellite 1, the signals from the satellite 30 form the relative deep FS shadow of passing cars. This shows that unlike the satellite 1, the satellite 30 does not fulfill the conditions for the occurrence of the FS effect.

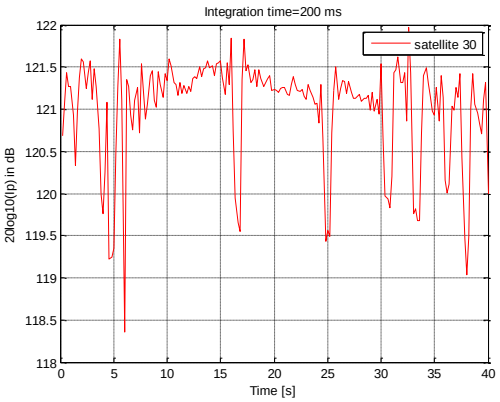

Figure 22: Integrated message from satellite 30

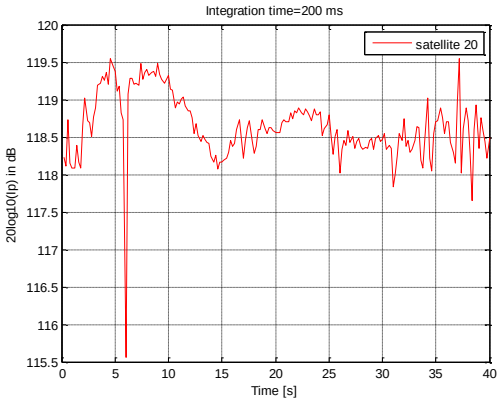

Figure 23: Integrated message from satellite 20

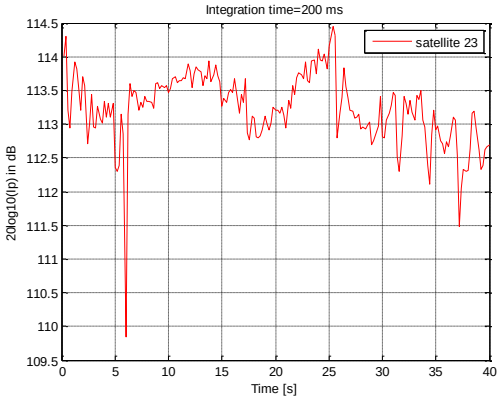

Figure 24: Integrated message from satellite 23

The integrated signals from satellites 20 and 23 are shown on Fig. 23 and 24. This satellites are high above the horizon ant the FS shadow is small. In this case the majority of the energy of the transmitted signal passes over the target and the signals from these satellites cannot be used for detection of the FS shadow created by cars.

5 CONCLUSIONS

Using a small commercial GPS antenna and GPS receiver it is made a number of experiments with moving and stationary objects and moving and stationary receiver. Topology of the experiment suggests the presence of the conditions of occurrence of FS effect. This means that the satellite receiver and a transmitter are located on the same line, which crosses the object. Experiments have shown that mobile and stationary object as well as mobile and stationary GPS receiver can registrate the occurrence of the FS radio shadow. Experiments have shown that the FS shadow can provide information about the parameters of the object (size, speed and direction of movement, distance to the receiver), from the width, shape and length of the received FS shadow.

The occurrence of FS shadow is essential physical phenomena, which can be used to extract some useful information about the objects that create it. The information obtained can be used in various applications like those in the classic radar, including radio barriers, security, classification and identification of moving and stationary objects.

ACKNOWLEDGEMENTS

This work is partly supported by the projects DDVU02/50/2010, MU-FS_05/2007 and NIP-01-2014.

REFERENCES

[1] Cherniakov M., (ed.), "Bistatic Radar: Principles and Practice", *Wiley & Sons*, 2007.

[2] Koch, V., R. Westphal, "New approach to a multistatic passive radar sensor for air/space defense", *IEEE AES Systems Magazine*, pp. 24-32, November 1995.

[3] Suberviola I., I. Mayordome, J. Mendizabal, "Experimental results of air target detection with GPS forward scattering radar, 2012, In *IEEE Geoscience and Remote Sensing Letters*, vol. 9, no. 1, pp.47-51 January 2012.

[4] Behar V., Chr. Kabakchiev, "Detectability of Air Target Detection using Bistatic Radar Based on GPS L5 Signals", *Proc. IRS'2011*, Leipzig, 2011, pp. 212-217.

[5] V. Behar, Chr. Kabakchiev, H. Rohling," Air Target Detection Using Navigation Receivers Based on GPS L5 Signals", *Proc. of ION GNSS' 2011*, Portland OR, 2011, pp. 333-337.

[6] Kabakchiev C., I. Garvanov, V. Behar, H. Rohling, "*The Experimental Study of Possibility for Radar Target Detection in FSR Using L1-Based Non-Cooperative Transmitter*", Proc. of IRS'13, Dresden, Germany, 2013, pp.625-630.

[7] Kabakchiev C., I. Garvanov, V. Behar, H. Rohling, A. Lazarov, "*The Experimental Study of Target FSR Shadows Detection using GPS signals*", Proc. of the Third International Symposium on Radio Systems and Space Plasma, Sofia, Bulgaria, 2013, pp. 64-73.

[8] Borre K., D. Akos, N. Bertelsen, P. Rinder, S. Jensen, "A Software-Defined GPS and Galileo Receiver: Single-Frequency Approach", *Birkhäuser*, Boston, MA, 2006.

Terahertz Wireless Communications Using Resonant Tunneling Diodes as Transmitters and Receivers

Tadao Nagatsuma, Masayuki Fujita, Ai Kaku, Daiki Tsuji, and Shunsuke Nakai
Graduate School of Engineering Science, Osaka University,
1-3 Machikaneyma, Toyonaka 560-8531, Japan
nagatuma@ee.es.osaka-u.ac.jp

Kazuisao Tsuruda, and Toshikazu Mukai
Photonics R&D Center, Rohm Co., Ltd.,
21 Saiin Mizosaki-cho, Ukyo-ku, Kyoto 615-8585, Japan

Keywords: Terahertz, communication, resonant tunneling diode, transmitter, receiver, transceiver

Abstract: This paper presents a transceiver module employing a resonant tunneling diode (RTD), which can be operated as both a transmitter and a receiver just by changing the bias voltages. Error-free wireless transmission experiments have successfully been demonstrated at 300 GHz at bit rates of 10 Gbit/s and 2.5 Gbit/s by using an RTD receiver and a transceiver, respectively.

1 INTRODUCTION

Recently, there has been an increasing interest in the application of terahertz (THz) waves (0.1 THz ~ 10 THz) to the ultrahigh-speed wireless communications. In particular, the use of carrier frequencies above 275 GHz is one of the strong attentions among radio scientists and engineers, because these frequency bands have not yet been allocated to specific active services, and there is a possibility to employ extremely large bandwidths for ultra-broadband wireless communications (Kleine-Ostmann and Nagatsuma, 2011, Song and Nagatsuma, 2011).

A 300-GHz band wireless link at a bit rate of over 40 Gbit/s has been reported, in which a photonics-based transmitter and a Schottky-barrier diode (SBD) detector are used (Nagatsuma et al., 2013). To bring the THz wireless communications technology to a widespread consumer marketplace, the development of transmitters based on compact semiconductor electronic devices is urgently required. Among various semiconductor electronic devices and integrated circuits, resonant tunneling diodes (RTDs) have exhibited the highest oscillation frequency at over 1 THz (Asada et al., 2008, Suzuki et al., 2010). In this paper, we first describe the application of RTDs to receivers in THz wireless communications. Sensitivity enhancement due to strong nonlinearity of direct current (DC) current-voltage (I-V) characteristics is discussed both theoretically and experimentally. Receiver modules integrated with an MgO lens are developed for broadband operation at a bit rate of over 10 Gbit/s with a carrier frequency of 300 GHz. Finally, multi-gigabit wireless transmission experiments are demonstrated using RTDs as both the transmitter and receiver at 300 GHz.

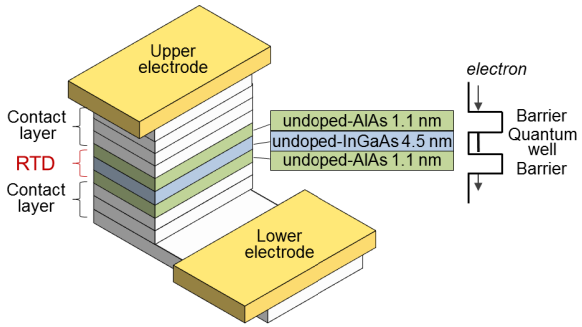

Figure 1: Typical device layer structure of RTD.

2 DEVICE STRUCTURES AND OPERATION PRINCIPLE

Figure 1 shows a typical device layer structure of the RTD on InP substrate. The resonant tunneling region of the diode is composed of an InGaAs/AlAs double barrier structure. By making upper and lower contact layers asymmetric, DC I-V characteristics become

asymmetric with a polarity of DC voltage or current as shown in Fig. 2. A wide negative resistance (NDR) region (Point A) is suitable to the oscillator operation, while the peak point with the opposite polarity (Point B) is appropriate for the detector operation.

Usually, the RTD is integrated with a planar antenna such as dipole and tapered slot antennas. The antenna-integrated RTD chip is mounted on the coplanar waveguide substrate with the co-axial connector via bonding wire as shown in Fig. 3.

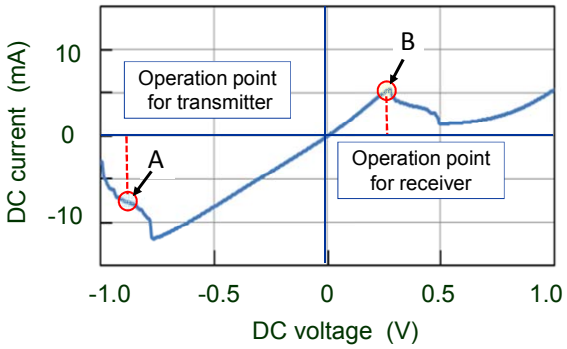

Figure 2: DC I-V characteristics of the RTD and operation points for transmitter (A) and receiver (B).

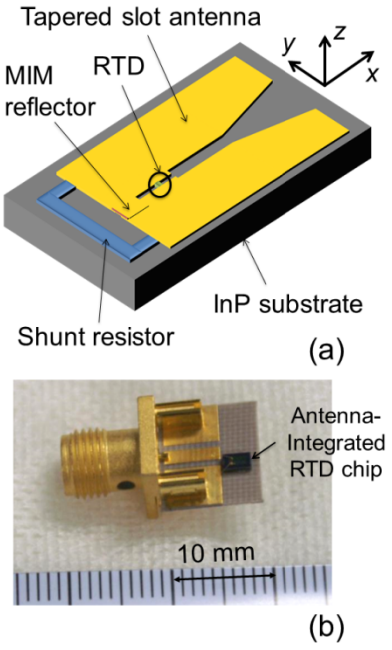

Figure 3: (a) Schematic of antenna-integrated RTD. (b) Photograph of a connectorised RTD module.

3 APPLICATIONS TO RECEIVERS

3.1 Responsivity Evaluation

Receiver responsivity can be estimated from DC I-V characteristics based on the square-low detection theory (Cowley and Sorenson, 1966). The detected power is expressed in the case of 50-ohm load as

$$P = \left\{ \frac{\left(A^2/4\right) f^{(2)}(V_{Bias}) + \left(A^4/64\right) f^{(4)}(V_{Bias})}{f^{(1)}} \right\}^2 \Big/ 50 \qquad (1),$$

where $f(V)$ $(= I)$ is the I-V function, $f^{(1)}$, $f^{(2)}$, and $f^{(4)}$ are derivatives of $f(V)$ with respect to V, and A is an amplitude of the input radio frequency (RF) voltage applied to the RTD.

We have conducted the experiment to verify the above theory by using the receiver module, where the RTD chip is bonded to a tapered slot antenna on a glass epoxy substrate (FR-4) as shown in Fig. 4. In order to evaluate an intrinsic responsivity of the RTD avoiding the influence of a conductor loss and parasitic elements, 35-GHz signals were received by the module with the RTD chip which has a cut-off frequency above 300 GHz. 35-GHz signals were amplitude-modulated at 100 kHz, and demodulated signals by the receiver was measured by a spectrum analyzer tuned at 100 kHz.

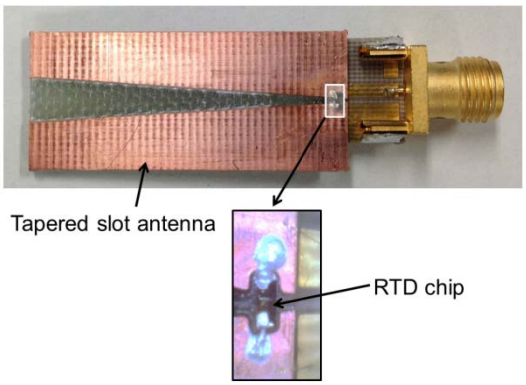

Figure 4: Photograph of the RTD receiver module for 35-GHz experiment.

Figure 5 shows a dependence of the received power measured as a function of the DC bias voltage. The DC I-V characteristics are also plotted in the figure. A solid line (measured) and a broken one (calculated) agree quite well. Relative responsivity

becomes maximum at the peak voltage just before the NDR region as expected. In the NDR region, the output voltage becomes unstable and a noise level increases.

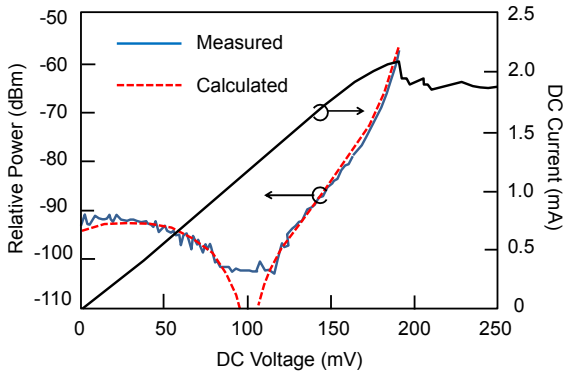

Figure 5: Relative responsivity and DC current as a function of DC bias voltage.

3.2 Receiver Modules

We simulated antenna radiation patterns of the RTD chip of Fig. 3(a) (1.9 mm long, 0.9 mm wide and 0.6 mm thick) for frequencies of 295 GHz, 300 GHz, and 305 GHz, by finite-difference time-domain (FDTD) method as shown in Fig. 6. Due to relatively thick InP substrate with a high relative dielectric constant, ε_r (12.1), the radiation patterns become diverse and vary considerably with the frequency. The electromagnetic waves do not propagate along the tapered slot antenna, but are attracted into the InP substrate (Yngveson et al., 1989), which results in Fabry-Perot resonance inside the substrate, and a maximum antenna gain of 8.8 dBi.

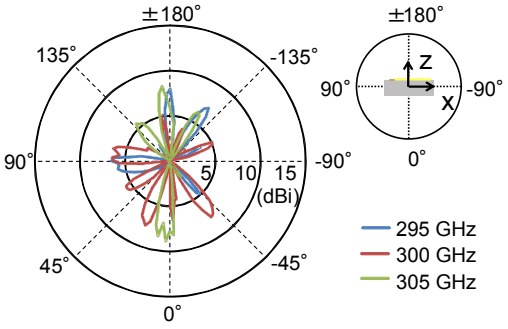

Figure 6: Simulated antenna patterns on H-plane of the RTD chip shown in Fig. 3 for various frequencies.

We examined an integration of an MgO hyper-hemispherical lens (Nakajima et al., 2004) with the RTD chip in order to improve the antenna pattern. Attaching a hyper-hemispherical lens to substrate can lead to the efficient coupling of THz radiation to the free space from the substrate with a collimation effect and low aberration (Van Rudd et al., 2002). The reflection at the InP-MgO interface is small since the relative dielectric constant of MgO is $\varepsilon_r \sim 9.7$ for 300 GHz, which is close to that of the InP substrate. MgO is almost transparent both for THz waves and visible light. Thus we can easily integrate the lens while aligning the position of the RTD chip. The chip is glued to the center of the cross-section of the lens by ultraviolet cure adhesive. Figure 7 shows the simulated antenna patterns of the RTD chip integrated with the MgO lens. The directivity is almost the same for 290–300 GHz. The maximum antenna gain is 12.5 dBi.

Figure 8 shows photographs of the RTD receiver module with the MgO lens.

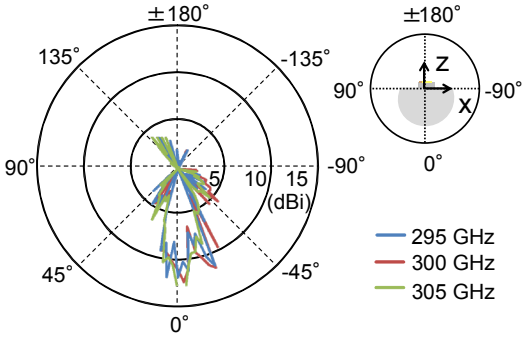

Figure 7: Simulated antenna patterns on H-plane of the RTD chip with MgO lens for various frequencies.

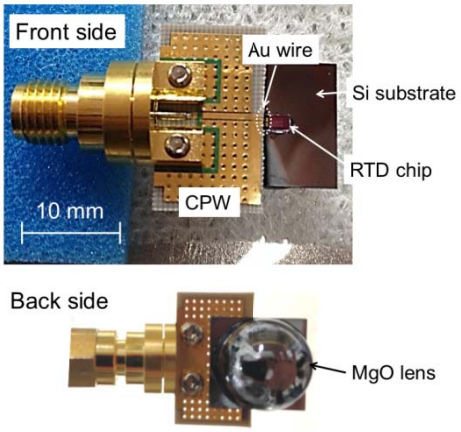

Figure 8: Photographs of the RTD receiver module with MgO lens.

We conducted wireless transmission experiments using a frequency-multiplier-based transmitter and the RTD receiver. Figure 9 depicts a schematic diagram of the experimental setup. The output signal from the up-converter, which mixes the RF signal from a synthesizer (32–36 GHz) and the digital signal from a pulse-pattern generator, is multiplied by nine times to generate THz signals at 288–324 GHz. THz signals are radiated into the free space by a horn antenna (25 dBi), and are detected by the RTD receiver module. Demodulated signals are amplified and re-shaped by a preamplifier and a limiting amplifier, respectively.

Figure 10 shows bit error rate (BER) characteristics and eye diagrams. Error-free (BER<10^{-11}) transmission has been confirmed up to the bit rate of about 11 Gbit/s. Currently, the maximum bit rate is limited by the modulation bandwidth of the transmitter based on the frequency multiplier. Our design of the receiver module ensures the bit rate of over 20 Gbit/s.

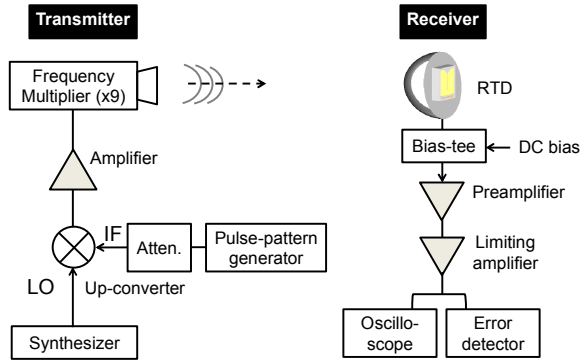

Figure 9: Block diagram of wireless transmission experiment using a frequency-multiplier-based transmitter and the RTD receiver.

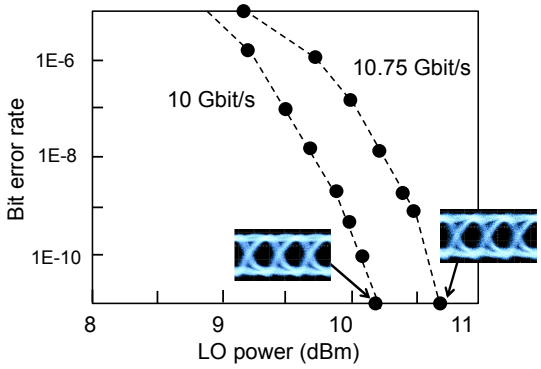

Figure 10: Bit error rate characteristics and eye diagrams at 300 GHz.

4 APPLICATIONS TO ALL RTD-BASED TRANSCEIVERS

For the operation of the RTD as a transmitter, the amplitude of the applied voltage is changed to perform the on-off keying (OOK) modulation as shown in Fig. 11. The amplitude of both the DC bias and RF modulation voltages was carefully adjusted so that the output power from the RTD became maximum (Mukai et al., 2011).

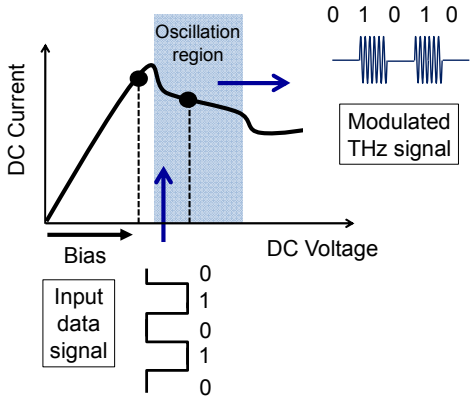

Figure 11: Operation of the RTD as a transmitter with OOK modulation scheme.

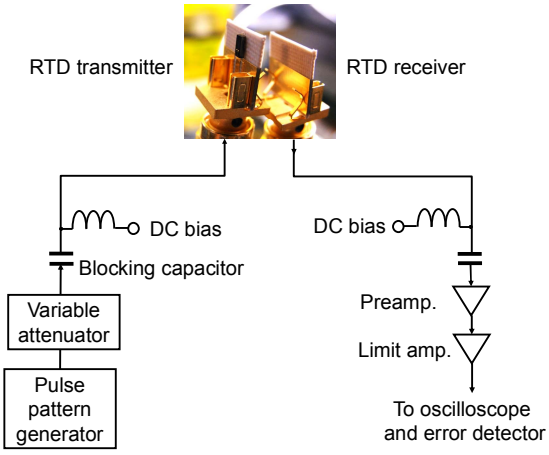

Figure 12: Experimental setup of proximity wireless transmission experiment using two sets of RTD modules.

By using two sets of RTD modules without MgO lens (Fig. 3(b)), we conducted a close-proximity wireless transmission experiment, placing the two modules at a distance from a few millimeters to several tens of millimeters as shown in Fig. 12. For

the transmitter, the data signal (RF voltage) from the pulse-pattern generator was applied to the module with an appropriate DC bias voltage through a bias-T. For the receiver, just a DC bias voltage was applied to the RTD to maximize the sensitivity. The demodulated baseband data signal was amplified with the preamplifier followed by the limiting amplifier.

The oscillation frequency depends on the parallel inductance and capacitance of RTD chip, and the output power is proportional to the widths of the current and voltage of the NDR region (Asada et al., 2008). The oscillation frequency and the output power of the RTD used for the experiments were approximately 300 GHz and several μW, respectively.

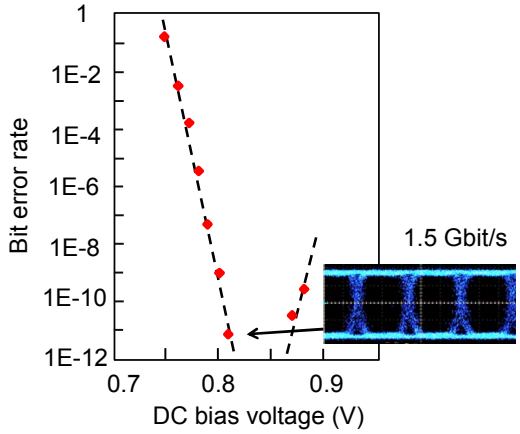

Figure 13: BER characteristics plotted against the DC bias voltage and eye diagram at 1.5 Gbit/s.

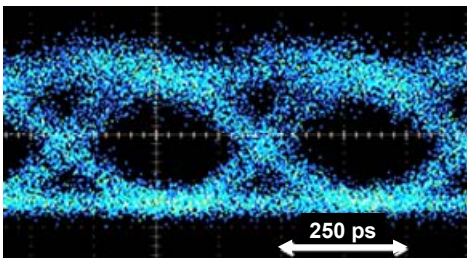

Figure 14: Demodulated eye diagram at 2.5 Gbit/s.

Figure 13 shows a dependence of the BER on the applied DC bias voltage when the amplitude of the data signal was 160 mVp-p. At 0.85 V, an error-free transmission at 1.5 Gbit/s was achieved as shown in the eye diagram of Fig. 13. There were optimum DC bias voltages depending on the RF voltage amplitude. By carefully adjusting the DC bias voltage, the achieved maximum data rate was 2.5 Gbit/s (Fig. 14), which is mainly limited by the frequency-dependent radiation pattern as discussed in Sec. 3.2, and the bandwidth of the packaging (Shiode et al., 2011, 2012). Use of RTD transceiver modules with MgO lens will increase the bit rate over 10 Gbit/s.

5 CONCLUSIONS

We have described a small and cost-effective transceiver module employing resonant-tunnelling diodes (RTDs) towards wide-spread consumer THz wireless applications such as a close-proximity instantaneous data transfer and a wireless interconnection.

The RTD-based receiver module with MgO hyper-hemispherical lens has exhibited over 10-Gbit/s performance at 300 GHz. Using the RTD-based transmitter and receiver, a close-proximity wireless transmission at 2.5 Gbit/s has been demonstrated with an error-free condition. Future works should be placed on the increase of data rate and transmission distance by improving the packaging and the antenna structure, respectively.

ACKNOWLEDGEMENT

This work was supported in part by the Strategic Information and Communications R&D Promotion Programme (SCOPE), from the Ministry of Internal Affairs and Communications, Japan.

REFERENCES

Asada, M., Suzuki S., Kishimoto, N., 2008. Resonant tunneling diodes for sub-terahertz and terahertz oscillators. *Jpn. J. Appl. Phys*., Vol. 47, No. 6, pp. 4375–4384, 2008.

Cowley A. M., Sorenson, H. O., 1966. Quantitative comparison of solid-state microwave detectors. *IEEE Trans. Microwave Theory and Tech.*, vol. 14, pp. 588–602.

Kleine-Ostmann, T., Nagatsuma, T., 2011. A review on terahertz communications research. *J. Infrared Milli. Terhz. Waves*, vol. 32, no. 2, pp. 143–171.

Mukai T., M. Kawamura, M., Takada, T., Nagatsuma, T., 2011. 1.5-Gbps wireless transmission using resonant tunneling diodes at 300 GHz. *Tech. Dig. Optical Terahertz Science and Technology (OTST2011)*, MF42, Santa Barbara.

Nagatsuma, T., Ito, H., Ishibashi, T., 2009. High-power RF photodiodes and their applications. *Laser Photon. Rev.*, vol. 3, no. 1-2, pp. 123–137.

Nagatsuma, T. et al., 2013. Terahertz communications based on photonics technologies, *Optics Express*, vol. 21, no. 20, pp. 23736–23747.

Nakajima, M., Uchida, K., Tani, M., Hangyo, M., 2004. Strong enhancement of terahertz radiation from semiconductor surfaces using MgO hemispherical lens coupler. *Appl. Phys. Lett.*, vol. 85, no. 2, pp. 191–193.

Shiode, T., Mukai, T., Kawamura, M., Nagatsuma, T., 2011. Giga-bit wireless communication at 300 GHz using resonant tunneling diode detector. *Proc. Asia-Pacific Microwave Conference (APMC2011),* Melbourne.

Shiode, T., Kawamura, M., Mukai, T., Nagatsuma, T., 2012. Resonant-tunneling diode transceiver for 300 GHz-band wireless link. *Tech. Dig. Asia-Pacific Microwave Photonics Conf. (APMP2012)*, WC-1, Kyoto.

Song, H.-J., Nagatsuma, T., 2011. Present and future of terahertz communications. *IEEE Trans. Terahertz Science and Technology*, vol.1, no. 1, 256–264.

Suzuki, S., Asada, M., Teranishi, A., Sugiyama H., Yokoyama, H., 2010. Fundamental oscillation of resonant tunneling diodes above 1 THz at room temperature. *Applied Physics Letters*, vol. 97, no. 24, pp. 242102–242102-3.

Van Rudd J., Mittleman, D. M., 2002. Influence of substrate-lens design in terahertz time-domain spectroscopy. *J. Opt. Soc. Am. B*, vol. 19, no. 2, pp. 319–328.

Yngveson, K. S., Korzeniowski, T. L., Kim, Y.-S., Kollberg, E. L., Johansson, J. F., 1989. The tapered slot antenna- A new integrated element for millimeter-wave applications. *IEEE Trans. Microwave Theory and Tech.*, vol. 37, no. 2, pp. 365–374.

Feasibility Study on Microwave Power Transmission to an Airplane for Future Mars Observation

Tomohiko Mitani, Masashi Iwashimizu, Akihito Nagahama, and Naoki Shinohara
Research Institute for Sustainable Humanosphere, Kyoto University, Gokasho, Uji-shi, 611-0011 Japan
mitani@rish.kyoto-u.ac.jp

Koichi Yonemoto
Graduate School of Engineering, Kyushu Institute of Technology,
1-1 Sensui-cho, Tobata-ku, Kitakyushu-shi, Fukuoka, 804-8550 Japan

Keywords: Microwave Power Transmission, Magnetron, Rectenna.

Abstract: The objective of the present study is to investigate the feasibility of microwave power transmission to an airplane for future Mars observation. Airplane is a possibility of Mars observation with wide range and high resolution, compared to rover or satellite. Since the surface pressure of Mars atmosphere is much thinner than the Earth, weight reduction is essential to realize airplane flight on Mars. We therefore propose long-time flight on Mars by using microwave power transmission. We conducted terrestrial experiments of microwave power transmission to a prototype airplane. We developed a magnetron-based microwave transmitting system, the frequency of which was fixed with signal injection locking method. Rectennas (receiving antenna + rectifying circuit) were mounted on the prototype airplane for driving a propeller connected to an electric motor. Although autonomous flight was not successful yet, we demonstrated that the prototype airplane could fly by receiving the microwave power.

1 INTRODUCTION

Mars, the fourth planet from the sun, is always of interest to space scientists and astronomers. Lots of Mars exploration programs have been executed since 1960s. The Mars rover “Curiosity”, launched in 2011 and landed on Mars in 2012, provides numerous observation data including images of Martian landscape and properties of Martian rocks and soils.

Airplane is expected as an alternative Mars observation sysytem to satellite and rover. It can move around more widely and quickly than rover, and can take images with better resolution than satellite. However the airplane is technically difficult to gain sufficient aerodynamic lift, because the surface pressure of Mars is only 0.6 % on Mars of that of the Earth. Weight reduction of the airplane is therefore essential to realize the flight on Mars.

We propose microwave power transmission (MPT) as power supply to a Mars observation airplane. MPT can reduce the airplane weight by replacing battery or fuel with rectenna (receiving antenna + rectifying circuit). It can also realize a long-time flight by supplying electricity continuously from a long distance. Figure 1 shows a conceptual image of a Mars observation airplane driven by MPT. The transmitting system will be placed on Mars and electricity will be transferred to the airplane via microwave. With detecting the airplane position, the microwave beam will be always focused on the airplane.

The objective of the present study is to investigate the feasibility of MPT to an airplane for future Mars observation. In this paper we describe a magnetron-based microwave transmitting system, a prototype airplane, and terrestrial MPT demonstration to the prototype airplane, with referring to the previous research outcomes (Iwashimizu, 2014, Nagahama, 2012, 2011).

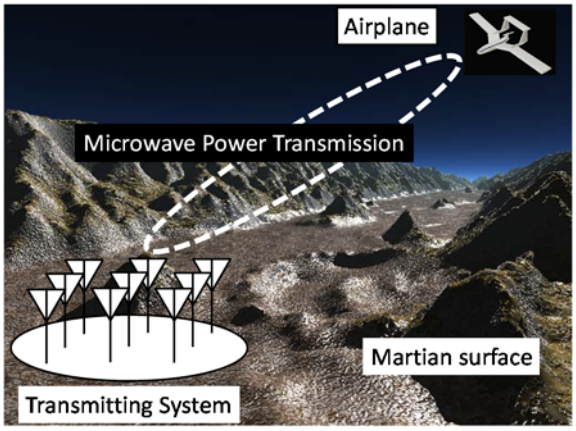

Figure 1: Conceptual image of a Mars observation airplane driven by microwave power transmission.

2 SYSTEM REQUIREMENTS OF TERRESTRIAL EXPERIMENTS

Specifications of Mars observation airplane under consideration are shown in Table 1. When we utilize MPT for a Mars observation airplane, the power required for a propeller motor must be transferred continuously. Then the power density at the main wing, on which rectennas will be mounted, is estimated to be 818 W/m^2, assuming that the rf-dc conversion efficiency of the rectenna is 63 %. Since we cannot conduct MPT from such a long distance of 100 m as a feasibility study, the estimated power density becomes the criterion for the power density of terrestrial MPT experiments.

Table 1: Specifications of Mars observation airplane (under consideration).

Airplane weight	1.81 kg
Velocity	50.9 m/s
Main wing area	0.256 m^2
Power required for motor	132 W
Flight altitude	Order of 100 m

The objective of terrestrial experiments is to realize battery-less stable flight by MPT. A schematic of the terrestrial experiments is shown in Figure 2. The experiments were conducted in an anechoic chamber and the distance from the transmitting system to a prototype airplane is about 3 m. Under the configuration, kW-class microwave power is necessary to meet the required power density. We therefore adopt magnetron, which is available for microwave oven, as microwave generator.

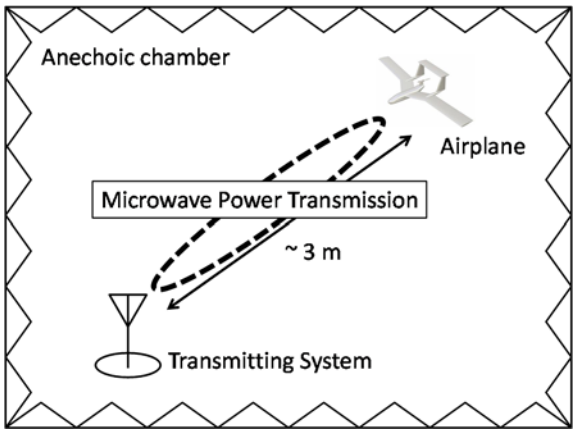

Figure 2: Schematic of terrestrial MPT experiments to a prototype airplane.

3 MAGNETRON-BASED MICROWAVE TRANSMITTING SYSTEM

The transmitting frequency of MPT must be fixed from the viewpoint of rectenna design with high rf-dc conversion efficiency. Also the output power must be controlled to realize stable flight because the distance between the transmitting systems and the airplane fluctuate constantly. Moreover, the output phase of each transmitting antenna element must be controlled when we introduce phased array for the transmitting system. However a magnetron is a free-running oscillator and its frequency shifts by its driving current (anode current), temperature and output load.

We therefore developed a power-variable phase-controlled magnetron (PVPCM). A great feature of PVPCM is that its output power can be controlled with keeping its frequency and phase locked to those of reference signal. A schematic diagram of a PVPCM is shown in Figure 3. An injection locking method (Sivan, 1994) is used for locking the magnetron frequency to the reference signal frequency. Also phase synchronization is realized by comparing phases of the magnetron output and the reference signal and adjusting the reference signal phase via the phase shifter 2. The phase shifter 1 is used for controlling the microwave beam direction when we apply phased array to the transmitting system.

We succeeded in developing a PVPCM, whose frequency was fixed at 2.44575 GHz and whose output power could be controlled from 450 W to 860 W (Nagahama, 2011).

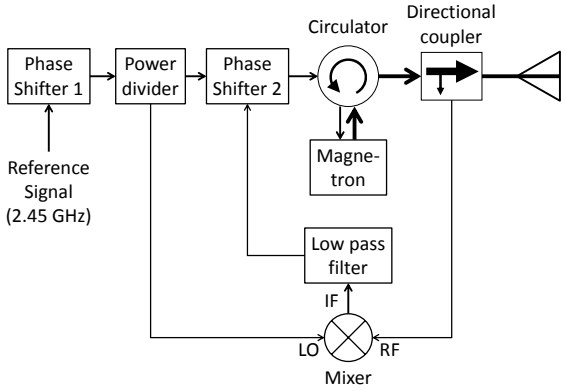

Figure 3: Schematic diagram of a power-variable phase-controlled magnetron (PVPCM).

We demonstrated microwave beam forming by a phased array composed of two PVPCMs. Figure 4 shows a photograph of the PVPCM phased array. Two PVPCMs were set in a horizontal plane. The horn antenna spacing was 0.409 m.

Figure 5 shows experimental results of microwave beam patterns by the PVPCM phased array. When two PVPCMs were in phase, the microwave beam was focused on the broadside direction. We confirmed that the beam direction was controlled by setting the phase difference between two PVPCMs. We obtained the antenna gain of 20 dBi including array factor and element factor of horn antenna. Also we confirmed that we could adjust the power density at the receiving point by controlling the output power.

Figure 4: Photograph of a PVPCM phased array. The phased array was composed of two PVPCMs.

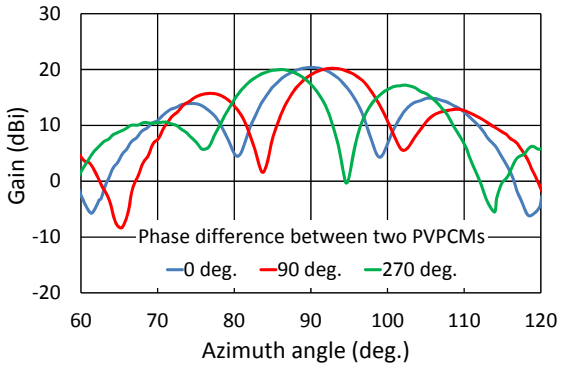

Figure 5: Experimental results of microwave beam patterns of the PVPCM phased array.

4 PROTOTYPE AIRPLANE

Figure 6 shows a schematic of a prototype airplane. The prototype airplane was made of polystyrene foam, and driven by a propeller attached to an electric motor. The red circles in Figure 6 indicate the places where rectennas were allocated. Six rectennas were mounted on the airplane without interfering with each other in the light of electromagnetic field.

Figure 7 shows a photograph of our developed rectenna. The rectenna consisted of cross dipole antenna and rectifying circuit. The cross dipole antenna was chosen because it can receive sufficient microwave power even under a various attitude of the airplane. The measured rf-dc conversion efficiency of the rectrenna was 63 % when the output load was 100 Ω (Nagahama, 2012). On the airplane, all the rectennas were connected in pallalel for the purpose of impedance matching with the electric motor.

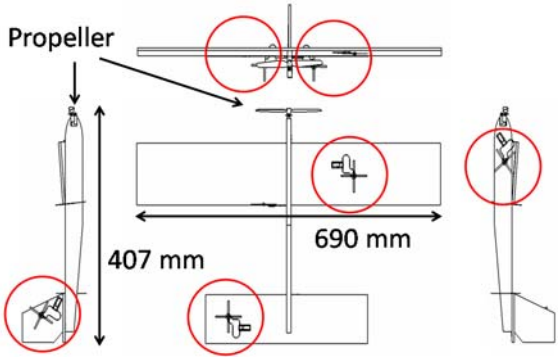

Figure 6: Schematic of a prototype airplane. The red circles indicate the places where rectennas were allocated.

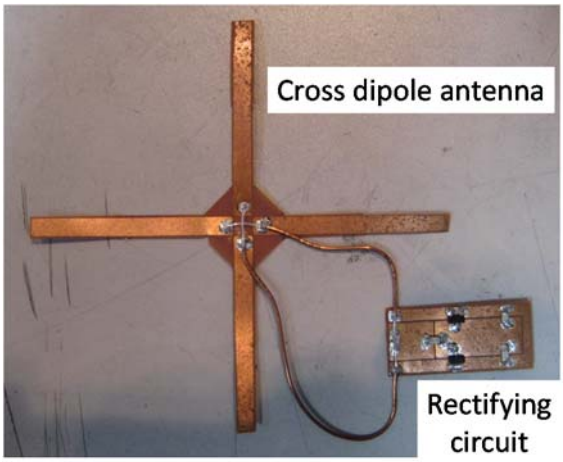

Figure 7: Photograph of a rectenna. The rectenna was composed of cross dipole antenna and rectifying circuit.

5 DEMONSTRATION FLIGHT

We conducted two types of demonstration flight in the anechoic chamber: straight flight and circular flight. Figure 8 shows a photograph of the demonstration of circular flight. In both cases, the transmitting system was composed of a single magnetron and horn antenna. The horn antenna direction was mechanically controlled towards the prototype airplane. The output power was 800 W. In the case of circular flight, the prototype airplane was suspended from above by gut. We confirmed that the prototype airplane was driven by MPT in both cases.

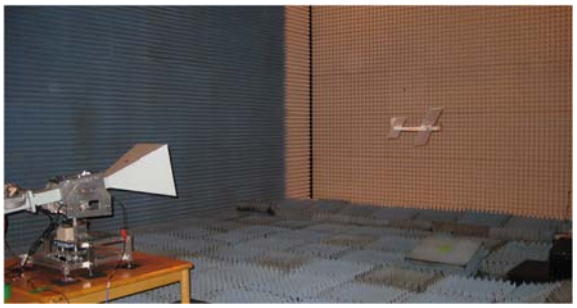

Figure 8: Photograph of demonstration flight. The transmitting system was composed of a single magnetron. The transmitting antenna direction was mechanically controlled towards the prototype airplane.

6 CONCLUSION

We succeeded in demonstration flight of the prototype airplane by MPT without battery and fuel. Adoption of phased array for the transmitting system will be the next step for a long-distance and long-time flight. Precise direction detection of the prototype airplane will be also necessary to realize autonomous flight.

ACKNOWLEDGEMENTS

This work was supported by JSPS KAKENHI, Grant-in-Aid for Challenging Exploratory Research, Grant Number 25630391.

REFERENCES

Iwashimizu, M., Mitani, T., Shinohara, N., Sasaki, G., Hiraoka, K., Matsuzaki, K., Yonemoto K., 2014. Study on Direction Detection in a Microwave Power Transmission System for a Mars Observation Airplane. In *IEEE Wireless Power Transfer Conference (WPTC 2014)*.

Nagahama, A., Mitani, T., Shinohara, N., Fukuda, K., Hiraoka, K., Yonemoto K., 2012. Auto Tracking and Power Control Experiments of a Magnetron-based Phased Array Power Transmitting System for a Mars Observation Airplane. In *2012 IEEE MTT-S International Microwave Workshop Series (IMWS) on Innovative Wireless Power Transmission: Technologies, Systems, and Applications (IMWS-IWPT 2012)*.

Nagahama, A., Mitani, T., Shinohara, N., Tsuji, N., Fukuda, K., Kanari, Y., Yonemoto K., 2011. Study on a Microwave Power Transmitting System for Mars Observation Airplane. In *2011 IEEE MTT-S International Microwave Workshop Series (IMWS) on Innovative Wireless Power Transmission: Technologies, Systems, and Applications (IMWS-IWPT 2011)*.

Sivan, L., 1994. *Microwave Tube Transmitters*, Chapman & Hall, London.

Choice of the Definition Method for the Total Electron Content to Describe the Conditions in the Ionosphere

Olga Maltseva
Institute of Physics Southern Federal University, Stachki, 194, Rostov-on-Don, Russia
mal@ip.rsu.ru

Keywords: GPS. Total electron content TEC. Ionospheric models. Radio wave propagation. Geomagnetic disturbances.

Abstract: Conditions of radio-wave propagation in the ionosphere, influencing functioning of the modern navigation and communication systems, are defined by the critical frequency foF2 and an electron density distribution termed the N(h)- profile. In the given paper, the experimental values of the total electron content TEC(obs) are used for their determination. It is shown that the median of the equivalent slab thickness of the ionosphere is the good calibration factor, allowing to obtain values of foF2 from TEC(obs) of any global map though in most cases values of foF2, the closest to foF2(obs), are provided with the JPL map. For coordination of the N(h)-profile with values of TEC(obs), coefficient K(PL), modifying a plasmaspheric part of a profile, is entered (up to heights of navigation and geostationary satellites). In this case, the CODE map is the best one. It is necessary to have models of the TEC parameter to support navigation system operation. It is shown that the big progress in modeling of this parameter is reached during the last years: appearance of various models allows us to compare and use them at forecast TEC for any level of solar activity. It is especially important, because values of solar spots and the F10.7 parameter and also geomagnetic indexes of Kp, Dst, AE are well enough predicted.

1 INTRODUCTION

The ionosphere plays an important role in the life of mankind: it mitigates the blows of solar wind and provides wave propagation of various frequency bands. The systems connected to the ionosphere are most full presented in Tab. 1 from the paper (Goodman, 2005).

Category 1 involves those systems that depend upon the ionosphere (i.e., involve the ionosphere as part of the system), and category 2 involves those systems for which the ionosphere is simply a nuisance. The special role for description of the ionospheric conditions is played by models, and the model, capable to provide high accuracy of description of ionospheric characteristic distribution, should be adapted for the experimental information in a real time mode.

Table 1: Categories of radio systems in terms of ionospheric dependence

Category 1: systems that depend upon the ionosphere	Category 2: systems for which the ionosphere is simply a nuisance
VLF–LF communication and navigation	Satellite communication
MF communication	Satellite navigation (e.g., GPS&GLONASS)
HF communication	Space-based radar and imaging
HF broadcasting (‘‘short-wave’’ listening)	Terrestrial radar surveillance and tracking
OTH radar surveillance	Meteor-burst communication
HFDF and HF SIGINT	Any other system for which the ionosphere is not necessary for conveyance

The data which can be used in such an approach should be available and operatively updated.

Traditional parameters meeting such requirements are the critical frequency foF2 and maximum height hmF2. Because the total electron content TEC is the most important parameter of the ionosphere for the operation of technological systems, in the given paper it is used for this purpose. TEC data are available and is updated in several Internet archives. From huge number of possible applications of TEC, in the present paper the preference is given for an estimation of possibility of determination of propagation conditions. It means usage of TEC for determination of foF2 (or too NmF2) and N(h)- profiles. The huge need exists in the forecast of these parameters, and, hence, of TEC. It is possible to select three methods of the TEC determination: (1) measurements, (2) empirical modeling, (3) integration of theoretical or empirical N(h)-profiles. Information and results are given for each of these methods.

2 MEASUREMENT METHODS

The most widespread are global maps JPL, CODE, UPC, ESA, created by Jet Propulsion Laboratory of California Institute of Technology (Pasadena, USA), the Center for Orbit Determination in Europe (CODE) of the International GPS Service for Geodynamics (Switzerland), Astronomy and Geomatics of the Polytechnical University of Catalonia, Barcelona, Spain (UPC), European Space Agency (Germany) respectively as TEC experimental data (e.g. Schaer et al., 1995; Mannucci et al., 1998; Hernandez-Pajares et al., 1997; Sardon et al., 1994; Jakowski et al., 1996). For specific coordinates and time, the maps can be derived from the IONEX (IONosphere map Exchange) files (ftp://cddis.gsfc.nasa.gov/pub/gps/products/ionex/). Owing to the big differences of methods (on determination of biases, approximating functions, etc.), values of TEC for various maps and other methods of determination TEC are strongly differed. Traditional examples of such differences are Figures from the paper (Arikan et al., 2003).

Now, the GPS community selected the average IGS values as the standard (Hernandez et al., 2009), therefore in the given paper all maps, including IGS, are used. These maps are given on the same site and already start to be used, e.g. (Lean et al., 2011). We use all maps for comparison. However, under the valid remark of (Lastovicka, 2013), such selection does not remove the restrictions inherent in each method. JPL is used in paper (Gulyaeva and Stanislawska, 2008), CODE is used in paper (Jakowski et al, 2006). Other methods also yield comparable results.

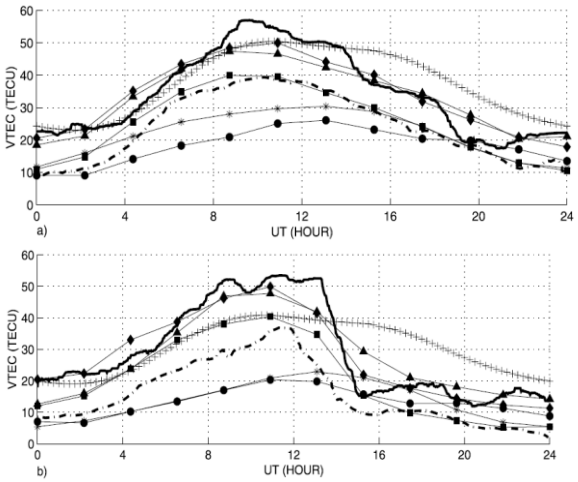

Figure 1: Comparison of the estimated TEC values from the algorithm with other models of TEC for Kiruna, estimated VTEC from the developed algorithm (solid line), RCRU (dashed line), IRI model (pluses), gAGE/UPC (triangles and a solid line), JPL-GNISD (diamonds and a solid line), ESA/ESOC (circles and a solid line), NRCan (stars and a solid line), CODE (squares and a solid line). (a) 25 April 2001 and (b) 28 April 2001.

3 METHODS OF EMPIRICAL MODELING

Empirical modeling plays an important role both for the forecast of ionospheric parameters, and for validation of models. For modeling of TEC, basically, the method of orthogonal components is used (Zhang et al., 2012; Ivanov et al., 2011), however authors do not give appropriate coefficients and functions. Besides, there is a difficulty of the forecast at an output for temporal boundaries of the used data, therefore the main attention is given for avaiable and new models. Many long years, the most simple model of Klobuchar (Klobuchar, 1987) was unique for adjustment of delay of signals in the ionosphere and till now is widely used for systems with single-frequency receivers though the authors using it note a row of shortcomings, for example (Chen and Gao, 2005). The model (Kakinami, 2009) is an example of models for specific station which should possess the high accuracy. The model is based on values of the instrumental biases given by the JPL laboratory. Results of the test of this model

in the form of correspondence between model and experimental values are given on Fig. 2.

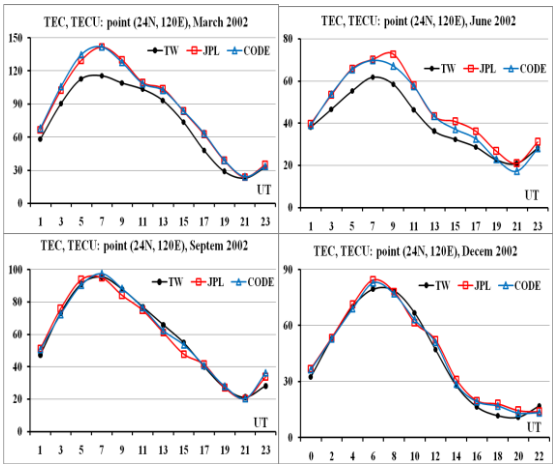

Figure 2: Comparison of model and observational TEC for the Taiwan model near to a maximum of solar activity.

Seasonal course of TEC at the given latitude and the full conformity of model and observational TEC for autumn and winter months is perfectly seen. In the spring and in the summer, the model underestimates values. Range of the root mean square (RMS) deviation makes 4-14 TECU, the relative RMSD makes 6-18 %. On Fig. 3, results for a minimum of solar activity are yielded. Additionaly, values of IGS are shown by asterisks.

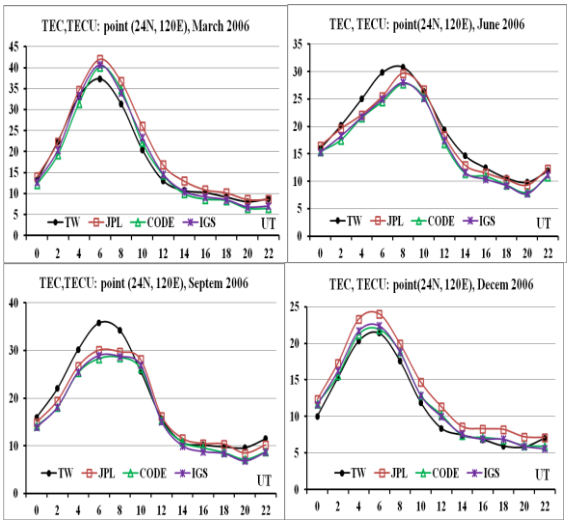

Figure 3: Comparison of model and observational TEC for the Taiwan model near to a minimum of solar activity.

It is seen that values of TEC can be in 2-3 times less, than in a maximum of solar activity. The model can both to underestimate and to overestimate the observational values. The range of absolute deviations has made 1-10 TECU. Absolute (σ, TECU) and relative (σ, %) RMSD are presented to Tab. 2 for four months of three years.

Table 2: Absolute and relative RMS deviations for the model (Kakinami, 2009).

σ, TECU	Mar	Jun	Sep	Dec
2002	13.5	8.0	3.5	4.0
2006	3.0	1.7	2.6	2.2
2010	5.6	2.8	5.9	5.6
σ, %	Mar	Jun	Sep	Dec
2002	15.8	17.2	6.0	8.9
2006	14.7	9.5	14.6	16.2
2010	24.3	16.3	26.2	24.3

If to compare these results with 50 % - estimation for the model (Klobuchar, 1987) then improving in 2-5 times may be got. Important property of the model is dependence of TEC on a daily index. The previous Figures 2 and 3 showed results for medians. The following Fig. 4 gives comparison of daily model and experimental values for August 2002.

Good correspondence of dynamics of TEC variations is seen. That proves to be true by quantitative estimations of absolute deviations 6.4 TECU, absolute RMS deviations 8.3 TECU and relative RMSD 16.4 %. These results show high efficiency of the model and a way of its construction. It can be used for validation of other models.

One more aspect of use of models is connected with reconstruction of TEC values for those periods when there were no regular measurements of TEC (before 1998). The possibility of such reconstruction is illustrated on Fig. 5 according to GPS measurements at the Taiwan station in the morning since September 1996 till August 1997 (Wu et al., 2004). Icon TEC represents measurements, TW - values of the Taiwan model.

It is seen that results are satisfactory as a first approximation. They give representation also about possibilities of forecast forward.

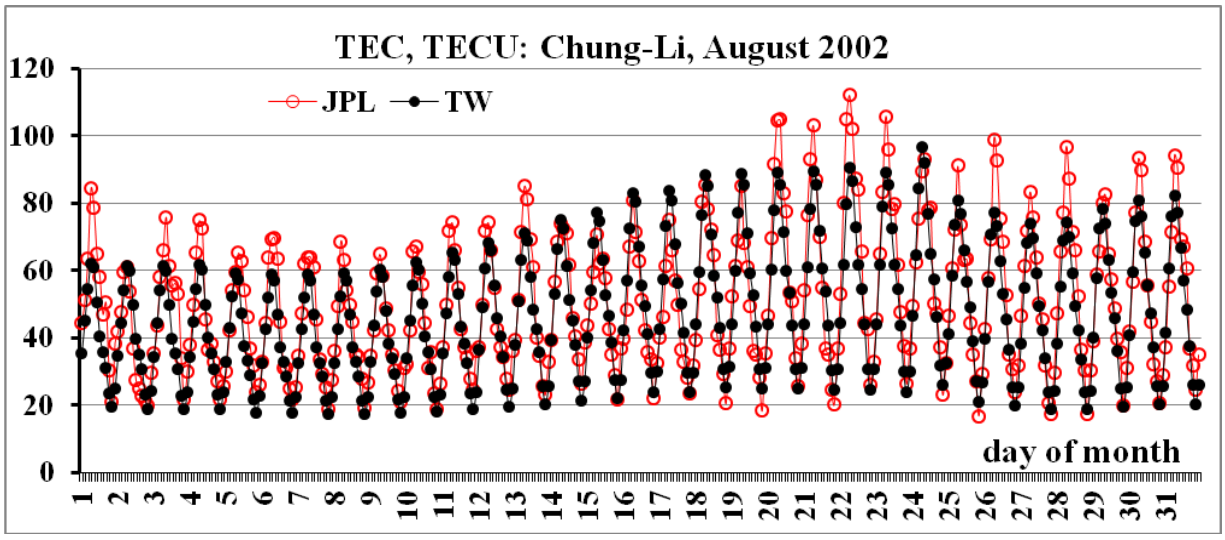

Figure 4: Comparison of daily model and experimental TEC for August 2002.

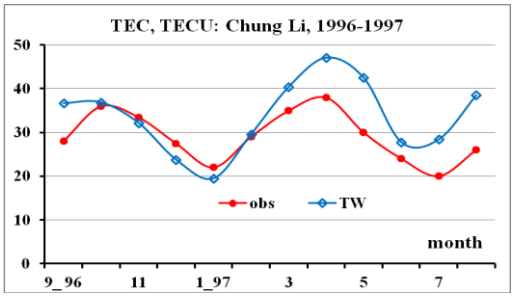

Figure 5: Comparison of model and observational TEC in years 1996-1997.

The Neustrelitz Global Model (NGM) unlike the Taiwan model is global one (Jakowski et al., 2011). Except the TEC model, it includes models of other parameters (NmF2, hmF2) (Hoque and Jakowski, 2011, 2012). Authors of this model have fulfilled own validation however it is not enough for certain conclusions about efficiency of their model. Results of more extensive validation are given in (Maltseva et al., 2013c) for a middle-latitude region and in (Maltseva et al., 2013b) for low-latitude area in which the greatest advantages were expected. Results of additional validation for low-latitude stations Niue and Sao Luis are given on Fig. 6, for high-altitude stations are given on Fig. 7.

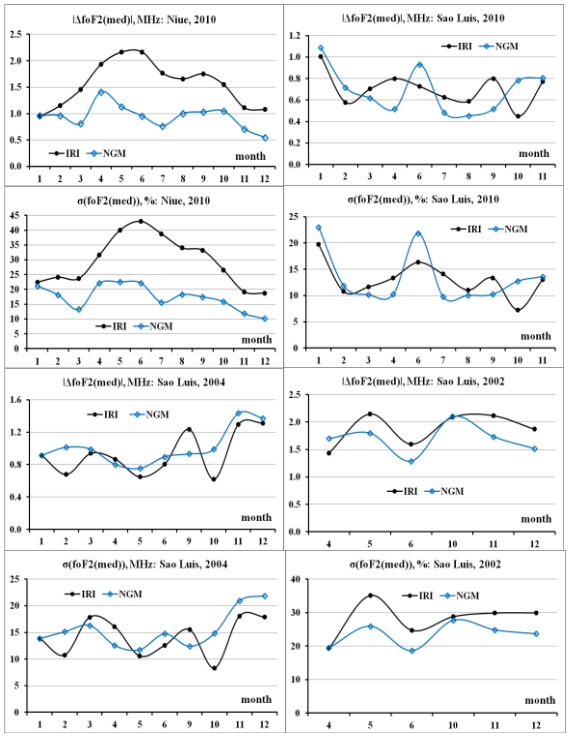

Figure 6: Cases of the NGM model advantage at definition of foF2 (two low-latitude stations, 2010, 2004, 2002).

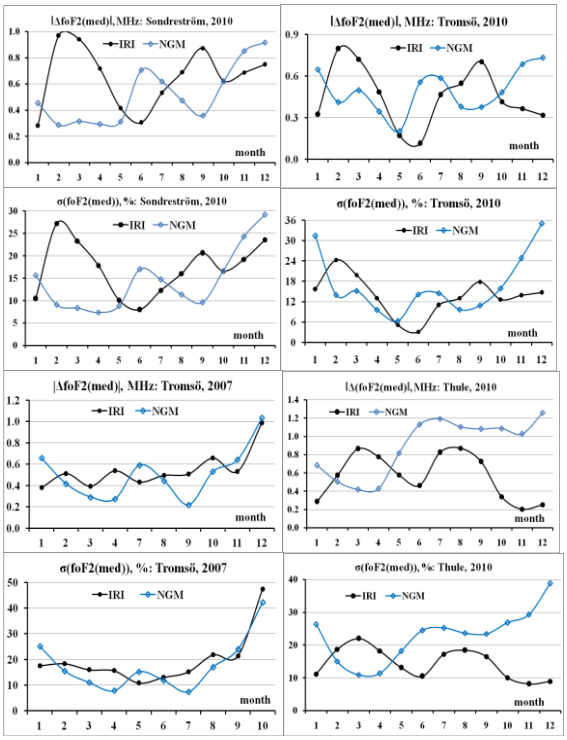

Figure 7: Cases of the NGM model advantage at definition of foF2 (three high-altitude stations, 2010, 2007).

In these cases, periods of the NGM model advantages are seen, however the major statistics on all regions shows that the NGM model not always yields the best results, than the IRI model. Discrepancy between radio occultation and ionosonde values of NmF2 may be one of the reasons why insert of great number of radio occultation measurements has not led to improvement of the NGM model, e.g. (Hajj and Romans, 1998; Tsai and Tsai, 2004). Nevertheless, it can be recommended for use in low- and high-latitude areas.

Process of model development continues constantly that is additional confirmation of an urgency of this process. The latest model is the model of authors (Mukhtarov et al., 2013a, b). It, on the one hand, is the most physically proved, on the other hand, according to estimates of authors, their model is two times more exact, than the NGM model. In papers (Mukhtarov et al., 2013a, b), not only the TEC model is developed, but also model of its error (Mukhtarov et al., 2013b). Difference from the NGM model is the consideration not only components, caused by sunlight, but also the regular wave structure of the tidal nature influencing from the lower atmosphere. The model is constructed according to the CODE map for 1999-2011. As the starting parameter, not only coefficient F10.7 is chosen, but also its linear velocity of change K_F. It is one more difference of this model from all previous options. For all array of the used data, the following estimates are obtained: mean (systematic) error ME=0.003TECU, at such ME, root of mean square error (RMSE) and an error of a standard deviation (STDE) were equal and have made RMSE=STDE=3.387TECU. These estimates are compared to estimates for the TEC(NGM) model (Jakowski et al., 2011): ME =-0.3TECU, RMSE=7.5TECU. Thus, the Bulgarian model has a smaller error in two times. However it is worth to note that both models are climatological, i.e. they describe a mean state in quiet geomagnetic conditions, and the difference in number of coefficients (12 against 4374) is underlined. Authors of (Mukhtarov et al., 2013a) absolutely validly do not consider a great number of coefficients as a model deficiency because these coefficients are calculated once, however they are inaccessible. Coefficients of the TEC(NGM) model are published and may be used by any user. In turn, we can note that there are "tails" in an error distribution of any model. It is important to determine, what latitudinal areas and to what conditions of solar activity they concern. As any model cannot work equally well in all latitudinal areas and meet the possible requirements, validation of models does not cease to be an actual problem. These requirements are connected with limitation of approaches, the used data, distinction of physical processes.

Thus, it is possible to specify major progress in modeling of parameter TEC: occurrence of various models allows us to compare and use them at forecast of TEC for any level of solar activity. It is especially important because values of solar spots and parameter F10.7, and also geomagnetic coefficients of Kp, Dst, AE are well enough predicted (e.g. Pesnell, 2012; Tobiska et al., 2013).

4 DEFINITION OF FoF2 ON CURRENT VALUES OF TEC

Definition of foF2 on current values of TEC in the this paper is based on use of median of the equivalent slab thickness of the ionosphere τ. Empirical models of τ have appeared earlier, than empirical models of TEC. Definition of TEC under formula TEC=τ*NmF2, where the independent empirical model of τ should be used, was one of

main applications of the τ model. NmF2 is possible to take from the IRI model or any another. The simple relation for τ =TEC/NmF2 shows that τ is width of a slab in the form of a rectangle with constant concentration NmF2. For definition of TEC and NmF2, the τ(IRI) model was traditionally used (e.g. Houminer and Soicher, 1996; Gulyaeva, 2003) though it also is not empirical in the same sense in what the TEC(IRI) model is not empirical model of TEC. On the basis of expression foF2=foF2(IRI)* SQRT(TEC(obs)/TEC(IRI)), GIM-TEC adaptive ionospheric weather assessment and forecast system was constructed (Gulyaeva et al., 2013). It is easy to show that value which can be designated τ(obs,IRI) is used in this case. It means that model values of NmF2 and the observational values of TEC are used at definition of τ(obs,IRI). It differs as from τ(IRI, IRI), and from τ(obs, obs) which are designated τ(IRI) and τ(obs) for brevity of records. Papers (Maltseva et al., 2012a, b) are devoted results of use of median τ(med) from values τ(obs). Empirical models of ionospheric parameters are known to include median or mean values hence they characterize a mean state, close to the quiet. Advantage of median τ(med) is that it allows to determine foF2 on current values of TEC. These foF2 values differ from averages and are closer to the real. In paper (Maltseva et al., 2012a), it is shown that the median τ(med) allows to determine foF2 during disturbances or to fill gaps of the foF2 data. The estimate of efficiency of use of values τ is done by means of calculation of deviations |ΔfoF2| of calculated foF2 from the observational ones. The observational values of TEC form the whole array: JPL, CODE, UPC, ESA, La Plata, IONOLab TEC, RAL and others. To each of these values, the various values of τ correspond. The example of τ behavior for the JPL map is shown on Fig. 8 for the Juliusruh station for April 2000 (near to a maximum of solar activity) and April 2009 (near to a minimum of solar activity).

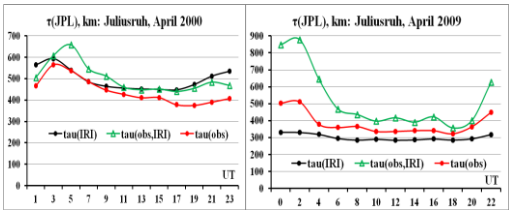

Figure 8: An example of comparison of τ for various options of TEC and NmF2.

Example of the foF2 definition by means of various τ is given on Fig. 9 together with experimental values of TEC for the JPL map. These values are shown together with medians. This picture specifies presence of disturbance.

Tab. 3 shows results of |ΔfoF2| calculation for four global maps JPL, CODE, UPC, ESA. These are monthly average values of deviations for the instantaneous quantities foF2(ins). Values of |ΔfoF2| for τ(IRI) are given for comparison.

The table illustrates the most general regularities: the greatest deviations are proper τ(IRI) in the initial model, the little smaller deviations correspond to τ(obs, IRI). The best conformity is given by median of τ(obs). From four maps, the best conformity concerns the JPL map in this case. And though it gives the best conformity in most cases, there are conditions and regions in which the best conformity can be given and by other maps. More often it is CODE, sometimes - UPC. And even there was a station (Sao Luis) for which the best conformity is given by the ESA map in certain cases. The huge statistics of calculations for more, than 30 stations and 10 years, shows that deviations of the calculated frequencies from the observational values have the greatest quantity for τ(IRI), the least - for τ(obs), i.e. τ(med). Deviations for τ(obs, IRI) lie between them, closer to |ΔfoF2| for τ(IRI) more often. New results, including the data for values IGS, are given in Tab. 4 for high- and low-latitude stations which determine boundaries of values |ΔfoF2|, because values for middle-latitude stations are always less. Values, averaging for 2013, are given.

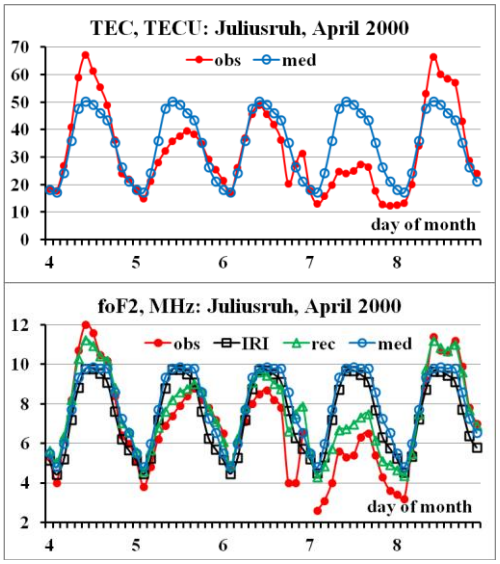

Figure 9: An example of use of median of τ for definition of foF2.

Table 3: Deviations |ΔfoF2| for various options of τ definition.

|ΔfoF2|, MHz	April 2000 τ(IRI)→ 1.034		April 2009 τ(IRI)→ 0.554	
	τ (obs,IRI)	τ(obs)	τ (obs,IRI)	τ(obs)
JPL	0.660	0.452	0.497	0.205
CODE	0.677	0.484	0.501	0.222
UPC	0.731	0.544	0.472	0.237
ESA	1.013	0.907	0.496	0.242

Table 4: Correspondence between experimental and calculated foF2 according to three stations.

|ΔfoF2|	τ(IRI)	τ(obs, IRI)					τ(obs)				
station	IRI	JPL	CODE	UPC	ESA	IGS	JPL	CODE	UPC	ESA	IGS
Thule	0.82	0.71	0.75	0.71	0.75	0.71	0.41	0.45	0.41	0.45	0.41
Longyear	0.69	0.61	0.67	0.59	0.63	0.62	0.40	0.49	0.38	0.43	0.41
Niue	2.19	2.09	2.16	2.15	2.13	2.13	1.01	1.10	1.09	1.06	1.04

Value for IGS is inscribed in the general statistics and more often there is a little above, than a value for the best map. It is worth to note that the proximity of values |ΔfoF2| for various maps testifies that τ is good calibration coefficient for TEC.

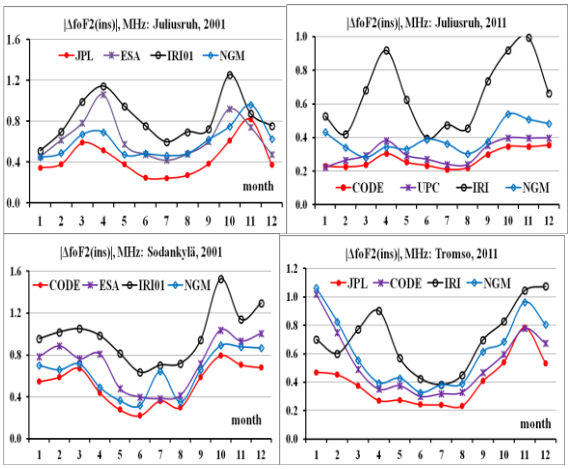

Figure 10: Comparison of results of foF2 definition with use of various τ.

In connection with such results, there is a question on empirical model of τ. One of possibilities is to pay attention to the NGM model which allows to calculate NmF2(NGM) and TEC(NGM). Having values NmF2(NGM) and TEC(NGM), it is possible to calculate values of the equivalent slab thickness of the ionosphere τ(NGM) =TEC(NGM)/NmF2(NGM). The purpose is to estimate, how much the model τ(NGM) is closer to τ(obs) than τ(IRI). Such estimate is done by comparison of instantaneous values |ΔfoF2(ins)|. For the NGM model, values of foF2(ins) are obtained from values TEC(CODE) with use of τ(NGM). On Fig. 10, examples of comparison of critical frequencies for two global maps are given ("best" and "worst" from the point of view of definition of foF2 in each specific case) and two models (IRI and NGM) for middle-latitude and two high-altitude stations in the conditions of various solar activity.

It is seen that near to a maximum of activity (2001) the NGM model yields the best results than the IRI model and the ESA map. In the conditions of low activity (2006) at middle-latitude station, it yields results, close to IRI. At high latitudes, the NGM model gives major deviations in winter and autumn, and it is seen that the CODE map yields the worst results in these cases. At an increase of solar activity in 2011 and the corresponding increase of the TEC, the NGM model again starts to yield results, the best than the IRI model. Thus, in most cases τ(NGM) provides results, the best than τ(IRI), however its deviations do not come nearer anywhere to the values given by τ(JPL). In the conditions of a minimum of activity, the NGM model has no advantages to low-latitude stations.

As a whole, it is possible to tell that τ(NGM) may carry out a role of the empirical model of τ. At use of other map instead of the CODE map, probably, results would be better.

4 N(h)-PROFILE S OF THE IONOSPHERE AND VALUES OF TEC

As it is known, conditions in the ionosphere are determined by distribution of concentration, or N(h)-profile. N(h)-profile can be divided into three parts: bottom side, topside and plasmaspheric. The bottom side is determined by the experimental critical frequency foF2. The topside is improved by means of the plasma frequencies measured on satellites, but there is a residual of TEC. It is possible to use coefficient K(PL) which is selected for the full conformity with the observational TEC. However there is no data for development and validation of the K(PL) model yet. Having such model, it will be possible even to improve determination of foF2. Details of use of TEC for determination of N(h)-profile to heights of navigation satellites are the following. In paper (Maltseva et al., 2013c), it has been shown that use of the plasma frequencies measured on satellites allows to improve the shape of the topside side. As a result, values of TEC for the several N(h)-profiles transiting through the critical frequency foF2 and a various combination of plasma frequencies are obtained: (1) satellite s1, (2) satellite s2, (3) both satellites s1 and s2. Two first options are realized in most cases. The third option is realized in case of simultaneous passage of two satellites over the given point. The illustration of obtained values of TEC is given for the Juliusruh station on Fig. 11. Simultaneous passages took place for 6 days specified in Tab. 5 in UT=13 and UT=23. Values for the initial IRI model are shown by black circles. Red circles show the observational values. Green triangles show values for the first option, by violet crosses - for the second one, blue asterisks – for the third case. Orange circles show TEC for the N(h)-profiles transiting through both plasma frequencies and adapting by coefficient K(PL). All values are given for four maps in decreasing order of values. This order is specified in Tab. 5.

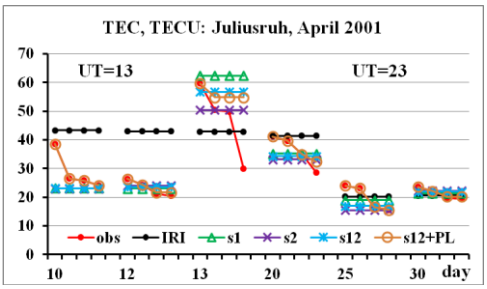

Figure 11: TEC, calculated for N(h)-profiles, transiting through the critical frequency foF2 and a various combination of plasma frequencies.

Table 5: Days, hours and names of maps in decreasing order of TEC for simultaneous passages of satellites over the Juliusruh station in April 2001.

day	hour	map			
10	13	ESA	JPL	UPC	CODE
12	13	JPL	UPC	CODE	ESA
13	13	JPL	CODE	UPC	ESA
20	13	JPL	UPC	CODE	ESA
25	23	UPC	JPL	ESA	CODE
30	23	JPL	UPC	CODE	ESA

Big difference between TEC for the corrected N(h)-profiles and TEC for the initial model, corresponding to quiet conditions, speaks about influence of disturbances. N(h)-profiles transiting through frequency of one of satellites, are close each other. That can testify both to "interchangeability" of profiles, and about their ambiguity. In most cases, orange circles coincide with red points. It testifies that the N(h)-profile, transiting through plasma frequencies of both satellites, provides the observational value of TEC. It is reached by selection of coefficient K(PL) shown on Fig. 12 also for four maps.

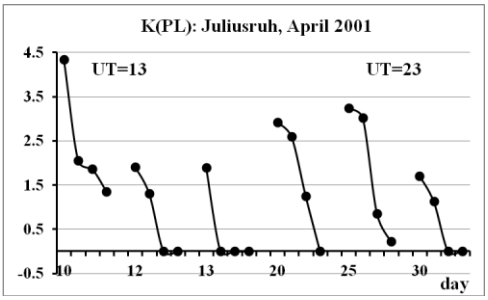

Figure 12: Behavior of coefficient K(PL) for four global maps of TEC in cases of simultaneous passages of satellites.

It is seen that values of K(PL) decrease with decreasing TEC(obs). Relation K(PL) =1 specifies the full conformity of model TEC and TEC(obs). It is obvious that it is possible to select the TEC value to which relation K(PL) =1 corresponds. There are some cases with the negative value K(PL) =-0.001. They can be identified by misfit of orange and red circles on Fig. 13. It means that the N(h)-profile, providing TEC(obs), is not found. It occurs when TEC for N(h)-profiles s1 exceed TEC(obs).

The N(h)-profiles corresponding to these TEC are given on Fig. 13.

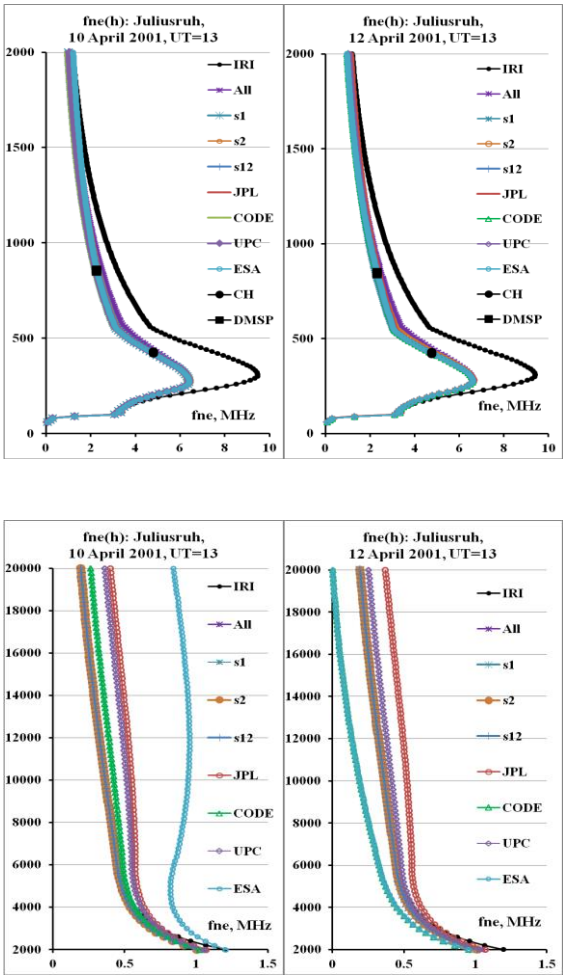

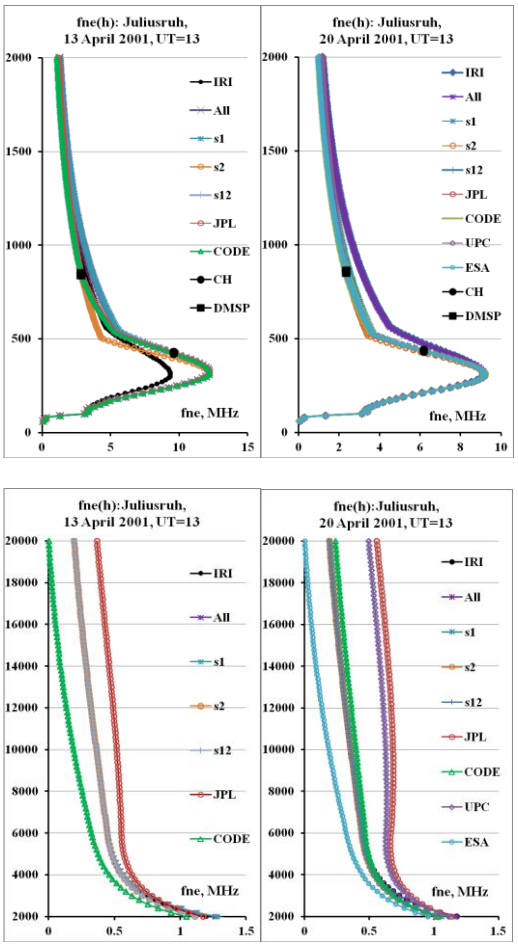

Figure 13: Topside and plasmaspheric parts of N(h)-profiles corresponding various global maps of TEC.

4 CONCLUSIONS

In recent years, the TEC has become an important parameter to describe the state of the propagation medium. However, its use encounters certain difficulties associated with a variety of values. This diversity leads to ambiguity of parameters determined through TEC and models. This paper makes the following recommendations. 1. The best method of TEC modeling is the EOC. 2. To determine foF2, it is possible to use τ, which is a good calibration factor, including τ(NGM). 3. Using plasma frequencies measured on satellites allows us to construct N(h)-profiles, closer to the real part in the topside part. 4. For full proximity of N (h)-profiles with experimental TEC(obs), we must enter the factor K(PL), modifying plasmaspheric part of profile. Its value depends on the choice of TEC(obs). In this regard, we can focus on IGS.

ACKNOWLEDGEMENTS

Author thanks organizations and scientists who are developing the IRI model, providing data of SPIDR, JPL, CODE, UPC, ESA, and Dr M. Hoque for detailed comments on the NGM model.

REFERENCES

Arikan, F., Erol C.B., Arikan O., Regularized estimation of vertical total electron content from Global Positioning System data. 2003. *J. Geophys. Res., 108, A12, 1469, doi:10.1029/2002JA009605, 12p.*

Chen, K., Gao Y. Real-time precise point positioning using single frequency data. *Proceedings of IONGNSS 18th International Technical Meeting of the Satellite Division, Long Beach, CA, 2005, 1514-1523.*

Goodman, J.M., 2005. Operational communication systems and relationships to the ionosphere and space weather. *Adv. Space Res., 36, 2241–2252.*

Gulyaeva, T.L., 2011. Storm time behavior of topside scale height inferred from the ionosphere-plasmosphere model driven by the F2 layer peak and GPS-TEC observations. *Adv. Space Res., 47, 913-920.*

Gulyaeva, T.L., Arikan F., Hernandez-Pajares M., Stanislawska I. 2013. GIM-TEC adaptive ionospheric weather assessment and forecast system. *J. Atm. Solar-Terr. Phys., 102, 329-340.*

Gulyaeva, T.L., Bilitza D., 2011. Towards ISO standard Earth ionosphere and plasmasphere model. In: *Larsen, R.J. (Ed.), New developments in the standard model. NOVA Publishers, USA, 11–64.*

Gulyaeva, T.L., Stanislawska, I., 2008. Derivation of a planetary ionospheric storm index. *Ann. Geophys., 26, 2645–2648.*

Hajj, G.A., Romans L.J., 1998. Ionospheric electron density profiles obtained with the Global Positioning System: results from the GPS/MET experiment. *Radio Sci., 33, 175–190.*

Hernandez-Pajares, M., Juan, J. M., Orus, R., Garcia-Rigo, A., Feltens, J., Komjathy, A., Schaer, S. C., and Krankowski, A.: The IGS VTEC maps: a reliable source of ionospheric information since 1998. *J. Geod., 2009, 83, 263–275.*

Hernandez-Pajares, M., Juan, J.M., Sanz, J., 1997. High-resolution TEC monitoring method using permanent ground GPS receivers, *Geophys. Res. Lett., 24, 1643-1646.*

Hoque, M.M., Jakowski N., 2011. A new global empirical NmF2 model for operational use in radio systems. *Radio Sci., 46, RS6015, 1-13.*

Hoque, M.M., Jakowski N., 2012. A new global model for the ionospheric F2 peak height for radio wave propagation. *Ann. Geophys., 30, 797-809.*

Houminer, Z., Soicher H., 1996. Improved short –term predictions of foF2 using GPS time delay measurements. *Radio Sci., 31(5), 1099-1108.*

Ivanov, V.B., Gefan G.D., Gorbachev O.A., 2011. Global empirical modeling of the total electron content of the ionosphere for satellite radio navigation systems. *J. Atm. Solar-Terr. Phys., 73, 1703–1708.*

Jakowski, N., Hoque M.M., Mayer C. A new global TEC model for estimating transionospheric radio wave propagation errors, Journal of Geodesy, 2011, 85(12), 965-974.

Jakowski, N., Sardon E., Engler E., Jungstand A., Klahn D., 1996. Relationships between GPS-signal propagation errors and EISCAT observations. *Ann. Geophys., 14, 1429-1436.*

Jakowski, N., Stankov S.M., Schlueter S., Klaehn D., 2006. On developing a new ionospheric perturbation index for space weather operations. *Adv. Space Res., 38, 2596-2600.*

Kakinami, Y., Chen C.H., Liu J.Y., Oyama K.-I., Yang W.H., Abe S., 2009. Empirical models of total electron content based on functional fitting over Taiwan during geomagnetic quiet condition. *Ann. Geophys., 27, 3321-3333.*

Klobuchar, J.A., 1987. Ionospheric time-delay algorithm for single-frequency GPS users. IEEE Transactions on aerospace and electronic systems. 1987AES-23(3), 325-331.

Lastovicka, J. Are trends in total electron content (TEC) really positive? J. Geophys. Res.: Space Physics, 2013, 118, 3831–3835, doi:10.1002/jgra.50261.

Lean, J., Emmert J.T., Picone J.M., Meier R. R. Global and regional trends in ionospheric electron content. J. Geophys. Res., 2011, 116, A00H04, doi:10.1029 /2010JA016378.

Maltseva, O.A., Mozhaeva N.S, Zhbankov G.A., 2012a. A new model of the International Reference Ionosphere IRI for telecommunication and navigation systems. *Proceedings of the First International Conference on Telecommunications and Remote Sensing, Sofia, Bulgaria 29-30 August 2012, 129-138,* http://www.math.bas.bg/ursi/ICTRS2012 proceedings.pdf

Maltseva, O.A., Mozhaeva N.S, Poltavsky O.S., Zhbankov G.A., 2012b. Use of TEC global maps and the IRI model to study ionospheric response to geomagnetic disturbances. *Adv. Space Res., 49, 1076-1087.*

Maltseva, O. A., Zhbankov G. A., Mozhaeva N.S., 2013a. Advantages of the new model of IRI (IRI-Plas) to study ionospheric environment. *Adv. Radio Sci., 11, 907–911, doi:10.5194/ars-11-1-2013.*

Maltseva, O.A., Mozhaeva N.S, T.V. Nikitenko, 2013b. Validation of the Neustrelitz Global Model according to the low latitude ionosphere. *Adv. Space Res., http://dx.doi.org/10.1016/j.asr.2013.11.005.*

Maltseva, O., Mozhaeva N., Vinnik E., 2013c. Validation of two new empirical ionospheric models IRI-Plas and NGM describing conditions of radio wave propagation in space. Proceedings of Second International Conference on Telecommunications and Remote Sensing, Noordwijkerhout, The Netherlands, 11-12 July, 109-118.

Mukhtarov, P., Pancheva D., Andonov B., Pashova L., 2013a. Global TEC maps based on GNSS data: 1.

Empirical background TEC model. *J. Geophys. Res.: Space Physics, 118, 4594–4608, doi:10.1002/ jgra.50413.*

Mukhtarov, P., Pancheva D., Andonov B., Pashova L., 2013b. Global TEC maps based on GNNS data: 2. Model evaluation. *J. Geophys. Res.: Space Physics, 118, 4609–4617, doi:10.1002/jgra.50412.*

Mannucci, A. J., Wilson B. D., Yuan D. N., Ho C. H., Lindqwister U.J., Runge T.F., 1998. A global mapping technique for GPS-derived ionospheric total electron content measurements. *Radio Science, 33(3), 565-582.*

Mukhtarov, P., Pancheva D., Andonov B., Pashova L., 2013. Global TEC maps based on GNSS data: 1. Empirical background TEC model. *J. Geophys. Res.: Space Physics, 118, 4594–4608, doi:10.1002/ jgra.50413.*

Pesnell, W.D. Solar Cycle Predictions (Invited Review), Solar Phys, 2012, 1-26, DOI 10.1007/s11207-012-9997-5.

Sardon, E., Rius A., Zarraoa N., 1994. Estimation of the receiver differential biases and the ionospheric total electron content from Global Positioning System observations. *Radio Sci., 29, 577-586.*

Schaer, S., Beutler G., Mervart L., Rothacher M., Wild U., 1995. Global and regional ionosphere models using the GPS double difference phase observable. *IGS Workshop, Potsdam, Germany, May 1995, 1-16.*

Tobiska, W. K., D. Knipp, W. J. Burke, D. Bouwer, J. Bailey, D. Odstrcil, M. P. Hagan, J. Gannon, and B. R. Bowman, 2013. The Anemomilos prediction methodology for Dst. SpaceWeather, 11, 490–508, doi:10.1002/swe.20094.

Tsai, Lung-Chih, Tsai Wei-Hsiung, 2004. Improvement of GPS/MET Ionospheric Profiling and Validation Using the Chung-Li Ionosonde Measurements and the IRI model. Terr. Atmos. Ocean. Sci., 15(4), 589-607.

Wu, Chin-Chun, Fryb C.D., Liuc J.-Y., Lioud K., Tseng C.-L., 2004. Annual TEC variation in the equatorial anomaly region during the solar minimum: September 1996–August 1997. *J. Atm. Solar-Terr. Phys., 66, 199–207.*

Wiener-Hopf Analysis of the Diffraction by a Finite Sinusoidal Grating: The Case of H Polarization

Toru Eizawa and Kazuya Kobayashi
Department of Electrical, Electronic, and Communication Engineering, Chuo University,
1-13-27 Kasuga, Bunkyo-ku, Tokyo 112-8551, Japan
eizawa@mth.biglobe.ne.jp, kazuya@tamacc.chuo-u.ac.jp

Keywords: Wiener-Hopf technique, perturbation method, scattering and diffraction, finite sinusoidal grating.

Abstract: The diffraction by a finite sinusoidal grating is analyzed for the H-polarized plane wave incidence using the Wiener-Hopf technique combined with the perturbation method. The scattered far field is evaluated with the aid of the saddle point method, and scattering characteristics of the grating are discussed via numerical examples of the far field intensity.

1 INTRODUCTION

The analysis of the diffraction by gratings is important in electromagnetic theory and optics. Various analytical and numerical methods have been developed and the diffraction phenomena have been investigated for many kinds of gratings (Ikuno and Yasuura, 1973; Shestopalov et al., 1973; Hinata and Hosono, 1976; Petit, 1980; Okuno, 1993).

The Wiener-Hopf technique is known as a rigorous approach for analyzing wave scattering problems related to canonical geometries, and can be applied efficiently to the analysis of the diffraction by specific periodic structures.

Most of the analyses in the relevant works done in the past are restricted to periodic structures of infinite extent and plane boundaries and hence, it is important to investigate the problems without these restrictions. In our previous paper, we have considered a finite sinusoidal grating as an example of gratings of finite extent and non-plane boundaries, and analyzed the E-polarized plane wave diffraction based on the Wiener-Hopf technique combined with the perturbation method (Kobayashi and Eizawa, 1991). This problem is important in investigating the end effect of finite gratings as well as the applicability of the Wiener-Hopf technique to obstacles with non-plane boundaries.

In this paper, we shall consider the same grating geometry as in Kobayashi and Eizawa (1991), and analyze the diffraction problem for the H-polarized plane wave incidence. Assuming that the corrugation amplitude of the grating is small compared with the wavelength, the original problem is approximately replaced by the problem of the H-polarized plane wave diffraction by a flat strip with a certain mixed boundary condition. We also expand the unknown scattered field using a perturbation series and separate the diffraction problem under consideration into the zero-order and the first-order boundary value problems.

Introducing the Fourier transform for the unknown scattered field and applying boundary conditions in the transform domain, the problem is formulated in terms of the zero- and first-order Wiener-Hopf equations, which are solved exactly via the factorization and decomposition procedure. However, the solution is formal in the sense that branch-cut integrals with unknown integrands are involved. These branch-cut integrals are then evaluated asymptotically for the width of the grating large compared with the wavelength, leading to an explicit high-frequency solution. Taking the Fourier inverse of the solution in the transform domain and applying the saddle point method, the scattered far field in the real space is derived. Based on these results, we have carried out numerical computation of the far field intensity for various physical parameters. Scattering characteristics of the grating are discussed in detail via numerical examples.

The time factor is assumed to be $e^{-i\omega t}$ and suppressed throughout this paper.

2 STATEMENT OF THE PROBLEM

We consider the diffraction of an H-polarized plane wave by a finite sinusoidal grating as shown in Fig. 1, where the grating surface is assumed to be infinitely thin, perfectly conducting, and uniform in the y- direction, being defined by

$$x = h\sin mz \ \ (m>0,\ h>0) \tag{1}$$

for $|\,z\,| \le a$. In view of the grating geometry and the characteristics of the incident field, this is a two-dimensional problem.

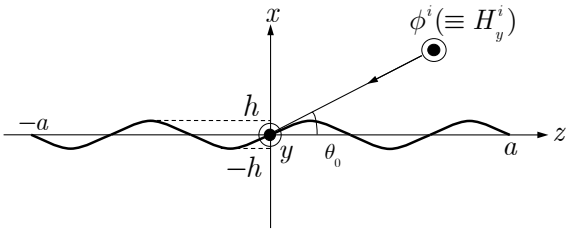

Figure 1: Geometry of the problem.

Let us define the total magnetic field $\phi^t(x,z)$ $[\equiv H_y^t(x,z)]$ by

$$\phi^t(x,z) = \phi^i(x,z) + \phi(x,z), \tag{2}$$

where $\phi^i(x,z)$ is the incident field of H polarization given by

$$\phi^i(x,z) = e^{-ik(x\sin\theta_0 + z\cos\theta_0)} \tag{3}$$

for $0 < \theta_0 < \pi\ /\ 2$ with $k[\equiv \omega(\varepsilon_0\mu_0)^{1/2}]$ being the free-space wavenumber. The scattered field $\phi(x,z)$ satisfies the two-dimensional Helmholtz equation

$$(\partial^2/\partial x^2 + \partial^2/\partial z^2 + k^2)\phi(x,z) = 0. \tag{4}$$

Once the solution of (4) has been found, nonzero components of the scattered electromagnetic fields are derived from the following relation:

$$(H_y, E_x, E_z) = \left(\phi, \frac{1}{i\omega\varepsilon_0}\frac{\partial\phi}{\partial z}, \frac{i}{\omega\varepsilon_0}\frac{\partial\phi}{\partial x}\right). \tag{5}$$

According to the boundary condition, tangential components of the total electric field $E_{\tan}^t$ satisfies

$$E_{\tan}^t = \frac{\partial\phi^t(h\sin mz, z)}{\partial n} = 0, \left|z\right| < a, \tag{6}$$

where $\partial/\partial n$ denotes the normal derivative on the grating surface. We assume that the corrugation depth $2h$ is small compared with the wavelength, and expand (6) in terms of a Taylor series around $x = 0$. Then by ignoring the $O(h^2)$ terms from the Taylor expansion, we obtain that

$$\frac{\partial\phi^t(0,z)}{\partial x} + h\left[\sin mz\frac{\partial^2\phi^t(0,z)}{\partial x^2} - m\cos mz\frac{\partial\phi^t(0,z)}{\partial z}\right] + O(h^2) = 0 \tag{7}$$

for $|\,z\,| < a$. Equation (7) is the approximate boundary condition used throughout the rest of this paper.

We express the unknown scattered field $\phi(x,z)$ in terms of a perturbation series expansion in h as

$$\phi(x,z) = \phi^{(0)}(x,z) + h\phi^{(1)}(x,z) + O(h^2), \tag{8}$$

where $\phi^{(0)}(x,z)$ and $\phi^{(1)}(x,z)$ are the zero-order and the first-order terms contained in the scattered field, respectively. Substituting (8) into (4) and using (2), (3), and (7), the original problem can be separated into the two perturbation problems.

The zero-order and first-order scattered fields $\phi^{(n)}(x,z)$ for $n = 0,1$ satisfy

$$(\partial^2\ /\ \partial x^2 + \partial^2\ /\ \partial z^2 + k^2)\phi^{(n)}(x,z) = 0, \tag{9}$$

where the boundary conditions are given by

$$\phi^{(0)}(+0,z) = \phi^{(0)}(-0,z)[\equiv \phi^{(0)}(0,z)], \tag{10}$$

$$\frac{\partial\phi^{(0)}(+0,z)}{\partial x} = \frac{\partial\phi^{(0)}(-0,z)}{\partial x}\left[\equiv\frac{\partial\phi^{(0)}(0,z)}{\partial x}\right], \tag{11}$$

$$\phi^{(1)}(+0,z) = \phi^{(1)}(-0,z)\left[\equiv \phi^{(1)}(0,z)\right], \tag{12}$$

$$\frac{\partial\phi^{(1)}(+0,z)}{\partial x} = \frac{\partial\phi^{(1)}(-0,z)}{\partial x}\left[\equiv\frac{\partial\phi^{(1)}(0,z)}{\partial x}\right] \tag{13}$$

for $|z| > a$, and

$$\phi^{(0)}(+0,z) - \phi^{(0)}(-0,z) = j^{(0)}(0,z), \tag{14}$$

$$\frac{\partial\phi^{(0)}(0,z)}{\partial x} = ik\sin\theta_0 e^{-ikz\cos\theta_0}, \tag{15}$$

$$\phi^{(1)}(+0,z) - \phi^{(1)}(-0,z) = j^{(1)}(0,z), \tag{16}$$

$$\frac{\partial\phi^{(1)}(0,z)}{\partial x} + \sin mz\frac{\partial^2\phi^{(0)}(0,z)}{\partial x^2} - m\cos mz\frac{\partial\phi^{(0)}(0,z)}{\partial z} = \frac{ik}{2}\left[k\sin^2\theta_0\sum_{n=1}^{2}(-1)^n e^{-ikz\cos\theta_n} - m\cos\theta_0\sum_{n=1}^{2}e^{-ikz\cos\theta_n}\right] \tag{17}$$

for $|z| < a$ with

$$\cos\theta_{1,2} = \cos\theta_0 \mp m/k. \tag{18}$$

In (14) and (16), $j^{(0)}(0,z)$ and $j^{(1)}(0,z)$ are the zero-order and first-order terms of the unknown surface currents induced on the grating surface, respectively. As seen from the above discussion, the zero-order problem corresponds to the diffraction by a perfectly conducting flat strip. On the other hand, the first-order problem is important since it contains the effect due to the sinusoidal corrugation.

3 WIENER-HOPF EQUATIONS

For convenience of analysis, we assume that the medium is slightly lossy as in $k=k_1+ik_2$ with $0<k_2\ll k_1$. Using the radiation condition, it follows from (8) that the zero- and first-order scattered fields $\phi^{(n)}(x,z)$ for $n=0,1$ show the asymptotic behavior

$$\phi^{(n)}(x,z)=O(e^{-k_2|z|\cos\theta_0}),\ |z|\to\infty. \tag{19}$$

Let us introduce the Fourier transform of the scattered field $\phi^{(n)}(x,z)$ with respect to z as in

$$\Phi^{(n)}(x,\alpha)=(2\pi)^{-1/2}\int_{-\infty}^{\infty}\phi^{(n)}(x,z)e^{i\alpha z}dz, \tag{20}$$

where $\alpha=\mathrm{Re}\,\alpha+i\,\mathrm{Im}\,\alpha(\equiv\sigma+i\tau)$. It follows from (19) and (20) that $\Phi^{(n)}(x,\alpha)$ for $n=0,1$ are regular in the strip $|\tau|<k_2\cos\theta_0$ of the complex α- plane. We also introduce the Fourier integrals as

$$\Phi_{\pm}^{(n)}(x,\alpha)=\pm(2\pi)^{-1/2}\cdot\int_{\pm a}^{\pm\infty}\phi^{(n)}(x,z)e^{i\alpha(z\mp a)}dz, \tag{21}$$

$$\Phi_1^{(n)}(x,\alpha)=(2\pi)^{-1/2}\int_{-a}^{a}\phi^{(n)}(x,z)e^{i\alpha z}dz, \tag{22}$$

$$J_1^{(n)}(0,\alpha)=\left(2\pi\right)^{-1/2}\int_{-a}^{a}j^{(n)}(0,z)e^{i\alpha z}dz. \tag{23}$$

Then it is seen that $\Phi_{\pm}^{(n)}(x,\alpha)$ are regular in $\tau\gtrless\mp k_2\cos\theta_0$ whereas $\Phi_1^{(n)}(x,\alpha)$ and $J_1^{(n)}(0,\alpha)$ are entire functions. It follows from (20)-(22) that

$$\Phi^{(n)}(x,\alpha)=e^{-i\alpha a}\Phi_-^{(n)}(x,\alpha)+\Phi_1^{(n)}(x,\alpha)+e^{i\alpha a}\Phi_+^{(n)}(x,\alpha). \tag{24}$$

Taking the Fourier transform of (9) and making use of (19), we derive that

$$[d^2/dx^2-\gamma^2(\alpha)]\Phi^{(n)}(x,\alpha)=0, \tag{25}$$

where $\gamma(\alpha)=(\alpha^2-k^2)^{1/2}$ with $\mathrm{Re}\,\gamma(\alpha)>0$. The solution of (25) is expressed as

$$\Phi^{(n)}(x,\alpha)=A^{(n)}(\alpha)e^{-\gamma(\alpha)x},\ x>0,$$
$$=B^{(n)}(\alpha)e^{\gamma(\alpha)x},\ x<0 \tag{26}$$

for $n=0,1$, where $A^{(n)}(\alpha)$ and $B^{(n)}(\alpha)$ are unknown functions. Setting $x=\pm0$ in (26) and arranging the results, we obtain that

$$\Phi^{(n)}(+0,\alpha)-\Phi^{(n)}(-0,\alpha)=A^{(n)}(\alpha)-B^{(n)}(\alpha), \tag{27}$$

$$\Phi^{(n)\prime}(+0,\alpha)-\Phi^{(n)\prime}(-0,\alpha)=-\gamma(\alpha)[A^{(n)}(\alpha)-B^{(n)}(\alpha)], \tag{28}$$

where the prime denotes differentiation with respect to x. Using the boundary conditions as given by (10)-(17), (26) is now expressed as

$$\Phi^{(0)}(x,\alpha)=\pm(1/2)J_1^{(0)}(\alpha)e^{\mp\gamma(\alpha)x}, \tag{29}$$

$$\begin{aligned}\Phi^{(1)}(x,\alpha)=&\pm(1/2)J_1^{(1)}(\alpha)e^{\mp\gamma(\alpha)x}\\&+[4i\gamma(\alpha)]^{-1}\{[\gamma^2(\alpha+m)-m(\alpha+m)]\\&\cdot J_1^{(0)}(\alpha+m)\\&-[\gamma^2(\alpha-m)+m(\alpha-m)]\\&\cdot J_1^{(0)}(\alpha-m)]\}e^{\mp\gamma(\alpha)x}\end{aligned} \tag{30}$$

for $x\gtrless0$. Equations (29) and (30) are the zero- and first-order scattered fields in the Fourier transform domain, respectively.

Setting $x=\pm0$ in (29) and (30) and carrying out some manipulations with the aid of the boundary conditions, we are led to

$$e^{-i\alpha a}U_-(\alpha)+K(\alpha)J_1^{(0)}(0,\alpha)+e^{i\alpha a}U_{(+)}(\alpha)=0, \tag{31}$$

$$e^{-i\alpha a}V_-(\alpha)+K(\alpha)J_1^{(1)}(0,\alpha)+e^{i\alpha a}V_{(+)}(\alpha)=0 \tag{32}$$

for $|\tau|<k_2\cos\theta_0$, where

$$U_-(\alpha)=\Phi_-^{(0)\prime}(0,\alpha)+\frac{A_0}{\alpha-k\cos\theta_0}, \tag{33}$$

$$U_{(+)}(\alpha)=\Phi_+^{(0)\prime}(0,\alpha)-\frac{B_0}{\alpha-k\cos\theta_0}, \tag{34}$$

$$V_-(\alpha)=\Psi_-(\alpha)-\sum_{n=1}^{2}(-1)^n\frac{A_nC_n}{\alpha-k\cos\theta_n}, \tag{35}$$

$$V_{(+)}(\alpha)=\Psi_+(\alpha)+\sum_{n=1}^{2}(-1)^n\frac{B_nC_n}{\alpha-k\cos\theta_n}, \tag{36}$$

$$K(\alpha)=\gamma(\alpha)/2 \tag{37}$$

with

$$\Psi_{\pm}(\alpha) = \Phi_{\pm}^{(1)\prime}(0,\alpha) + (1/2i) \cdot \{[\gamma^2(\alpha+m) - m(\alpha+m)] \cdot e^{\pm ima}\Phi_{\pm}^{(0)}(0,\alpha+m) - [\gamma^2(\alpha-m) - m(\alpha-m)] \cdot e^{\mp ima}\Phi_{\pm}^{(0)}(0,\alpha+m) + (2\pi)^{-1/2} m\cos ma\phi^{(0)}(0,a)\}, \quad (38)$$

$$\left.\begin{matrix} A_0 \\ B_0 \end{matrix}\right\} = -\frac{k\sin\theta_0 e^{\pm ika\cos\theta_0}}{(2\pi)^{1/2}}, \quad (39)$$

$$\left.\begin{matrix} A_n \\ B_n \end{matrix}\right\} = \frac{e^{\pm ika\cos\theta_n}}{(2\pi)^{1/2}},\ n = 1,2, \quad (40)$$

$$C_n = (k/2)[k\sin^2\theta_0 - (-1)^n m\cos\theta_0], \quad n = 1,2. \quad (41)$$

Equation (31) and (32) are the zero- and first-order Wiener-Hopf equations, respectively.

4 EXACT AND ASYMPTOTIC SOLUTIONS

In this section, we shall solve the zero- and first-order Wiener-Hopf equations to obtain exact and asymptotic solutions. First we note that the kernel function $K(\alpha)$ is factorized as

$$K(\alpha) = K_+(\alpha)K_-(\alpha), \quad (42)$$

where $K_{\pm}(\alpha)$ are the split functions defined by

$$K_{\pm}(\alpha) = 2^{-1/2}e^{-i\pi/4}(k\pm\alpha)^{1/2}. \quad (43)$$

Multiplying both sides of (31) by $e^{\mp i\alpha a}/K_{\pm}(\alpha)$ and applying the decomposition procedure with the aid of the edge condition, we arrive at the exact solution with the result that

$$U_{(+)}(\alpha) = K_+(\alpha) \cdot \left\{-\frac{B_0}{K_+(k\cos\theta_0)(\alpha - k\cos\theta_0)} + \frac{1}{2}[u_s(\alpha) - u_d(\alpha)]\right\}, \quad (44)$$

$$U_-(\alpha) = K_-(\alpha) \cdot \left\{\frac{A_0}{K_-(k\cos\theta_0)(\alpha - k\cos\theta_0)} + \frac{1}{2}[u_s(-\alpha) + u_d(-\alpha)]\right\}, \quad (45)$$

where

$$u_{s.d}(\alpha) = \frac{1}{\pi i}\int_k^{k+i\infty} \frac{e^{2i\beta a}U_{(+)}^{s,d}(\beta)}{K_-(\beta)(\beta+\alpha)}d\beta, \quad (46)$$

$$U_{(+)}^{s,d}(\alpha) = U_{(+)}(\alpha) \pm U_-(\alpha). \quad (47)$$

Equations (44) and (45) are formal since branch-cut integrals with the unknown integrands $U_{(+)}^{s,d}(\beta)$ are involved. Applying a rigorous asymptotic method developed by Kobayashi (2013), we obtain a high-frequency solution explicitly as in

$$U_-(\alpha) \sim K_-(\alpha) \cdot \frac{A_0}{K_-(k\cos\theta_0)(\alpha - k\cos\theta_0)} + K_-(\alpha)[C_1^u\xi(-\alpha) + B_0\eta_0^b(-\alpha)], \quad (48)$$

$$U_{(+)}(\alpha) \sim -K_+(\alpha) \cdot \frac{B_0}{K_+(k\cos\theta_0)(\alpha - k\cos\theta_0)} + K_+(\alpha)[C_2^u\xi(\alpha) + A_0\eta_0^a(\alpha)] \quad (49)$$

for $ka \to \infty$, where

$$C_{1,2}^u = \frac{K_+(k)}{1 - K_+^2(k)\xi^2(k)} \cdot [\chi_0^{a,b}(k) + K_+(k)\xi(k)\chi_0^{b,a}(k)], \quad (50)$$

$$\xi(\alpha) = -\frac{2a^{1/2}e^{2ika}}{\pi}\Gamma_1(1/2, -2i(\alpha+k)a), \quad (51)$$

$$\eta_0^{a,b}(\alpha) = \frac{\xi(\alpha) - \xi(\pm k\cos\theta_0)}{\alpha \mp k\cos\theta_0} \quad (52)$$

with

$$\chi_0^a(\alpha) = A_0\eta_0^a(\alpha) + B_0P_0^b(\alpha), \quad (53)$$

$$\chi_0^b(\alpha) = B_0\eta_0^b(\alpha) + A_0P_0^a(\alpha), \quad (54)$$

$$P_0^{a,b}(\alpha) = \frac{1}{\alpha \pm k\cos\theta_0} \cdot \left[\frac{1}{K_+(\alpha)} - \frac{1}{K_\mp(k\cos\theta_0)}\right]. \quad (55)$$

In (51), $\Gamma_1(\cdot,\cdot)$ is the generalized gamma function (Kobayashi, 1991) defined by

$$\Gamma_m(u,v) = \int_0^\infty \frac{t^{u-1}e^{-t}}{(t+v)^m}dt \quad (56)$$

for $\mathrm{Re}\, u > 0$, $|v| > 0$, $|\arg v| < \pi$, and positive integer m. This completes the solution of the zero-order Wiener-Hopf equation (31).

A similar procedure may also be applied to the first-order Wiener-Hopf equation (32). Omitting the whole details, we arrive at a high-frequency solution with the result that

$$V_-(\alpha) \sim -\sum_{n=1}^{2}(-1)^n \cdot \frac{C_n e^{ika\cos\theta_n}(\alpha-k)^{1/2}}{(2\pi)^{1/2}(k\cos\theta_n - k)^{1/2}(\alpha - k\cos\theta_n)} + K_-(\alpha)[D_1^v\xi(-\alpha) + B_1\eta_1^b(-\alpha) + B_2\eta_2^b(-\alpha)], \quad (57)$$

$$V_{(+)}(\alpha) \sim \sum_{n=1}^{2}(-1)^n \cdot \frac{C_n e^{-ika\cos\theta_n}(\alpha+k)^{1/2}}{(2\pi)^{1/2}(k\cos\theta_n + k)^{1/2}(\alpha - k\cos\theta_n)} + K_+(\alpha)[D_2^v\xi(\alpha) + A_1\eta_1^a(\alpha) + A_2\eta_2^a(\alpha)] \quad (58)$$

as $ka \to \infty$, where

$$D_{1,2}^v = \frac{K_+(k)}{1 - K_+^2(k)\xi^2(k)} \cdot \sum_{n=1}^{2}\left[\chi_n^{a,b}(k) + K_+(k)\xi(k)\chi_n^{b,a}(k)\right] \quad (59)$$

and

$$\eta_n^{a,b}(\alpha) = -(-1)^n C_n \frac{\xi(\alpha) - \xi(\pm k\cos\theta_n)}{\alpha \mp k\cos\theta_n}, \quad (60)$$

$$\chi_n^a(\alpha) = A_n\eta_n^a(\alpha) - (-1)^n B_n C_n P_n^b(\alpha), \quad (61)$$

$$\chi_n^b(\alpha) = B_n\eta_n^b(\alpha) - (-1)^n A_n C_n P_n^a(\alpha), \quad (62)$$

$$P_n^{a,b}(\alpha) = \frac{1}{\alpha \pm k\cos\theta_n} \cdot \left[\frac{1}{K_+(\alpha)} - \frac{1}{K_\mp(k\cos\theta_n)}\right] \quad (63)$$

for $n = 1,2$. Equations (48), (49) and (57), (58) yield high-frequency asymptotic solutions of the zero- and first-order Wiener-Hopf equations (31) and (32), respectively.

5 SCATTERED FAR FIELD

We shall now derive analytical expressions of the scattered field by using the results obtained in Section 4. The scattered field $\phi^{(n)}(x,z)$ with $n = 0,1$ in the real space can be derived by taking the inverse Fourier transform of (20) according to the formula

$$\phi^{(n)}(x,z) = (2\pi)^{-1/2} \cdot \int_{-\infty+ic}^{\infty+ic} \Phi^{(n)}(x,\alpha)e^{-i\alpha z}d\alpha, \quad (64)$$

where c is a constant satisfying $|c| < k_2\cos\theta_0$. Introducing the cylindrical coordinate

$$x = \rho\sin\theta,\ z = \rho\cos\theta,\ -\pi < \theta < \pi \quad (65)$$

and applying the saddle point method with the aid of (29)-(32), we derive, after some manipulations, that

$$\phi^{(0)}(\rho,\theta) \sim \mp[e^{ika\cos\theta}U_-(-k\cos\theta) + e^{-ika\cos\theta}U_{(+)}(-k\cos\theta)] \cdot \frac{k\sin|\theta|}{2K(-k\cos\theta)}\frac{e^{i(k\rho-\pi/4)}}{(k\rho)^{1/2}}, \quad (66)$$

$$\phi^{(1)}(\rho,\theta) \sim \mp[e^{ika\cos\theta}V_-(-k\cos\theta) + e^{-ika\cos\theta}V_{(+)}(-k\cos\theta)] \cdot \frac{k\sin|\theta|}{2K(k\cos\theta)}\frac{e^{i(k\rho-\pi/4)}}{(k\rho)^{1/2}} + \sum_{n=1}^{2}\frac{(-1)^n}{K(k\cos\theta^{(n)})}[4K^2(k\cos\theta^{(n)}) - (-1)^n mk\cos\theta^{(n)}] \cdot [e^{ika\cos\theta^{(n)}}U_-(-k\cos\theta^{(n)}) + e^{-ika\cos\theta^{(n)}}U_{(+)}(-k\cos\theta^{(n)})] \cdot \frac{k\sin|\theta|}{8iK(k\cos\theta)}\frac{e^{i(k\rho-\pi/4)}}{(k\rho)^{1/2}} \quad (67)$$

with $x \gtrless 0$ as $k\rho \to \infty$, where

$$\theta^{(1),(2)} = \cos^{-1}(\cos\theta \mp m/k). \quad (68)$$

It is to be noted that (66) and (67) are uniformly valid for arbitrary incidence and observation angles.

6 NUMERICAL RESULTS AND DISCUSSION

In this section, we shall present numerical examples on the far field intensity and discuss scattering characteristics of the grating. For convenience, let us introduce the normalized far field intensity as in

$$|\phi(\rho,\theta)|[\mathrm{dB}] = 20\log_{10}\left[\frac{\lim_{\rho\to\infty}|(k\rho)^{1/2}\phi(\rho,\theta)|}{\max\lim_{|\theta|<\pi\ \rho\to\infty}|(k\rho)^{1/2}\phi(\rho,\theta)|}\right], \quad (69)$$

where

$$\phi(\rho,\theta) = \phi^{(0)}(\rho,\theta) + h\phi^{(1)}(\rho,\theta). \quad (70)$$

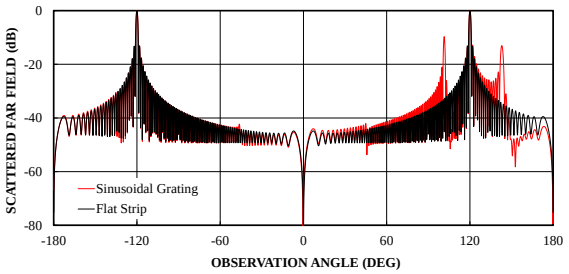

(a) $2h = 0.1\lambda$.

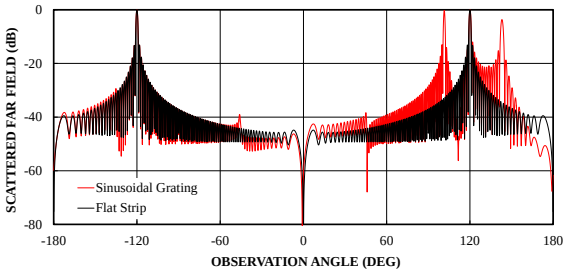

(b) $2h = 0.3\lambda$.

Figure 2: Normalized far field intensity $|\phi(\rho,\theta)|$ [dB] for $\theta_0 = 60^\circ$, $2a = 50\lambda, m/k = 0.3$.

Figure 2 shows numerical examples of the scattered far field intensity as a function of observation angle for $\theta_0 = 60^\circ$ and $2a = 50\lambda$, where red and black curves denote the sinusoidal grating with $2h = 0.1\lambda, 0.3\lambda$, $m/k = 0.3$, and a perfectly conducting flat strip. We see that the effect of sinusoidal corrugation is noticeable in the reflection region $90^\circ < \theta < 180^\circ$, and the far field intensity has sharp peaks at two particular observation angles around the specular reflection direction at $\theta = 120^\circ$. These angles are $101.5^\circ, 143.1^\circ$ and are found to be coincident with the directions of $\pi - \theta_1$ and $\pi - \theta_2$ deduced from (18), which correspond to the propagation directions of the (-1) and $(+1)$ order waves involved in the Floquet's space harmonic modes, respectively.

7 CONCLUSIONS

In this paper, we have analyzed the H-polarized plane wave diffraction by a finite sinusoidal grating using the Wiener-Hopf technique combined with the perturbation method. Our final solution is valid under the condition that the width and the depth of the grating is large and small compared with the wavelength. Based on the results, we have carried out numerical computation of the scattered far field with the choice of typical physical parameters, and investigated the effect of the sinusoidal corrugation of the grating. The results presented in this paper may be useful in design of corrugated reflector antennas.

REFERENCES

Ikuno, H. and Yasuura, K. (1973). Improved point-matching method with application to scattering from a periodic surface. *IEEE Trans. Antennas Propagat.*, 21, 657-662.

Shestopalov, V. P., Litvinenko, L. N., Masalov, S. A., and Sologub, V. G. (1973). *Diffraction of Waves by Gratings*. Kharkov: Kharkov University Press (in Russian).

Hinata, T. and Hosono, T. (1976). On the scattering of electromagnetic wave by plane grating placed in homogeneous medium - mathematical foundation of point-matching method and numerical analysis. *Trans. IECE Japan*, J59-B, 571-578 (in Japanese).

Petit, R. (Ed.) (1980). *Electromagnetic Theory of Gratings*. Berlin:Springer-Verlag.

Okuno, Y. (1993). An introduction to the Yasuura method. In Hashimoto, M., Idemen, M., and Tretyakov, O. A. (Eds.), *Analytical and Numerical Methods in Electromagnetic Wave Theory* (Chap. 11). Tokyo: Science House.

Kobayashi, K. and Eizawa, T. (1991). Plane wave diffraction by a finite sinusoidal grating. *IEICE Trans.*, E74, 2815-2826.

Kobayashi, K. (2013). Solutions of wave scattering problems for a class of the modified Wiener-Hopf geometries. *IEEJ Transactions on Fundamentals and Materials*, 133, 233-241 (*invited paper*).

Kobayashi, K. (1991). On generalized gamma functions occurring in diffraction theory. *J. Phys. Soc. Japan*, 60, 1501-1512.

SAR Image Change Detection Using SURF Algorithm

Seo Li Kang
School of Electronics and Telecomm. Eng., Korea Aerospace University, Hwajeon-Dong, Goyang, Republic of Korea
gemstone0319@gmail.com

Woo Kyung Lee
School of Electronics and Telecomm. Eng., Korea Aerospace University, Hwajeon-Dong, Goyang, Republic of Korea
wklee@kau.ac.kr

Keywords: SAR image fusion, geometrical correction, SURF, change detection, KI Thresholding .

Abstract: With the advent of high-resolution Synthetic Aperture Radar (SAR), applications of satellite SAR have a growing interest in this field and change detection is of high interest in both military and civil applications. Change detection techniques have attracted increased attentions and become a topic of major research. In change detection procedure, geometrical correction of image is essential for effective remote sensing applications. Unlike optical sensor, the geometrical correction of SAR images is highly complicated due to the signal interaction within the complex geometrical properties of the target structures and the inherent speckle noise. In this paper, we present an advanced yet efficient geometrical correction method that may be applied to multi-resolution satellite SAR images. For this purpose, SURF(Speeded-Up Robust Feature) is adopted and modified so as to make it fully applicable to SAR images. KI thresholding technique is constructed and applied to multi-SAR images to verify the performance.

1 INTRODUCTION

Change detection is the process of identifying differences in the state of an object or phenomenon by observing it at different times (Lu et al., 2004). The goal of change detection is to detect "significant" changes while rejecting "unimportant" ones (Radke et al., 2005). Generally, important changes reflect natural phenomenon or human activities in the Earth. In recent years, with the development of high-resolution imaging satellites, the remote sensing has rapidly advanced that the minute details of the Earth surface could be investigated. Naturally, techniques for change detection have attracted increased attentions and become a topic of major research. Unlike optical image, geometrical distortions commonly occur during image acquisition of SAR images due to the geometrical characteristics of the targets. Therefore, geometrical correction of images plays an important role in this area. Geometric correction of the SAR images could be performed by utilizing satellite's orbit and attitude information. However, due to the inevitable errors in measuring SAR sensor's orbit and attitude information, and the acquisition errors of Earth's geographical parameters, the reflected radar signals are contaminated with considerable geometric errors. In order to acquire more accurate geometrical corrections, error correction needs to be performed with respect to the ground control points. Regardless of the methodology adopted, int is prerequisite to carry out accurate geometrical correction for the change detection to be properly applied, especially when the image resolution improves below sub-meter levels.

In general, geometric correction techniques can be classified into three categories, which are based on intensity, transform domain and feature characteristic respectively. Feature-based technique is simple and steady and hence has been widely used for this purpose in the past. A number of detectors are known to be applicable for this purpose, which include Harris corner detector, Forstner detector, Moravec detector, Harris-Laplacian detector, Gaussian-determinant detector, Hessian detector and Fast-Hessian detector.

Among others, SIFT(Scale Invariant Feature Transform) is one of the most widely used method for point feature detection. SIFT algorithm is known to be steady and resistant to geometric deformations and illumination changes for partial target matching and recognition. When the feature points have good lamination changes for partial target matching and recognition, then feature points has stability in terms of geometrical variation. However SIFT algorithm suffers from a drawback of consuming a significant amount of time for searching and calculating the matching points. Hence SURF algorithm has been proposed as a means to replace the SIFT by simplifying complicated SIFT algorithm while the general feature of high accuracy and stability are well preserved. It is asserted that SURF is several times faster than SIFT and claimed by its authors to be more robust against different image transformations than SIFT. In this paper, we adopt the previous SURF algorithm for SAR change detection. Parameter estimation and optimization are carried out to obtain the best matching results.

1.1 SURF Algorithm

SURF is a useful tool for matching points between different images. After SURF is performed, RANSAC is applied to obtain optimal coordinate conversion functions using the extracted matching points. After ground point selection is completed and conversion function is obtained, projective transformation and second order polynomial transformation is used to rearrange the remaining pixels into the new coordinates. Projective transformation needs four or more ground points and second order polynomial needs minimum 4 ground points. Higher multinomial matrix might be required for the optimal geometrical correction depending on the level of distortion in the images and the number of extracted ground points.

SURF algorithm has been mainly applied to optical image cases due to its inherent nature of requiring high contrast of pixel values. Y.Murali has developed a MOSAIC image stitching method based on SURF algorithm. In other case, an input query imaging technique is proposed that SURF feature points detector algorithm is incorporated with the color edge matching method.(Ryo Mitsumori, 2009) A modified SURF algorithm is developed by adopting the color and relative location information of interest points.(KyungSeung Lee, 2012) However the majority of the previous researches have dealt with optical images are SAR images have rarely a topic of research. This is mainly attributed to the low level of contrast in radar image pixels and inherent speckle noises around feature points. For this reason, it has been considered a difficult task to apply SURF for SAR change detection purpose. In this paper, we have adopted higher multinomial matrix equation in the process of applying SURF to the SAR images. By doing this, the probability of erroneous feature point detection is reduced and the point matching can be better performed against target movement, rotation and scale. After desired ground points are selected, the remaining pixels are rearranged on the new coordinate plane using a cubic convolution. We show that the modified SURF algorithm can be easily applied to the conventional SAR images. The performance of the proposed algorithm is verified throughout medium-to-low level resolution satellite SAR images.

1.2 KI Thresholding

For a simple change detection purpose, image thresholding is the most straightforward technique. There are a number of known image thresholding techniques suitable for different applications. Sezgin et al, has shown that the clustering-based method by Kittler and Illingworth (1986) provides the most reliable thresholding result in their experiments. This technique has been called KI thresholding and is performed as: Step 1. Choose an arbitrary initial threshold T. Step 2. Compute priori probability, mean value, variance value. Step 3. Compute the updated threshold. Step 4. Compare old threshold with updated threshold. KI thresholding technique has been widely applied in the past since thanks to its robust performance. In this paper, we adopted KI technique variation for the purpose of change detection between two different SAR images.

2 EXPERIMENT RESULTS

In Fig. 1 and Fig.2 are shown Radarsat-1,2 images taken over Vancouver respectively and their characteristics are described in Table 1 and 2. SAR images can be seen totally different depending upon the sensor position and viewing angle over the same scene. In this case, we have attempted to detect changes for Radarsat-1 and Radarsat-2, which are distinguished by different resolutions and their performances are compared later. Since the scene coverage is different from each other, regions of interest are extracted first. Then SURF algorithms are applied to both images to find out the common feature points that matched with each other.

Table 1: RADARSAT-1 IMAGERY

Name	Characteristics of products		
	Acquisition date	*Orbit*	*description*
SSG	1999.07.25.	Descending 19427	Map image
SGF	1998.07.09	Ascending 13975	Path image

Table 2: RADARSAT-2 IMAGERY

Characteristics	Description
Name of Satellite	Radarsat-2
Beam mode	FineQuad15
Product type	SLC

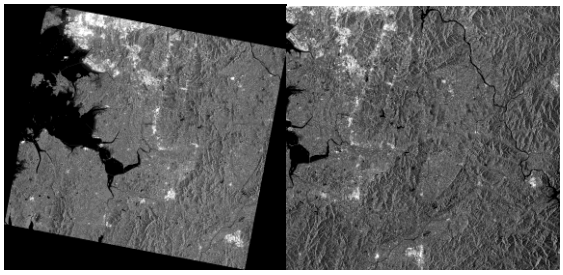

Figure 1: RadarSAT-1 Vancouver area, (a)SSG (b)SGFT

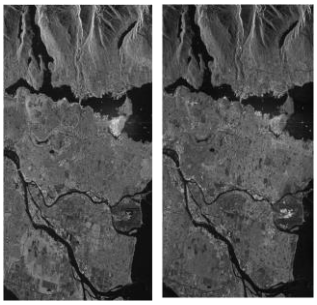

Figure 2: RadarSAT-2 Vancouver area, HH, HV data

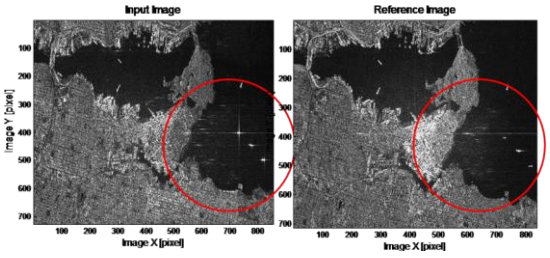

Figure 3: ROI(Region Of Interest) images in Fig.2

Figure 4 presents the number of interest points extracted from each SAR images according to the Hessian threshold. As the Hessian threshold value is increased, the number of extracted interest points is reduced. Figure 5 shows the number of matched points with respect to the varying SURF matching threshold values. SURF matching points are selected by calculating the Euclidean distance around extracted interest points. The number of the selected matching pixels increases as the SURF matching threshold value is increased from 0.4 to 0.9. Processing times to extract interest points and matched points are shown in Figure 6. As Hessian threshold is increased, processing time is reduced, but the number of matched point is decreased. Therefore, there should be an appropriate trade-off between time consumption and accuracy to guarantee the optimization of the image matching.

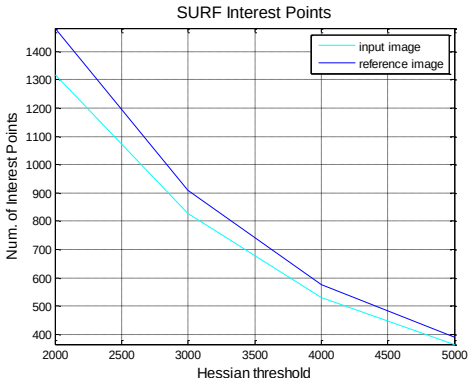

Figure 4: The number of interest point according to Hessian Threshold (Radarsat-2)

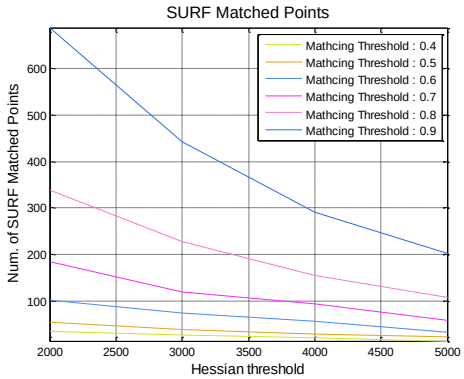

Figure 5: The number of matched points by Euclidean distance calculation (Radarsat-2)

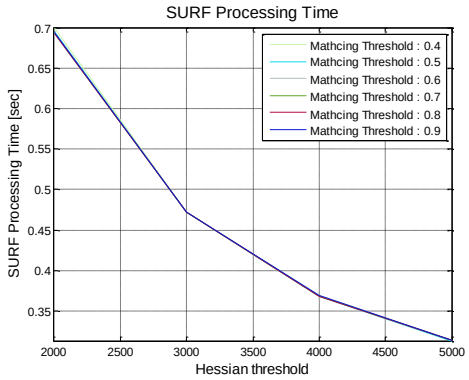

Figure 6: SURF Processing Time according to Hessian threshold (Radarsat-2)

Extracted interest points and matched points are shown in Figure 7 and Figure 8 for Radarsat-1. Similar procedure is performed against Radarsat-2 and shown in Figure 9 and Figure 10 respectively. As mentioned earlier, the performance of the matching algorithm depends upon the parameters in the SURF, particularly the threshold value. In our experiment for Radarsat-2 images, the Hessian threshold value of 2000 and matching threshold value of 0.5 have provided relatively good performance while the calculation burden is minimized. After the matching sequence is completed, geo-correction procedure is followed using the projective transform for image matching of two satellite images. The performance of image matching is measured as the distance of the dislocation of common pixels, calculated as residual sigma. The matching accuracy and error levels are calculated and compared with each other for Radarsat-1 and Radarsat-2 and summarized in Table 3. The result shows that matching accuracy in Radarsat-1 is 42.5% and matching accuracy in Radarsat-2 is 94.6%. Matching accuracy in low resolution images is smaller than high resolution image, which are as expected. It can be inferred that the Hessian threshold in low-resolution case has to be increased than that of the high-resolution image case.

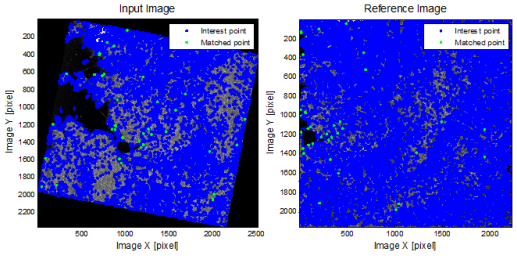

Figure 7: Extracted interest points and matched points (Radarsat-1)

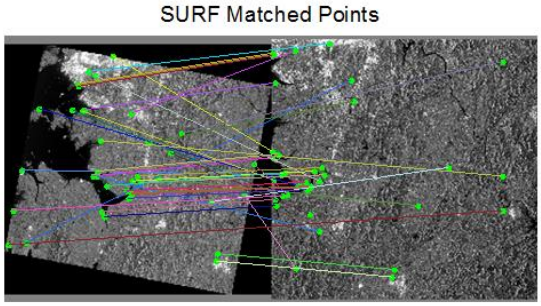

Figure 8: Result of SURF matching (Radarsat-1)

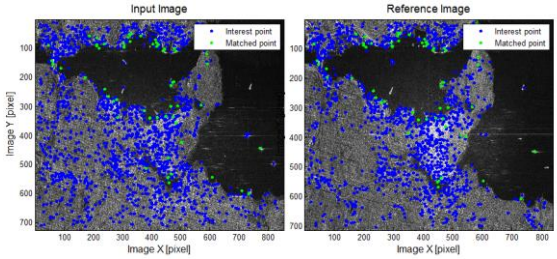

Figure 9: Extracted interest points and matched points (Radarsat-2)

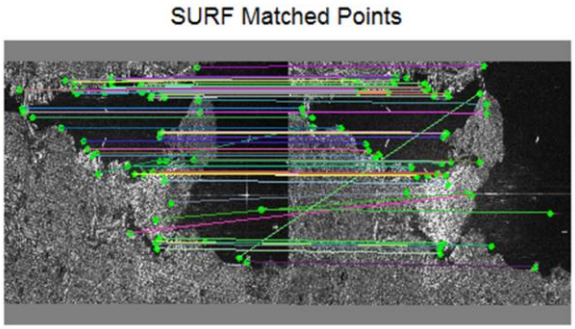

Figure 10: Result of SURF matching (Radarsat-2)

Table 3: Matching results between the satellite SAR images (Hessian threshold = 2000, Matching threshold = 0.5)

	Radarsat-1	**Radarsat-2**
SURF Interest Points	11865/23164	1319/1483
SURF Matched Points	40	56
Matching Accuracy	42.5%	94.6%
Residuals sigma_x [pixel]	1.303	1.018
Residuals sigma_y [pixel]	1.176	1.009

In SAR imaging mode, comparison between two different images is difficult due to the residing speckle noise and ratio comparison tend to be perferred for the high noise image application.

As in the SURF case, it is important to select a proper threshold value when KI thresholding method is applied. In our experiments, the optimal threshold value was chosen to be 0.057 for Radarsat-1 and 0.026 in Radarsat-2. Pixels with intensity values bigger than the optimal threshold are extracted in Figure 12. These areas are considered to implicate changes over the scenes. Here it is seen that high resolution SAR provide more realistic details of the changes between different images.

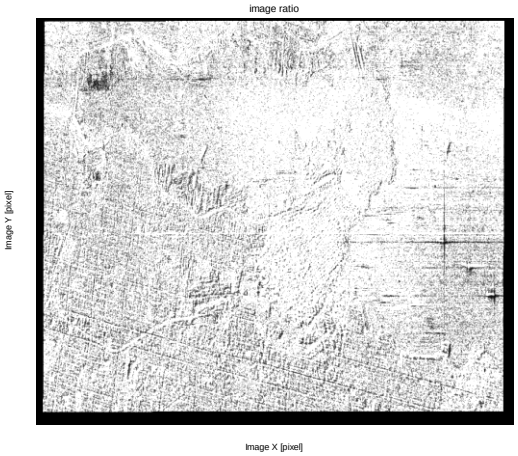

Figure 11: Ratio image (Radarsat-2)

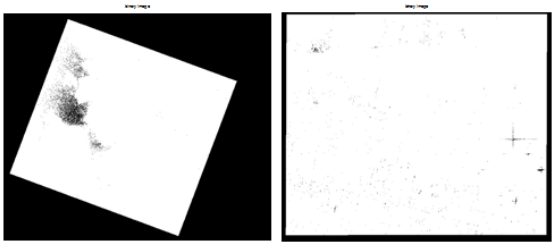

Figure 12: results of applying KI thresholding (a)Radarsat-1 (b)Radarsat-2

3 CONCLUSION

Accurate geometrical correction of radar imagery is essential for effective change detection procedure. The geometrical correction of SAR images is highly complicated due to the complex geometrical properties of the targets, signal interaction within target structures and speckle noise. In this paper, we present a modified SURF algorithm to geo-registration on SAR image. The KI thresholding technique has been applied to detect changes over medium resolution SAR images. It is shown that the parameter selection of SURF algorithm needs to be carefully designed on applying SAR image by adjusting the Hessian threshold value according to resolution of images.

ACKNOWLEDGEMENTS

The work is supported by KARI (Korea Aerospace Research Institute) of Republic of Korea.

REFERENCES

H. Bay, T. Tuytelaars, and L. V. Gool, "SURF : Speeded Up Robust Features", *European Conference on Computer Vision, Vol. 3951, pp. 404-417, 2006*

Kim, T. and Im, Y "Automatic satellite image registration by combination of matching and random sample consensus", *IEEE Trans. on Geoscience and Remote Sensing, Vol. 41, No. 5, pp. 1111-1117, 2003*

Goshtasby, A. A., "2-D and 3-D image registration - for medical, remote sensing, and industrial applications", *John Wiley & Sons Inc., New York, pp. 4-5, 2005.*

B. Zitova and J. Elusser, "Image registration methods: a survey", *Image and Vision Computing 21, pp. 977-1000, 2003*

Flora Dellinger, Julie Delon, Yann Gousseau, Julen Michel and Florence Tupin, "SAR-SIFT: A SIFT-LIKE ALGORITHM FOR SAR IMAGES", *Geoscience and Remote Sensing Symposium (IGARSS), 2012 IEEE International, pp. 3478 – 3481, 2012.*

Mark D Pritt, Kevin J LaTourette, "Automated Registration of Synthetic Aperture Radar Imagery to LiDAR, *IGARSS 2011, July 2011.*

T. Lindeberg, "Feature detection with automatic scale selection", *International Journal of Computer Vision, Vol. 30, No.3, PP. 79-116, 1998*

Kittler, J. and Illingworth, J., 'Minimum error thresholding', Pattern recognition 19(1), 41–47.1986

Sezgin, M. et al. 'Survey over image thresholding techniques and quantitative performance evaluation', *Journal of Electronic imaging 13(1), 146–168. 2004*

Y.MURALE., 'Image Mosaic Using Speeded Up Robust Feature Detection', *International Journal of Advanced Research in Electronics and Communication Engineering (IJARECE) Volume 1, Issue 3, September 2012*

Ryo Mitsumori, Hideaki Uchiyama, Hideo Saito, Myriam Servieres, and Guillaume Moreau, 'Change Detection Based on SURF and Color Edge Matching', *Proc.ACCV, 2009*

Kamel Besbes Rochdi Bouchiha, 'Automatic Remote-Sensing Image Registration Using SURF', *International Journal of Computer Theory and Engineering, Vol. 5, No. 1, February 2013*

Woo-Kyung Lee and Ah-Leum Kim, 'An Efficient Automatic Geo-Registration Technique for High Resolution Spaceborne SAR Image Fusion', *IGASS 2011, July, 2011*

KyungSeung Lee, Daehoon Kim, Seungmin Rho and Eenjun Hwang, 'Improving Matching Performance of SURF Using Color and Relative Position', *The Korea Navigation Institute, Vol.16., No.2, April, 2012*

Smith, J., 1998. *The book*, The publishing company. London, 2nd edition.

Maximum Message Flow and Capacity in Sensor Networks

Vassil S. Sgurev, Stanislav T. Drangajov, and Lyubka A. Doukovska
Institute of Information and Communication Technologies, Bulgarian Academy of Sciences
Acad. G. Bonchev str., bl. 2, 1113 Sofia, Bulgaria
vsgurev@gmail.com; sdrangajov@gmail.com, *doukovska@iit.bas.bg*

Keywords: Sensors, Receivers, Communication network, Network flow optimization methods.

Abstract: The present paper considers problems for defining of the maximal messages traffic in a communication network with limited capacities of the separate sections and with arbitrary location of sensors and receivers on it. The specific requirements are described which emerge from the operation of the sensors and receivers on the communication network. Network flow methods are proposed for calculating the maximum possible messages flow, including such a flow of min cost, as well as of the set of critical sections of the network, which block the possibility of further increase of the messages flow. These methods take in account the specific features at generating and receiving of information by the sensors and the receivers respectively. Two numerical examples are given which practically illustrate the solving of the problems pointed out above, and show the effectiveness of the methods proposed for modelling and optimization.

1 PRELIMINARY

Many areas of science and technologies exist where machines and apparatuses are used, equipped with multiple sensors and receivers for the signals and messages, emitted by the former. All of them are connected in sophisticated communication networks for information transfer and distribution; as such may be considered the different centers for physical experiments, machines and equipment in the energy industry – from solar plates to heavy oil sea stations, nuclear electrical power plants, transportation systems, and so on. In fact no area – production, social, or economical – exists where the information flows are not of great importance and as so the speed and reliability of the connections should be by no means neglected. This is of course directly connected with the tremendous flourish of information technologies, which propose possibilities for information flows control.

The network flow programming methods and algorithms (Ford, Fulkerson, 1956) propose a good ground for investigation and realization of the message planning and routing. These methods and algorithms, though a particular class of mathematical programming, turn to be very effective and quickly convergent (Shakkottai, Srikant, 2007; Sgurev, 1991).

2 THE SENSOR COMMUNICATION NETWORK

It is most convenient to represent the sensors communication network as an oriented graph $G(X, U)$ (Christofides, 1986) with a set of arcs U and a set of noes X, such that:

$$X = \bigcup_{i \in I} x_i;\ U = \bigcup_{(i,j) \in G} (x_i, x_i); \tag{1}$$

$$X = (S \bigcup T) \bigcup R;\ I = (I_s \bigcup I_t) \bigcup I_r; \tag{2}$$

$$S = \bigcup_{i \in I_s} x_i;\ T = \bigcup_{i \in I_t} x_i;\ R = \bigcup_{i \in I_r} x_i; \tag{3}$$

where S is the set of sensor points; T – the set of information receiver points; R – the set of intermediate points through the information is being transported without any processing; A – the set of pairs of indices of all arcs from U such that $A = \{(i, j) / (x_i, x_j) \in U\}$; x_{ij} – brief denotation of the arc (x_i, x_j); Ø – the empty set; I – the set of indices of all nodes from X; I_s, I_t, and I_r – subsets of indices of nodes from S, T, and R respectively, for which it is supposed that:

$$I_s \cap I_r = \emptyset;\ I_s \cap I_t = \emptyset;\ I_r \cap I_t = \emptyset \qquad (4)$$

The direct and reverse mapping on the indices I on the graph $G(X, U)$ may be represented in the following way (Christofides, 1986):

$$\Gamma_i^1 = \{ j / (x_i, x_j) \in U; x_j \in X \} \qquad (5)$$

$$\Gamma_i^{-1} = \{ j / (x_j, x_i) \in U; x_j \in X \} \qquad (6)$$

It is expedient the discrete messages from the separate sensors and for a given time gap Δt to be averaged by number and duration. This will allow them to be considered as a continuous flow of messages with an average statistical flow density (Sgurev, 1991), from one point to another.

If a possibility exists for simultaneous transmission of messages from x_i to x_j and vice versa, then the respective section (x_i, x_j) is replaced by a pair of oppositely directed arcs and namely $\{(x_i, x_j), (x_j, x_i)\} \subset U$.

The average statistical density of the message flow being emitted from the sensor of index $i \in I$ may be defined in the following way:

$$f_i = \frac{\sum\limits_{p \in D_i} \lambda_{ip}}{\Delta t}; i \in I_s; \qquad (7)$$

where λ_{ip} – duration of the k^{th} in order message from the sensor $i \in I_s$; D_i – the set of indices of the messages received from the sensor of index $i \in I_s$ in the time gap Δt.

For the receiver points with indices from It this value will look like this:

$$f_j = \frac{\sum\limits_{k \in H_j} \varphi_{jp}}{\Delta t}; \ j \in I_t; \qquad (8)$$

where φ_{jp} is the duration of the k^{th} in order message to the receiver of index $j \in I_t$; H_j – the set of indices of messages received by point j.

If we proceed from the assumption that no loss of messages is admissible at their transportation through the network, then equality is necessary between the sum of the densities of the messages emitted by all sensors of indices from I_s and the sum of densities of the messages, received by all receivers with indices from I_t, i.e.:

$$\sum_{i \in I_s} f_i = \sum_{j \in I_t} f_j = v; \qquad (9)$$

where v is the total density of all messages being transferred from all sensors to all receivers.

In most cases the increase or decrease of the flow density from any sensor of index $i \in I_s$ and to any receiver of index $j \in I_t$ is proportional to their inherent technical characteristics defined by the parameters f_i and f_j from (7) and (8) respectively. It follows then from (9) that for each $i \in I_s$ and $j \in I_t$ the following coefficients could be calculated:

$$k_i = \frac{f_i}{\sum\limits_{i \in I_s} f_i} = \frac{f_i}{v}; \ f_i = k_i v; \qquad (10)$$

$$k'_j = \frac{f_j}{\sum\limits_{i \in I_s} f_j} = \frac{f_j}{v}; \ f_j = k'_j v \ . \qquad (11)$$

If both sides of the equalities (10) and (11) are summed on $i \in I_s$ and $j \in I_t$ respectively, then:

$$\sum_{i \in I_s} k_i = \sum_{j \in I_t} k'_j = 1. \qquad (12)$$

The density of the message flow from x_i to x_j will be denoted by the arc flow function f_{ij} ; $(i, j) \in A$ and by c_{ij}; $(i, j) \in A$ will be denoted the capacity of the arc x_{ij}. Then the next requirement shows the physical impossibility the flow function density f_{ij} to exceed the capacity c_{ij} of the arc x_{ij} , i.e. for each $(i, j) \in A$:

$$0 \le f_{ij} \le c_{ij} \qquad (13)$$

The value of a unit of density of the messages flow will be denoted by the non-negative arc rate $a_{ij} \ge 0$; $(i, j) \in A$ on the respective arc (section) x_{ij}.
The following two important problems may be formulated on the sensor communication networks:
A. Find the maximum possible flow v_{max} from the sensor points S to receiver points T. This may be most effectively performed through the following network programming problem:

$$L = v \rightarrow \max \qquad (14)$$

subject to the following constraints, for each $i \in I$:

$$\sum_{j \in \Gamma_i^1} f_{ij} - \sum_{j \in \Gamma_i^{-1}} f_{ji} = \begin{cases} k_i v, \text{ if } i \in I_s; \\ 0, \text{ if } i \in I_r; \\ -k'_i, \text{ if } i \in I_t; \end{cases} \qquad (15)$$

$$f_{ij} \le c_{ij}, \text{ for each } (i,j) \in A \quad (16)$$

$$f_{ij} \ge 0, \text{ for each } (i,j) \in A \quad (17)$$

Solving the problem above results in:

$$L = v_{max} \quad (18)$$

Let cuts $(X_{0,}\overline{X}_0)$ be defined between *S* and *T* as sets of arcs, such that:

$$X_0 \subset X; \quad (19)$$

$$\overline{X}_0 = X \setminus X_0;\ X_0 \cap \overline{X}_0 = \varnothing;$$
$$(X_0, \overline{X}_0) = \{x_{ij} / x_i \in X_0; X_j \in \overline{X}_0; x_{ij} \in U\} \quad (20)$$

Then, according to the well-known min-cut max-flow theorem of Ford-Fulkerson (Ford, Fulkerson, 1956) a minimal cut $(X_0^*, \overline{X}_0^*)$ is the one for which:

$$f(X_0^*, \overline{X}_0^*) = c(X_0^*, \overline{X}_0^*);\ f(\overline{X}_0^*, X_0^*) = 0 \quad (21)$$

It follows then that the max flow value may be increased only if the capacity of some arcs of the minimal cut $x_{ij} \in (X_0^*, \overline{X}_0^*)$ is increased. Further on the arcs with equality between the capacity and the arc flow function will be called saturated and otherwise – unsaturated.

B. As it is possible several minimal cuts to exist the problem arises to find the one of them which is of minimal value of the parameter $\sum_{(i,j)\in A} a_{ij} f_{ij}$. For solving this problem it is necessary problem A. to be first solved, i.e. the max flow v_{max} from (18) to be found through relations (14) to (17) and then with fixed max flow the minimal cut of minimal cost to be defined. For this purpose the values of $\{k_i\ v / i \in I_s\}$ and $\{k'_j\ v / j \in I_t\}$ are calculated with known $v = v_{max}$ and the latter to be put down as fixed values in the right hand side of (15). Then finding of the minimal cut of minimal cost may be carried out by solving the following network flow programming problem:

$$L = \sum_{(i,j)\in A} a_{ij} f_{ij} \to \min \quad (22)$$

observing constraints (14) to (17).

This method provides a possibility for optimal distribution (max flow and min cost) of the messages traffic between the sensors and the receivers in the sensor communication network.

3 EXEMPLARY PROBLEM AND NUMERICAL SOLUTIONS

The numerical examples which follow demonstrate the abilities of the method proposed for finding the maximal flow from the sensors to receivers (Problem A.) and the minimal cut with minimal cost (Problem B.).

EXAMPLE: A sensor communication network with 9 nodes and 17 arcs (sections) is conditionally shown in Figure 1.

Three nodes are sensors, 3 – receivers, and 3 – intermediate, and namely:

$S = \{x_1, x_2, x_3\}$; $T = \{x_7, x_8, x_9\}$; $R = \{x_4, x_5, x_6\}$.

The oriented arcs in Figure 1 show from which initial node to which final node messages are being transmitted. The capacities $\{c_{ij}\}$ and the rates $\{a_{ij}\}$ for each arc of the network are shown in Table 1. The messages densities from sensors *S* to receiver points *T* are put down in Table 2. In the same table the values of coefficients $\{k_i\}$ and $\{k'_j\}$ are given, calculated according to formulae (10) and (11).

Table 1: Capacities and Rates

A	(1,2)	(1,4)	(1,5)	(1,7)	(2,3)	(2,4)	(3,4)	(3,6)	(3,9)	(4,5)	(4,6)	(5,7)	(5,8)	(6,8)	(6,9)	(8,7)	(9,8)
c_{ij}	5	3	7	6	7	6	6	9	4	8	5	7	8	6	11	5	6
a_{ij}	10	5	5	10	11	6	6	5	10	5	5	3	4	7	4	6	10

Table 2: Coefficients $\{k_i\}$ and $\{k'_j\}$

Nodes X	x_1	x_2	x_3	x_4	x_5	x_6	x_7	x_8	x_9
$\{f_i\}$	14	10	6	0	0	0	9	9	12
$\{k_i\} \cup \{k'_j\}$	0,47	0,33	0,2	-	-	-	0,3	0,3	0,4
Node type	Sensor			Intermediate			Receiver		

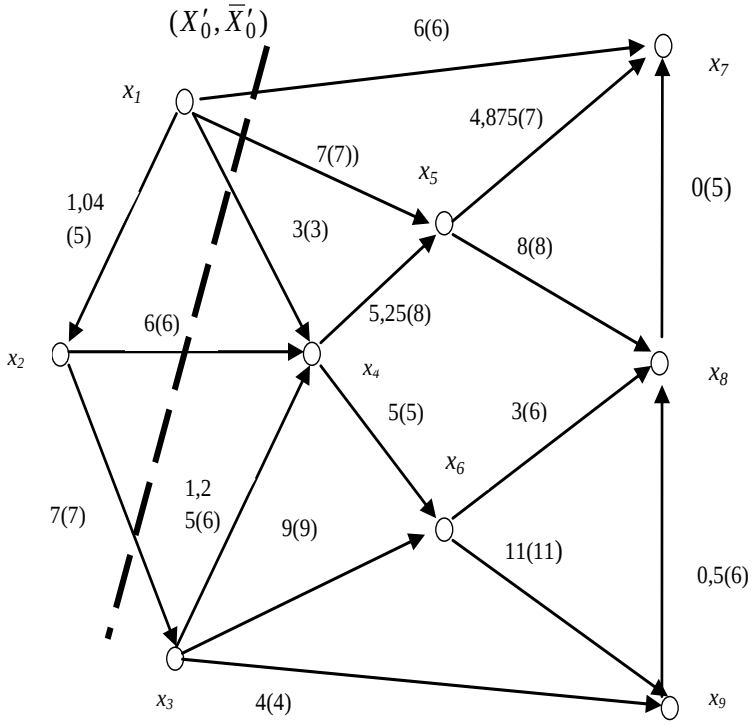

Figure 1: A sensor communication network with 8 nodes and 17 arcs

A. On the base of the data from Tables 1 and 2 the problem for finding the maximal flow v_{max} may be reduced to the following problem of network flow programming. Maximization of v from the linear form (14) observing the following equalities and inequalities:

$z_1)\ f_{1,2} + f_{1,4} + f_{1,5} + f_{1,7} = 0{,}47\ v$;
$z_2)\ f_{2,3} + f_{2,4} - f_{1,2} = 0{,}33\ v$;
$z_3)\ f_{3,4} + f_{3,6} + f_{3,9} + f_{2,3} = 0{,}2\ v$;
$z_4)\ f_{4,5} + f_{4,6} - f_{1,4} - f_{2,4} - f_{3,4} = 0$;
$z_5)\ f_{5,7} + f_{5,8} - f_{1,5} - f_{4,5} = 0$;
$z_6)\ f_{6,8} + f_{6,9} - f_{3,6} - f_{4,6} = 0$;
$z_7)\ f_{1,7} + f_{5,7} + - f_{8,7} = 0{,}3\ v$;
$z_8)\ f_{5,8} + f_{6,8} + f_{9,8} - f_{8,7} = 0{,}3\ v$;
$z_9)\ f_{3,9} + f_{6,9} - f_{9,8} = 0{,}4\ v$;

$z_{10})\ f_{1,2} \le 5$;
$z_{11})\ f_{1,4} \le 3$
$z_{12})\ f_{1,5} \le 7$;
$z_{13})\ f_{1,7} \le 6$;
$z_{14})\ f_{2,3} \le 7$
$z_{15})\ f_{2,4} \le 6$;
$z_{16})\ f_{3,4} \le 6$;
$z_{17})\ f_{3,6} \le 9$
$z_{18})\ f_{3,9} \le 4$;
$z_{19})\ f_{4,5} \le 8$;
$z_{20})\ f_{4,6} \le 5$
$z_{21})\ f_{5,7} \le 7$;
$z_{22})\ f_{5,8} \le 8$;
$z_{23})\ f_{6,8} \le 6$
$z_{24})\ f_{6,9} \le 11$;
$z_{25})\ f_{8,7} \le 5$;
$z_{26})\ f_{9,8} \le 6$
$z_{27})\ f_{i,j} \ge 0$ for each $(i, j) \in A$.

Table 3: Arc flow function density

Arc flow density $f_{i,j}$	$f_{1,2}$	$f_{1,4}$	$f_{1,5}$	$f_{1,7}$	$f_{2,3}$	$f_{2,4}$	$f_{3,4}$	$f_{3,6}$	$f_{3,9}$	$f_{4,5}$	$f_{4,6}$	$f_{5,7}$	$f_{5,8}$	$f_{6,8}$	$f_{6,9}$	$f_{8,7}$	$f_{9,8}$
Value	1,04	3	7	6	7	6	1,25	9	4	5,25	5	4,875	7,375	3	11	0	0,5

The problem described above was solved by the software product WebOptim (Genova et al., 2011). The results obtained are summarized in the next Table 3 with value of $\boldsymbol{v_{max} = 36,25}$.

If data above for $\{f_{ij}\}$ are used and also the arc rates $\{a_{ij}\}$ from Table 1, then the costs for messages transportation, corresponding to the maximal flow defined above, and namely:

$$\sum_{(i,j)\in A} a_{ij} f_{ij} = 491{,}25 \qquad (23)$$

On the base of the coefficients $\{k_i\}$ and $\{k'_j\}$ from Table 2 and the maximal flow achieved $\boldsymbol{v_{max} = 36,25}$ the maximum admissible flow densities of messages may be calculated from the sensors S to the receiver points T, i.e.:

$$k_1 v = 17{,}04;\ k_2 v = 11{,}96;\ k_3 v = 7{,}25 \qquad (24)$$

$$k'_7 v = 10{,}875;\ k'_8 v = 10{,}875;\ k'_9 v = 14{,}50 \qquad (25)$$

On each arc in Figure 1 its main parameters are shown – the arc flow function, and in brackets the arc capacity. On the same figure the cut is shown by thick dotted line $(X'_0, \bar{X}'_0) = \{x_{14}, x_{15}, x_{17}, x_{23}, x_{24}\}$ for which there is equality between the maximal possible flow and the minimal cut, i.e. for which requirements (21) are observed. Node x_3 cannot be added to the nodes $X'_0 = \{x_1, x_2\}$ of this cut $(X'_0, \bar{X}'_0)$ because its parameter $k_3 v$ is linearly related to $k_1 v$ and $k_2 v$ which are blocked by the minimal cut $(X'_0, \bar{X}'_0)$. Therefore $k_3 v$ cannot be increased although that a path exists from it $\{x_{34}, x_{45}, x_{57}\}$ to the receiver point x_7 with unsaturated arcs. This is a specific feature of the sensor communication networks reflected in (10) and (11) which does not allow Ford-Fulkeson theorem to be directly applied, but in an oblique way only. In case that increase of the flow v is needed from S to T this should be performed by increasing the capacity of an arc from the cut:

$$(X'_0, \bar{X}'_0) = \{x_{14}, x_{15}, x_{17}, x_{23}, x_{24}\} \qquad (26)$$

B. For calculating the maximal flow of minimal cost relations z_1 to z_{27} with the following changes:

- the right hand sides of equations z_1 to z_3 are replaced by the respective right hand parts of the three relations from (25);
- the right hand sides of equations z_7 to z_9 are replaced by the respective right hand parts of the three relations from (26). In this way the maximal possible flow v_{max} is fixed both in the sensors S and in the receivers T.

For finding the minimal value of this flow the following linear relation is used in thich the rates $\{a_{ij}\}$ are taken from Table 1:

$$L_1 = 10 f_{1,2} + 5 f_{1,4} + 5 f_{1,5} + 10 f_{1,7} + 11 f_{2,3} + 6 f_{2,4} + 6 f_{3,4} + 5 f_{3,6} + 10 f_{3,9} + 5 f_{4,5} + 5 f_{4,6} + 3 f_{5,7} + 4 f_{5,8} + 7 f_{6,8} + 4 f_{6,9} + 6 f_{8,7} + 10 f_{9,8} \rightarrow \min \qquad (27)$$

The problem (27) with the modified relations z_1 to z_{27} was solved by the software product mentioned above. The values of the arc flow functions and of the linear form (27) are summarized in the Table 4:

$$L_1 = 485{,}53 \qquad (28)$$

Table 4: Arc Flow Function

Arc flow function $f_{i,j}$	$f_{1,2}$	$f_{1,4}$	$f_{1,5}$	$f_{1,7}$	$f_{2,3}$	$f_{2,4}$	$f_{3,4}$	$f_{3,6}$	$f_{3,9}$	$f_{4,5}$	$f_{4,6}$	$f_{5,7}$	$f_{5,8}$	$f_{6,8}$	$f_{6,9}$	$f_{8,7}$	$f_{9,8}$
Value	1,03	3	7	6	7	6	1,24	9	4	5,87	4,37	4,87	8	2,87	10,5	0	0

These data are put down in the Figure 2 like in Figure 1. In both numerical examples – in case A (Figure 1) and in case B (Figure 2) the configuration of the graph $G(X,U)$, capacities $\{c_{ij}\}$, coefficients $\{k_i\}$ and $\{k'_j\}$, arc rates $\{a_{ij}\}$ and the max flow v_{max} are identical but there is a difference in the flow realization of $\{f_{ij}\}$. The flow value on the arc $x_{4,5}$ in case A is 5,25 and in case B – 5,87. There are

changes and on the arcs $\{x_{4,6}, x_{5,7}, x_{5,8}, x_{6,8}, x_{6,9}, x_{8,9}\}$. Some of them ($x_{4,6}$, $x_{6,9}$) has turned from saturated into unsaturated ones, another one ($x_{5,8}$) – from unsaturated into saturated, and third – ($x_{4,6}$, $x_{5,7}$, $x_{6,8}$, $x_{8,9}$), has only changed the flow function values.

The minimal cut $(X_0', \overline{X}_0')$; $X_0 = \{x_1, x_2\}$ remains the same as in Figure 1 and due to the same reasons it blocks the maximal flow increase. If the total value of the maximum possible traffic in both cases – A and B, then as expected from (23) and (29) for the max flow of min cost the total value L_1 is less by about 1,2% less than the analogical value L corresponding to the first case, i.e.:

$$\Delta L = L - L_1 = 491{,}25 - 485{,}53 = 5{,}72 \qquad (29)$$

The two examples given in the cases A and B demonstrate the effectiveness of the method proposed for finding of the maximum messages flow from sensor to receiver points on an arbitrary sensor communication network, and of max flow of min cost.

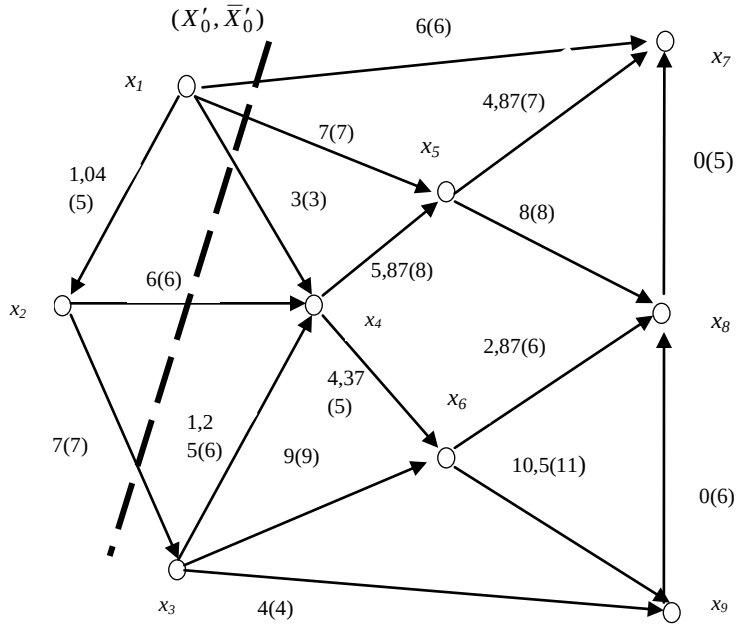

Figure 2: The same network with optimal values

4 SUMMARY

Here we show that the graph theory and network flow methods and algorithms are still up-to-date for control and optimization of the 'commodity' traffic in our case – messages from sensors to receivers, ensuring max flow at min cost of the traffic across the network. Two approaches are proposed for sensor networks, which maximize the flow from sensors to receivers and minimize the cost of this flow. In the first one the max flow is found and in the second one – alternative paths of min cost are found. The advantage of the network flow optimization is that it is independent on the nature and the physical characteristics of the network and operates with abstract and relative quantities, which when scaled in appropriate way are applicable to any type of real networks.

ACKNOWLEDGEMENTS

The research in the paper is partly supported by the project AComIn "Advanced Computing for Innovation", Grant 316087, funded by the FP7 Capacity Programme (Research Potential of Convergence Regions) and partly supported under the Project № DVU-10-0267/10.

REFERENCES

Sgurev V., 1991. Network Flows with General Constraints, Publishing House of the Bulgarian Academy of Sciences, Sofia (in Bulgarian).

Christofides N., 1986. Graph Theory: An Algorithmic Approach, London: Academic Press.

Shakkottai S., R. Srikant, 2007. Network Optimization and Control. Foundations and Trends in Networking, Vol. 2, № 3, pp. 271–379.

Ford L. R., D. R. Fulkerson, 1956. Maximal flow through a network. Canadian Journal of Mathematics, Vol. 8, pp. 399–404.

Bertsecas D., 1991. Linear Network Optimization, Massachusetts Institute of Technology.

Jensen P., J. Barnes, 1980. Network Flow Programming, John Wiley & Sons, NY, USA.

Genova K., L. Kirilov, V. Guliashki, B. Staykov, D. Vatov, 2011. A Prototype of a Web-based Decision Support, System for Building Models and Solving Optimization and Decision Making Problems, In: Proceedings of XII International Conference on Computer Systems and Technologies (Eds. B. Rachev, A. Smrikarov), Wien, Austria, 16-17 June 2011, ACM ICPS, Vol. 578, pp. 167–172.

Short Papers

Dual Frequency GPS Antennas for Space Monitoring

Hocine Hamoudi[1,2], Haddad Boualem[2] and Lognonne Phillipe[3]
[1]*Institut National de la Poste et des TIC (INPTIC), EUCALYPTUS, Algiers, Algeria*
[2]*Laboratoire de Traitement d'Image et Rayonnement (LTIR), FEI, USTHB, Algiers, Algeria*
[3]*Institut de Physique du Globe de Paris, (IPGP), Paris, France*
h_hamoudi@inptic.edu.dz, bhaddad_57@yahoo.fr, lognonne@ipgp.fr

Keywords: Antennas array, GNSS/GPS, Nanosatellite, patch antenna, TEC, tsunami alert.

Abstract: This work focuses on design and study of low cost corners truncated antennas arrays, printed on alumina, operating at L1/L2 GPS frequencies. This device consists on one patch antennas array to be integrated, in a warning system, with the aim of detecting ionosphere disturbances associated with land-based perturbations and tsunami's arrivals at the coast. To address such concerns, we studied a dual frequency patch antennas array. The performances of the antenna have been measured in terms of return loss, frequency of operation, axial ratio, bandwidth, and radiation pattern. Particularity and major advantage of this antenna, compared to conventional marketed GPS antennas, is the simultaneous use of both GPS frequencies L1 and L2.

1 INTRODUCTION

Natural disasters (volcanoes, tsunamis, floods ...) are creating significant property damage and casualties. Last decades, significant progress in detecting and modelling the atmosphere disturbances induced by climatic phenomena and seismic waves, were performed. This research is now an important part of the assignment and monitoring projects in the upper atmosphere (Lognonné, Artru, Garcia, Crespon, Ducic, Jeansou, Occhipinti, Helbert, Moreaux, and Godet, 2006). In this framework, we are particularly interested in the behavior of the ionosphere, which is considered as the seat of physical phenomena. Investigations of (Fenn, 2008) show that an antenna array with adaptive directional beams is a promising method to detect, using GPS /GNSS signals, some disturbances in the ionosphere. For microstrip antennas to be exploited in such systems, high polarization purity and isolation between orthogonal polarizations being linear or circular are needed. Many shapes of the patch like rectangular patch, elliptical patch, patch with loops, or Square ring microstrip antenna with truncated corners (Chen, Wu, and Wong, 1998) were used to obtain Circular Polarization (CP). The circular polarization can be obtained by well known method of a single-feed square microstrip antenna with truncating a pair of patch corners design. The main goal is the industrial manufacturing of a GNSS/GPS network of smart antennas. GNSS systems, however, offer other perspectives, not initially intended to designing the system, thanks to reflected GNSS signals. Therefore, could we use the GNSS satellites as opportunity of transmitters, and develop systems at ground surface, airborne or embedded for imaging GNSS reflections to deduce deformation of the Earth's surface, or maps of variation of sea level for tsunami survey and monitoring ? Especially after the Sumatra's tsunami on 2004 and Fukushima on 2011. The development of this new approach is the main objective of one of the 'Institut de Physique du Globe de Paris' (IPGParis) project, which focused on demonstration of the use of satellite navigation (GNSS) in existing and new application areas, such as the Land and sea monitoring. This is precisely the main objective of this work which will go through system design, based on GNSS antennas. The total size of the array is about 90 mm ×90 mm.

Compared to similar works in this area, the proposed antenna array offers relatively small dimensions, low weight, ease in fabrication, simple structure, smaller number of layers and works at the two GPS receiver frequencies, compared to conventional existing GPS antennas which work at L1 frequency only. The dual frequency antenna shall be passive and requires no electrical power.

In this paper, a 1× 4 dual frequency patch antenna array, suitable for use in space monitoring with Circular Polarization is presented.

2 CONTEXT & METHODOLOGY

GNSS which stands for Global Navigation Satellite Systems, allow to measure positions in real time with an accuracy ranging from a few meters to a few centimetres. In terms of public used, GPS receiver requires compact, low power lightweight, low cost, high reliability and with mobility capability. In the field of natural hazards, they are also used to measure deformations, such as volcanoes or to monitor changes in sea level in order to confirm a tsunami and estimate its height in the open sea. The development of a technique to detecting tsunami, thanks to the GPS data, could therefore improve warning systems in the seismogenic and tsunamigenic zones. The information provided by this method is complementary to those provided by classical seismology. Hence, the proposed methodology is the study of dual frequency antenna to be used in Global Positioning System (GPS) receivers operating at Ll (1575.42 MHz) and L2 (1227.6 MHz) frequency bands.

3 SIMPLE ELEMENT ANTENNA CONFIGURATION

Low profile, light weight, ease in fabrication, rugged, conformal, and in some cases lower cost than comparable antennas, are among favourable features which help microstrip antenna to be used in a broad range of modern applications. Microstrip antennas have been designed and incorporated in very wide range of systems, from commercial car navigation GPS systems, biomedical systems, to sophisticated satellite communication system.

The configuration of a single element of the array is shown in Figure 1. To reduce the cost of antenna manufacturing and making it more rigid, FR4 substrates are used, in a first time (Hamoudi, Haddad and Lognonne, 2012) (Hamoudi Haddad and Lognonne, 2013), but given constraining specifications of the project such as satellite, it was necessary to reduce the size of the device. For this purpose, the miniaturization of the radiating element using a substrate of acceptable cost and suitable for space missions (mechanical properties, electrical and thermal stresses) was our guideline. We also consider the design of another antenna with dual frequency. Our choice, for dielectric material, fell on alumina (ε_r=9.8 and h = 0.635 mm). To achieve a CP operation, we have chosen a truncated corner antenna, which consists of a squared patch with two opposites corners cut in angle of 45°. After computation, using equations (Sainati, 1996) and simulation we obtain: a) A L2 antenna with the dimension of 38mm and truncated length 2mm and b) L1 truncated square patch with the dimension of 30 mm and truncated length 4mm. The initial truncation length is kept 0.5mm, which is subsequently increased by 0.5mm in each successive step while obtain satisfactory performances.

We note that with a substrate constant about 9.8 it was possible to reduce, significantly, the antenna size from 43.1 mm and 57.4 mm (for epoxy glass) to 30 mm and 38 mm, so a reduction of approximately 35%. To verify the proposed design, a prototype of the single element antennas with optimized dimensions has been simulated. The simulation results show the impedance bandwidth (VSWR < 2) of 4% at L1 and 3.5% at L2 frequencies. For the operating frequency, a peak antenna gain of 4.8 dB is observed The simulated radiation patterns in two principle planes at 1.57 GHz and 1.22 GHz are satisfactory and suitable for our application.

With this configuration, we have shown that we have two separate antennas for L1 and L2 frequencies, but we have not yet been able to optimize the dimensions and size. The goal of this work is then precisely the study of a two GPS frequencies that fit to the same specifications previously mentioned for receiving antennas

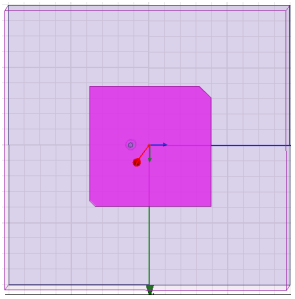

Figure 1: Simple element antenna geometry.

Dual frequency antennas consist of a single radiating structure, which exhibits a resonant behavior, both in terms of radiation and impedance matching at two separate frequencies. In microstrip antenna technology, dual frequency operation can be achieved through several numbers of different configurations. The basic three categories are

mentioned in (Sharma and Gupta, 1983). As discussed in the cavity model, two different modes can be excited on a single rectangular patch to obtain dual frequency operation by adjusting the width and the length of the patch according to the two separate resonant frequencies. Orthogonal modes can be excited either by using a single feed or by using two separate feeds. The choice depends on the type of application. When separate field configuration is used, as long as the spacing between the feed points is physically realizable, feeds must be positioned close to the centre of the corresponding edges in order to obtain good isolation levels between the ports. Following this approach and based on the previous results of two single patch antennas and using EM simulator, we obtain a rectangular patch printed on alumina with a length about 39 mm and width of 30 mm excited by two feed located at P1 (-0.75,+1) and P2 (-0.75,+1).

By packaging this antenna configuration into a compact patch type structure it will be suitable for use on a 3U Nano-satellite for spatial missions. The simple structure of microstrip antenna, previously, was used to form two configurations of antennas with 2 patches and four patches. The compact configurations of microstrips antennas dual-band with 2 patches and 4 patches is shown on Fig. 2.

4 NTENNA ARRAY DESIGN

In the case of single patch element, it has been observed that the antenna gain is quite low. That is why we consider using an array of antennas in order to increase the gain and improve the radiation characteristics. The major advantage of antenna arrays compared to a single antenna element is the electronic scanning capability. To reduce the cost of antenna fabrication and making it more rigid during construction, FR4 substrates are used, in a first time (Hamoudi et al., 2012) (Hamoudi et al., 2013), but given specifications of the project such as satellite geometry, volume and weight allocated to the antenna, we were forced to reduce the size of the device. To verify the proposed design, a prototype of the single element antennas with optimized dimensions has been simulated. We note that with a substrate constant about 9.8 it was possible to reduce, significantly, the antenna size from 43.1mm and 57.4 mm (for epoxy glass) to 30 mm and 38 mm, which corresponds to a reduction of approximately 35%. A single patch antenna can be used in a great majority of applications; nevertheless, the gain of these antennas is typically not sufficient to overcome path loss. For this reason, we use an antenna array. The gain of an array is typically many times larger than the gain provided by a single radiating element. Therefore, it is necessary to employ a number of elements in an array combination to achieve the required gain and pattern characteristics.

First, a two element array is simulated (1*2). The most important points in the design of an antenna array are the feed network and the element spacing (d). In our case, we have opted for a parallel feed. The parallel feed, also called the corporate feed, where the patch elements are fed in parallel by the power division transmission lines. The transmission line divides into two branches and each branch divides again until it reaches the patch elements. This is first constructed by connecting two adjacent elements together with a transmission line, calculated from (1) and (3). Now, two separate groups need to be connected together with a transmission line drawn between the centre of the 4 mm wide transmission line.

$$W/t \geq 1$$

$$Z_0 = \frac{\eta_0}{\sqrt{\varepsilon_{eff}}}\left[\frac{W_e}{t} + 1.393 + 0.667\ln\left(\frac{W_e}{t} + 1.444\right)\right]^{-1} \quad (1)$$

and, for $W/t \leq 1$

$$Z_0 = \frac{\eta_0}{2\pi\sqrt{\varepsilon_{eff}}}\ln\left(\frac{8t}{W_e} + 0.25\frac{W_e}{t}\right) \quad (2)$$

Where

For $W/t \leq 1/2\pi$

$$\frac{W_e}{t} = \frac{W}{t} + \frac{1.25}{\pi}\frac{h}{t}\left[1 + \ln\left(\frac{4\pi\pi}{h}\right)\right] \quad (3)$$

For $W/t \geq 1/2\pi$

$$\frac{W_e}{t} = \frac{W}{t} + \frac{1.25}{\pi}\frac{h}{t}\left[1 + \ln\left(\frac{2\pi}{h}\right)\right] \quad (4)$$

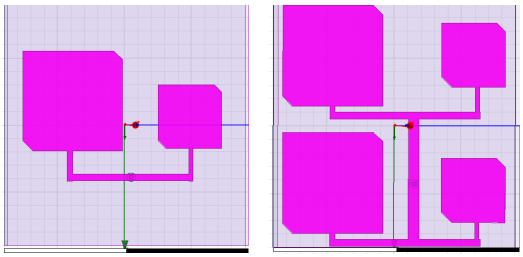

Figure 2: (1*2) and (1*4) element antennas geometry.

Where W_e is the effective width of the patch, t is the thickness of the dielectric substrate, and ε_{eff} effective dielectric constant of the patch, Z_0 is the impedance of the transmission line and η_0 is the free space intrinsic impedance (120π). The transmission line is split using T-junction with equal power split.

In general, the array elements should be as far as possible from each other, so the mutual coupling becomes negligible. In our case, the inter-element distance at set and fixed at 25 mm. Once the performance of the single antenna (2 patches) established, we went further to the study and simulation of the network (1*4) (four patches) in terms of S_{11}, VSWR, radiation pattern and gain. The major characteristics of adaptation and radiation are shown, in table 1

Table 1: Antennas array parameters.

Parameters	antenna array	
Frequency	1575.42 MHz	1227.6 MHz
LxW	(90 x 90)mm^2	
Truncated length	4 mm	2 mm
V.S.W.R	1.8 dB	0.3 dB
Return loss (S_{11})	-17 dB	-46 dB
Gain (G)	10 dB	
Axial Ratio	Good (<3dB)	
Bandwidth	3.5 %	4%
Polarization	RHCP	

The civilian signals issued from GNSS satellites are all right hand circularly polarized (RHCP). These antennas are made of Right Hand Circular Polarization. This property will be used for our antenna. Recall that circularly polarized antenna arrays are more often used in wireless communication systems as they can be easily mounted on mobile devices. They provide: (1) more focused radiation beams for better weather penetration and (2) good cross polarization rejection.

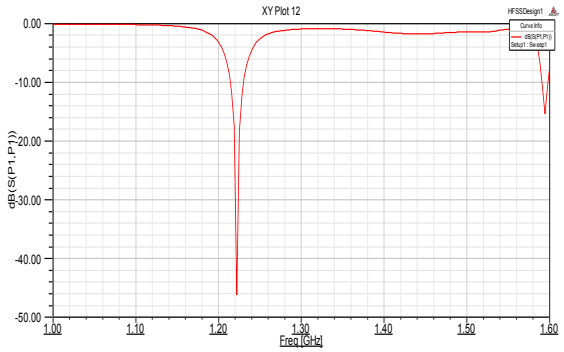

Figure 3: S_{11} diagram for (1*4) antennas array.

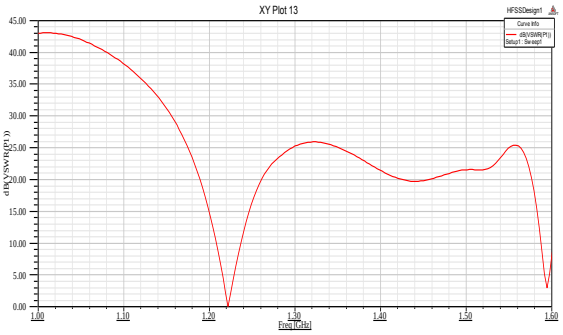

Figure 4: V.S.W.R diagram for (1*4) antenna array.

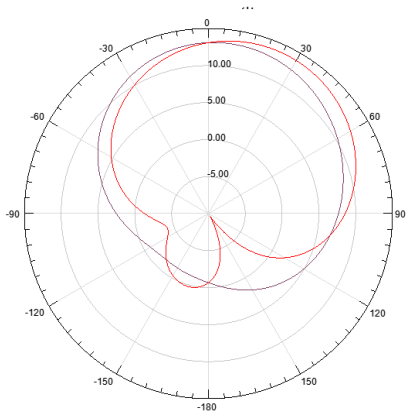

Figure 5: Simulated E&H plane radiation pattern at L1.

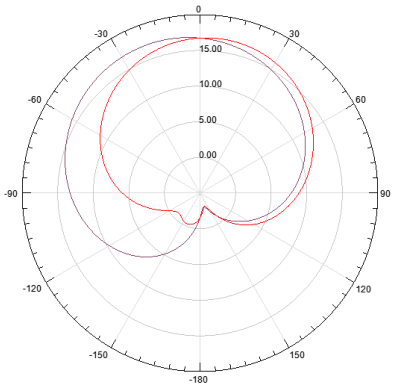

Figure 6: Simulated E&H plane radiation pattern at L2.

A good agreement of the return loss value is obtained at the operating frequencies, -17 dB and -46 dB, respectively, at L1 and L2. As can be seen in comparison with single element and two elements array, the return loss performance is increased. The dual antenna VSWR is well below 2 at L1 and L2 frequency. Radiation patterns of all the proposed antennas are derived using Electromagnetic Simulator. The results at their resonating frequencies are shown on Fig.5 and Fig.6. The antenna radiates to the upper half-space, ideally to track visible satellite,

with a beamwidth at 3 dB of approximately 60º. Moreover, we went from a gain of 4.8 dB for a configuration with one patch to a gain of about 10 dB with a configuration of 4 elements. The measured performance of this antenna showed good agreement with the specifications required to meet the application needs.

5 CONCLUSION

A compact and low cost dual frequency array antenna, operating at L1 and L2 is proposed. The simulated characteristics of the proposed configuration satisfy the requirements for GPS application and spatial mission. The study of printed antennas shows that, we were able to design an antennas arrays consisting of four truncated square elements, which will be used for tsunami warning system and Total Electronic Content (TEC) measurement.

As it is seen on Section 4, simulation results are satisfactory for input reflection coefficient, VSWR, radiation patterns, beam-width at 3 dB and axial ratio. The present network thus proposed with acceptable gain, ease in manufacturing, low cost, lightweight and small footprint meets our goal. In comparison with similar works in this area, the proposed antennas array offers relatively small dimensions, simple structure, low cost and the major advantage is operation at both GPS L1 and L2 frequencies at the same time. The antenna prototypes will, thereafter, be related to a GPS OEM board and integrated to a NanoSat "triple cube" designed for space monitoring. As perspective to this work, we will consider the study of a dual frequency network with 4 bi-frequency elements.

REFERENCES

Chen W.S., Wu C.K., and Wong K.L. (1998). *Single feed squarering microstrip antenna with truncated corner for compact circular polarization operation*, Electronics Letters (UK), vol. 34.

Fenn A.J. (2008), *Adaptive Antennas and Phased Arrays for Radar and Communications*. Boston: Artech House.

Hamoudi H., Haddad B., and Lognonné P. (2012). *Design of an antenna array for GNSS/GPS network*. In Image and Signal Processing, A. Elmoataz et al. Eds. *ICISP2012*. Lectures Notes in Computer Science (7340), Springer, 183-190.

Hamoudi, H., Haddad B., and Lognonné P. (2013). *Design of an antenna array for GNSS/GPS network*, IEEE, 7th EUCAP2013, Goteborg, Sweden, 2111-2115.

Lognonne P., Artru J., Garcia R., Crespon F., Ducic V., Jeansou E., Occhipinti G., Helbert J., Moreaux G., and Godet P. (2006). *Ground-based GPS imaging of ionospheric post-seismic signal*, Planetary and Space Science, 54.

Sainati R.A. (1996). *CAD of micro strip antenna for wireless applications*. Inc.: Artech House.

Sharma P.C., and Gupta K.C. (1983). *Analysis and optimised design of single point feed circularly polarised microstrip antennas*, *IEEE Transaction on Antenna Propagation* (USA), vol. AP-31

Electromagnetic Linear Micro Drives for Braille Screen: Characteristics, Control and Optimization

Dimitar N. Karastoyanov, Lyubka A. Doukovska, and Vassia K. Atanassova
Institute of Information and Communication Technologies, Bulgarian Academy of Sciences
Acad. G. Bonchev str., bl. 2, 1113 Sofia, Bulgaria
dkarast@iinf.bas.bg; doukovska@iit.bas.bg; vassia.atanassova@gmail.com

Keywords: Linear actuators, Braille screen, Optimization, Permanent magnets, Force characteristics, Finite element method.

Abstract: The graphical interfaces based on visual representation and direct manipulation of objects made the adequate use of computers quite difficult for people with reduced sight. A new type graphical Braille screen is developed. Permanent magnet linear actuator intended for driving a needle in Braille screen has been optimized. Finite element analysis, response surface methodology and design of experiments have been employed for the optimization. The influence of different parameters of the construction of a recently developed permanent magnet linear electromagnetic actuator for driving a needle in a Braille screen is discussed. The static force characteristics and magnetic field distribution is studied when varying the parameters.

1 INTRODUCTION

Permanent magnets have been intensively used in the constructions of different actuators in recent years. One of the reasons for their application is the possibility for development of energy efficient actuators. New constructions of permanent magnet actuators are employed for different purposes. One such purpose is the facilitation of perception of images by visually impaired people using the so called Braille screens.

Recently, different approaches have been utilized for the actuators used to move Braille dots (Nobels, et al., 2002; Cho, et al., 2006; Hernandez, et al., 2009; Green, et al., 2006; Chaves, et al., 2009; Kwon, et al., 2008; Kato, et al., 2005; Kawaguchi, et al., 2010). A linear magnetic actuator designed for a portable Braille display application is presented in (Nobels, et al., 2002). Actuators based on piezoelectric linear motors are given in (Cho, et al., 2006; Hernandez, et al., 2009). A phase-change microactuator is presented in (Green, et al., 2006) for use in a dynamic Braille display. Similar principle is employed in (Chaves, et al., 2009), where actuation mechanism using metal with a low melting point is proposed. In (Kwon, et al., 2008), Braille code display device with a poly-dimethylsiloxane membrane and thermopneumatic actuator is presented. Braille sheet display is presented in (Kato, et al., 2005) and has been successfully manufactured on a plastic film by integrating a plastic sheet actuator array with a high-quality organic transistor active matrix. A new mechanism of the Braille display unit based on the inverse principle of the tuned mass damper is presented in (Kawaguchi, et al., 2010).

Different electromagnetic actuators have been studied by the authors in (Yatchev, et al., 2011c; Karastoyanov, 2010; Karastoyanov, Simeonov, 2010; Karastoyanov, Simeonov, et al., 2010; Karastoyanov, Yatchev, et al., 2011).

In the present paper, recently developed permanent magnet linear actuator for driving a needle (dot) in Braille screen is studied and its magnetic field and static force-stroke characteristics have been obtained using the finite element method (Yatchev, et al., 2011a; Yatchev, et al., 2011b).

2 ACTUATOR CONSTRUCTION

The principal actuator construction is shown in Figure 1. The moving part is axially magnetized cylindrical permanent magnet.

The two coils are connected in series in such way that they create magnetic flux of opposite directions in

the region of the permanent magnet. In this way, depending on the polarity of the power supply, the permanent magnet will move either up or down. When motion up is needed, the upper coil should create flux in the air gap coinciding with the flux of the permanent magnet. Lower coil at the same time will create opposite flux and the permanent magnet will move in upper direction. When motion down is needed, the polarity of the power supply is reversed. The motion is transferred to the Braille dot using non-magnetic shaft, not shown in Figure 1.

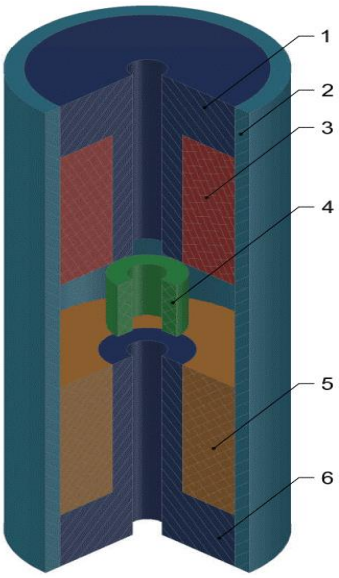

Figure 1: Principal construction of the studied actuator. 1 – upper core; 2 – outer core; 3 – upper coil; 4 – moving permanent magnet; 5 – lower coil; 6 – lower core.

The actuator features increased energy efficiency, as the need of power supply is only during the switching between the two end positions of the mover. In each end position, the permanent magnet creates holding force, which keeps the mover in this position.

3 STATIC FORCE CHARACTERISTICS

The static force characteristics are obtained for different construction parameters of the actuator. The outer diameter of the core is 7 mm. The air gap between the upper and lower core, the length of the permanent magnet and the coils height has been varied.

In Figures 2–5, the force-stroke characteristics are given for different values of the permanent magnet height *hm*, coil height hw, magnetomotive force *Iw* and apparent current density in the coils *J*. With c1 and c2, supply of the coils is denoted. The notation "c1 = –1, c2 = 1" means supply for motion up; "c1 = 1; c2 = –1" means supply for motion down, while "c1 = 0, c2 = 0" means no current in the coil, i.e. this is the force due only to the permanent magnet.

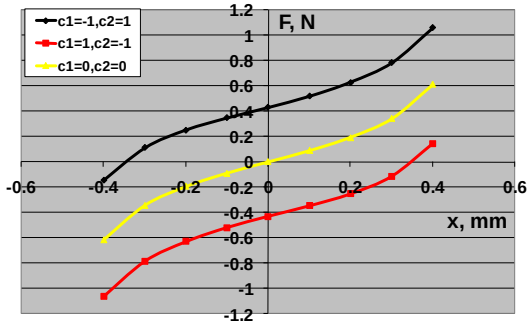

Figure 2: Force-stroke characteristics for *hm* = 2mm, δ = 3mm, *hw* = 5mm, *Iw* = 180A, *J* = 20A/mm^2.

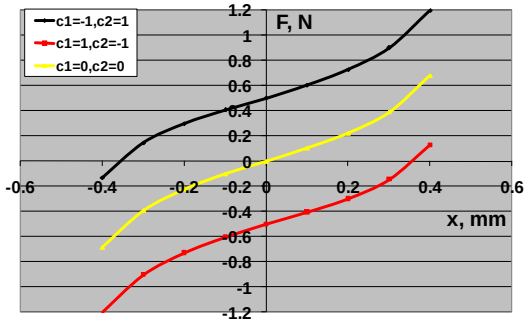

Figure 3: Force-stroke characteristics for *hm* = 3mm, δ = 4mm, *hw* = 5mm, *Iw* = 180A, *J* = 20A/mm^2.

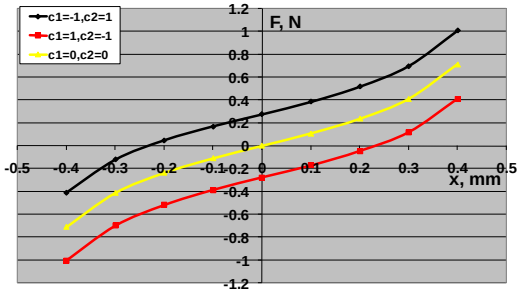

Figure 4: Force-stroke characteristics for *hm* = 4mm, δ = 5mm, *hw* = 5mm, *Iw* = 90A, *J* = 10A/mm^2.

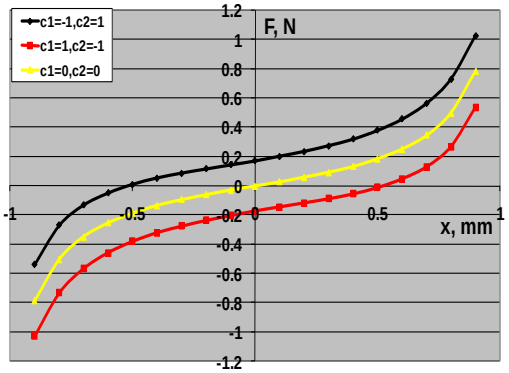

Figure 5: Force-stroke characteristics for hm = 2mm, δ = 5mm, hw = 10mm, Iw = 180A, J = 10A/mm^2.

As seen, the major part of the characteristics is suitable for Braille screen application.

4 OPTIMIZATION

The objective function is minimal magneto motive force of the coils. The optimization parameters are dimensions of the permanent magnet, ferromagnetic discs and the cores. As constraints, minimal electro-magnetic force acting on the mover, minimal starting force and overall outer diameter of the actuator have been set. The optimization is carried out using sequential quadratic programming, (Yatchev, Karastoyanov, 2012).

The canonic form of the optimization problem is:

$$\min\{NI\}$$

$$\left|\begin{array}{c} 5 \le hw \\ 0.5 \le hm \\ 0.3 \le hd \\ 0 \le J \le 25A/mm2 \\ Fh \ge 0.3N \\ Fs \ge 0.05N \end{array}\right.$$

where:

- NI — ampere-turns — minimizing energy consumption with satisfied force requirements;
- Fh — holding force — mover (shaft) in upper position, no current in the coils;
- Fs — starting force — mover (shaft) in upper or lower position and energized coils;
- J — coils current density;
- hw, hm, hd — geometric dimensions.

Minimization of magneto-motive force NI is direct subsequence of the requirement for minimum energy consumption.

Constraints for Fs and Fh have already been discussed. The lower bounds for the dimensions are imposed by the manufacturing limits and the upper bound for the current density is determined by the thermal balance of the actuator.

The radial dimensions of the construction are directly dependent by the outer diameter of the core – D which fixed value was discussed earlier. The influence of those parameters on the behavior of the construction have been studied in previous works, that make clear that there is no need radial dimensions to be included in the set of optimization parameters.

The optimization is carried out by sequential quadratic programming. The optimization results are as follows:

$$NI_{opt} = 79.28 \text{ A},$$
$$hw_{opt} = 5 \text{ mm},$$
$$hm_{opt} = 2.51 \text{ mm},$$
$$hd_{opt} = 1.44 \text{ mm},$$
$$J_{opt} = 19.8 \text{ A}$$

The optimal parameters were set as input values to the FEM model. The force-stroke characteristics of the optimal actuator are shown in Figures 6 and 7.

In Figures 8 and 9, the magnetic field of the optimal actuator is plotted for two cases.

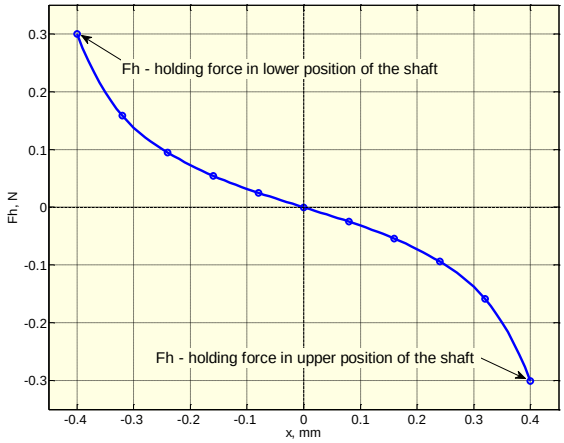

Figure 6: Force-stroke characteristic of the optimal actuator. The force is created by the permanent magnet only (no current in the coils).

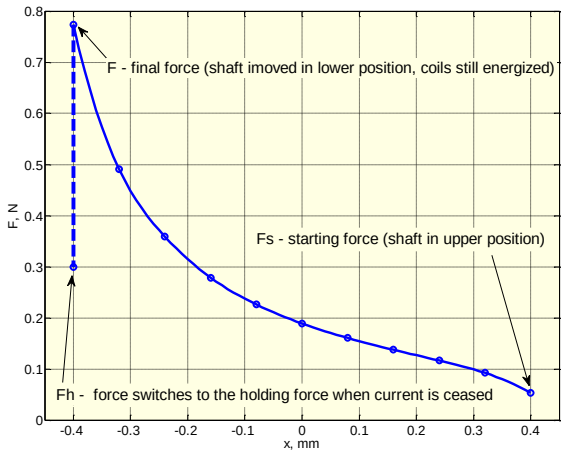

Figure 7: Force-stroke characteristic of the optimal actuator. Coils are energized. The shaft is displaced from final upper to final lower position.

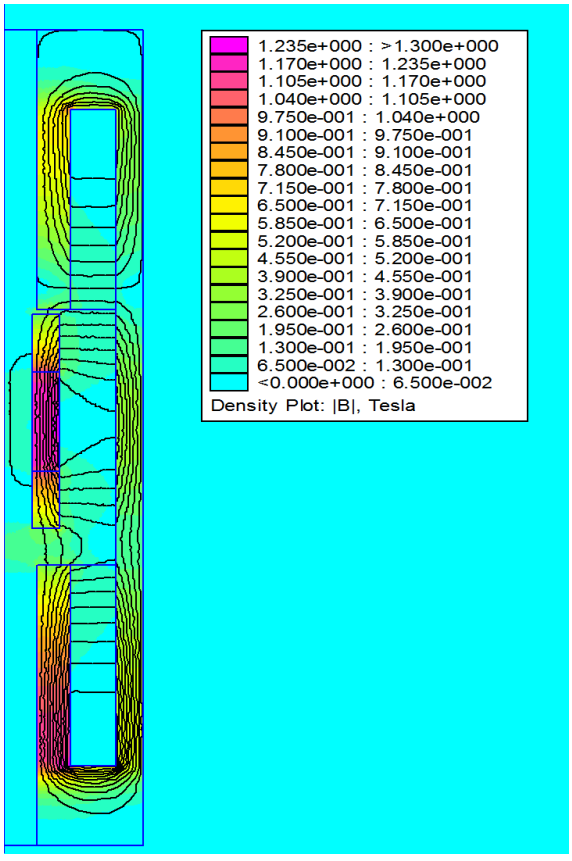

Figure 8: Magnetic field of the optimal actuator with shaft in upper position and coils energized to create downward force.

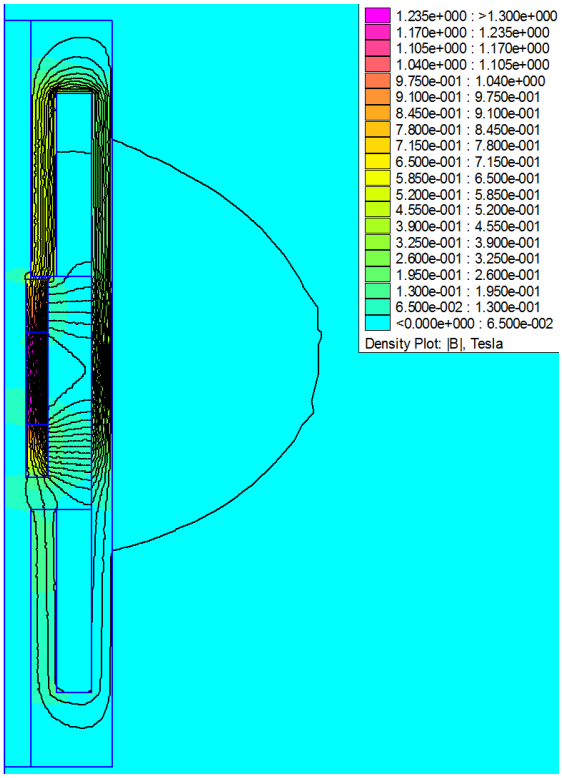

Figure 9: Magnetic field of the optimal actuator with no current in the coils.

The force constraints for *Fs* and *Fh* are active which can be expected when minimum energy consumption is required. The active constraint for *hw* is also expected because longer upper and lower cores size which respectively means longer coils will increase the leakage coil flux and corrupted coil efficiency.

5 CONTROL

The developed actuator has static force characteristics which are suitable for Braille screen application, as illustrated on Figure 10.

The employed approach has confirmed its robustness for solution to the optimization problem for the actuator. The obtained optimal solution satisfies the requirements for actuators for Braille screen. The presented variant of the linear electromagnetic actuator is energy efficient because of the impulse way of its work, (Balabozov, et al., 2012). All the three varied parameters influence the characteristics and especially the initial force, which is significant for these actuators.

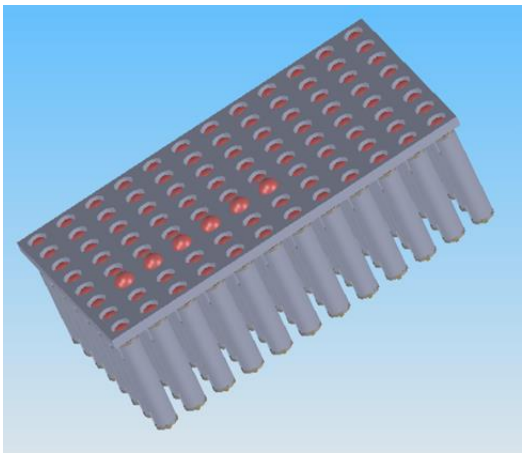

Figure 10: Braille screen with needles (dots) driven by linear actuators.

For better resolution of the graphical images the Braille screen must be larger, for example 96×64 linear micro drives (pixels). It is more than 6000 elements in human hand size with 4 coil connectors for each. In this case we need a strong electro-mechanical test of the entire circuit. We plan to use micro robots for positioning and testing, (Georgiev, et al., 2010; Genova, et al., 2010; Kotev, et al., 2011). We develop a smart micro robot with 3 DOF and piezo effectors, shown on Figure 11.

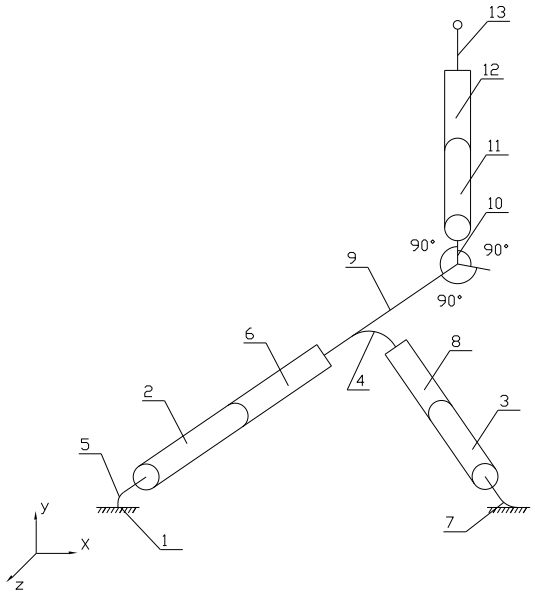

Figure 11: Micro manipulator with 3 degree of freedom and piezo effectors, where: 1 – base; 2, 3, 11 – mobile links; 4, 5, 7 – elastic connections; 6, 8, 12 – piezo actuators; 9, 10 – hard connections; 13 – sensing element.

6 CONCLUSION

Based on the results obtained the following conclusions can be drawn:

- The developed actuator has static force characteristics which are suitable for Braille screen application;
- Increasing the height of the coil has important influence on the force-displacement characteristics and the holding force. Above a certain value, thought, further increase does not lead to significant change;
- The maximal stroke influences more significantly the initial force than the holding one and its minimal value could be recommended;
- Higher outer diameter of the actuator leads to significant increase of both holding and initial force;
- Current density of 15 A/mm2 could ensure enough initial force at lower starting position of the mover.

ACKNOWLEDGEMENTS

The research work reported in the paper is partly supported by the project AComIn "Advanced Computing for Innovation", grant 316087, funded by the FP7 Capacity Programme (Research Potential of Convergence Regions).

REFERENCES

Balabozov I., I. Yatchev, K. Hinov, D. Karastoyanov, Influence of Different Factors on The Static Force Characteristics of a Permanent Magnet Linear Actuator for Braille Screen, *SIELA 2012*, May 28-30 2012, Bourgas, Bulgaria, vol. 2, 20–26.

Chaves D., I. Peixoto, A.C.O. Lima, M. Vieira, C. J. de Araujo, Microtuators of SMA for Braille display system. *IEEE International Workshop on Medical Measurements and Applications*. MeMeA 2009, 64–68.

Cho H. C., B. S. Kim, J. J. Park, J. B. Song, Development of a Braille Display using Piezoelectric Linear Motors. *International Joint Conference SICE-ICASE*, 2006, 1917–1921.

Hernandez H., E. Preza, R. Velazquez, Characterization of a Piezoelectric Ultrasonic Linear Motor for Braille Displays. *Electronics, Robotics and Automotive Mechanics Conference CERMA 2009*, 402–407.

Georgiev G., V. Kotev, T. Tiankov, Accuracy and calibration of micropositioning robotic Systems., *Journal ACTA Technica corviniensis – Bulletin of*

engineering, Fascicule 3, July – September, tome III, 2010, 125–130.

Genova P., V. Kotev, F. Ionescu, K. Kostadinov, Linkage mechanisms with piezo- structured ceramic actuators., *Proceedings of 2010 International Conference on Optimisation of the Robots and Manipulators*, Calimanesti, Romania, 28–30 May, 2010, 211–214.

Green S., B. Gregory, N. Gupta, Dynamic Braille Display Utilizing Phase-Change Microactuators. *5th IEEE Conference on Sensors*, 2006, 307–310.

Karastoyanov D., *Braille screen*, Bulgarian Patent announce No 110731, 10.08.2010.

Karastoyanov D., S. Simeonov, *Braille display*, Bulgarian Patent announce No 110794, 11.11.2010.

Karastoyanov D., S. Simeonov, A. Dimitrov, *Braille display*, Bulgarian Patent announce No 110795, 11.11.2010.

Karastoyanov D., I. Yachev, K. Hinov, T. Rachev, *Braille screen*, Bulgarian Patent announce No 111055, 13.10.2011.

Kato Y. et al., A flexible, lightweight Braille sheet display with plastic actuators driven by an organic field-effect transistor active matrix. IEEE International Electron Devices Meeting, 2005.

Kawaguchi Y., K. Ioi, Y. Ohtsubo, Design of new Braille display using inverse principle of tuned mass damper. *Proceedings of SICE Annual Conference 2010*, 379–383.

Kotev V., K. Kostadinov, P. Genova, Design of incurporated macro-micro robots for macro and micro operations., *8th Int. Conference on Informatics in Control, Automation And Robotics* (ICINCO 2011), 28-31 July 2011, Noordwijkerhout, The Netherlands. Proceedings ICINCO 2011, vol. 2, 2011, 273–276.

Kwon H.-J., S. W. Lee, S. S. Lee, Braille code display device with a PDMS membrane and thermopneumatic actuator. *21st IEEE International Conference on Micro Electro Mechanical Systems MEMS 2008*, 527–530.

Nobels T., F. Allemeersch, K. Hameyer, Design of a High Power Density Electromagnetic Actuator for a Portable Braille Display. *International Conference EPE-PEMC 2002*, Dubrovnik & Cavtat, 2002.

Yatchev I., D. Karastoyanov, Optimization of Permanent Magnet Linear Actuator for Braille Screen., *International Symposium IGTE 2012*, September 16-18, 2012, Graz, Austria, 59–63.

Yatchev I. et al. Finite element modelling of electromagnets for Braille screen. Proceedings of PES 2011 Conference, Nis, Serbia, 2011.

Yatchev I., et al. Force characteristics of an electromagnettic actuator for Braille screen, *Proceedings of International Conference on Electrical Machines, Drives and Power Systems ELMA 2011*, 21-22 October 2011, Varna, Bulgaria, 338–341.

Yatchev I. et al. Static force characteristics of electromagnetic actuators for Braille screen. *Facta Universitatis, Ser.: Elec. Energ.* vol. 24, No. 2, August 2011, 157–167.

Plane Wave Diffraction by a Thin Material Strip: Higher Order Asymptotics

Takashi Nagasaka, Kazuya Kobayashi
Department of Electrical, Electronic, and Communication Engineering, Chuo University
1-13-27 Kasuga, Bunkyo-ku, Tokyo 112-8551, Japan
glong169@gmail.com, kazuya@tamacc.chuo-u.ac.jp

Keywords: material strip, approximate boundary conditions, asymptotic expansion, radar cross section, Wiener-Hopf technique

Abstract: The plane wave diffraction by a thin material strip is analyzed using the Wiener-Hopf technique together with approximate boundary conditions. An asymptotic solution is obtained under the condition that the thickness and the width of the strip are small and large compared with the wavelength, respectively. The scattered field is evaluated asymptotically based on the saddle point method and a far field expression is derived. Scattering characteristics of the strip are discussed via numerical results of the radar cross section.

1 INTRODUCTION

The analysis of the scattering by material strips is an important subject in electromagnetic theory and radar cross section (RCS) studies. Volakis (1988) analyzed the plane wave diffraction by a thin material strip using the dual integral equation approach (Clemmow, 1951) and the extended spectral ray method (Herman and Volakis, 1987) together with approximate boundary conditions (Senior and Volakis, 1995). In his 1988 paper, Volakis first solved rigorously the diffraction problem involving a single material half-plane, and subsequently obtained a high-frequency solution to the original strip problem by superposing the singly diffracted fields from the two independent half-planes and the doubly/triply diffracted fields from the edges of the two half-planes. Therefore his analysis is mathematically not rigorous from the viewpoint of boundary value problems, and may not be applicable unless the strip width is relatively large compared with the wavelength.

In this paper, we shall consider the same problem as in Volakis (1988), and analyze the plane wave diffraction by a thin material strip for both H and E polarizations with the aid of the Wiener-Hopf technique. Analytical details are presented only for the H-polarized case, but numerical results will be shown for both H and E polarizations.

Introducing the Fourier transform of the scattered field and applying approximate boundary conditions in the transform domain, the problem is formulated in terms of the simultaneous Wiener-Hopf equations, which are solved exactly via the factorization and decomposition procedure. However, the solution is formal since branch-cut integrals with unknown integrands are involved. We shall further employ an asymptotic method established by Kobayashi (2013) to derive a high-frequency solution to the Wiener-Hopf equations, which is expressed in terms of an infinite asymptotic series and accounts for all the higher order multiple diffraction effects rigorously. It is shown that the higher-order multiple diffraction is explicitly expressed in terms of the generalized gamma function introduced by Kobayashi (1991). Our solution is valid for large strip width and requires numerical inversion of an appropriate matrix equation. The scattered field in the real space is evaluated asymptotically by taking the Fourier inverse of the solution in the tranform domain and applying the saddle point method. It is to be noted that our final solution is uniformly valid in incidence and observation angles. Numerical examples of the RCS are presented for various physical parameters and far field scattering characteristics of the strip are discussed in detail. Some comparisons with Volakis (1988) are also given. The results presented in this paper provide an important extension of our earlier analysis of the same problem (Koshikawa and Kobayashi, 2000; Nagasaka and Kobayashi, 2013).

The time factor is assumed to be $\mathrm{e}^{-\mathrm{i}\omega t}$ and suppressed throughout this paper.

2 FORMULATION OF THE PROBLEM

We consider the diffraction of an H-polarized plane wave by a thin material strip as shown in Fig. 1, where the relative permittivity and permeability of the strip are denoted by ε_r and μ_r, respectively. Let the total magnetic field $\phi^t(x,z)[\equiv H_y(x,z)]$ be

$$\phi^t(x,z) = \phi^i(x,z) + \phi(x,z), \tag{1}$$

where $\phi^i(x,z)$ is the incident field given by

$$\phi^i(x,z) = \mathrm{e}^{-\mathrm{i}k(x\sin\theta_0 + z\cos\theta_0)} \tag{2}$$

for $0 < \theta_0 < \pi/2$ with $k[=\omega(\varepsilon_0\mu_0)^{1/2}]$ being the free-space wavenumber. The term $\phi(x,z)$ in (1) is the unknown scattered field and satisfies the two-dimensional Helmholtz equation.

If the strip thickness is small compared with the wavelength, the material strip can be replaced by a strip of zero thickness satisfying the second order impedance boundary conditions (Senior and Volakis, 1995). Then the total electromagnetic field satisfies the approximate boundary conditions as given by

$$\Big[E_z(+0,z) + E_z(-0,z)\Big] - 2R_e\Big[H_y(+0,z) - H_y(-0,z)\Big] = 0, \tag{3}$$

$$\left[\frac{1}{2R_m} + \frac{1}{2\tilde{R}_e}\left(1 + \frac{1}{k^2}\frac{\partial^2}{\partial x^2}\right)\right]\cdot\Big[H_y(+0,z) + H_y(-0,z)\Big] - \Big[E_z(+0,z) - E_z(-0,z)\Big] = 0, \tag{4}$$

where

$$\left.\begin{aligned} R_e &= \mathrm{i}Z_0 / \Big[kb(\varepsilon_r - 1)\Big], \\ \tilde{R}_e &= \mathrm{i}\varepsilon_r Y_0 / \Big[kb(\varepsilon_r - 1)\Big], \\ R_m &= \mathrm{i}Y_0 / \Big[kb(\mu_r - 1)\Big] \end{aligned}\right\} \tag{5}$$

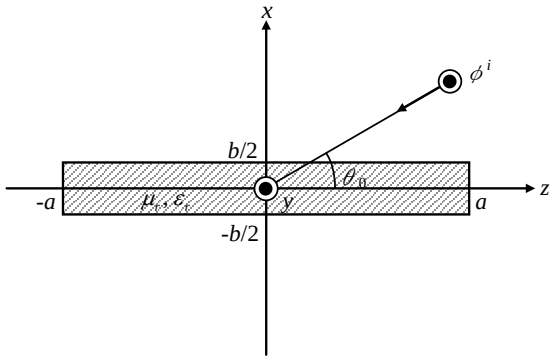

Figure 1: Geometry of the problem.

with Z_0 and Y_0 being the intrinsic impedance and admittance of free space, respectively. In the following, we shall assume that the medium is slightly lossy as in $k = k_1 + \mathrm{i}k_2$ with $0 < k_2 \ll k_1$. The solution for real k is obtained by letting $k_2 \to +0$ at the end of analysis.

In view of the radiation condition, it follows that

$$\phi(x,z) = O(\mathrm{e}^{-k_2|z|\cos\theta_0}) \tag{6}$$

as $|z| \to \infty$. We define the Fourier transform $\Phi(x,\alpha)$ of the scattered field $\phi(x,z)$ with respect to z as

$$\Phi(x,\alpha) = (2\pi)^{-1/2}\int_{-\infty}^{\infty}\phi(x,z)\,\mathrm{e}^{\mathrm{i}\alpha z}\,\mathrm{d}z, \tag{7}$$

where $\alpha(\equiv \mathrm{Re}\,\alpha + \mathrm{i}\,\mathrm{Im}\,\alpha) = \sigma + \mathrm{i}\tau$. Then we see that $\Phi(x,\alpha)$ is regular in the strip $|\tau| < k_2\cos\theta_0$ of the α-plane. Introducing the Fourier integrals as

$$\Phi_{\pm}(x,\alpha) = \pm(2\pi)^{-1/2}\int_{\pm a}^{\pm\infty}\phi(x,z)\,\mathrm{e}^{\mathrm{i}\alpha(z\mp a)}\,\mathrm{d}z, \tag{8}$$

$$\Phi_1(x,\alpha) = (2\pi)^{-1/2}\int_{-a}^{a}\phi(x,z)\,\mathrm{e}^{\mathrm{i}\alpha a}\,\mathrm{d}z, \tag{9}$$

it follows that $\Phi_+(x,\alpha)$ and $\Phi_-(x,\alpha)$ are regular in the half-planes $\tau > -k_2\cos\theta_0$ and $\tau < k_2\cos\theta_0$, respectively, whereas $\Phi_1(x,\alpha)$ is an entire function. In view of the notation as given by (8) and (9), $\Phi(x,\alpha)$ is expressed as follows:

$$\Phi(x,\alpha) = \mathrm{e}^{-\mathrm{i}\alpha a}\Phi_-(x,\alpha) + \Phi_1(x,\alpha) + \mathrm{e}^{\mathrm{i}\alpha a}\Phi_+(x,\alpha). \tag{10}$$

Taking the Fourier transform of the two-dimensional Helmholtz equation, we find that

$$\Big(\mathrm{d}^2/\mathrm{d}x^2 - \gamma^2\Big)\Phi(x,\alpha) = 0 \tag{11}$$

for any α in $|\tau| < k_2\cos\theta_0$, where $\gamma = (\alpha^2 - k^2)^{1/2}$. Since γ is a double-valued function of α, we choose a proper branch of γ such that γ reduces to $-\mathrm{i}k$ when $\alpha = 0$. According to the choice of this branch, we can show that $\mathrm{Re}\,\gamma > 0$ for any α in the strip $|\tau| < k_2$. Equation (11) is the transformed wave equation. Solving (11) and applying the boundary conditions, we derive, after some manipulations, that

$$-M(\alpha)J_m(\alpha) = \mathrm{e}^{-\mathrm{i}\alpha a}U_-(\alpha) + \mathrm{e}^{\mathrm{i}\alpha a}U_{(+)}(\alpha), \tag{12}$$

$$-K(\alpha)J_e(\alpha) = 2\Big[\mathrm{e}^{-\mathrm{i}\alpha a}V_-(\alpha) + \mathrm{e}^{\mathrm{i}\alpha a}V_{(+)}(\alpha)\Big], \tag{13}$$

where

$$M(\alpha)=1-\frac{\mathrm{i}kY_0}{2\gamma}\left[\frac{1}{R_m}+\frac{1}{\tilde{R}_e}\left(1+\frac{\gamma^2}{k^2}\right)\right], \quad (14)$$

$$K(\alpha)=\gamma-2\mathrm{i}kY_0R_e, \quad (15)$$

$$U_{(\pm)}(\alpha)=\tilde{\Phi}_{\pm}(\alpha)\mp\frac{A_{1,2}}{\alpha-k\cos\theta_0}, \quad (16)$$

$$V_{(\pm)}(\alpha)=\Phi'_{\pm}(\alpha)\mp\frac{B_{1,2}}{\alpha-k\cos\theta_0}, \quad (17)$$

$$J_m(\alpha)=\frac{\mathrm{i}}{\omega\varepsilon_0}\left[\frac{\mathrm{d}\Phi_1(+0,\alpha)}{\mathrm{d}x}-\frac{\mathrm{d}\Phi_1(-0,\alpha)}{\mathrm{d}x}\right], \quad (18)$$

$$J_e(\alpha)=\Phi_1(+0,\alpha)-\Phi_1(-0,\alpha) \quad (19)$$

with

$$\tilde{\Phi}_{\pm}(\alpha)=\left(\frac{1}{R_m}+\frac{1}{\tilde{R}_e}\right)\Phi_{\pm}(0,\alpha)+\frac{1}{\tilde{R}_e k^2}\frac{\mathrm{d}^2\Phi_{\pm}(0,\alpha)}{\mathrm{d}x^2}, \quad (20)$$

$$\Phi'_{\pm}(\alpha)=\frac{\mathrm{d}\Phi_{\pm}(0,\alpha)}{\mathrm{d}x}, \quad (21)$$

$$A_{1,2}=\frac{1}{(2\pi)^{1/2}\mathrm{i}}\left(\frac{1}{R_e}+\frac{\cos^2\theta_0}{\tilde{R}_m}\right)\mathrm{e}^{\mp\mathrm{i}ka\cos\theta_0}, \quad (22)$$

$$B_{1,2}=-\frac{k\sin\theta_0}{(2\pi)^{1/2}}\mathrm{e}^{\mp\mathrm{i}ka\cos\theta_0}. \quad (23)$$

Equations (12) and (13) are the Wiener-Hopf equations satisfied by unknown spectral functions, where $U_{(+)}(\alpha)$ and $V_{(+)}(\alpha)$ are regular in the upper half-plane $\tau>-k_2\cos\theta_0$ except for a simple pole at $\alpha=k\cos\theta_0$.

3 FACTORIZATION OF THE KERNEL FUNCTIONS

The solutions of (12) and (13) require factorization of the kernel functions defined by (14) and (15) in the form

$$M(\alpha)=M_+(\alpha)M_-(\alpha)=M_+(\alpha)M_+(-\alpha), \quad (24)$$

$$K(\alpha)=K_+(\alpha)K_-(\alpha)=K_+(\alpha)K_+(-\alpha). \quad (25)$$

In order to factorize (14) and (15), let us introduce the auxiliary functions $N_n(\alpha)$ for $n=1,2,3$ as

$$N_n(\alpha)=N_{n+}(\alpha)N_{n-}(\alpha)=1+\frac{\mathrm{i}}{k\delta_n}\gamma, \quad (26)$$

where

$$\delta_{1,2}=-\frac{\tilde{R}_e}{Y_0}\left[1\pm\left(1+Y_0^2\frac{\tilde{R}_e+R_m}{R_m\tilde{R}_e^2}\right)^{1/2}\right], \quad (27)$$

$$\delta_3=2Y_0R_e. \quad (28)$$

Substituting (26) into (14) and (15), it follows that

$$M(\alpha)=\frac{kY_0}{\mathrm{i}\gamma}\left(\frac{\tilde{R}_e+R_m}{2\tilde{R}_eR_m}\right)N_1(\alpha)N_2(\alpha), \quad (29)$$

$$K(\alpha)=-2\mathrm{i}kY_0R_eN_3(\alpha). \quad (30)$$

Applying the method developed by Noble (1958), $N_n(\alpha)$ for $n=1,2,3$ are factorized as

$$\begin{aligned}N_{n\pm}(\alpha)=&\left(1+\delta_n^{-1}\right)^{1/2}\\&\cdot\exp\left\{-\frac{\delta_n}{\pi}\int_{\pi/2}^{\arccos(\pm\alpha/k)}\frac{t\cos t}{\sin^2 t-\delta_n^2}\mathrm{d}t\right.\\&\pm\frac{\mathrm{i}}{2\pi}\ln\left[\delta_n+(\delta_n^2-1)^{1/2}\right]\\&\cdot\ln\left[\frac{\mathrm{i}k(\delta_n^2-1)^{1/2}+\alpha}{\mathrm{i}k(\delta_n^2-1)^{1/2}-\alpha}\right]\\&\left.+\frac{1}{4}\ln\left[1+\frac{\alpha^2}{k^2(\delta_n^2-1)}\right]\right\}.\end{aligned} \quad (31)$$

From (29)-(31), we find that the split functions $M_{\pm}(\alpha)$ and $K_{\pm}(\alpha)$ are expressed as follows:

$$M_{\pm}(\alpha)=\left[\frac{kY_0(\tilde{R}_e+R_m)}{2\tilde{R}_eR_m}\right]^{1/2}\frac{N_{1\pm}(\alpha)N_{2\pm}(\alpha)}{(k\pm\alpha)^{1/2}}, \quad (32)$$

$$K_{\pm}(\alpha)=(2kY_0R_e)^{1/2}\,\mathrm{e}^{-\mathrm{i}\pi/4}\,N_{3\pm}(\alpha). \quad (33)$$

4 FORMAL SOLUTION

Multiplying both sides of (13) by $\mathrm{e}^{\pm\mathrm{i}\alpha a}/K_{\mp}(\alpha)$ and applying the decomposition procedure with the aid of the edge condition, we derive, after some manipulations, that

$$\begin{aligned}&\frac{V^{s,d}_{(+)}(\alpha)}{K_+(\alpha)}+\frac{B_1}{K_+(k\cos\theta_0)(\alpha-k\cos\theta_0)}\\&\mp\frac{1}{2\pi\mathrm{i}}\int_{-\infty+\mathrm{i}c}^{\infty+\mathrm{i}c}\frac{\mathrm{e}^{2\mathrm{i}\beta a}V^{s,d}_{(+)}(\beta)}{K_-(\beta)(\beta+\alpha)}\mathrm{d}\beta=0,\end{aligned} \quad (34)$$

where c is a constant such that $0<|\tau|<c<k_2\cos\theta_0$, and

$$V^{s,d}_{(+)}(\alpha)=V_{(+)}(\alpha)\pm V_-(-\alpha). \quad (35)$$

It is verified from (17), (33), and (35) that the singularities associated with the integral in (34) for $\mathrm{Im}\,\beta>c$ are a simple pole at $\beta=k\cos\theta_0$ and a branch point at $\beta=k$. We now choose a branch cut emanating from $\beta=k$ as a straight line that is parallel to the imaginary axis and goes to infinity in

the upper half-plane. Evaluating the integral by enclosing the contour into the upper half-plane, we derive that

$$V_{(+)}^{s,d}(\alpha)=K_+(\alpha)\Bigg[-\frac{B_1}{K_+(k\cos\theta_0)(\alpha-k\cos\theta_0)} \mp\frac{B_2}{K_-(k\cos\theta_0)(\alpha+k\cos\theta_0)}\pm v_{s,d}(\alpha)\Bigg], \quad (36)$$

where

$$v_{s,d}(\alpha)=\frac{1}{\pi\mathrm{i}}\int_k^{k+\mathrm{i}\infty}\frac{\mathrm{e}^{2\mathrm{i}\beta a}(\beta-k)^{1/2}}{\beta+\alpha} \cdot V_{(+)}^{s,d}(\beta)T_+(\beta)\mathrm{d}\beta, \quad (37)$$

$$T_+(\beta)=\frac{(\beta+k)^{1/2}K_+(\beta)}{\beta^2-k^2+4k^2Y_0^2R_e^2}. \quad (38)$$

Equation (36) provides the exact solution to the Wiener-Hopf equation (13), but it is formal in the sense that the branch-cut integrals $v_{s,d}(\alpha)$ with unknown integrands are involved.

Equation (12) can be solved in a similar manner, but the solution will not be discussed here. In the next section, we shall derive explicit high-frequency solutions to the Wiener-Hopf equations.

5 HIGH-FREQUENCY ASYMPTOTIC SOLUTION

In order to eliminate the singularities of $V_{(+)}^{s,d}(\alpha)$ at $\alpha=k\cos\theta_0$, we introduce

$$\Phi_+'^{s,d}(\alpha)=\Phi_+'(\alpha)\pm\Phi_-'(-\alpha). \quad (39)$$

Then (36) can be written in the following form:

$$\Phi_+'^{s,d}(\alpha)=K_+(\alpha)\Bigg[\chi_{s,d}^v(\alpha)+\frac{C_{s,d}}{\pi\mathrm{i}} \cdot\int_k^{k+\mathrm{i}\infty}\frac{\mathrm{e}^{2\mathrm{i}\beta a}(\beta-k)^{1/2}}{\beta+\alpha}\Phi_+'^{s,d}(\beta)T_+(\beta)\mathrm{d}\beta\Bigg]. \quad (40)$$

In (40), several quantities are defined by

$$\chi_{s,d}^v(\alpha)=B_1\Bigg[Q_1(\alpha)\pm\sum_{n=0}^{\infty}T_n\eta_{2n}(\alpha)\Bigg] \pm B_2\Bigg[Q_2(\alpha)\pm\sum_{n=0}^{\infty}T_n\eta_{1n}(\alpha)\Bigg], \quad (41)$$

$$C_{s,d}=\pm1 \quad (42)$$

with

$$T_n=\left.\frac{T_+^{(n)}(\beta)}{n!}\right|_{\beta=k}, \quad (43)$$

$$Q_{1,2}(\alpha)=\frac{K_+^{-1}(\alpha)-K_\pm^{-1}(k\cos\theta_0)}{\alpha\mp k\cos\theta_0}, \quad (44)$$

$$\eta_{1n,2n}(\alpha)=\frac{\xi_{0n}^{1/2}(\alpha)-\xi_{0n}^{1/2}(\pm k\cos\theta_0)}{\alpha\mp k\cos\theta_0}, \quad (45)$$

$$\xi_{pn}^{1/2}(\alpha)=\frac{\mathrm{e}^{\mathrm{i}[2ka+(\pi/2)(n-p-1/2)]}}{\pi(2a)^{1/2+n-p}}(-1)^p\,p! \cdot\Gamma_{p+1}\big(3/2+n,-2\mathrm{i}(\alpha+k)a\big). \quad (46)$$

In (46), $\Gamma_{p+1}(\cdot,\cdot)$ is the generalized gamma function (Kobayashi , 1991) defined by

$$\Gamma_m(u,v)=\int_0^\infty\frac{t^{u-1}\,\mathrm{e}^{-t}}{(t+v)^m}\mathrm{d}t \quad (47)$$

for $\mathrm{Re}\,u>0,|v|>0,|\arg v|<\pi$, and positive integer m. Applying the method established by Kobayashi (2013) to the integral in (36), we can obtain a high-frequency asymptotic expansion of (36) with the result that

$$T_+(\alpha)\Phi_+'^{s,d}(\alpha)\sim T_+(\alpha)K_+(\alpha) \cdot\Bigg[\chi_{s,d}^v(\alpha)+C_{s,d}\sum_{n=0}^{\infty}f_n^{vs,vd}\xi_{0n}^{1/2}(\alpha)\Bigg] \quad (48)$$

for $ka\to\infty$, where

$$f_n^{vs,vd}=\frac{1}{n!}\left.\frac{\mathrm{d}^n\left[T_+(\alpha)\Phi_+'^{s,d}(\alpha)\right]}{\mathrm{d}\alpha^n}\right|_{\alpha=k}. \quad (49)$$

We can show that the unknowns $f_n^{vs,vd}$ for $n=0,1,2,\cdots$ in (48) satisfy the system of linear algebraic equations as in

$$f_m^{vs,vd}-C_{s,d}\sum_{n=0}^{\infty}A_{mn}^v f_n^{vs,vd}\sim B_m^{vs,vd} \quad (50)$$

for $m=0,1,2,\cdots$, where

$$A_{mn}^v=\sum_{p=0}^{m}\frac{h^{(m-p)}(k)\xi_{pn}^{1/2}(k)}{p!(m-p)!}, \quad (51)$$

$$B_m^{vs,vd}=\sum_{p=0}^{m}\frac{h^{(m-p)}(k)g_{vs,vd}^{(p)}(k)}{p!(m-p)!}, \quad (52)$$

$$h^{(m-p)}(k)=\left.\frac{\mathrm{d}^{m-p}\left[T_+(\alpha)K_+(\alpha)\right]}{\mathrm{d}\alpha^{m-p}}\right|_{\alpha=k}, \quad (53)$$

$$g_{vs,vd}^{(p)}(k)=\left.\frac{\mathrm{d}^p\chi_{s,d}^v(\alpha)}{\mathrm{d}\alpha^p}\right|_{\alpha=k}. \quad (54)$$

Equation (48) together with the matrix equations (50) provides a high-frequency asymptotic solution of (40) for the strip width large compared with the wavelength. Making use of the above results and

carrying out further manipulations, we finally arrive at an explicit asymptotic solution to the Wiener-Hopf equation with the result that

$$V_{(+)}^{s,d}(\alpha) \sim K_+(\alpha)\Bigg\{-\frac{B_1}{K_+(k\cos\theta_0)(\alpha - k\cos\theta_0)} \mp \frac{B_2}{K_-(k\cos\theta_0)(\alpha + k\cos\theta_0)} \pm \sum_{n=0}^{\infty} T_n\left[B_1\eta_{2n}(\alpha) \pm B_2\eta_{1n}(\alpha)\right] \pm \sum_{n=0}^{\infty} f_n^{vs,vd}\xi_{0n}^{1/2}(\alpha)\Bigg\} \quad (55)$$

as $ka \to \infty$. It is to be noted that this solution rigorously takes into account the multiple diffraction between the edges of the strip. A similar procedure may also be applied to (12) for a high-frequency solution but the details will not be discussed here.

6 SCATTERED FAR FIELD

Using the boundary condition, the scattered field in the Fourier transform domain is expressed as

$$\Phi(x,\alpha) = \tilde{\Phi}(\alpha)\,\mathrm{e}^{-\gamma|x|}, \quad (56)$$

where

$$\tilde{\Phi}(\alpha) = -\frac{\mathrm{i}kY_0\left[\mathrm{e}^{-\mathrm{i}\alpha a}\,U_-(\alpha) + \mathrm{e}^{\mathrm{i}\alpha a}\,U_{(+)}(\alpha)\right]}{2\gamma M(\alpha)} \mp \frac{\mathrm{e}^{-\mathrm{i}\alpha a}\,V_-(\alpha) + \mathrm{e}^{\mathrm{i}\alpha a}\,V_{(+)}(\alpha)}{K(\alpha)}, \quad x \gtrless 0. \quad (57)$$

The scattered field in the real space is obtained by taking the inverse Fourier transform of (56) according to the formula

$$\phi(x,z) = (2\pi)^{-1/2}\int_{-\infty+\mathrm{i}c}^{\infty+\mathrm{i}c} \tilde{\Phi}(\alpha)\,\mathrm{e}^{-\gamma|x| - \mathrm{i}\alpha z}\,\mathrm{d}\alpha, \quad (58)$$

where c is constant such that $|c| < k_2\cos\theta_0$. We introduce the cylindrical coordinate (ρ,θ) centered at the origin as

$$x = \rho\sin\theta, \quad z = \rho\cos\theta \quad (59)$$

for $0 < |\theta| < \pi$. Then a far field expression of (58) can be derived with the aid of the saddle point method, leading to

$$\phi(\rho,\theta) \sim \tilde{\Phi}(-k\cos\theta)k\sin|\theta| \cdot \frac{\mathrm{e}^{\mathrm{i}(k\rho - \pi/4)}}{(k\rho)^{1/2}}, \quad x \gtrless 0 \quad (60)$$

as $k\rho \to \infty$. Equation (60) is uniformly valid for arbitrary incidence and observation angles.

7 NUMERICAL RESULTS AND DISCUSSION

We shall now present numerical results on the RCS for both H and E polarizations, and discuss far field scattering characteristics of the strip in detail. The normalized RCS per unit length is defined by

$$\sigma / \lambda = \lim_{\rho\to\infty}\left(k\rho\left|\phi / \phi^i\right|^2\right) \quad (61)$$

with λ being the free-space wavelength.

Figures 2 shows the bistatic RCS as a function of observation angle θ, where the width and the thickness of the strip are taken as $2a = 2\lambda, 7\lambda$ and $b = 0.05\lambda$, respectively. In numerical computation, we have chosen the ferrite with $\varepsilon_r = 2.5 + \mathrm{i}1.25$, $\mu_r = 1.6 + \mathrm{i}0.8$ as an example of existing lossy materials. The incident angle θ_0 is fixed as 60°. It is seen from the figure that the RCS shows noticeable peaks along the reflected $(\theta = 120^\circ)$ and incident $(\theta = -120^\circ)$ shadow boundaries. We also notice that the RCS exhibits sharp oscillation with an increase of the strip width as can be expected. Comparing the RCS characteristics between H and E polarizations, we observe that the RCS level for H polarization is lower than that for E polarization in the reflection region $(0^\circ < \theta < 180^\circ)$ but the results for both polarizations show close features in the shadow region $(-180^\circ < \theta < 0^\circ)$.

Figure 3 shows the monostatic RCS versus incidence angle θ_0, where the same parameters as in Fig. 2 have been chosen for computation. We see from the figure that the RCS level for H polarization is lower than that for E polarization except in the neighbourhood of the specular reflection direction at $\theta_0 = 90^\circ$. Figure 4 shows comparison with the results obtained by Volakis (1988), where the strip dimension is $2a = 2\lambda$, $b = 0.05\lambda$, and the material parameters are $\varepsilon_r = 1.5 + \mathrm{i}0.1$, $\mu_r = 4.0 + \mathrm{i}0.4$. It is seen from the figure that our results agree well with Volakis's results over $45^\circ < \theta_0 < 90^\circ$, but there are some discrepancies for $0^\circ < \theta_0 < 45^\circ$. These discrepancies are perhaps due to the fact that Volakis's solution is constructed based on the solutions for the two independent half-planes and becomes less accurate at relatively low frequencies $(2a = 2\lambda)$.

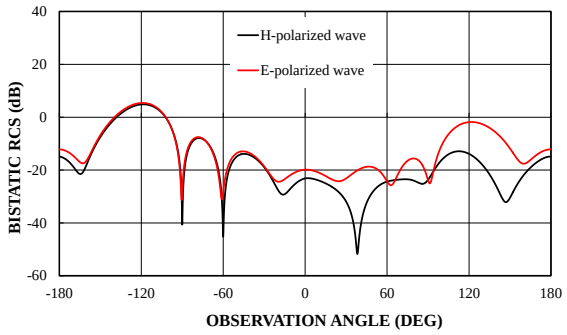

(a) $2a = 2\lambda$.

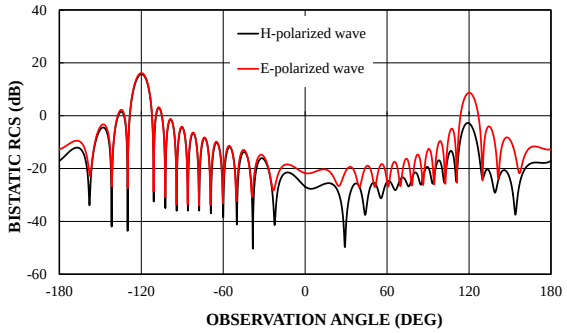

(b) $2a = 7\lambda$.

Figure 2: Bistatic RCS versus observation angle for $\theta_0 = 60^\circ, b = 0.05\lambda, \varepsilon_r = 2.5 + \mathrm{i}1.25, \mu_r = 1.6 + \mathrm{i}0.8$.

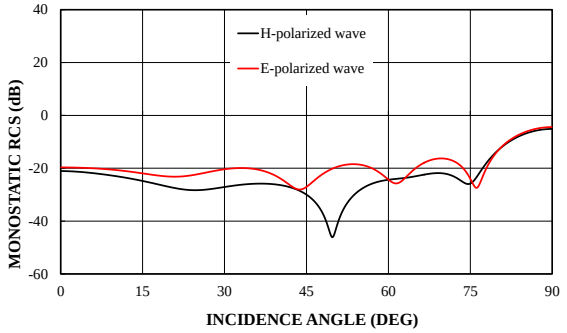

(a) $2a = 2\lambda$.

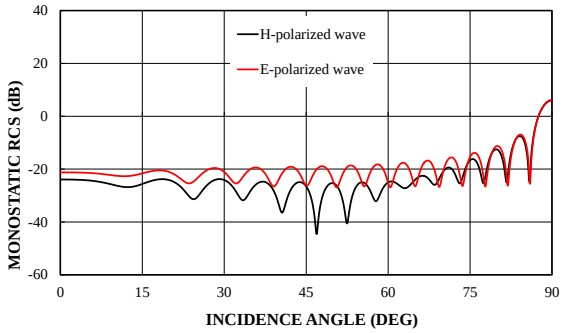

(b) $2a = 7\lambda$.

Figure 3: Monostatic RCS versus incidence angle for $b = 0.05\lambda, \varepsilon_r = 2.5 + \mathrm{i}1.25, \mu_r = 1.6 + \mathrm{i}0.8$.

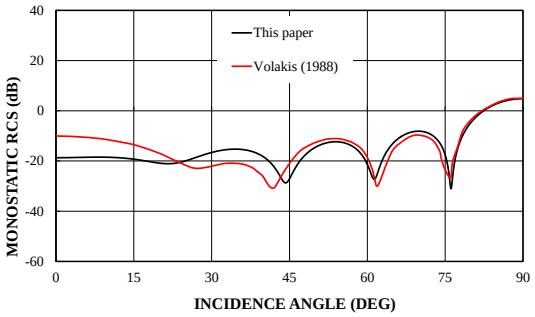

Figure 4: Monostatic RCS versus incidence angle for H polarization, $2a = 2\lambda$, $b = 0.05\lambda$, $\varepsilon_r = 1.5 + \mathrm{i}0.1$, $\mu_r = 4.0 + \mathrm{i}0.4$ and its comparison with Volakis (1988).

8 CONCLUSIONS

In this paper, we have analyzed the plane wave diffraction by a thin material strip for both H and E polarizations using the Wiener-Hopf technique and approximate boundary conditions. Employing a rigorous asymptotics, a high-frequency solution for large strip width has been obtained. Illustrative numerical examples on the RCS are presented, and far field scattering characteristics of the strip have been discussed in detail. Some comparisons with the other existing method have also been provided.

REFERENCES

Volakis, J. L. (1988). High-frequency scattering by a thin material half plane and strip. *Radio Science*, 23, 450-462.

Clemmow, P. C. (1951). A method for the exact solution of a class of two-dimensional diffraction problems. *Proc. R. Soc. London, Series A*, 205, 286-308.

Herman, M. I. and Volakis, J. L. (1987). High-frequency scattering by a resistive strip and extensions to conductive and impedance strips. *Radio Science*, 22, 335-349.

Senior, T. B. A. and Volakis, J. L. (1995). *Approximate Boundary Conditions in Electromagnetics*, London: IEE.

Kobayashi, K. (2013). Solutions of wave scattering problems for a class of the modified Wiener-Hopf geometries. *IEEJ Transactions on Fundamentals and Materials*, 133, 233-241 (*invited paper*).

Kobayashi, K. (1991). On generalized gamma functions occurring in diffraction theory. *J. Phys. Soc. Japan*, 60, 1501-1512.

Koshikawa, S. and Kobayashi, K. (2000). Wiener-Hopf analysis of the high-frequency diffraction by a thin material strip. *Proc. ISAP 2000*, 149-152.

Nagasaka, T. and Kobayashi, K. (2013). Wiener-Hopf analysis of the diffraction by a thin material strip. *PIERS 2013 Stockholm Abstracts*, 804.

Noble, B. (1958). *Methods Based on the Wiener-Hopf Technique for the Solution of Partial Differential Equations*, London: Pergamon.

Agricultural Drought Monitoring Using Satellite-Based Products in Romania

Gheorghe Stancalie[1], Argentina Nertan[1] , and Florin Serban[2]
[1]*National Meteorological Administration, 97 Sos. Bucuresti-Ploiesti, Bucharest, Romania*
[2]*Advanced Studies and Research Center, 4, Verii street, Bucharest, Romania*
{gheorghe.stancalie, argentina.nertan}@meteoromania.ro, florin.serban@asrc.ro

Keywords: agricultural drought, satellite, vegetation indices.

Abstract: In Romania, the complex agricultural drought is a climatic hazard inducing the worst consequences ever occurred in agriculture. The paper presents the results of recent studies developed in the National Meteorological Administration, in the framework of national and European R&D projects, regarding the use of satellite-derived products for agricultural drought monitoring. In this respect, different vegetation indices, biophysical parameters and physically-based vegetation state indicators have been used and tested in study areas over Romania, in order to monitor and assess the drought impact on crops, at different phenological dates. The main sources of satellite data and related products were provided by TERRA/AQUA-Modis, SPOT-Vegetation and Landsat TM/ETM+. By examining spatial and temporal patterns of satellite-derived products and comparing/correlating with the field conditions measured on site, it was determined that the NDVI, NDWI and NDDI vegetation indices, the leaf area index (LAI) and the fraction of absorbed photosynthetical active radiation (fAPAR) proved to be good indicators of the vegetation condition and relevant for the settlement, duration and intensity of the agricultural drought.

1 INTRODUCTION

Among the problems Europe is facing at the beginning of the third millennium, the reduction of water resources, their degrading quality and the occurrence of ever more severe and frequent droughts are of crucial importance.

In Romania, the complex agricultural drought is a climatic hazard phenomenon inducing the worst consequences ever occurred in agriculture.

The most frequent, the agricultural areas in Romania are affected by drought (7 mil. ha), water erosion and landslides (6.4 mil. ha), temporary water excess (4 mil. ha.) and compaction (2.8 mil. ha). Drought is the limiting factor affecting the widest surface as regards the crops. The area subjected to desertification, characterized by an arid, semi-arid or dry sub humid climate is around 30% of the total surface of Romania, being mostly situated in the South-Eastern (Dobrogea), Eastern (Moldavia), Southern parts of the Romanian Plain and in the Western Plain. These areas are prevailingly used for agriculture (around 80% of the total, 60% of which is arable land) (Romanian Ministry of Agriculture and Rural Development, 2008).

In the extremely droughty years the drought phenomenon may engulf the whole Romania's territory, as it happened more recently in 2000, 2003 and 2007. Large precipitation deficits were recorded in 1907, 1924, 1928, 1934, 1945, 1946, 1948, 1953, 1982 and 1983, then in 1992 and 1993 and more recently in 2000, 2001, 2003, 2007, 2009 and 2011.

In Romania, the use of remote sensing data in agriculture is a quickly developing and promising trend. For a better operative surveillance of the agricultural areas, starting with 2005, the Romanian National Meteorological Administration has implemented a dedicated service based on satellite-derived products. The satellite geoinformation products, elaborated by the Remote Sensing and GIS Lab, are included and analysed in the weekly Agrometeorological Bulletin issued by the Agrometeorological Laboratory.

2 SATELLITE DATA USED

The main sources of satellite data which have been used are TERRA/AQUA-Modis, SPOT-Vegetation and Landsat TM/ETM+. Due to cloudiness, most of the satellite products are averaged in time, producing composites based on data from periods of 8-16 days.

The MODIS instrument is one a key instruments onboard the US satellites of the EOS series (Terra and Aqua). The bands most applicable for rangeland studies are bands 1-7 that gather data in the visible and infrared range at a 250 m and 500 m spatial resolution.

The SPOT VEGETATION S10 product (ten days synthesis) with 1 km- resolution is composed by merging atmospherically corrected segments (data strips) acquired over a ten days interval. All the segments of this period (decade) are compared again pixel by pixel to pick out the 'best' ground reflectance values.

PROBA-V is a new ESA satellite mission, launched in May 2013, with the main task of mapping land cover and vegetation growth across the Earth every two days. This mission is extending the data set of the long-established SPOT Vegetation, but with an improved 350m spatial resolution.

The LANDSAT TM/ETM+ imagery is a unique resource for global change research and applications in agriculture. The main ETM+ image features are: a panchromatic band with a 15 m-spatial resolution (band 8); visible (reflected light) bands in the spectrum of blue, green, red, near-infrared (NIR), and mid-infrared (MIR) with a 30 m-spatial resolution (bands 1-5, 7); a thermal infrared channel with a 60 m-spatial resolution (band 6).

3 AGRICULTURAL DROUGHT MONITORING USING SATELLITE-BASED RODUCTS

3.1 The vegetation indices

The vegetation indices (VIs) are among the most commonly used satellite data products for the evaluation, monitoring, and measurement of vegetation cover, condition, biophysical processes, and change. They have been used for over last decades in a broad variety of applications, including monitoring the effects of drought over regional, national, and even multinational areas (Basso et al., 2004). The VIs are an important tool for drought monitoring and evaluation because of the accurate discrimination of vegetation and correlations with biophysical parameters which determine the vegetation state.

The most important VIs for vegetation monitoring include the "broadband greenness" category (e.g.: Normalized Difference Vegetation Index - NDVI, Soil Adjusted Vegetative Index - SAVI, Enhanced Vegetation Index - EVI, etc) and the "canopy water content" category (e.g.: Normalized Difference Water Index - NDWI, Normalized Difference Drought Index – NDDI, etc) (Gu et al., 2007; Huete, 1997; Penuelas, 1995).

3.1.1 The Normalized Difference Vegetation Index (NDVI)

The NDVI is one of the most well known and most frequently used vegetation indices, being considered as a measure of the amount and vigour of vegetation. The combination of its normalized difference formulation and use of the highest absorption and reflectance regions of chlorophyll make it robust over a wide range of conditions (GU et Al., 2007; Peters et al., 2002). The value of NDVI ranges from -1 to 1. The common range for green vegetation is 0.2 to 0.8.

The NDVI values have been used in correlations with various meteorological parameters. For example, figure 1 shows a good correlation between the SPOT Vegetation 10 days synthesis NDVI values and the precipitation, over the study area situated in the lower basin of the Mures River, located in the Western part of Romania (Pecica agricultural area). In this agricultural area the sun flower and oats crops were identified on the Landsat ETM+ satellite image (and validated by GPS ground measurements); the precipitation values were recorded at Arad weather station, the closest to the study area. The analysis covers periods from March to June 2011.

Figure 2 reveals that in the period 6.03 - 6.04.2003, the NDVI values were lower, compared to the rest, mainly because of the lack of precipitation in March which have caused a delay of the vegetation season start. The NDVI time series analysis is very important for the crop state monitoring. Such a complex analysis was made using MODIS/TERRA NDVI products (MOD13A1) for the following years: 2000 and 2003 (as drought years), 2005 (as normal year) and 2010 (as rainy year) and for different vegetation phases. The year 2010, on the other hand, presents greater NDVI values due to high amount of precipitation. The

NDVI maps show a rather equal set of values between the four years, with a slight grow in 2005 and 2010 compared to 2000 and 2003 for the periods: from the 7th of April to the 8th of May and from the 9th of May to the 9th of June.

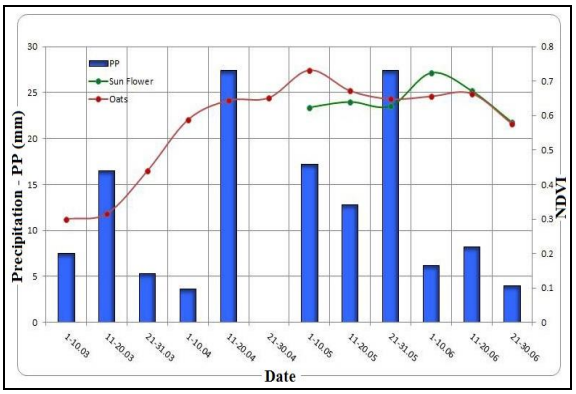

Figure 1: The correlation between NDVI (extracted from SPOT Vegetation) and precipitation (recorded at Arad weather station) for the sun flower and oats crops, in the study area situated in the lower basin of the Mures River, in the Western part of Romania.

Only during the last vegetation phenological phase a visible difference occurs between 2000 and 2003 on one hand, and between 2005 and 2010 on the other hand. The analysis clearly shows the effect of low precipitation and high temperatures in 2000 and 2003 (very droughty years) over the agricultural areas.

The NDVI-based analysis for crop state monitoring was also performed using high-resolution satellite images, such as LANDSAT TM/ETM+ data (Jackson, 2007). Figure 3 presents an example of using LANDSAT TM/ETM+ data for 14.08.2003, 22.08.2006 and 17.08.2010, in the same study area, located in the Western part of Romania.

The figure 3a shows a "hot-spot" area, associated with very low NDVI values (pixels in orange and red), in the central-eastern part of the image acquired on 14.08.2003 (up left image) and normal NDVI values in the other 2 images acquired on 22.08.2006 and on 17.08.2010, respectively. In order to isolate only the parts affected by drought a "low-vegetation" NDVI threshold was applied to highlight only two classes (figure 3b).

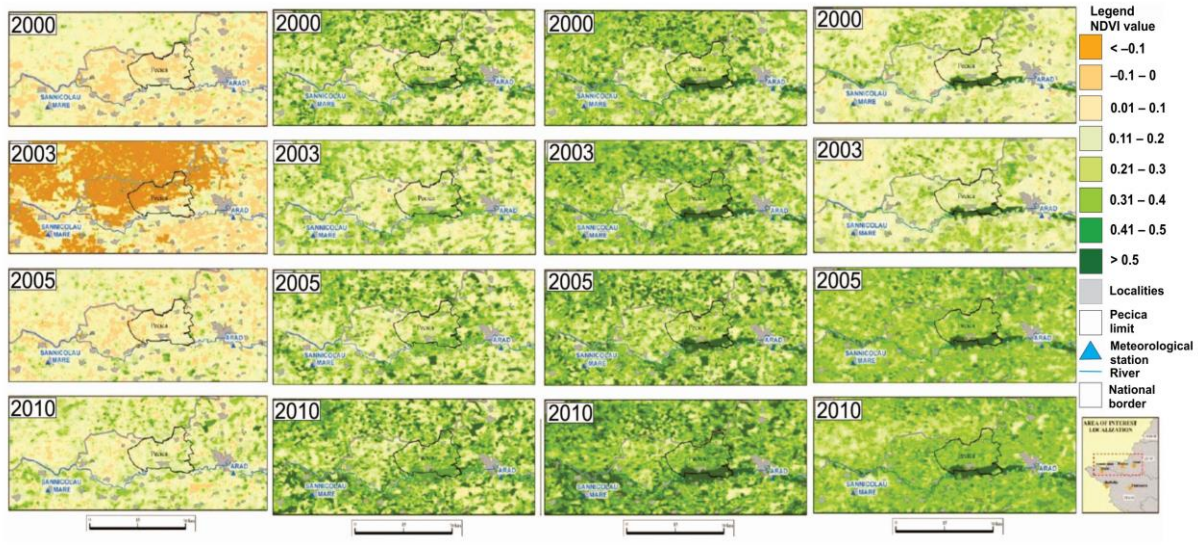

a) b) c) d)

Figure 2: Spatial variation of average NDVI values:)a – in the period 6.03 - 6.04; b) – in the period 7.04 - 8.05; c) – in the period 9.05 - 9.06; d) – in the period 10.06 - 28.08.

The threshold value able to separate the dry and normal conditions was set up using the NDVI histograms (figure 3c). For this study, an NDVI value of 0.22 was used as "drought threshold". These two classes representation excludes the "normal" NDVI values while keeping the low ones. Areas represented in brown in figure 5b can be therefore associated with dry areas.

3.1.2 The Normalized Difference Water Index (NDWI)

The NDWI is a satellite-derived index from the Near-Infrared (NIR) and Short Wave Infrared (SWIR) reflectance channels (Gao, 1996). The SWIR reflectance reflects changes in both the vegetation water content and the spongy mesophyll structure in vegetation canopies, while the NIR reflectance is affected by leaf internal structure and leaf dry matter content but not by water content. NDWI holds considerable potential for drought monitoring because the two spectral bands used for its calculation are responsive to changes in the water content (SWIR band). This index increases with vegetation water content or from dry soil to free water (Chen et al., 2005; Gu et al., 2007). The NDWI value ranges from –1 to 1. The common range for green vegetation is –0.1 to 0.4.

Figure 4 presents an example for NDWI maps over Romania, obtained from MOD09A1 products (8-day composite) for 2005 – rainy year (figure 4.a) and for 2007 – droughty year (figure 4.b).

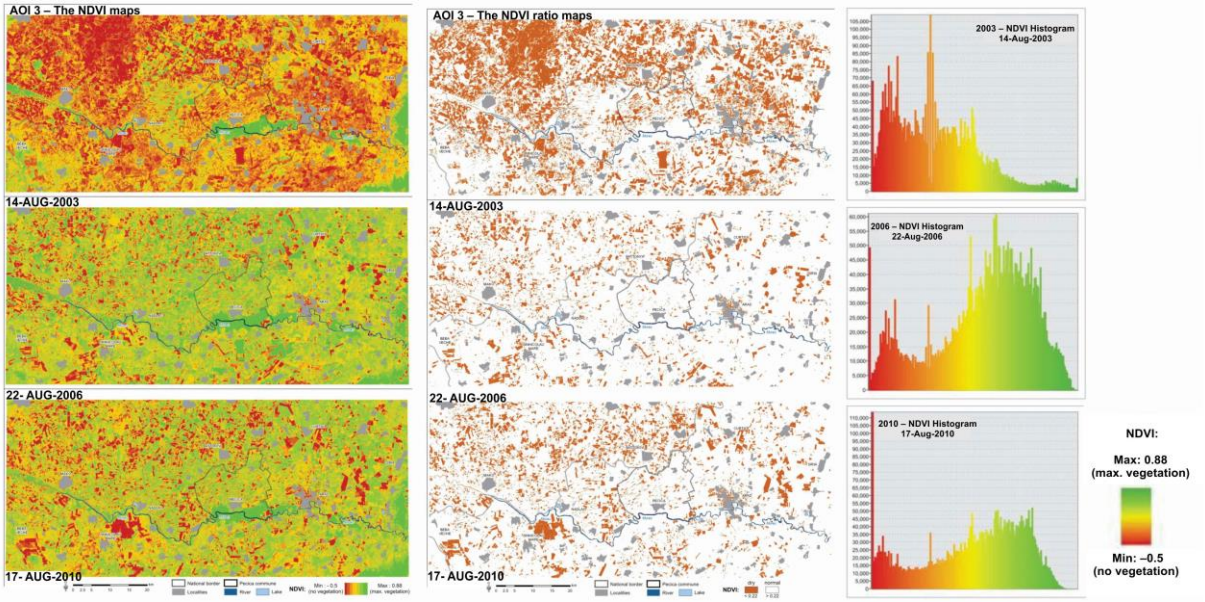

a) b) c)

Figure 3: a) – The NDVI maps extracted from LANDSAT data; b) – The two classes NDVI maps obtained by applying a "low-vegetation" NDVI threshold; c) – NDVI histograms.

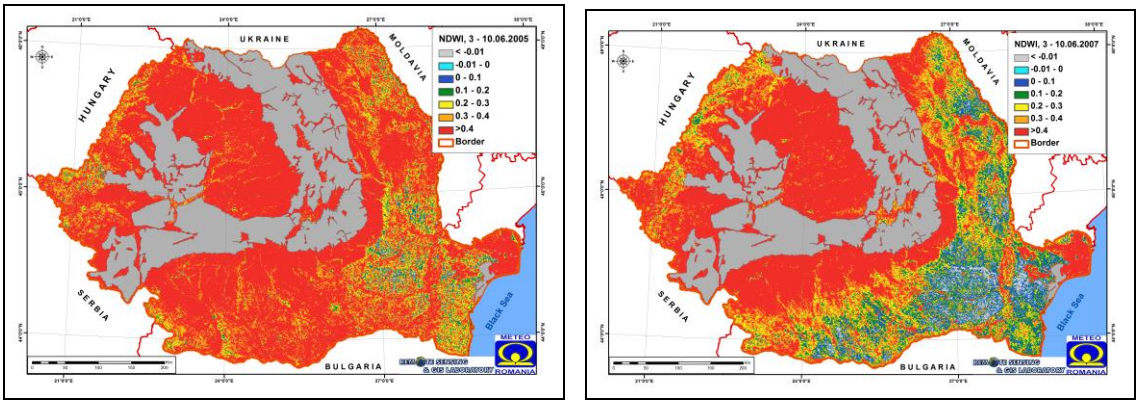

a) b)

Figure 4: NDWI maps over Romania, obtained from MOD09A1 products (8-day composite): for 03-10.06.2005 (a) and 03-10.06.2007 (b).

The figure clearly emphasized the large areas affected by drought in 2007, in the Eastern, South-eastern and Western agricultural regions of Romania.

3.1.3 The Normalized Difference Drought Index (NDDI)

The NDDI is a satellite-derived index defined by the equation:

$$NDDI = (NDVI - NDWI) / (NDVI + NDWI) \quad (1)$$

The NDDI can offer an appropriate measure of the dryness of a particular area, because it combines information on both vegetation and water. The NDDI has a stronger response to summer drought conditions than a simple difference between NDVI and NDWI, and is therefore, a more sensitive indicator of drought. In case of common range of values for vegetation moniotoring the NDDI values vary between 0.33 to 3, a higher range indicating more severe drought. This index can be an optimal complement to in-situ based indicators or for other indicators based on remote sensing data (Gu et al., 2007).

The figure 5 shows the NDDI over Romania, obtained from MODIS MOD09A1 products (8-day composite) for 2005 (rainy year) and 2007 (droughty year). The figure also highlights the areas affected by drought in 2007, especially the Eastern, South-eastern and Southern agricultural regions of Romania.

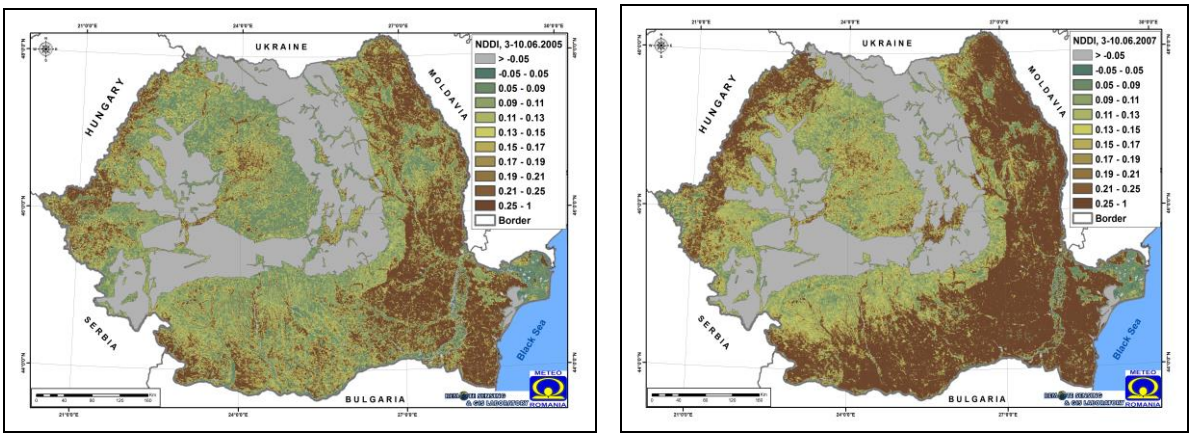

a) b)

Figure 5: NDDI maps over Romania, obtained from MOD09A1 products (8-day composite): for 03-10.06.2005 (a) and 03-10.06.2007 (b).

3.2 The biophysical parameters and physically-based vegetation state indicators

3.2.1 The Leaf Area Index (LAI)

The LAI, defined, as half the total leaf area per unit ground surface area, is a key biophysical canopy indicator, which play a major role in vegetation physiological processes and ecosystem functioning. Assessment of crop LAI and its spatial distribution are of importance for crop growth monitoring, vegetation stress, crop forecasting, yield predictions, management practices, and climate simulations. Along with the fAPAR, the LAI is a biophysical variable describing canopy structure and are closely related to the rate of energy consumed in the functional processes and exchange mass. Drought monitoring, corresponding to the state and dynamics of vegetation, in a given time may be accounting for LAI values derived from satellite data.

The algorithm for generating the MODIS LAI products uses surface reflectance (MOD09) and land cover (MOD12) products. The MODIS LAI algorithm is based on the analysis of multispectral and multidirectional surface reflectance signatures of vegetation elements. The figures 6 (a, b) show the spatial evolution of average LAI values, as well as the deviation from the multi-annual average (2000 – 2009) for the years 2000, 2003 (dry years) and 2005, 2010 (rainy ones), in the study area located in the Western part of Romania.

4 CONCLUSIONS

Remote sensing techniques could enhance and improve the crop vegetation state monitoring and the drought analysis, especially considering the limited

availability of ground measured agrometeorological data. The use of remote sensing data in agrometeorology is a quickly developing and promising trend.

The main sources of satellite data for crop vegetation state studies and monitoring are the TERRA/AQUA – MODIS, LANDSAT-TM/ETM+ and SPOT-Vegetation archives. The satellite-derived vegetation indices data and biophysical parameters prouved to be good indicators of vegetation condition and relevant for the installation, duration and intensity of the agricultural drought.

The MODIS imagery still represents one of the most important type of satellite data available free of charge and can be successfully used in determining the vegetation status at one point or to predict the changes that may appear in plants activity.

By examining the spatial and temporal patterns of vegetation indices and comparing/correlating with the field conditions measured on site, it was determined that NDVI, NDWI and NDDI, are more suitable for agricultural drought characteristics monitoring.

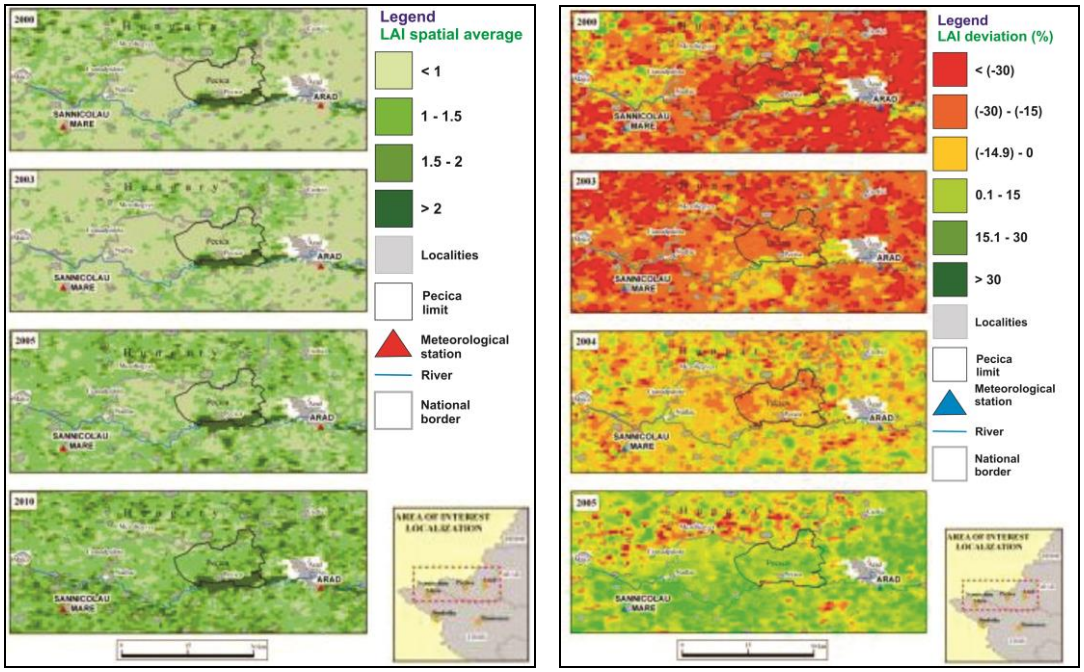

a) b)

Figure 6: a - Spatial variation of average LAI values (from the 6th of March to the 28th of August); b - The LAI deviation from the multi-annual average (2000 – 2009) (from 6 March to 28 August).

ACKNOWLEDGEMENTS

The presented work was done in the frame of STAR 2012 (Space Technology and Advanced Research Program), project DROMOSIS *(Drought monitoring based on space and in-situ data).*

REFERENCES

Basso, B., Cammarano1, D., and De Vita, P., 2004. Remotely sensed vegetation indices: theory and applications for crop management, *Rivista Italiana di Agrometeorologia* , 36-53 (1).

Chen, D., J. Huang, and Jackson, T. J., 2005. Vegetation water content estimation for corn and soybeans using spectral indices derived from MODIS near- and short-wave infrared bands, *Remote Sens. Environ*., 98, 225– 236.

Gao, B., 1996. NDWI—A normalized difference water index for remote sensing of vegetation liquid water from space, *Remote Sens. Environ*., vol., 58, 257–266.

Gu, Y., J. F. Brown, J. P. Verdin, and Wardlow, B., 2007. A five-year analysis of MODIS NDVI and NDWI for grassland drought assessment over the central Great Plains of the United States, *Geophys. Res. Lett*., 34, L06407.

Huete, A.R., H. Liu, K. Batchily, and van Leeuwen, W., 1997. A Comparison of Vegetation Indices Over a Global Set of TM Images for EOS-MODIS. *Remote Sensing of Environment* 59(3):440-451.

Jackson, J. T., D. Chen, M. Cosh, F. Li, M. Anderson, C. Walthall, P. Doriaswamy, and Hunt, E. R., 2004. Vegetation water content mapping using Landsat data derived normalized difference water index for

corn and soybeans, *Remote Sens. Environ*., 92, 475–482 (2004).

Penuelas, J., I. Filella, C. Biel, L. Serrano, and Save, R., 1995. Reflectance at the 950-970 Region as an Indicator of Plant Water Status. *Intern. Journal of Remote Sensing* 14:1887-1905.

Peters, A. J., E. A. Walter-Shea, J. Lei, A. Vina, M. Hayes, and Svoboda M. R., 2002. Drought monitoring with NDVI-based standardized vegetation index, *Photogramm. Eng. Remote Sens*., 68, 71–75.

Monitoring Protected Areas Using Remote Sensing Technology

Zahra Ghofrani[1], Kali Prasad Nepal[1] , and Adham Beykikhoshk[2]
[1]*School of Engineering, Faculty of Science, Engineering and Built Environment, Deakin University, Geelong, Australia*
[2]*Centre for Pattern Recognition and Data Analytics, Deakin University, Geelong, Australia*
ghofrani@deakin.edu.au, kali.nepal@deakin.edu.au, abeyki@deakin.edu.au

Keywords: change detection, remote sensing, protected areas

Abstract: Due to irrational use of natural resources, human society is facing unprecedented threats. Remote sensing is one of the essential tools to determine changes in various forms of biological diversity over time. There are many methods to determine changes in protected areas, using satellite images. In this paper after introducing different change detection methods and their advantages and disadvantages, a hybrid method is used to analyse changes in forests and protected areas in a national park. Two Landsat images of Golestan National Park in Iran (taken in 1998 and 2010) were used. This hybrid approach combines Change Vector Analysis (CVA) for flagging the occurrence of changes, followed by signature extension to assign labels to changed pixels. The main objective of this paper is to propose a method for discovering and assessing environmental threats to natural treasures.

1 INTRODUCTION

Selecting the most appropriate change detection method for a given application is difficult, and requires consideration of the change type of interest (Fraser, Olthof, and Pouliot, 2009). Wide range of change detection algorithms are now available which may be broadly grouped as classification methods (Chen and Chen, 2012), (Hermitte, Verbesselt, Verstraeten, and Coppin, 2011) and spectral approaches (Fraser et al., 2009). If sources of image noise are adequately controlled, spectral approaches quantify the magnitude of reflectance changes between different dates, which relate to a land surface change.

One advantage is the potential to fine-tune change detection sensitivity, while a limitation is the inability to provide information on the nature of change e.g. class label (Xiaolu and Bo, 2011). Examples of spectral-based methods include: image differencing, regression and change vector analysis (Fraser, Li, and Cihlar, 2000), (Johnson and Kasischke, 1998), (Prakash and Gupta, 1998), (Fraser, Olthof, and Pouliot, 2009).

Classification approaches such as post-classification comparison and two-date image clustering, in contrast identify both the occurrence of changed pixels and the type of change by directly labelling land cover at two time periods. However, they are susceptible to generating high levels of commission error due to the multiplication of individual errors (Yuan, Sawaya, Loeffelholz, and Bauer, 2005), (Fraser, Olthof, and Pouliot, 2009). There are also hybrid change detection procedures that exploit the advantages of each approach, while attempting to minimize their limitations (Luque, 2000), (Petit, Scudder, and Lambin, 2001), (Silapaswan, Verbyla, and McGuire, 2001).

This paper presents a hybrid change detection algorithm. In this approach, a mask of potential changed pixels is first created by thresholding a two-date change vector analysis (CVA) product. Land cover class is then updated for changed areas only by spectral signature extension, whereby changed pixels are matched to the most similar labelled cluster from a baseline land cover map.

This method exploits the benefits of both spectral and classification type methods, and reduces their weaknesses (Fraser et al., 2009). Thus, the accuracy of this hybrid method is expected to be higher than each method individually. It is also focused on decreasing the role of human operators in the process. This method extracts image data better than the others and also enables labelling to be done automatically using post classification comparison and pre-existing knowledge of the land cover data.

This paper is organized as follows: Section 2 describes the case study area and the required data for

analysis. Section 3 represents the proposed change detection algorithm. Section 4 describes the environmental analysis. Finally, in section 5, our conclusions are drawn.

2 CASE STUDY AND REQUIRED DATA

Golestan National Park with 92,000 hectares area is the biggest and oldest registered national park in Iran. This forest was registered with the UNESCO World Heritage List in 1976 as one of the 50 vital protected areas on earth. The geographical area of Golestan National Park is between 55° 43' 16" to 56° 15' 31" longitudes and 37° 16' 51" to 37° 32' 27" latitudes. The average elevation of this park is 1378 meters.

Different data types used in this study are introduced below.

2.1 Topographic Map

The only map available for the study area is a 1:250,000 topographic map produced in the spring of 1998 by a group of forestry research organizations using Landsat ETM+ images (Figure 1).

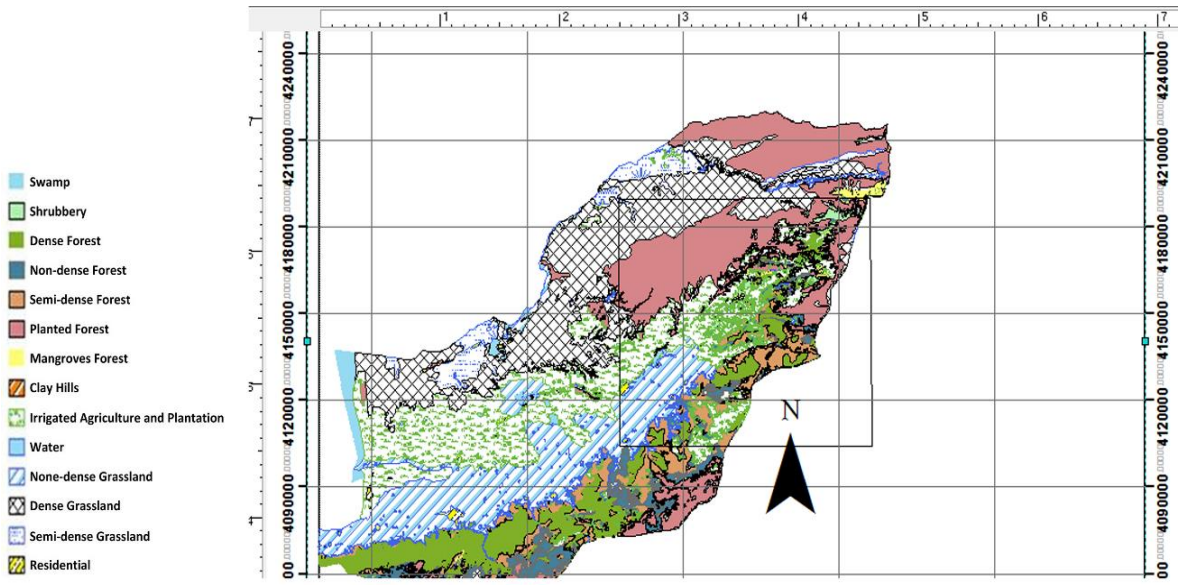

Figure 1: The topographic map of the study area in 1998

2.2 Landsat Images

For this research, two Landsat images taken in August 1998 and 2010 (a period of 12 years, which is an appropriate period for assessing environmental changes) were used. The radiometric and geometric calibration parameters of these images are available and cloud cover over the area in the images is negligible. Image dimensions are 8091 × 7231 pixels and the field of view is about 185 × 175 km (Figure 2). For Landsat TM images, the UTM system and WGS84 ellipsoid were used for geo-referencing.

2.3 High Resolution Images

Since there was no updated map for the case study area, in order to evaluate the accuracy of the method, we used Geoeye high-resolution images for 2010. The mosaic Geoeye images have been cut to the thresholds of Landsat images' latitude and longitude (Figure 3).

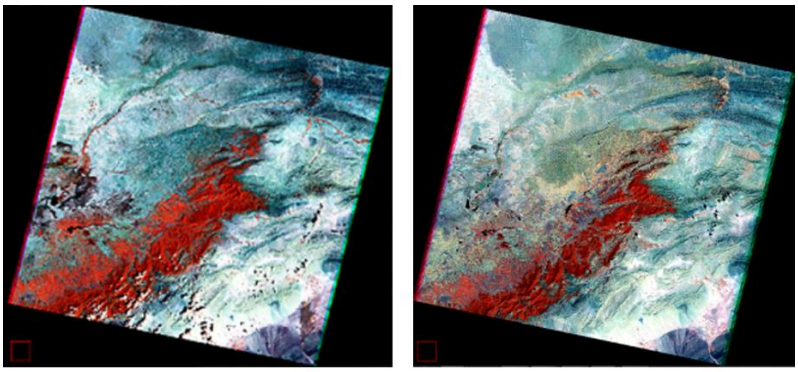

(a) (b)

Figure 2: Landsat images (false colour composites), of the study area (a) August 1998 and (b) August 2010.

3 CHANGE DETECTION ALGORITHM

This method consists of four main steps. Pre-processing level as the first step, includes obtaining images and reference maps, image registration and normalization. The purpose of this step is to prepare the images for the next step.

In the second step, thematic map is produced from satellite images and available maps of the area, by clustering an image as the baseline (master) image and labelling the clusters based on the reference maps. Then based on the post- classification comparison method, the changes' nature are labelled. Post-classification comparison applies a comparison between the feature vector of each changed pixel and the centre of the labelled clusters. Based on this comparison the changed pixels will be labelled (change map).

Finally in the last step, a reference map is produced using the high-resolution Geoeye image which is needed for accuracy assessment.

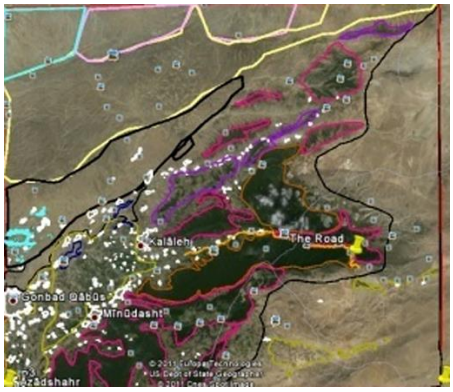

Figure 3: Mosaic Geoeye image of the study area, 2010.

3.1 Pre-processing

Image pre-processing stage, includes both the geometric correction and normalization of images that have been taken at different times from the same area. Pre-processing consists of the following operations.

3.1.1 Geometric Correction

In this study, the geo-referencing of the 1998 image is performed using the 1:250,000 topographic maps. After geo-referencing of 1998 image, the 2010 image is registered to 1998 image. Sub-pixel accuracy for image registration is obtained.

3.1.2 Image Normalization

After a careful image-to-image spatial registration the images must be radiometrically normalized. Accurate normalization is essential for the combined CVA and post classification comparison change detection approach, since both methods assume that a pixel's reflectance is stable through time unless a land cover change occurs (Fraser, Olthof and Pouliot, 2009). Histogram Matching is a common technique for this reason which uses the histograms for image processing and colour adjustment between images.

3.2 Thematic Map Generation

The change detection procedure requires a baseline land cover classification from which changes are detected at nominal 12-year intervals. The thematic map is produced using an unsupervised clustering approach that combines features of the Enhancement Classification (ECM) and Classification by Progressive Generalization (CPG) methods.

The enhanced imagery is clustered to a number of spectral clusters. Visual quality checking is an important part of this and each subsequent generalization step, and is performed by comparing the previous generalization with the current one to ensure that no significant land cover information is lost. The overall coverage of the Earth's classes such as soil, water, plant and etc., are determined. Generalization proceeds by progressively merging spectrally similar and spatially adjacent clusters to generate conceptual classes. Final cluster merging and labeling to a land cover classification is based on expert image interpretation and available reference data (Fraser, Olthof, and Pouliot, 2009).

In this research the 1998 Landsat image is divided into 22 clusters using Iso-data clustering method. The number of clusters is chosen to be twice as the number of conceptual classes which are 11 in the case of this study area. The output for this level is a clustered image (22 clusters), which is labelled based on 1:250,000 topographic map and converted to 11 conceptual classes.

3.3 Change Detection Process

In this section, the sub-steps of change detection process will be explained in the following stages.

3.3.1 Tasseled Cap Transformation

Tasseled Cap transformation is a well-known methods of enhancing spectral information content for Landsat TM data. Tasseled Cap transformation especially optimizes data viewing for vegetation studies. Tasseled Cap index was calculated from data of the related six TM bands (King and O'Hara, 2001). Three of the six tasseled cap transform bands are often used:

- Band 1, brightness as a measure of soil
- Band 2, greenness as a measure of vegetation
- Band 3, wetness as interrelationship of soil and canopy moisture

This transformation is used to calculate brightness and greenness of both images (1998 and 2010), which are the input for CVA analysis.

3.3.2 Applying Change Vector Analysis

A change vector can be described by an angle of change (vector direction) and a magnitude of change from date 1 to date 2 (Fraser et al., 2009), (Chen, Gong, He, and Shi, 2003). We used brightness and greenness as inputs of CVA to measure and monitor reforestation and deforestation of the region of study. The bands are observed in measurement space with brightness placed along the X-axis and greenness placed along the Y-axis.

Change direction is achieved by measuring the angle between corresponding pixels in different times (1998 - 2010) and the magnitude of change is achieved using Euclidean distance between vectors.

Magnitude of change vector and its direction are described by Eq. (1) and Eq. (2) respectively.

$$S = \sqrt[2]{(G_2 - G_1)^2 + (B_2 - B_1)^2} \quad (1)$$

$$\tan \alpha = \frac{G_2 - G_1}{B_2 - B_1} \quad (2)$$

G1, G2, B1, and B2 are values of greenness and brightness in two images, which are obtained from Tasseled cap transformation. To specify the reforestation and deforestation of the jungles, greenness and brightness values should be compared (Kuzera, 2005). Angles measured between 90 and 180 degrees, show reduction in brightness and increase in greenness, this change is considered as reforestation. Angles measured between 270 and 360 degrees, show reduction in greenness and increase in brightness, this change is considered as deforestation (Kuzera, 2005). Angles measured from 0 to 90 and 90 to 180 degrees, show reduction or increase for both greenness and brightness, respectively. This is known as a stable condition, indicating no change in the vegetation of the area (Kuzera, 2005).

According to the magnitude of change vectors, damaged pixels are categorized into 4 levels of low, moderate, severe and very severe deforestation. For this reason four equal intervals are applied as below:

- Interval [1-100]: Low change
- Interval [100-200]: Moderate change
- Interval [200-300]: Severe change
- Interval [300-400]: Very severe

Values less than 1 are considered as noise and values higher than 400 as outlier. The thresholds defined are quite tentative. In Figure 4, the various degrees of grayscale represent different degrees of degradation, the darker shades show more severe deforestation and vice versa.

3.3.3 Post Classification Comparison

Change labeling is accomplished by iteratively updating land cover starting from the baseline classification for only those pixels identified as

changed in the CVA change mask. Post-classification comparison method involves comparison of the new feature vector of each changed pixel with the major feature vector of the cluster centres (determined in the first image). New classes of land cover pixels are determined by assigning a pixel to the most similar cluster and corresponding existing land cover maps, so the new cluster of changed pixels are achieved.

Figure 4: Result of applying the CVA method to two Landsat images of the study area, for 1998 and 2010.

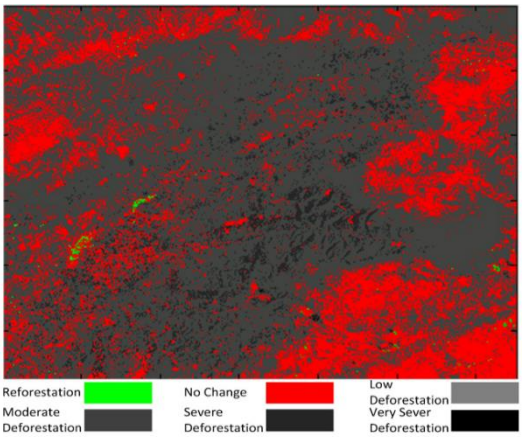

Figure 4: Result of applying the CVA method to two Landsat images of the study area, for 1998 and 2010

To understand the change trends, the feature vector of each changed pixels of 2010 image, is compared with feature vector of classification cluster centres of 1998 image. The changed pixel is assigned to the cluster with the most similarity with cluster centre. Since in 1998 image, each cluster has a distinct relation with an information class, finding the most similar cluster is the same as labelling changed pixels in 2010 image with a new information class.

This model is used for cost-effective classification in large and remote areas and regions where it is difficult to collect data. The main benefit of this approach is that by using post-classification comparison method and a strong knowledge of land cover data the labelling process will be done automatically.

3.4 Accuracy Evaluation

Since there is no updated reference map available for the area, in order to evaluate the accuracy of the obtained change detection results, a reference map is produced by using both the Landsat (2010) and a high-resolution Geoeye image. Geoeye image is taken at the same time as the Landsat image (2010) and covers the whole Golestan national park. It is later cropped so it covers the same latitudes and longitudes that Landsat image covers.

To produce the reference map, Landsat 2010 image is first clustered into 33 clusters. The obtained clusters are compared to the information classes recognized from the high-resolution Geoeye image. In this way the correspondence between clusters and conceptual classes are determined which leads to the classification of 2010 Landsat image. This image is used as the reference map to evaluate the change detection results. We gained 85% accuracy for the proposed change detection method.

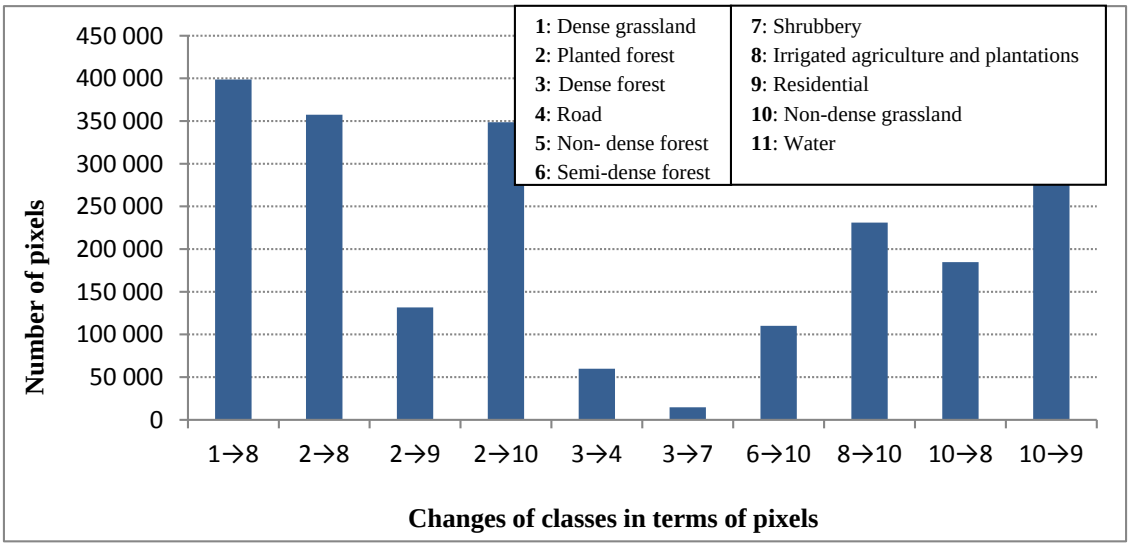

Figure 5: Changes of classes in terms of pixels

4 ENVIRONMENTAL ANALYSIS

Figure 5 shows the classes which have the most change rate and magnitude of their change in terms of pixels. As the statistics show from 1998 to 2010 the number of pixels which converted from planted forest, semi-dense forest, dense forest, and dense grassland classes to road, residential, low density grassland, irrigated agriculture, plantations, shrubbery and non-dense forest classes is very high and this represents a serious degradation in this area. Road construction in forests regardless of its negative effects on the forest, inappropriate urban development, human progression in nature, cutting trees for fuel, human farming in the forests to provide food supply, and etc. are some main reasons for degradation in this area.

A similar research was developed and demonstrated by Fraser using six national parks in Canada. It covered a range of geographical and ecological conditions and was subject to a variety of change agents including forest harvesting, wildfire, land use development, and climate/weather (Fraser, Olthof and Pouliot, 2009). In contrast to Golestan National Park area that is located on one Landsat scene and there is no need to mosaic Landsat images, the area of Fraser's study was vast and required more than one Landsat frame to provide complete coverage. They used 30m resolution Landsat EM and ETM+, from 1990 to 2005 to generate baseline land cover classification at five years intervals. Due to huge height difference, removing haze and topographic effects for Canada's national parks was necessary. However in Golestan National Park, topographical elevations are fairly smooth and there was no need to apply topological corrections in pre-processing. Moreover, radiometric normalization in Canada national parks was done by using filtering, while for Golestan National Park it was done by histogram matching. In both methods, identifying the changed pixels and labelling them, were determined using CVA and signature extension. Finally in Canada baseline land cover and changes were validated by updated available maps and in Golestan National Park by high-resolution Geoeye images (due to the lack of updated maps). Fraser reported 92% correctly identified changed pixels and 8% omission error rate in Canada's parks.

5 CONCLUSION

Timely and accurate change detection of Earth's surface features is extremely important for understanding relationships and interactions between human and natural phenomena in order to promote better decision making. Remote sensing data are primary sources extensively used for change detection in recent decades and many change detection techniques have been developed based on them. The common goal of all these algorithms is to improve the accuracy of the information extracted from remote sensing images. In this paper, a change detection method was proposed to determine changes in the forests of Northern Iran (Golestan National Park). Using the combination of spectral and classification methods lead to an acceptable accuracy.

In comparison with the conducted research on national parks of Canada, lack of updated reference maps, has a direct impact on the final accuracy. The results of the assessment indicated that change detection method should be developed based on local knowledge. While this method provides a set of generic procedures and tools for change detection, its successful application requires an analyst experienced in land cover interpretation and image processing. In particular, the baseline land cover labeling, assessing results from the image correction methods, determining a CVA change threshold, and development of signature extension rules, are subjective and will determine the final accuracy of the land cover change products. This algorithm is a cost-effective change detection method in large areas and tries to minimize the role of the human operator. It can be implemented for most forests regardless of their vegetation. This study is intended to explorer use of high resolution images in the future in order to investigate its capabilities to determine the change of plant species. In future this method also can be elevated using optimisation methods to find the best values for CVA thresholds, number of clusters, and similarity measure and result in an extended intelligent version of current change detection method.

REFERENCES

Chen, J., Gong, P., He, C., Shi, R. & P. (2003). *Land-Use/Land-Cover Change Detection Using Improved Change-Vector Analysis*.

Chen, X., Chen, J. (2012). *An automated approach for updating land cover maps based on integrated change*

detection and classification methods. ISPRS Journal of Photogrammetry and Remote Sensing, 71, 86-95.

Fraser, R. H., Li, Z., Cihlar, J. (2000). *Hotspot and NDVI differencing synergy (HANDS): A new technique for burned area mapping over boreal forest*. Remote Sensing of Environment, 74, 362-376.

Fraser, R. H., Olthof, I., Pouliot, D. (2009). *Monitoring land cover change and ecological integrity in Canada's national parks.* Remote Sensing of Environment, 113, 1397-1409.

Hermitte, S. L., Verbesselt, J., Verstraeten, W. W., Coppin, P. (2011). *A comparison of time series similarity measures for classification and change detection of ecosystem dynamics*. Remote Sensing of Environment, 115 (12), 3129-3152.

Johnson, R. D., Kasischke, E. S. (1998). *Change vector analysis: A technique for the multi spectral monitoring of land cover and condition.* International Journal of Remote Sensing, 19, 411-426.

King, R., O'Hara, C. (2001). *Tasseled Cap Transformation.* Computational Geospatial Technologies Center, Mississippi State University.

Kuzera, K. (2005). *Monitoring vegetation regeneration and deforestation using change vector analysis: Mount St. Helen's study area.*

Luque, S. S. (2000). *Evaluating temporal changes using Multi-Spectral Scanner and Thematic Mapper data on the landscape of a natural reserve: The New Jersey Pine Barrens, a case study*. International Journal of Remote Sensing, 21, 2589-2611.

Petit, C., Scudder, T., Lambin, E. (2001). *Quantifying processes of land-cover change by remote sensing: Resettlement and rapid land-cover changes in south-eastern Zambia.* International Journal of Remote Sensing, 22, 3435-3456.

Prakash, A., Gupta, R. P. (1998). *Land-use mapping and change detection in a coal mining area—a case study in the Jharia coalfield, India*. International Journal of Remote Sensing, 19, 391-410.

Silapaswan, C., Verbyla, D., McGuire, A. (2001). *Land cover change on the Seward Peninsula: The use of remote sensing to evaluate the potential influences of climate warming on historical vegetation dynamics*. Canadian Journal of Remote Sensing, 27, 542-554.

Xiaolu, S., Bo, C. (2011). *Change Detection Using Change Vector Analysis from Landsat TM Images in Wuhan*. Procedia Environmental Sciences, 11(A), 238-244.

Yuan, F., Sawaya, K. E., Loeffelholz, B. C., Bauer, M. E. (2005). *Land cover classification and change analysis of the Twin Cities (Minnesota) Metropolitan Area by multitemporal Landsat remote sensing*. Remote Sensing of Environment, 98, 317-328.

Implementation of a Service Oriented Architecture in Smart Sensor Systems Integration Platform

Alexander K. Alexandrov and Vladimir V. Monov
Institute of Information and Communication Technologies, Bulgarian Academy of Sciences
Acad. G. Bonchev str., bl. 2, 1113 Sofia, Bulgaria
akalexandrov@gmail.com, vmonov@iit.bas.bg

Keywords: SOA, Sensor networks, WSN, SSN, Data integration.

Abstract: The paper describes a new developed platform for smart sensor network (SSN) data integration based on Service Oriented Architecture (SOA). SOA is a software design and software architecture design pattern based on discrete pieces of software providing application functionality as services to other applications. This is known as service oriented technology which is independent of any vendor, product or technology. Our platform is layer based and defines Network Layer, Data Integration layer and Application layer. The proposed architecture improves the information flow, has ability to expose internal functionality, improves reliability and scale operations to meet different demand levels. The platform supports mechanisms for cooperative data mining, self organization, networking, and energy optimization to build higher level service structures. The development of applications is improved and simplified by the use of optional administration tools and components.

1 INTRODUCTION

Service oriented architecture (SOA) is a software design based on discrete pieces of software providing application functionality as services to other applications. This is known as Service orientation. It is independent of any vendor, product or technology (WWW Consortium, 2001).

A service is a self contained unit of functionality, such as retrieving an online bank statement (The Open Group, 2007). Services can be combined by other software applications to provide the complete functionality of a large software application (Kodali, 2005).

Each service implements one action, such as submitting an online application for an account, retrieving an online bank statement or modifying an online booking or airline ticket order. Within a SOA, services use defined protocols that describe how services pass and parse messages. The purpose of SOA is to allow users to combine together fairly large amount of functionality to form *ad hoc* applications.

SOA as an architecture relies on service orientation as its fundamental design principle. If a service presents a simple interface that abstracts away its underlying complexity, then users can access independent services without knowledge of the service's platform implementation .(Svetle, 2010).

The main benefit of SOA is to allow simultaneous use and easy mutual data exchange between applications of different vendors without additional programming or making changes to the services. These services are also reusable, resulting in lower development and maintenance costs and providing more value once the service is developed and tested. Having reusable services readily available also results in quicker time to market (Bacchanalina, Toggle, 2003).

Depending on the adopted approach, each SOA service is designed to perform one or more activities by implementing one or more service operations. As a result, each service is built as a discrete piece of code.

SOA also defines how to integrate widely disparate applications for a Web based environment and uses multiple implementation platforms. Rather than defining an API, SOA defines the interface in terms of protocols and functionality. An *endpoint* is the entry point for such a SOA implementation. For somedevelopers, SOA can be seen as modular programming, software as a service (SaaS), and

cloud computing (which some authors (Erl, 2007) see as the offspring of SOA).

One of the core characteristics of services developed using service orientation design paradigm is that they are composition centric. Services with this characteristic can potentially address novel requirements by recomposing the same services in different configurations. Service composition architecture is itself a composition of the individual architectures of the participating services.

In our study SOA makes it easy for smart sensors connected over a network or within a smart sensor system to succefully cooperate. Smart Sensor System (SSS) is a term describing system which integrate two or more smart sensor networks or part of them. Every smart sensor can run an arbitrary number of services, and each service is built in a way that ensures that the service can exchange information with any other service in the network without human interaction and without the need to make changes to the underlying program itself.

In this paper we propose a service-oriented, flexible and adaptable platform for sensor systems integration. Our approach allows high-level applications to easily configure the data-gathering level and exploit the available functionalities. In the remainder of the paper, some related work is briefly analyzed in Section 2, whilst Section 3 describes the architecture of the developed platform. Concluding remarks are given in Section 4.

2 RELATED WORK

The main goal of the proposed platform for sensor systems integration is the effective and seamless integration of pervasive technologies into the information system of networked enterprises. This issue has already been tackled in the literature, for example in (Samaras *et al.*, 2009) and (Delicato *et al.*, 2003). However, those two proposals are aimed at implementing a service oriented middleware directly on sensor nodes, by forcing SOA compatible protocol stacks (like (OASIS, 2009)) in resource constrained devices.

In our opinion, this approach has the major drawback of imposing too much complexity in devices that are not enough powerful to transmit and elaborate XML messages. To overcome such constraints, the authors propose to adopt *a priori* knowledge in XML message definition, thus losing middleware flexibility. Moreover, the usage of web services in resource constrained devices imposes a certain energy and latency overhead (as an example, cost for such implementations has been quantified in (Priyantha *et al.*, 2008)).

By contrast, our approach concentrates the logic of the Integrated Smart Sensor Networks(ISSN) on a powerful platform, to which the various heterogeneous sensor systems are connected. Such solution is not new, for example it has been used in (Gil-Martinez-Abarca *et al.*, 2006) for enabling management of remote bootstrap of network nodes through the Internet; and in (Grosky *et al.*, 2007) for building a peer to peer infrastructure for sharing sensors through the Internet. However, such works address a wide area of pertinence and they do not explicitly address typical WSN issues, like the energy management of nodes and the QoS support for applications.

A gateway based solution has been also proposed in (Moeller, Sleman, 2008), aiming at integrating WSNs into other existing IP based networks. However, as their work is addressed to the ambient intelligence at home, they only abstract the functionality of single sensors, i.e. applications are aware of the network deployment and request services directly to a node. Our approach instead abstracts functionalities of the various numbers of sensor networks, i.e. applications request services for a geographic area without the need to know how many nodes are deployed there or how they communicate to each other.

It is worth to note that our approach completely differs from that of querying systems like TinyDB (Madden *et al.*, 2011). In fact, such systems permits to extract data from a WSN but they do not generally provide high level interfaces for QoS configuration and management. Moreover, such systems usually exploit low level techniques for gathering data and can thus be considered as tight extensions of a particular WSN technology. For this reason, they could in turn be used for developing a WSN whose configuration and management are provided by our architecture, that is, as explained in the next section, independent by design of the underlying WSN technology.

3 SOA BASED PLATFORM FOR SMART SENSOR SYSTEMS INTEGRATION.

The services of the proposed integrated sensor systems platform are Apache and WSDL based and implement service oriented architecture. They have some functional building blocks accessible over

standard Internet protocols especially SOAP. These services can represent either new applications or just wrappers around existing sensor systems to make them network enabled.

Each SOA building block in the platform can play one or both of two roles:

Service provider: The service provider creates a web service and possibly publishes its interface and access information to the service registry. Each service provider must decide which services to expose, how to make tradeoffs between security and easy availability, how to price the services, or (if no charges apply) how/whether to exploit them for other value. The provider also has to decide what category the service should be listed in for a given service. It registers what services are available within it, and lists all the potential service recipients. Furthermore, the amount of the offered information has to be decided. Depending on the data information requests, the service provider can attempt to maximize lookup requests, number of listings or accuracy of the listings. The Universal Description Discovery and Integration (UDDI) specification defines a way to publish and discover sensor data information about Web services.

Service consumer: The service consumer or web service client locates entries in the service registry using various find operations and then binds to the service provider in order to invoke one of its web services. Whichever service the service consumers need, they have to take it into the brokers, bind it with respective service and then use it. They can access multiple services if the service provides multiple services.

In the proposed sensor system integration platform we build SOAs using web services standards especially SOAP and RPC that have gained broad industry acceptance after recommendation of Version 1.2 from the W3C (World Wide Web Consortium) in 2003 (WWW Consortium, 2001). These standards (also referred to as web service specifications) also provide greater interoperability One can, however, implement SOA using any service based technology, such as Jini, CORBA or REST.

SOAP, originally defined as Simple Object Access Protocol, is a protocol specification for exchanging structured information in the implementation of Web Services in computer networks. It relies on XML Information Set for its message format, and usually relies on other Application Layer protocols, most notably Hypertext Transfer Protocol (HTTP) or Simple Mail Transfer Protocol (SMTP), for message negotiation and transmission.

Remote procedure call (RPC) is an interprocess communication that allows a computer program to cause a subroutine or procedure to execute in another address space (commonly on another computer on a shared network) without the programmer explicitly coding the details for this remote interaction. When the software in question uses object oriented principles, RPC is called remote invocation or remote method invocation.

The main purpose of the new developed SOA based platform is to integrate various heterogeneous sensor networks based on different hardware and using different communication technologies in one Integrated Smart Sensor System (ISSS). This conception enables us full integration of the sensor data and the possibility for data interchange between the sensor networks included in the platform and/or between the smart sensors from different networks too. The implemented in the platform 6LoWPan based technology allows direct access to every sensor unit and sensor node and direct sensor data interchange. Based on this technology, the developed platform provides the unique possibility of ad-hoc Virtual Sensor System (VSS) building and exploration.

The proposed custom design platform is based on the WSO2 Carbon SOA framework. OSGi-based WCO2 framework includes common capabilities shared by all WSO2 products, such as built-in registry, user management, transports, security, logging, clustering, caching and throttling services, co-ordination, and a GUI framework.

In the current version of the platform we defined and released 3 layers: **1. Application layer, 2. Data Integration layer and 3. Network layer** (Figure 1).

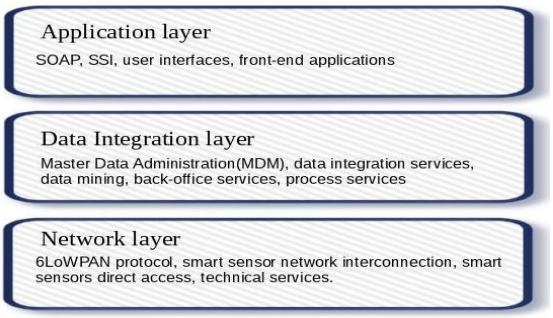

Figure 1: Integrated sensor system SOA platform

Application layer. The Application layer of the current platform is based mainly on SOAP. It relies on XML Information Set for its message format. Additionally we include in the current platform Application layer SSI and RPC protocols too. The

SSI ("Simple Sensor Interface") protocol is a communications protocol designed for data transfer between computers or user terminals and smart sensors.

Data Integration Layer. The Integration Layer marks the transition from raw sensor data to integrated data (Figure 2). This is the data that has been consolidated and rationalized. This layer represents the passage of the data through the process of integration, rather than the storage area for the data. For data with multiple sensor sources, a mastering and tuning process is required.

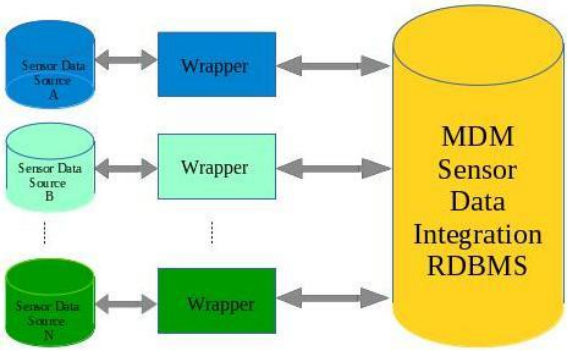

Figure 2: Data Integration layer

The core functionality of the Data Integration Layer is the Master Data Management.

Master Data Management (MDM) is the process by which data from different sensor networks or sub systems included in the platform is matched and processed to realize a single copy of data.

The MDM process should attach all relevant attribution related to the core entity. It is possible to have the MDM only process those attributes that are sourced from multiple systems. For those with a single source, no conflict exists to be resolved. The MDM system has its own internal data structures. These structures are oriented towards the structure of the source files or the target System of Record. For data with multiple sources, a mastering process is required.

Network layer. The main task of the network layer is to provide functional and procedural means of transferring variable-length data sequences from a source to a destination host via one or more sensor systems. Currently the network layer of the proposed platform for smart sensor systems integration supports the following two main protocols:

- **IPv6/6LoWPAN protocols.** 6LoWPAN is an acronym of IPv6 over Low power Wireless Personal Area Networks. The 6LoWPAN concept originated from the idea that "the Internet Protocol could and should be applied even to the smallest devices," (Mulligan, 2007) and that low-power devices with limited processing capabilities should be able to participate in the Internet of Things (Shelby, Bormann, 2011), (Shelby, Bormann, 2009).

  The base specification developed by the 6LoWPAN IETF group is RFC 6282. The problem statement document is RFC 4919.
- **Internet Control Message Protocol** version 6 (ICMPv6) is the implementation of the Internet Control Message Protocol (ICMP) for Internet Protocol version 6 (IPv6) defined in RFC 4443 [14]. ICMPv6 is an integral part of IPv6 and performs error reporting and diagnostic functions (e.g., ping), and has a framework for extensions to implement future changes.

Several extensions have been published, defining new ICMPv6 message types as well as new options for existing ICMPv6 message types. Neighbour Discovery Protocol (NDP) is a node discovery protocol in IPv6 which replaces and enhances functions of ARP. Secure Neighbour Discovery Protocol (SEND) is an extension of NDP with extra security. Multicast Router Discovery (MRD) allows discovery of multicast routers.

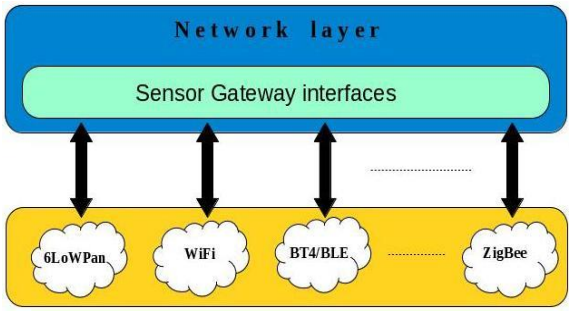

Figure 3: Network layer

The main components of the Smart Sensor System Integration Platform (SSSIP) are:

- application server running custom design modified WCO2 Carbon framework
- data base server running MySQL RDBMS
- gateway servers with related interfaces to access heterogeneous sensor networks or single addressed smart sensors.
- custom design software interfaces supporting ZigBee 802.15.4, 6LoWPan, WiFi 802.11/bgn and BT4/BLE protocols for data exchange.

The structure of the platform is open and can be easily upgraded with different functionality depending on the specific requirements.

4 CONCLUSION

The paper describes a SOA based platform developed for smart sensor systems integration. It has services to manage different heterogeneous sensor networks or group of smart sensors in one sensor system which provides the necessary interoperability. The developed services allow for easy integration of heterogeneous sensors and creation of data views for application developers. The platform is hardware independent and the developers based on the proposed services can easily access data from every sensor network or smart sensor without the need of knowledge how the sensor system work and which kind of communication protocols are running. There are services allowing data compression and messages encryption. Many smart sensor networks wireless or not can be integrated in one smart sensor system under common management and QoS. The process of integration is transparent and geographically independent. This means that sensor networks based on different countries and with different topology and functionality can act as one sensor system.

Based on developed communication interfaces, currently the platform supports ZigBee, WiFi and BT4/BLE communication technologies. The long range RoIP based communication platform is under development too. Also, there is an opportunity of building of Virtual Sensor Systems accepting specific requirements by simply developed services. The implemented 6LoWPan protocol management as service in the platform allows for direct access to smart sensor devices supporting this protocol, as for example the devices from Texas Instrument CC2538, CC1180 etc.

ACKNOWLEDGEMENTS

The research work reported in the paper is partly supported by the project AComIn "Advanced Computing for Innovation", grant 316087, funded by the FP7 Capacity Programme (Research Potential of Convergence Regions).

REFERENCES

Bacchanalian H., Toggle, 2003. Migrating to a service oriented architecture, *IBM Developer Works*, pp. 117–121.

Delicato F., P. Pires, L. Pinnez, L. Fernando, L. da Costa, 2003. A flexible web service based architecture for wireless sensor networks. In: *Proceedings of the 23rd International Conference on, Distributed Computing Systems Workshops*, pp. 730–735.

Erl T., 2007. *SOA: Principles of Service Design*. Prentice Hall/PearsonPTR.

Gil-Martinez-Abarca J., J. F. Macia-Perez, D. Marcos-Jorquera, V. Gilart-Iglesias, 2006. Wake on LAN over internet as web service, In *Proceedings of the ETFA '06 IEEE Conference on Emerging Technologies and Factory Automation*, pp. 1261–1268.

Grosky W., A. Kansal, S. Nath, J. Liu, F. Zhao, 2007. Senseweb: An infrastructure for shared sensing. *Multimedia, IEEE*, 14(4), pp. 8–13.

Kodali R., 2005. *What is service-oriented architecture?* http://www.javaworld.com/article/2071889/soa/what-is-service-oriented-architecture.html

Madden S. R., M. J. Franklin, J. M. Hellerstein, W. Hong, 2011. TinyDB: an acquisitional query processing system for sensor networks. *ACM Trans. Database Syst.*, 30(1), pp. 122–173.

Moeller R., A. Sleman, 2008. Wireless networking services for implementation of ambient intelligence at home. In *Proceedings of the 7th International Caribbean Conference on Devices, Circuits and Systems, ICCDCS*, pp. 1–5.

Mulligan G., 2007. The 6LoWPAN architecture, In *Proceedings of the 4th workshop on Embedded net-worked sensors, EmNets '07, ACM*.

OASIS Standard, 2009.D*evices profile for web services (DPWS)* Version 1.1.

Priyantha N. B., A. Kansal, M. Goraczko, F. Zhao, 2008. Tiny web services: design and implementation of interoperable and evaluable sensor networks. In: *Proceedings of the 6th ACM conference on Embedded network sensor systems*, pp. 253–266, ACM, New York.

Samaras I. K., J. V. Gialelis, G. D. Hassapis, 2009. Integrating wireless sensor networks into enterprise information systems by using web services. In *Proceedings of the 3rd International Conference SENSORCOMM '09*, pp. 785–791

Shelby Z., C. Bormann, 2011. Part 1: Why 6LoWPAN? In: *6LoWPAN: The wireless embedded Internet*, John Wiley & Sons Ltd.

Shelby Z., C. Bormann, 2009. *6LoWPAN: The Embedded Internet*, Wiley Inter science.

Svelte A. T., 2010. *Cloud Computing: A Practical Approach*. McGrow Hill.

The Open Group, 2007. *Service Oriented Architecture (SOA) in the Real World*. Chapter 1. http://msdn. microsoft.com/enus/library/bb833022.aspx .

World Wide Web Consortium, 2001. *SOAP Specifications* http://www.w3.org/TR/2001/WD-soap12-20010709/.

Abstracts

Generation Mechanism of Electromagnetic Rising-tone Emissions in the Magnetosphere

Yoshiharu Omura
Institute *Research Institute for Sustainable Humanosphere, Kyoto University Gokasho, Uji, Kyoto 611-0011, Japan*
omura@rish.kyoto-u.ac.jp

Keywords: nonlinear wave particle interaction, space plasma, radiation belts, particle simulation.

Abstract: The We describe the generation mechanism of electromagnetic waves known as whistler-mode chorus emissions with right-handed polarization and electromagnetic ion cyclotron (EMIC) triggered emissions with left-handed polarization interacting with energetic electrons and protons, respectively, through cyclotron resonance. These waves are frequency observed in the magnetospheres of the magnetized planets such as Earth, Jupiter, and Saturn. They are coherent waves with increasing frequencies generated at the magnetic equator and propagating along the magnetic field. The resonant particles undergo nonlinear trapping motion around the resonance velocity, and they form electromagnetic electron/ion holes in the velocity phase space. In the presence of the inhomogeneity due to the frequency variation and the gradient of the magnetic field, the electron holes or hills result in resonant currents generating rising-tone emissions [1,2,3]. After formation of a coherent wave at a frequency of the maximum linear growth rate, triggering of nonlinear wave growth with the increasing frequency takes place when the wave amplitude is close to the optimum wave amplitude [4,5]. The wave amplitude also has to be greater than the threshold amplitude [2,3] so that the nonlinear wave growth can occur as an absolute instability at the magnetic equator. The triggering process is repeated at progressively higher frequencies, generating subpackets of a rising-tone element. These electromagnetic emissions control the dynamics of radiation belts. Whistler-mode chorus emissions are responsible for acceleration of relativistic electrons [6,7,8], while EMIC triggered emissions induces precipitation of relativistic electrons into the atmosphere through anomalous cyclotron resonance [9,10].

REFERENCES

Moore, R., Lopes, J., 1999. Paper templates. In *TEMPLATE'06, 1st International Conference on Template Production*. SCITEPRESS.

[1] Y. Omura,Y. Katoh, and D. Summers, Theory and simulation of the generation of whistler-mode chorus, Journal of Geophysical Research, 113, A04223, 2008.

[2] Y. Omura, M. Hikishima, Y. Katoh, D. Summers, and S. Yagitani, Nonlinear mechanisms of lower band and upper band VLF chorus emissions in the magnetosphere, Journal of Geophysical Research, 114, A07217, 2009.

[3] Y. Omura, J. S. Pickett, B. Grison, O. Santolik, I. Dandouras, M. Engebretson, P. M. E. Decreau, A. Masson, Theory and observation of electromagnetic ion cyclotron triggered emissions in the magnetosphere, Journal of Geophysical Research, 115, A07234, 2010.

[4] Y. Omura and D. Nunn, Triggering process of whistler mode chorus emissions in the magnetosphere, Journal of Geophysical Research, 116, A05205, 2011.

[5] M. Shoji and Y. Omura, Triggering process of electromagnetic ion cyclotron rising tone emissions in the inner magnetosphere, Journal of Geophysical Research, 118, pp.5553–5561, 2013.

[6] Y. Omura, N. Furuya, D. Summers, Relativistic turning acceleration of resonant electrons by coherent whistler-mode waves in a dipole magnetic field, Journal of Geophysical Research, 112, A06236, 2007.

[7] D. Summers and Y. Omura, Ultra-relativistic acceleration of electrons in planetary magnetospheres, Geophysical Research Letters, 34, L24205, 2007.

[8] N. Furuya, Y. Omura, and D. Summers, Relativistic turning acceleration of radiation belt electrons by whistler mode chorus, Journal of Geophysical Research, 113, A04224, 2008.

[9] Y. Omura and Q. Zhao, Nonlinear pitch-angle scattering of relativistic electrons by EMIC waves in the inner magnetosphere, Journal of Geophysical Research, 117, A08227, 2012.
[10] Y. Omura and Q. Zhao, Relativistic electron microbursts due to nonlinear pitch-angle scattering by EMIC triggered emissions, Journal of Geophysical Research, 118, pp. 5008-5020, 2013.
.

Some Linguistic Problems with the Modelling of Speech Production

Damyan Atanasov Damyanov
Technical University of Sofia, Bulgaria
Sofia, Bulgaria
ellov@abv.bg

Keywords: Speech signal processing, speech production modelling, linguistic modelling.

Abstract: This paper focuses on the linguistic problems, when modelling the speech production. Most of the speech production algorithms, widely used in the practise, are developed in the early 70-ties. Moreover, when these algorithms were sophisticated in the 80-ties and 90-ties, the made the assumption, that the speaker speaks an Indo-European language, and more specific an Anglo-Saxon language. The paper throws some light on the linguistic problems when modelling the speech production of a speaker, which speaks a non-Indo-European language, such as Uralic or Altaic one. The paper presents new algorithms for speech production modelling, which are completely independent of the language, which the speaker is speaking, and are with accordance with computational power the state of the art computer systems.

Author Index

Author Index

ICTRS 2014

Proceedings of ICTRS 2014
Third International Conference on Telecommunications and Remote Sensing
ISBN: 978-989-758-033-8
http://www.ictrs.org